NASA/TM–2016-218973

Finite Element Analysis and Test Results Comparison for the Hybrid Wing Body Center Section Test Article

Adam Przekop, Dawn C. Jegley,
Marshall Rouse, and Andrew E. Lovejoy
Langley Research Center, Hampton, Virginia

April 2016

NASA STI Program . . . in Profile

Since its founding, NASA has been dedicated to the advancement of aeronautics and space science. The NASA scientific and technical information (STI) program plays a key part in helping NASA maintain this important role.

The NASA STI program operates under the auspices of the Agency Chief Information Officer. It collects, organizes, provides for archiving, and disseminates NASA's STI. The NASA STI program provides access to the NTRS Registered and its public interface, the NASA Technical Reports Server, thus providing one of the largest collections of aeronautical and space science STI in the world. Results are published in both non-NASA channels and by NASA in the NASA STI Report Series, which includes the following report types:

- TECHNICAL PUBLICATION. Reports of completed research or a major significant phase of research that present the results of NASA Programs and include extensive data or theoretical analysis. Includes compilations of significant scientific and technical data and information deemed to be of continuing reference value. NASA counter-part of peer-reviewed formal professional papers but has less stringent limitations on manuscript length and extent of graphic presentations.

- TECHNICAL MEMORANDUM. Scientific and technical findings that are preliminary or of specialized interest, e.g., quick release reports, working papers, and bibliographies that contain minimal annotation. Does not contain extensive analysis.

- CONTRACTOR REPORT. Scientific and technical findings by NASA-sponsored contractors and grantees.

- CONFERENCE PUBLICATION. Collected papers from scientific and technical conferences, symposia, seminars, or other meetings sponsored or co-sponsored by NASA.

- SPECIAL PUBLICATION. Scientific, technical, or historical information from NASA programs, projects, and missions, often concerned with subjects having substantial public interest.

- TECHNICAL TRANSLATION. English-language translations of foreign scientific and technical material pertinent to NASA's mission.

Specialized services also include organizing and publishing research results, distributing specialized research announcements and feeds, providing information desk and personal search support, and enabling data exchange services.

For more information about the NASA STI program, see the following:

- Access the NASA STI program home page at http://www.sti.nasa.gov

- E-mail your question to help@sti.nasa.gov

- Phone the NASA STI Information Desk at 757-864-9658

- Write to:
  NASA STI Information Desk
  Mail Stop 148
  NASA Langley Research Center
  Hampton, VA 23681-2199

NASA/TM–2016-218973

Finite Element Analysis and Test Results Comparison for the Hybrid Wing Body Center Section Test Article

Adam Przekop, Dawn C. Jegley,
Marshall Rouse, and Andrew E. Lovejoy
Langley Research Center, Hampton, Virginia

National Aeronautics and
Space Administration

Langley Research Center
Hampton, Virginia 23681-2199

April 2016

Available from:

NASA STI Program / Mail Stop 148
NASA Langley Research Center
Hampton, VA 23681-2199
Fax: 757-864-6500

Abstract

This report documents the comparison of test measurements and predictive finite element analysis results for a hybrid wing body center section test article. The testing and analysis efforts were part of the Airframe Technology subproject within the NASA Environmentally Responsible Aviation project. Test results include full field displacement measurements obtained from digital image correlation systems and discrete strain measurements obtained using both unidirectional and rosette resistive gauges. Most significant results are presented for the critical five load cases exercised during the test. Final test to failure after inflicting severe damage to the test article is also documented. Overall, good comparison between predicted and actual behavior of the test article is found.

Table of Contents

List of Figures

List of Tables

1. Introduction

1.1. Background

The Environmentally Responsible Aviation (ERA) Project was created to explore and document the feasibility, benefits and technical risk of new vehicle concepts and enabling technologies to reduce aviation's impact on the environment, primarily by reducing fuel burn and, consequently, emissions, as well as lowering community noise levels.[1] These activities support the NASA Aeronautics Research Mission Directorate Strategic Thrust 3, defined as "ultra-efficient commercial vehicles: pioneer technologies for big leaps in efficiency and environmental performance." The Airframe Technology subproject within the ERA Project was charged with developing structural concepts to enable airframe weight reduction of at least 10% compared to state-of-the art airframe technologies.[2]

Finite element analysis (FEA) was applied throughout the task as the primary analysis tool. FEA was first used to develop structural concepts and to design test articles, including the large-scale test article described in this document. FEA was also used to guide the test sequence and instrumentation. Thus, successful completion of the task was largely predicated on developing and exercising a reliable FEA. This report documents the post-test comparison of acquired measurements using predictive FEA.

1.2. Hybrid Wing Body Configuration

One of the vehicle concepts explored within the ERA Project was the hybrid wing body (HWB) configuration shown in Figure 1. Relative to a conventional "tube-and-wing" configuration, the HWB concept offers a potential for significantly improved aerodynamics, in particular, reduced drag and improved lift-to-drag ratio. The HWB configuration can also be advantageous in reducing community noise by using its large projected body surface to shield the noise generated by a top-mounted propulsion system. The HWB concept, however, presents several inherent challenges, including those stemming from the requirement to transfer wing loads through the entire pressurized center fuselage section that is confined by flat or nearly flat panels. A schematic of multi-axial loads acting on the HWB center section crown panel is also shown in Figure 1.

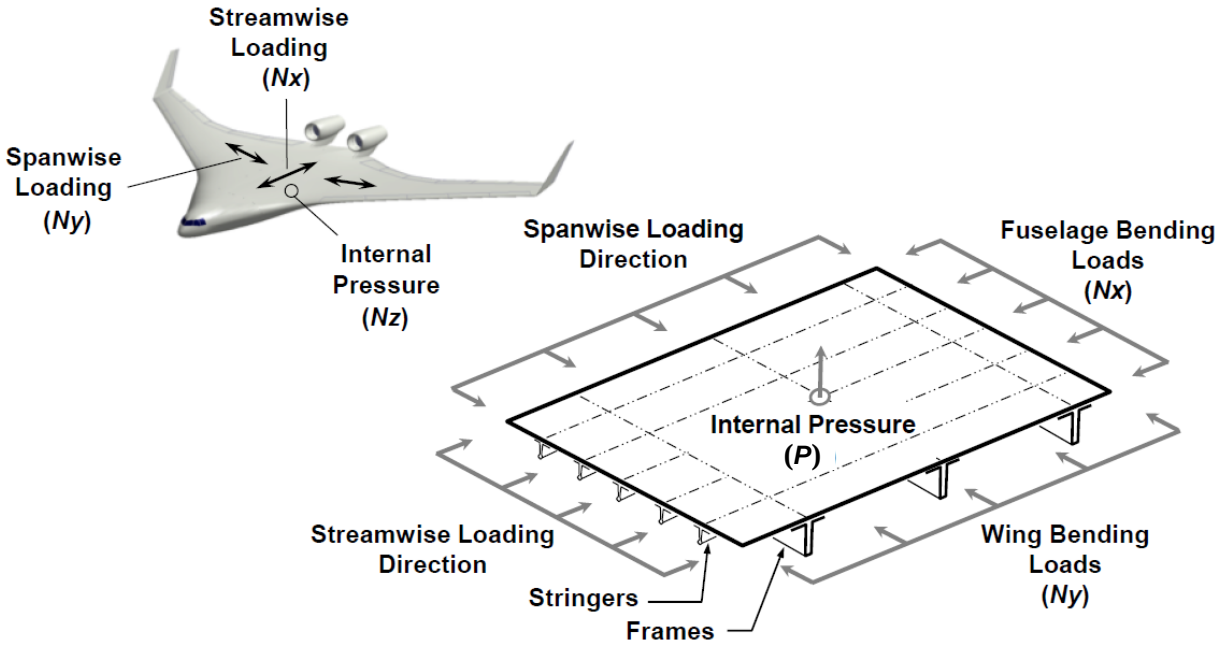

Figure 1. HWB configuration and center section crown panel loads.

1.3. Stitched Composite Structural Concept

The primary structural concept being pursued as an important part of the next generation airframe technology, capable of meeting the demanding structural requirements of the HWB configuration is the Pultruded Rod Stitched Efficient Unitized Structure (PRSEUS) concept[2-7] illustrated in Figure 2. The concept is being developed in a collaboration between NASA and The Boeing Company (Boeing). The PRSEUS structure is highly integrated, structurally efficient, and has damage-arresting capabilities. In this concept, a stitched carbon-epoxy material system is used. By stitching through the thickness of a dry material system, the labor associated with panel fabrication and assembly can be significantly reduced. When stitching through the thickness of pre-stacked skin, stringers, and frames, the need for mechanical fasteners is almost eliminated. In addition, stitching reduces delamination and improves damage tolerance, allowing for a lighter structure with more gradual failures than traditional layered composites that do not have through-the-thickness reinforcement.

The PRSEUS concept consists of carbon-epoxy panels fabricated from dry components stitched together, after which the resin is infused in an oven while the panel is subjected to vacuum pressure. Skins, flanges, and webs are composed of layers of carbon material that are knitted into multi-ply stacks. A single stack has the thickness of 0.052 in. and comprises seven plies with stacking sequence [+45, −45, 0, 90, 0, −45, +45] and percentages of the 0, 45 and 90-degree fibers equal to 44.9, 42.9, and 12.2, respectively. Several knitted stacks are used to build up the desired thickness and configuration. Stiffener flanges are stitched to the skin using Vectran thread, and no mechanical fasteners are used for joining. To maintain the panel geometry during fabrication, first stiffeners, and then the skin, are placed in a tool for stitching prior to moving the assembly to a curing tool for consolidation in the oven. The stiffeners running in the 1-direction direction (stringers) consist of webs with unidirectional carbon fiber rods at the top of the web. The stack material forming the stiffener web overwraps the rod to form the stiffener cap. The stiffeners in the 2-direction (frames) are foam-filled sandwich structures. The manufacturing process is described in detail in reference 4.

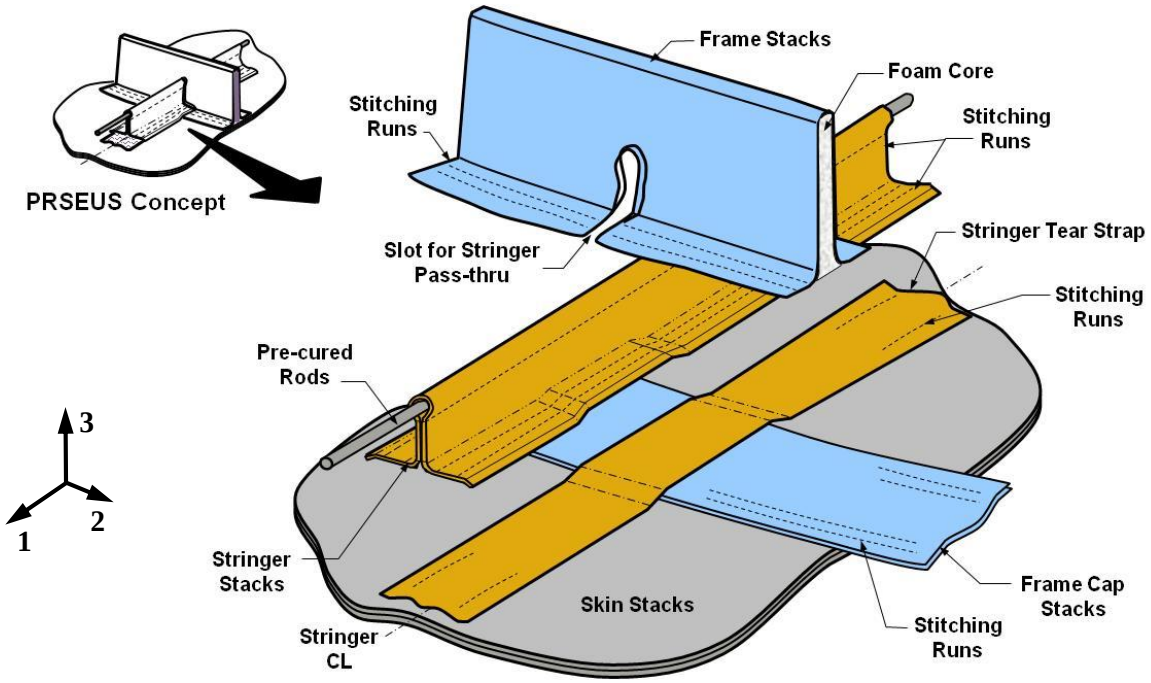

Figure 2. PRSEUS general assembly concept.

1.4. Hybrid Wing Body Center Section Test Article

The overall goal of the airframe technology subproject was to demonstrate that the PRSEUS concept can meet the demanding requirements of the next generation airframe technology. To meet this goal, achieving two key related objectives was necessary. The first key element was designing, manufacturing and testing a large test article representative of a HWB structure constructed using the PRSEUS concept under a combined loads environment.[4] The second key element was development and validation of an analysis methodology capable of reliably predicting the behavior of the afore-mentioned test article.[8-10] To achieve this goal, a preliminary design of a HWB aircraft in a 400,000 lb. maximum take-off weight category[5] was adopted as a reference configuration. The most critical center section of such an aircraft was scaled to 80% of its original size to comply with the limitations of the test apparatus and the manufacturing facilities.

The HWB center section test article is shown in Figures 3 and 4. The test article was approximately 30 ft. in span (along the X-axis, including the adaptor boxes shown in Figure 3), 14 ft. tall (along the Z-axis from the center keel to the crown panel), and 7 ft. wide (along the Y-axis between the bulkheads). The test article assembly comprised 11 PRSEUS panels and four sandwich panels. As shown in Figure 3, the 11 PRSEUS panels were: one crown, one floor, one center keel, two side keels (left and right), two upper bulkheads (forward and aft), two lower bulkheads (forward and aft), and two outer ribs (left and right). The four sandwich panels were two upper inner ribs and two lower inner ribs. All of the composite panels were mechanically joined at their edges by metallic fittings and fasteners.

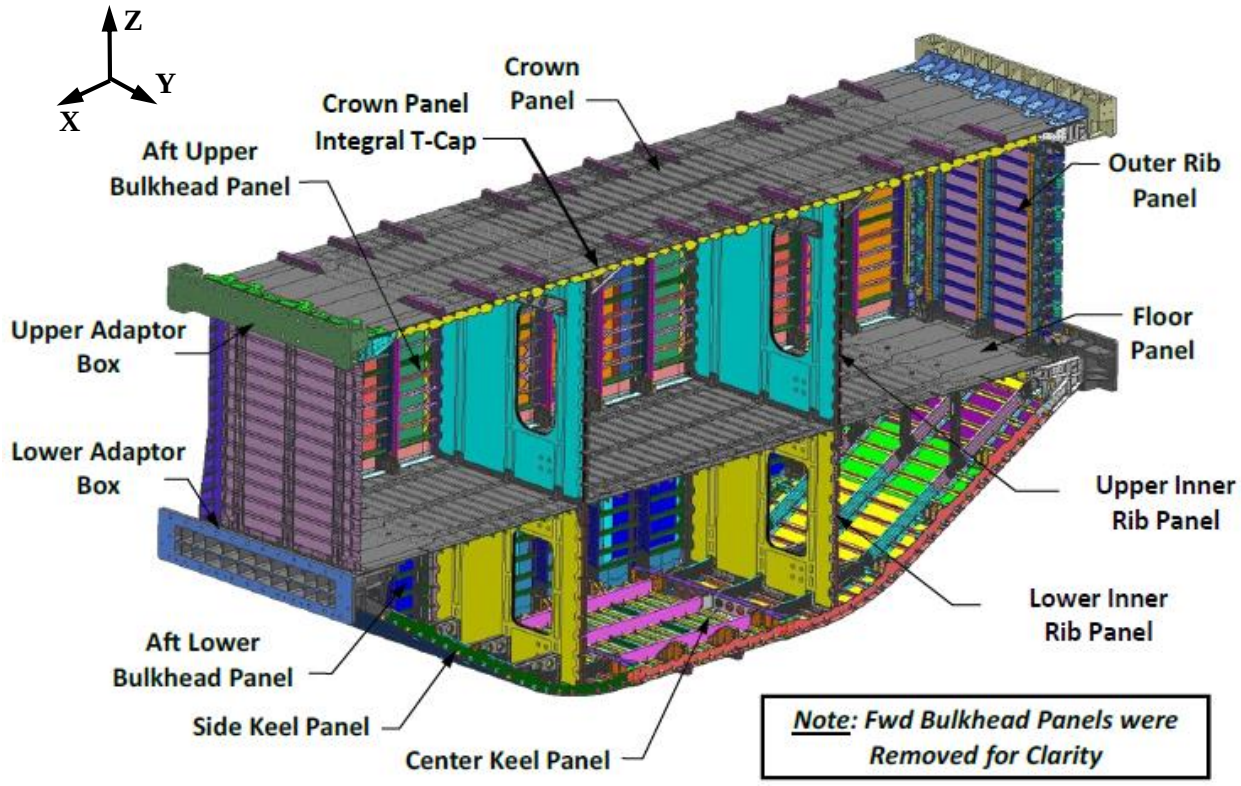

Figure 3. HWB center section test article isoview.

The crown, floor, center keel and side keel panels were each stiffened by three equally spaced frames oriented in the span-wise direction, i.e., along the X-axis. These panels also featured integral T-caps running parallel to frames in the proximity of panel edges. Unlike frames, T-caps not only transferred the span-wise loads, but were also used in the assembly process to mate the perpendicular panels. In the aforementioned panels, the stringers were oriented along the Y-axis. The outer rib panels and the upper and lower bulkhead panels had their frames running in the vertical (Z-axis) direction, while their stringers were running in the horizontal directions.

Figure 4. HWB center section test article in a transportation fixture.

The HWB center section article testing was performed at the Combined Loads Test System (COLTS) Facility[11] located at the NASA Langley Research Center (LaRC). Detailed reports and technical papers documenting testing,[12] imparting barely visible impact damage (BVID),[13] acoustic emission[14] and fiber optic strain measurements,[15] as well as non-destructive evaluations[16] not discussed in this report have been recently published.

2. Finite Element Model and Analysis

A finite element model (FEM) of the composite panels, metallic fittings, mechanical fasteners, and the COLTS test fixture was developed to support the test article design effort and is shown in Figure 5. Shell elements were used to represent composite panels and metallic fittings. The top sections of frames and the pultruded rods in panel stringers were represented by beam elements. Connector elements were used to represent fasteners. The loading fixtures of the COLTS facility were modeled using a combination of shell and beam elements and are annotated in Figure 5 to illustrate boundary conditions and the mechanical load introduction. The FEM contained approximately 4.5 million degrees of freedom. Material properties used in the analysis are presented in Table 1.

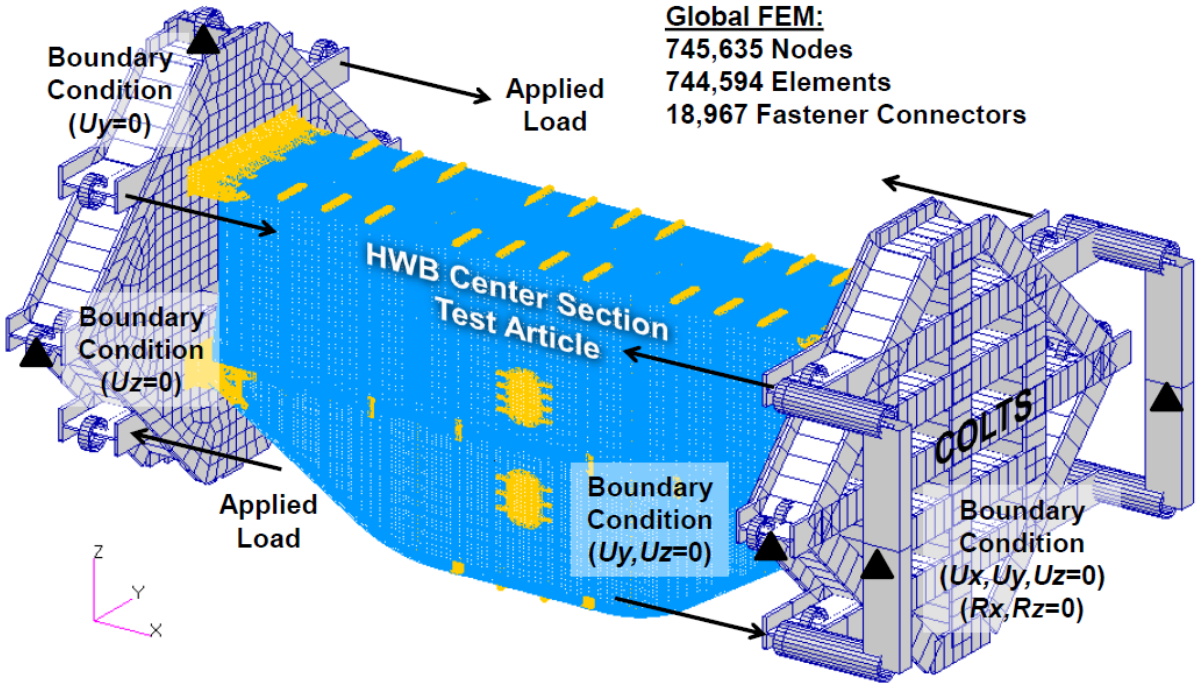

Figure 5. FEM of the test article and COLTS test fixture.

Table 1. Material properties.

Material	E or E_{11}/E_{22} (Msi)	ν or ν_{12}	G or G_{12} (Msi)
Composite Laminate (One Stack)	9.74/4.865	0.40	2.37
Stringer Rod	20.1	0.30	7.67
Frame Foam Core	0.01882	0.30	0.00725
Frame Fiberglass Core	1.7	0.30	0.65
Aluminum Fitting	10.3	0.33	3.87
Titanium Fastener	16.9	0.31	6.45
Inconel® Fastener	29.0	0.29	11.2

2.1. Critical Load Conditions

All test loads were guided by the transport aircraft category certification rquirements.[17] Based on the previously accomplished vehicle-level studies, five critical load cases were identified.[5] The first four were the flight conditions corresponding to pitch up and pitch down maneuvering loads, i.e., 2.5-g and −1.0-g, with and without the internal pressurization load of 1P. The fifth condition was the overpressure load. Considering an intended pressurization and cruising altitudes, the 1P load was chosen to be equal to 9.2 psi. The testing was conducted first up to the design limit load (DLL) levels followed by the design ultimate load (DUL) levels, where the DUL levels are 150% of the DLL levels. The list of the considered loads is presented in Table 2. Abbreviated load case names are used throughout the remainder of this document. For the first four load cases in Table 2 the DLL value is used as the load case abbreviation while for the pressure load only the DUL value is designated as such.

Table 2. Load cases considered.

Load Case	DLL	DUL
Pitch Down	−1.0-g	−1.5-g
Pitch Down with Pressure	−1.0-g + 1P	−1.5-g + 1.5P
Pitch Up	2.5-g	3.75-g
Pitch Up with Pressure	2.5-g + 1P	3.75-g + 1.5P
Overpressure	1.33P	2P

The applied loading vectors, as shown in Figure 5, correspond to the positive g-loads or wing up-bending. Under such a condition, the tops of the platens are pulled closer together while the bottoms of the platens are pushed farther apart. Under the negative g-loads or wing down-bending, the loading vectors are reversed relative to those shown in Figure 5. To gain a better insight into how the actuation presented using the FEM in Figure 5 was realized in the test facility, reference Figure 6 in which the platens and the hydraulic actuators of the COLTS facility are shown.

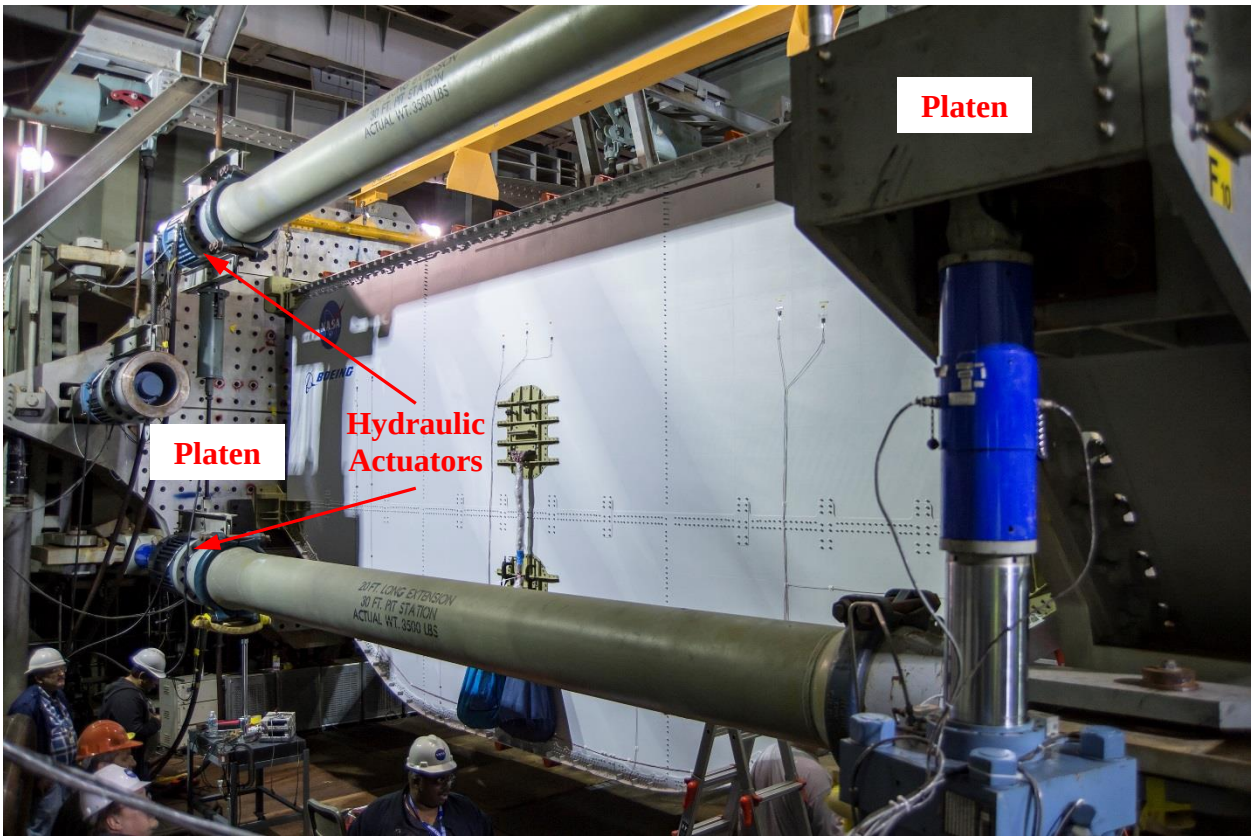

Figure 6. HWB test article installed in the COLTS facility.

2.2. Pristine and Damaged Conditions

The article was initially tested in the pristine condition under the loads shown in Table 2. With few exceptions discussed later in this section, loads were applied one-at-a-time, as a simple load-and-unload sequence, first to DLL and later to DUL levels. No known damages were identified after all the pristine condition tests were completed;[16] tests with intentionally inflicted BVIDs[18] followed the same sets of loads. The locations and energies used to inflict BVIDs are introduced in section 3.2. Since the tests with BVIDs have also not resulted in any immediately known damages (other than those intentionally inflicted), two out of five loads shown in Table 2 were extended to levels beyond DUL. Namely, the 2.5-g load was extended to 165% DLL (4.125-g) and the 2.5-g + 1P load was extended to 165% DLL of the 2.5-g load component (4.125-g), while the pressure load was kept constant at 150% DLL (13.8 psi). The loading sequence in which the above two loads were applied is shown in Figure 7. Segment 1 (shown as a black line) in Figure 7 corresponds to the last BVID DUL test, while segments 2 and 5 (shown as red lines) correspond to the beyond DUL tests. Segments 3, 4, and 6 (shown in blue) correspond to transitions between the two beyond-DUL conditions and the final unloading portion of the test. Since the beyond-DUL BVID did not result in immediately known damages, a severe damage, referred to later as a discrete source damage (DSD),[18] was inflicted to the crown panel before loading the test article until catastrophic failure was reached. The description of the DSD, including modification of the FEM, is presented in section 3.3.

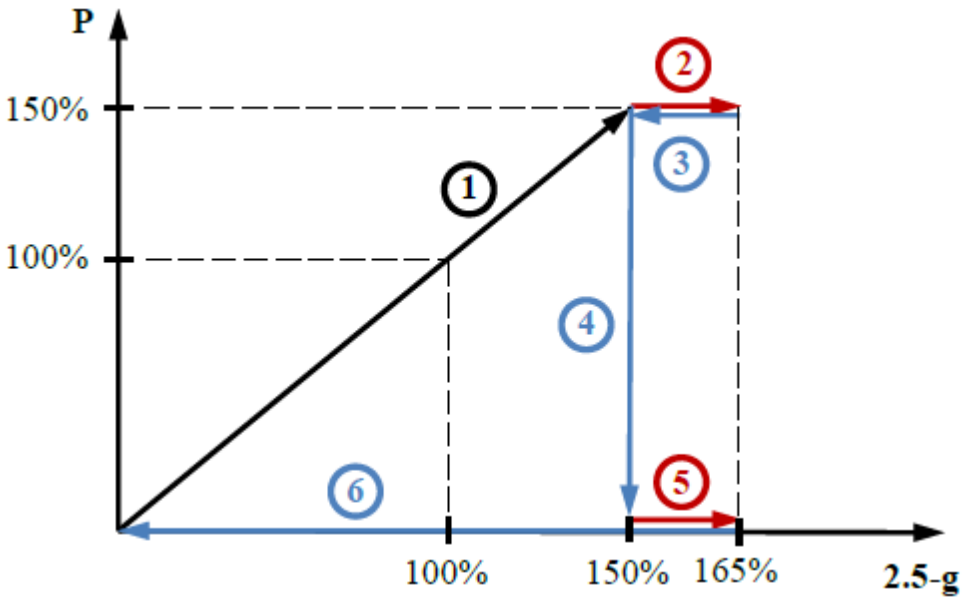

Figure 7. Beyond DUL test sequence.

While the tests in pristine and BVID conditions were conducted in two distinct test series, the FEA was executed only in the pristine condition, and no attempt was made to model BVIDs. Test results confirmed that the BVIDs did not produce any appreciable effects on the far-field response of the test article. The results corresponding to the far-field response are discussed first in the results section 3.1.

2.3. Numerical Simulation

A nonlinear solver available in the commercial FEA code MSC Nastran (solution 400)[19] was used to obtain the results presented herein. The previously obtained results from the initial linear FEA[10] (via MSC Nastran solution 101) are also presented on selective bases when they are deemed helpful in highlighting similarities or differences between test results and nonlinear and linear solutions.

3. Results

As indicated in section 2.2, the tests in pristine and BVID conditions were conducted in two separate series. The FEA, however, was executed only in the pristine condition, and no attempt was made to model BVIDs. Comparison of the test results from the pristine and BVID tests confirmed that the BVIDs produced no appreciable effects on the far-field response of the test article. Consequently, the comparison of the FEA and test results presented in this section is divided into two subsections pertaining to pristine or far field locations (section 3.1) and BVID locations (section 3.2). The FEM reflecting the DSD and results obtained for the DSD test are presented last, in section 3.3.

Several measurement techniques were used during testing, including: (1) video image correlation in three dimensions (VIC-3D),[20] which is one of commercially available digital image correlation products; (2) strain gauge measurements (both unidirectional and rosettes); (3) fiber-optic strain measurements; and (4) acoustic emission measurements. Still photography, video recordings inside and outside of the test article, and audio recordings were also acquired. The two most extensive and complete sets of measurements, i.e., VIC-3D and strain gauge measurements, are the primary scope of this document. The remaining fiber optic and acoustic emission measurements are documented in separate reports.[14, 15]

While VIC-3D measurements were limited to the outer moldline (OML) surfaces of the crown, bulkhead, and center keel panels, strain gauge data were acquired from both OML and inner moldline (IML) sides of the entire structure. Consequently, in the remainder of this section, the out-of-plane nonlinear displacement predictions at DUL are introduced first and compared with available full-field measurements obtained using the VIC-3D system. Deformations of selected panels for which the VIC-3D measurements were not available are illustrated with the FEA results only. Next, discrete strain FEA results are compared with strain gauge measurements at selected characteristic locations on the test article. Displacement plots introduced earlier are used to define general locations where the strain gauge data are compared with FEA predictions (the locations are designated with letters repeated later next to the strain figures). Strain figures also include insets showing schematics of a specific strain gauge placement. For the unidirectional strain gauges, their colors in insets match the colors of test curves. Strain gauge numbers consistent with all other test documentation are included in the strain gauge plots. For the unidirectional gauges, their numbers are shown directly in plot legends. Since including much longer strain gauge rosette numbers was not practical within the plot legends, their designations are included in figure captions. The strain gauge numbering scheme adopted during the HWB center section testing is shown in Appendix A. The numbering scheme enables rapid identification of a specific panel, that panel's component, i.e., frame, stringer, T-cap or skin, and the surface on which a particular gauge was installed.

Strain gauge test measurements, strains obtained from the linear analysis, and strains obtained from the nonlinear analysis are presented as a function of the applied load. Such plots help to identify sections of the test article which responded in a nonlinear fashion and at what load level the nonlinear effects became apparent and significant. Results for the 2P load case are shown as a function of the pressure load where the 1P condition corresponds to 9.2 psi. For the remaining four load cases (−1-g, −1-g + 1P, 2.5-g, and 2.5-g + 1P), the results are shown as a function of the actuator load. For the −1-g + 1P and 2.5-g + 1P load cases, during both analyses and tests, pressure was applied proportionally to the actuator load. Minor departures from this nominal relationship in the test are discussed later in this section. The −1-g DLL and DUL levels correspond to actuator loads of 63.6 kips and 95.4 kips, respectively. The 2.5-g DLL and DUL levels correspond to actuator loads of 159 kips and 238.5 kips, respectively. The 2.5-g 165% DLL load corresponds to 262.4 kips actuator loads.

Minor manufacturing imperfections of the crown panel OML surface resulted in a rework of some sections of the panel. Specifically, repair patches were co-bonded to the skin sections as shown in Figure 8 with blue areas. The light blue sections correspond to the single-stack patch thickness and the dark blue sections correspond to the two-stack thickness. The presence of the repair patches was accounted for in the FEM. Local departures from symmetry in the measured and predicted displacement field results, shown subsequently in this section arise, at least partially, from the presence of these patches.

The pink features shown in Figure 8 are the external metallic fittings. Due to inherent limitations of the VIC-3D technique, the system was unable to acquire measurements in the vicinities of large surface discontinuities. Thus, the surroundings of such discontinuities will be blanked out in the VIC-3D images shown later in this section. The metallic fittings at the crown panel edges were not, however, the only features that interfered with the VIC-3D measurements and are presented here only as an example. Similar VIC-3D acquisition interferences were caused also on other panels and, apart from the external metallic fittings, stemmed from the presence of other sensors and associated wiring.

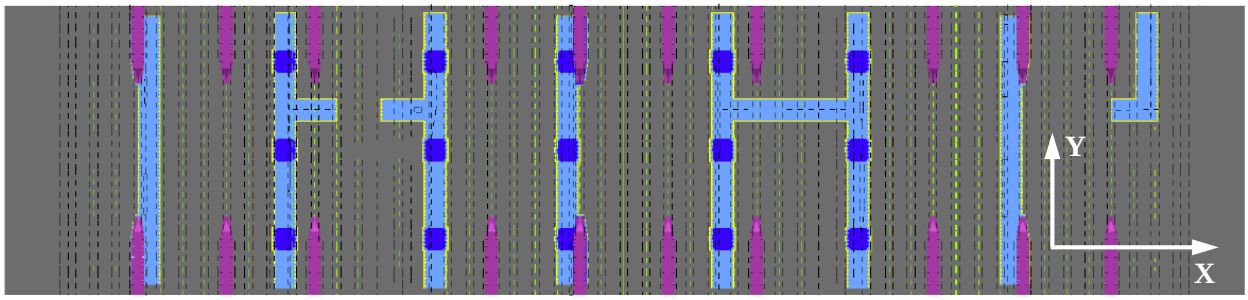

Figure 8. Co-bonded repair patches and external metallic fittings of the crown panel.

Finally, one unintended behavior of the COLTS testing apparatus noted during the tests warrants discussion. Namely, while reviewing displacements and strain recordings from the initial tests, it was concluded that one of the pins in the COLTS loading system was not rotating completely freely. A behavior consistent with the "sticky" pin effect was noticeable in several strain gauge plots as instantaneous small-amplitude strain jumps around an otherwise smooth and continuous strain trend developing as the loading was being applied. By examining magnitudes of the behavior recorded in particular sections of the structure, it was concluded that the location of the "sticky" pin was most likely on the loading platen side. Despite efforts to resolve the problem, the behavior persisted throughout the entire test effort. Consequently, unless a strain discontinuity is specifically discussed and attributed to another factor, small jumps in strain gauge plots should be regarded as originating from the imperfection of the COLTS load introduction system.

3.1. Pristine Locations

The load cases in this section are discussed in the order in which the BVID tests were conducted. This sequence was determined before the tests based on the predictive nonlinear FEA. The loads were applied beginning with the one resulting in the largest predicted margin-of-safety (MoS)[9] and concluding with the one resulting in the lowest MoS. Such a load application sequence was regarded as a risk mitigation measure.

3.1.1. −1-g Load

Under the −1-g load, the top of the test article was tensioned, while the bottom section was compressed. Out-of-plane deformations of crown, upper bulkhead, center keel, and side keel panels at DUL are presented in Figures 9 through 12, respectively. For the first three panels, FEA results are compared with available VIC-3D measurements, while for the side keel panel only the FEA results are shown.

It is seen in Figure 9 that the crown panel flexed upwards as the test article assembly was compressed at the bottom and tensioned at the top. The tensioning of the crown panel draped thin sections of the skin on the orthogonal grid of the substructure that comprises span-wise frames and perpendicular stringers. The location of the crown panel strain results are annotated in Figure 9. It is seen in Figure 13 (corresponding to location A in Figure 9) that the tensile strains on the top of the center frame at the mid-span location are

low, reaching only approximately 0.0012 in./in. at DUL, and exhibit nearly linear dependence on the applied load. The skin of the crown panel also experiences low strain levels under the −1-g DUL, as shown in Figure 14 (corresponding to location B in Figure 9) using the mid-bay back-to-back strains in the center section of the panel and in Figure 15 (corresponding to location C in Figure 9) using maximum and minimum principal strains in the side section of the panel. The skin strains also exhibit almost linear dependence on the applied loading. Good agreement between FEA and test results is found.

Due to the absence of pressure loading, the upper bulkhead did not experience meaningful strain levels that warrant discussion. Very small upper bulkhead out-of-plane deformations shown in Figure 10 attest to that observation.

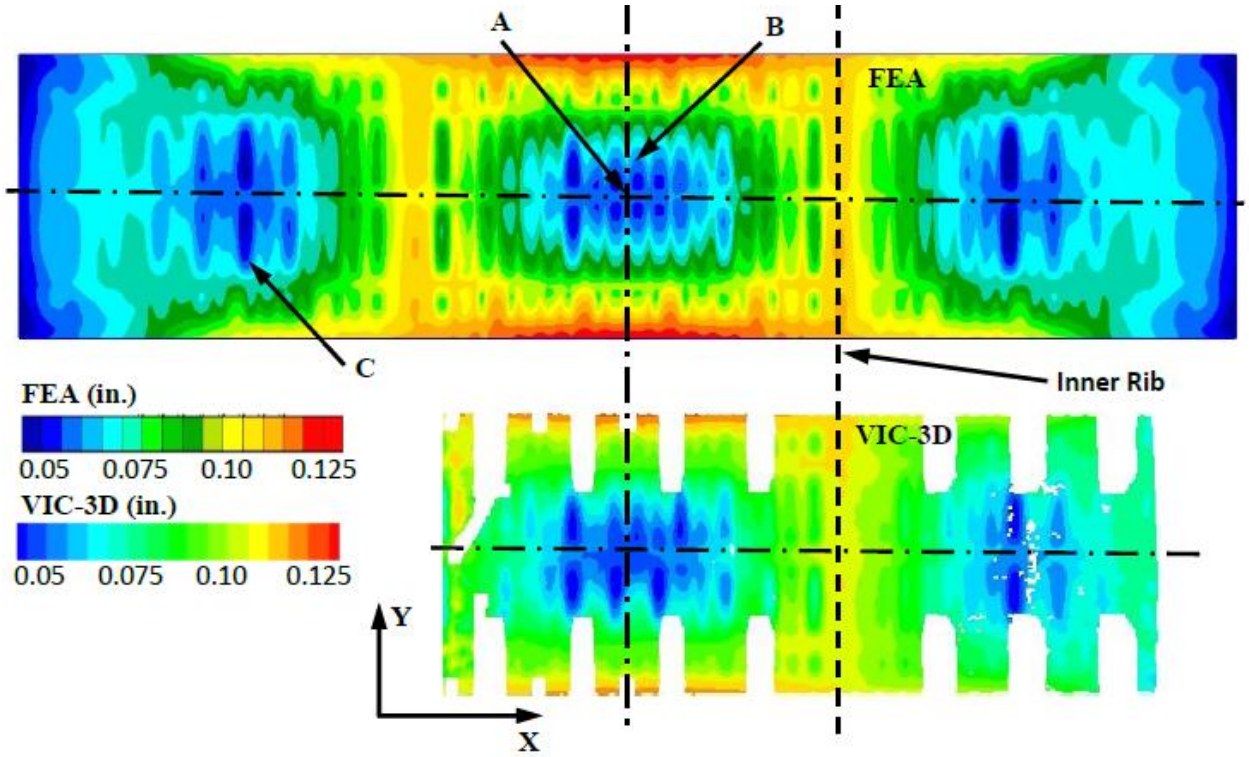

Figure 9. Out-of-plane deformation of the crown panel under −1-g DUL.

Under the −1-g load, the center keel panel was compressed span-wise. Strains in the center frame web of the center keel panel just above a frame-stringer intersection are shown in Figure 16 and correspond to location A in Figure 11. Compressive strain at DUL reaches a moderate level (approximately −0.0035 in./in.) and overall shows nearly linear characteristic. The back-to-back skin strains shown in Figure 17 (corresponding to locations B and C in Figure 11) display a very different behavior. The thin skin sections between frames and stringers buckle at a very low load of approximately 40 kips actuator load, corresponding to about −1-g. What is interesting to observe in the two plots in Figure 17 is that in the top plot, the nonlinear solution and test results agree well, while in the bottom plot, the top gauge prediction matches closely the bottom gauge test measurement and vice versa. Since the frames and stringers are placed in equal intervals of 24 in. and 6 in., respectively, the skin bay arrangement can be considered periodic within the panel. Each identical skin bay section buckles at nearly identical load and has two stable post-buckled equilibria, deformed inward and outward, as a trivial isotopic compressed beam would have. Small manufacturing imperfections, not reflected in the FEM can, therefore, determine which of the two post-buckled deformations is triggered. Similarly, in the FEA, small numerical solver perturbations (e.g., finite precision of computations) can affect which equilibrium is adopted in the numerical solution. Consequently, the comparison of the nonlinear solution and test results is considered good for both locations

shown in Figure 17, while the linear solution clearly lacks the ability to capture the dominant buckling behavior. Furthermore, the behavior where a buckled skin section of a panel deforms in the direction opposite to the one predicted by FEA is not unique to the center keel panel nor the −1-g load case. An additional example of a similar behavior occurring on the crown panel under the 2.5-g load is discussed later in section 3.1.4.

Contrary to the center keel panel, skin buckling does not occur in the side keel panel at load less than the DUL, as shown in Figure 12. Strains at the top of the center frame of the side keel panel are shown in Figure 18. The minimum strain of approximately −0.0014 in./in. at DUL is considered low, and in general, strain levels in the side keel panel are lower than those in the center keel panel. Side keel panel stringers do not carry appreciable loads due to the absence of a pressure load. As a result, a more detailed discussion of the side keel panel results is not warranted for the −1-g load.

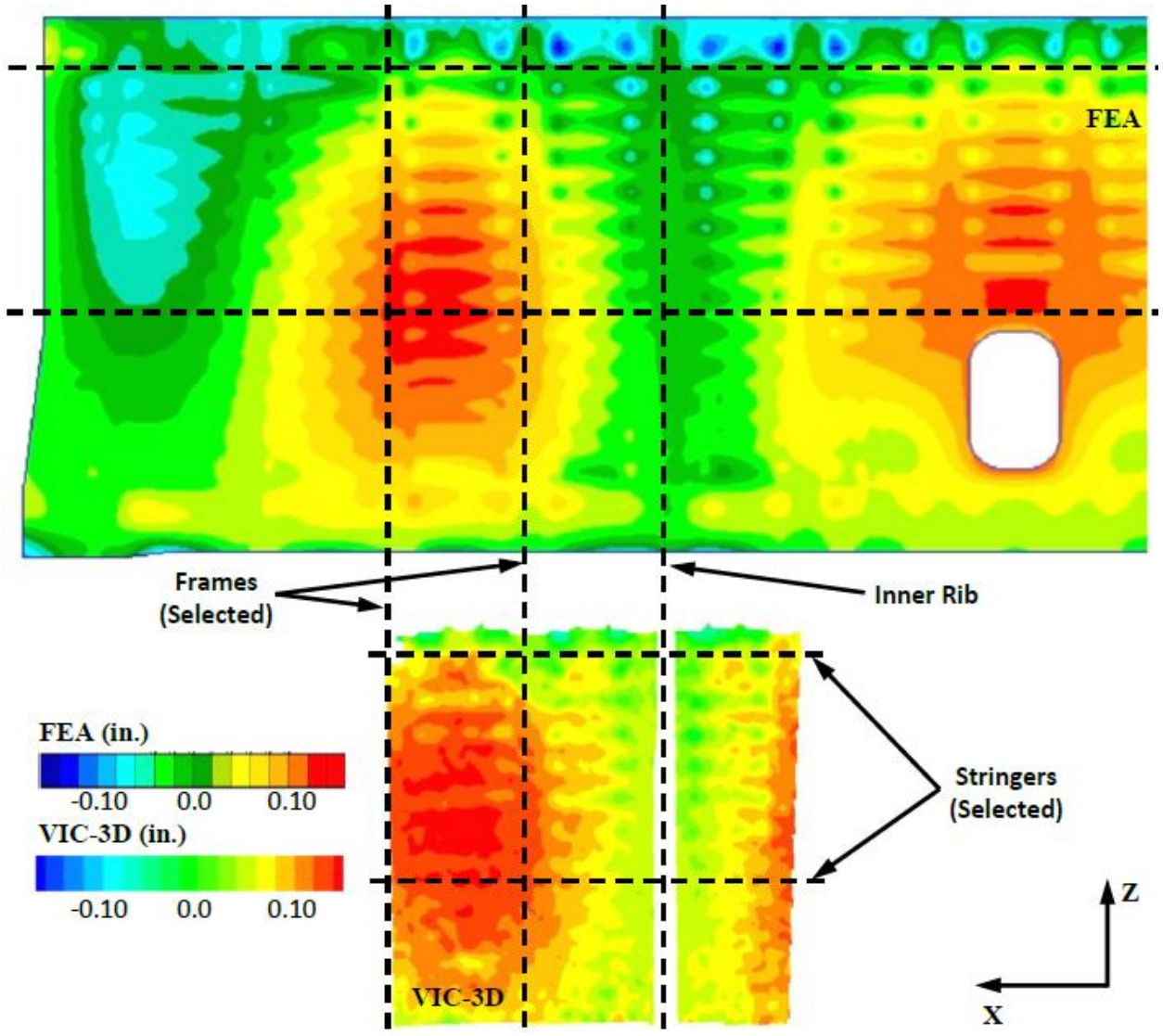

Figure 10. Out-of-plane deformation of the upper aft bulkhead panel under −1-g DUL.

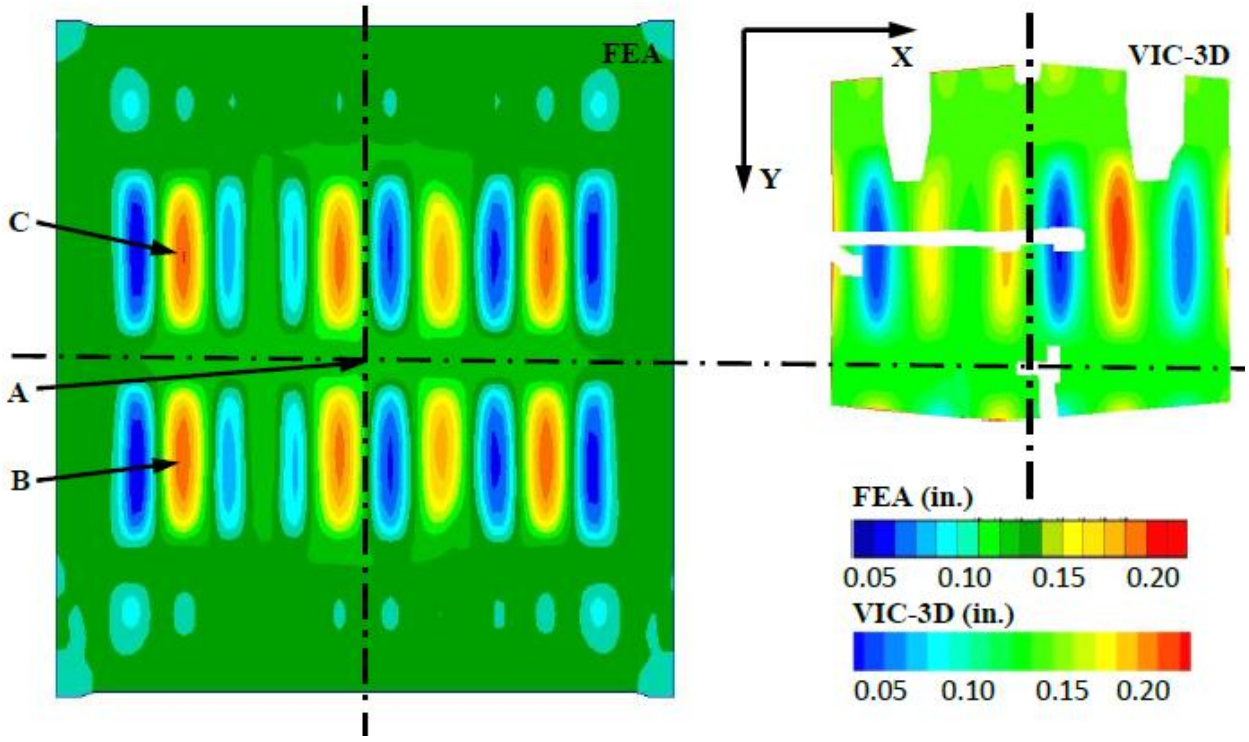

Figure 11. Out-of-plane deformation of the center keel panel under −1-g DUL.

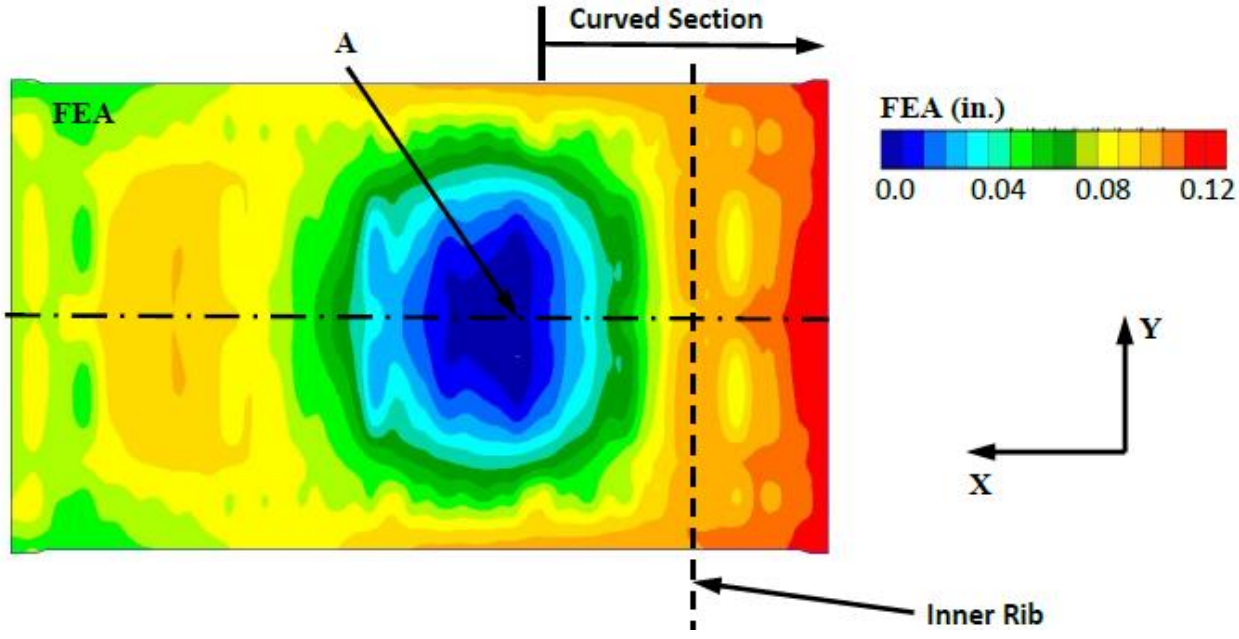

Figure 12. Z-component deformation of the side keel panel under −1-g DUL.

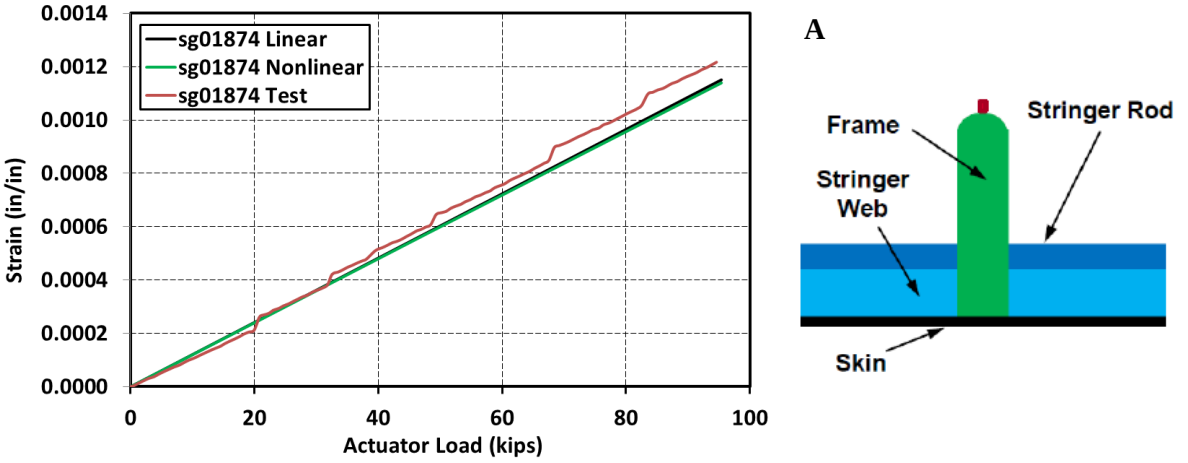

Figure 13. Strains at the top of the crown panel center frame up to −1-g DUL.

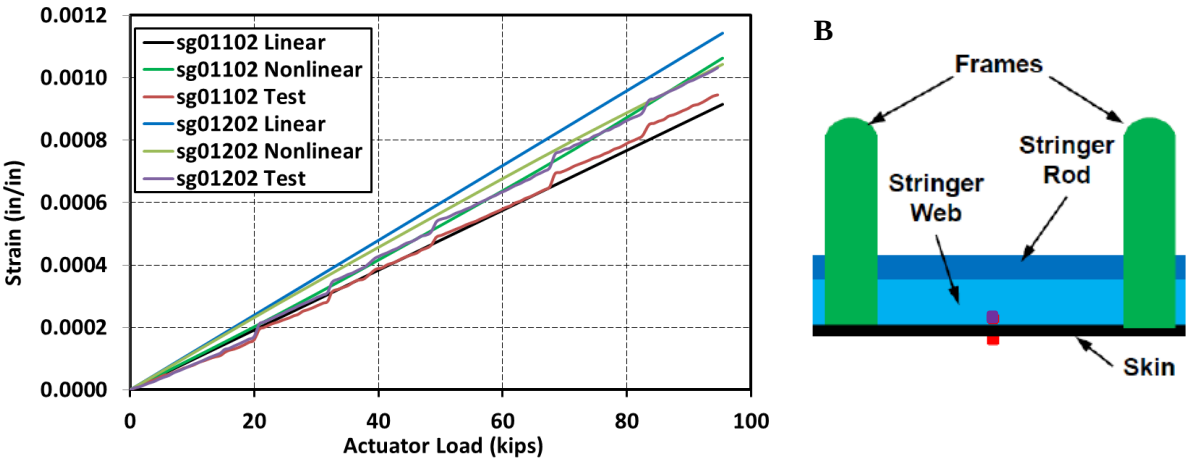

Figure 14. Crown panel back-to-back skin strains up to −1-g DUL.

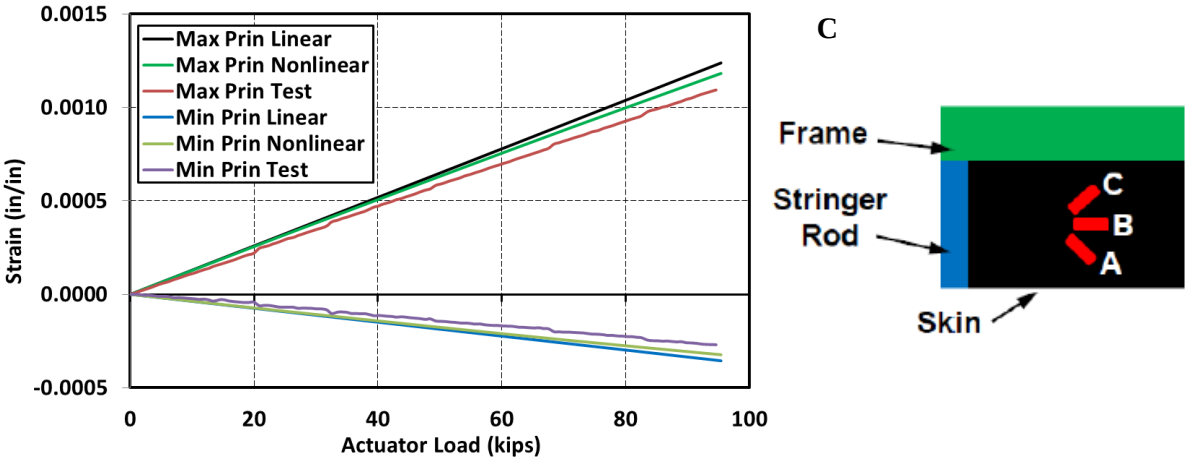

Figure 15. Principal strains in the crown panel skin up to −1-g DUL (sg01287A/sg01288B/sg01289C).

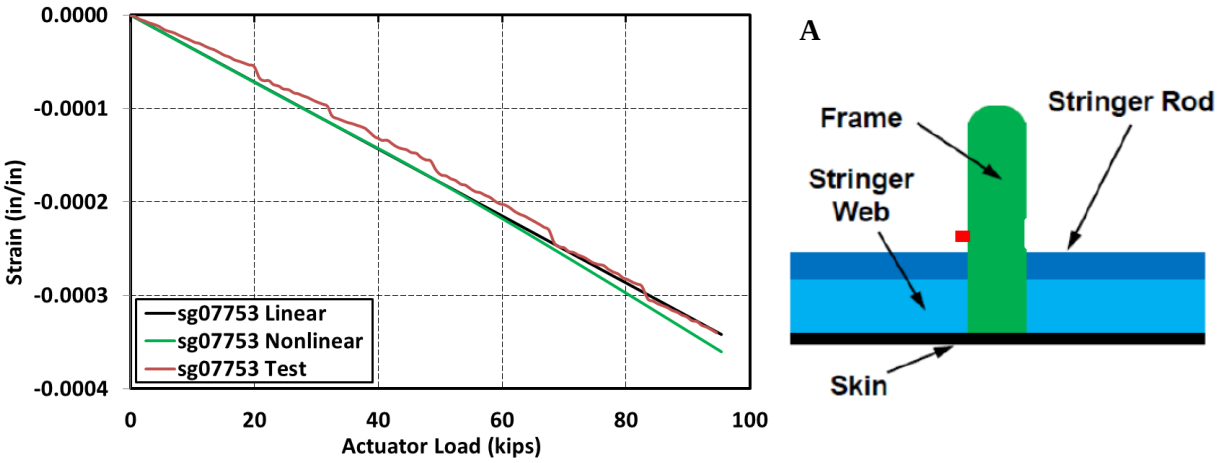

Figure 16. Strains in the web of the center keel frame up to −1-g DUL.

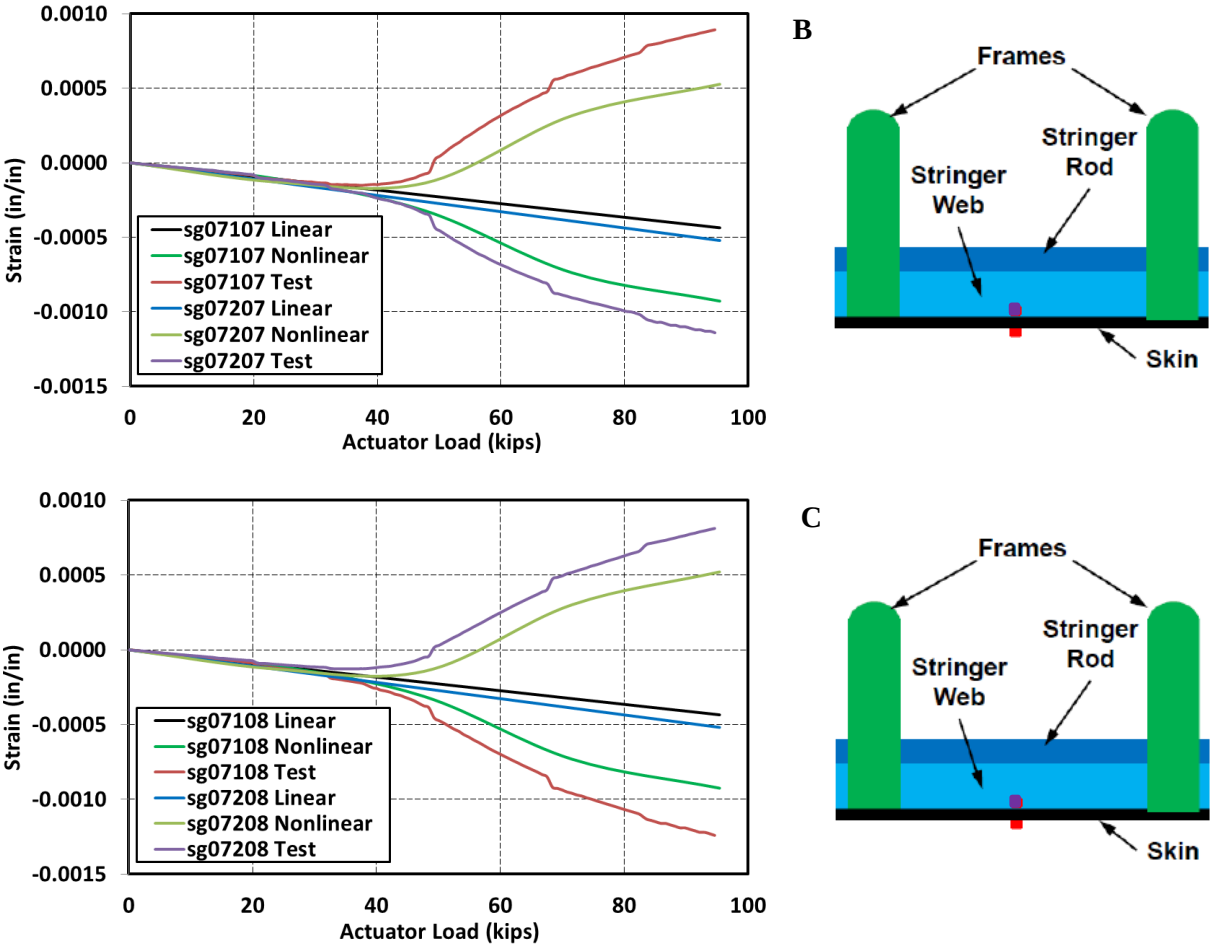

Figure 17. Center keel back-to-back skin strains up to −1-g DUL.

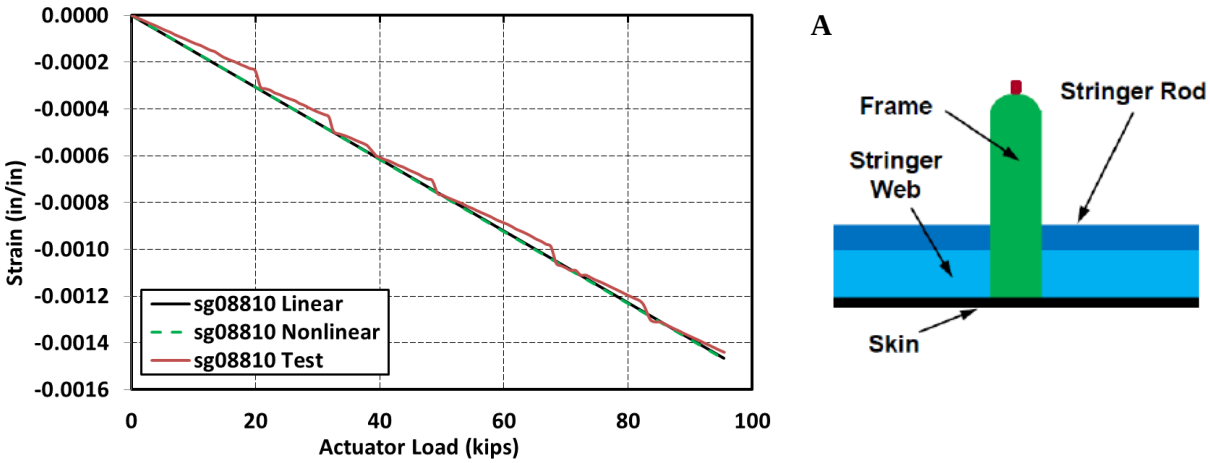

Figure 18. Strains at the top of the side keel frame up to −1-g DUL.

3.1.2. −1g + 1P Load

Under the −1-g + 1P load, the top of the test article was tensioned while the bottom section was compressed by the mechanical loads and the pressure load bowed outward unsupported sections of the external panels. Out-of-plane deformations of the crown, upper bulkhead, center keel, and side keel panels at DUL are presented in Figures 19 through 22, respectively. For the first three panels, the FEA results are compared with available VIC-3D measurements, while for the side keel panel only the FEA results are shown.

It is seen in Figure 19 that the entire crown panel not only flexes upwards as the test article assembly is compressed at the bottom and tensioned at the top (as previously shown for the −1-g DUL in Figure 9), but there is also a distinct contribution to the outward deformation attributable to the pressure load, best observed as the red area in the center of the panel. When comparing the out-of-plane deformation under the −1-g DUL and −1-g + 1P DUL one notices that the smallest deformations under the −1-g DUL are in the skin sections that drape over the frames and stringers (dark blue areas in Figure 9). By contrast, under the −1-g + 1P DUL, the same area experiences the largest out-of-plane deformations (red areas in Figure 19). The larger crown panel out-of-plane deformations, however, do not necessarily result in larger strain levels across the entire crown panel. It is seen in Figure 23 that the strain levels at the top of the mid-span center frame reached approximately only 0.0003 in./in. at DUL, i.e., are four times smaller than those under the −1-g DUL only (see Figure 13). At the same time, the strains vis-à-vis the frame on the OML skin surface, shown in Figure 24, are higher, reaching 0.0017 in./in. at DUL. Both, the frame top and the vis-à-vis OML skin location display nearly linear strain characteristics. To explain the smaller strain levels at the top of the frame under the −1-g + 1P DUL the following is considered. First, the mechanical load stretches the crown panel spanwise. Second, the internal pressure bows the panel outwards. Since the neutral bending axis of the frame is located somewhere between the frame root and the frame top, the outward bowing results in tension at the frame root and the adjacent OML skin, but in compression at the frame top. Thus, the pressure-induced compressive loads at the frame top compensate for a portion of the mechanically induced tension that is relatively uniform over the frame height. At the OML skin section, the tension loads resulting from pressure and mechanical load components are combined. This location therefore exhibits a much larger tension strain than the frame top.

Three features of the test strains in Figure 23 warrant additional discussion. First, the test strains depart from both linear and nonlinear predictions at the very beginning of the load application sequence (a red curve hump between 0 and 10 kips). This behavior is caused by the COLTS control system's inability to apply the pressure load proportionally to the mechanical load in the low load range. The second feature is the mild curve fluctuations after the initial hump. These fluctuations are caused by pressure range tolerance that the COLTS control system was exercising during the load application (effectively these are delays in

pressure system valves operations). The third feature is the test strain jump around 80 kips. This behavior likely originated from the "sticky" pin discussed in section 3, but is particularly obvious in Figure 23 due to a narrow strain scale range.

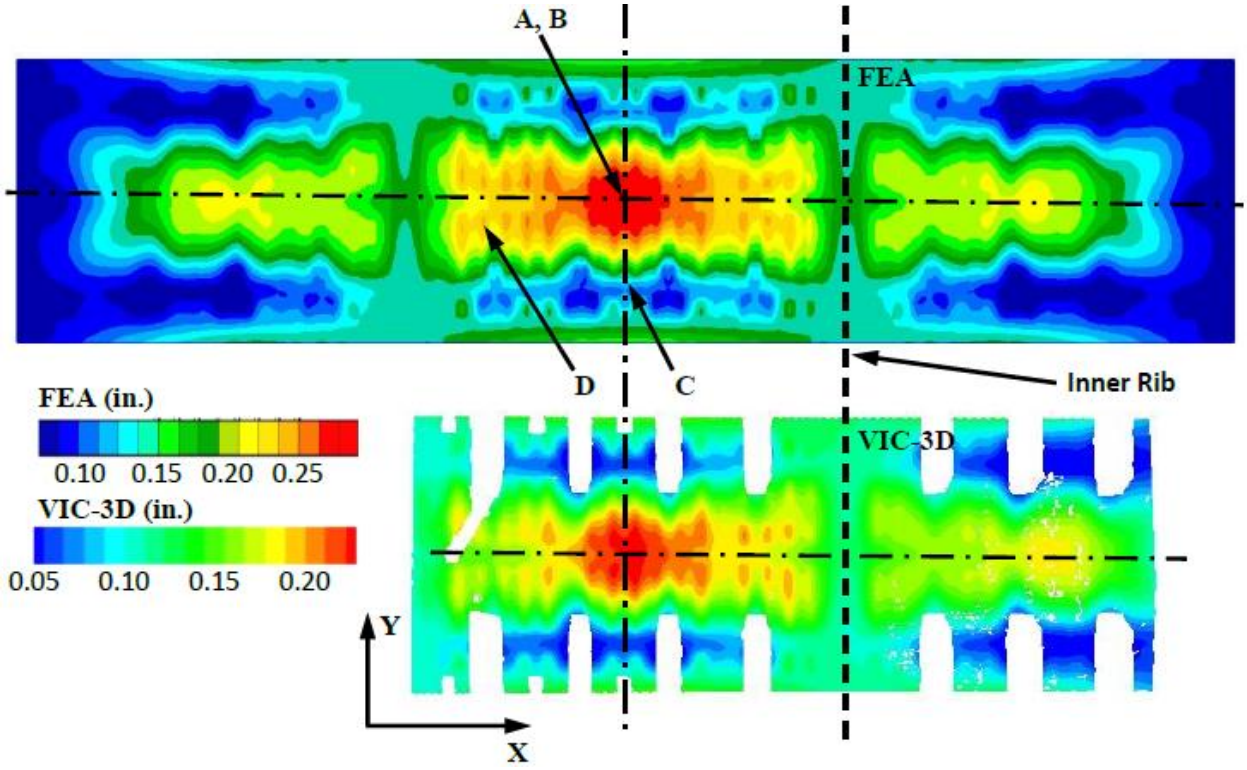

Figure 19. Out-of-plane deformation of the crown panel under −1-g + 1P DUL.

The strains on the top of the stringer cap (location C in Figure 19) are shown in Figure 25. While only negligible strains on stringer caps were predicted and measured under the −1-g DUL, the addition of the pressure load introduces meaningful loads to the stringers, resulting in strain levels of approximately 0.0026 in./in.

The back-to-back skin strains in the crown panel (location D in Figure 19) are shown in Figure 26 where a strongly nonlinear load versus strain characteristic can be observed. To explain the behavior, the in-plane and bending strain components of the total strain have to be discussed. By averaging the top- and bottom-measured (or OML surface- and IML surface-measured) strains, one can calculate the in-plane strain component. For all three sets of curves shown in Figure 26 (i.e., test, linear and nonlinear), this value at DUL of 95.4 kips is approximately 0.0015 in./in. Therefore, in terms of the in-plane strain component, all three data sets produce similar results. In contrast, the bending component, i.e., the difference between the in-plane strain and the top and bottom strains, is much larger for the linear solution than for the test data and nonlinear solution. The nonlinear analysis predicted the test behavior very well because it is capable of capturing the in-plane versus bending deformation coupling, which the linear analysis does not do. In other words, the structure has to experience in-plane stretching to permit large out-of-plane deformation. The larger the out-of-plane deformation, the even larger the in-plane stretching becomes, effectively acting to suppress the out-of-plane deformation in a nonlinear fashion. This behavior can be referred to as a hardening nonlinearity, as the constant rate of pressure-load application produces a lower and lower rate of out-of-plane deformation.

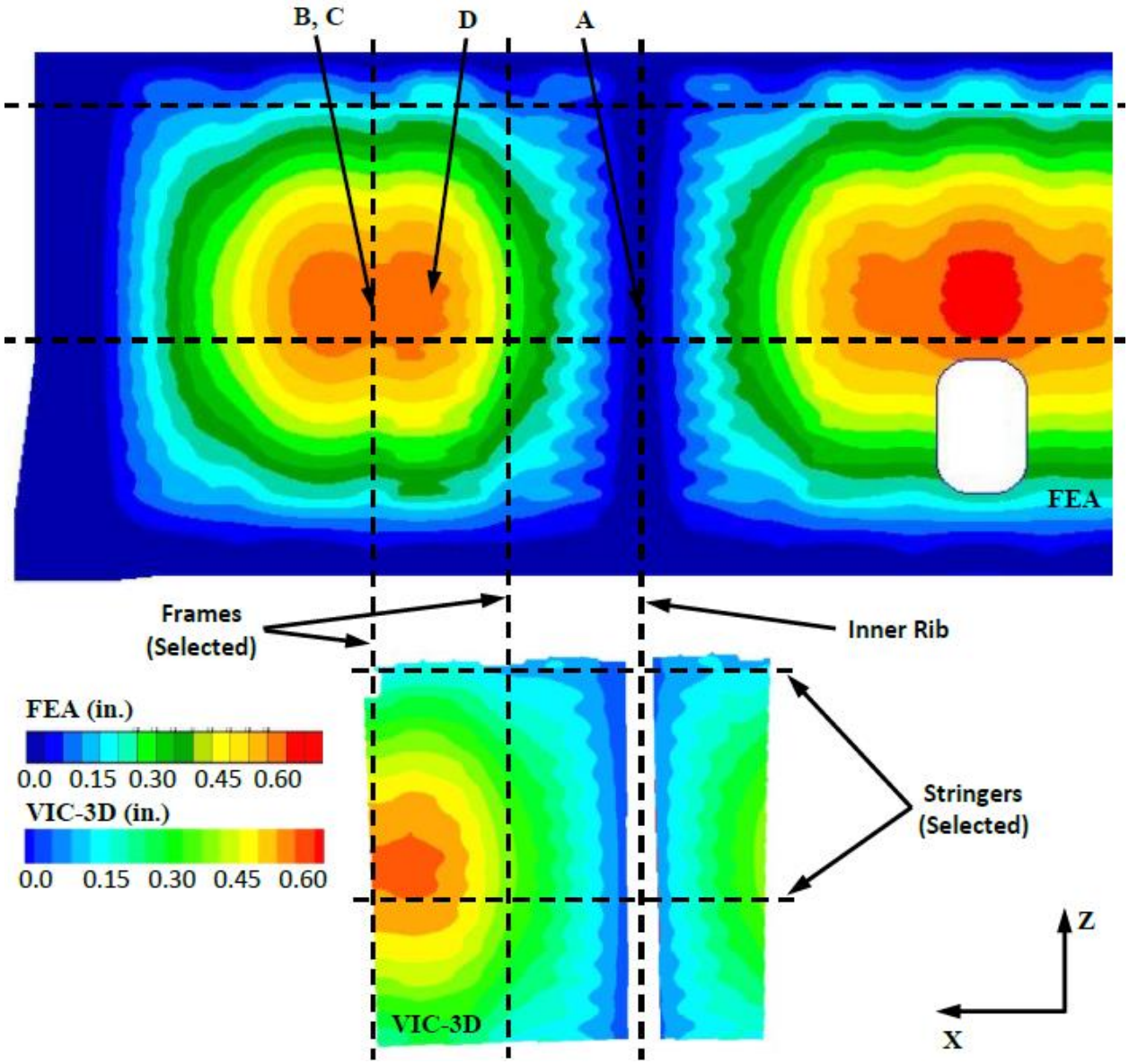

Figure 20. Out-of-plane deformation of the upper aft bulkhead panel under −1-g + 1P DUL.

The out-of-plane deformation of the upper aft bulkhead was clearly dominated by the pressure effects that caused the unsupported sections of the panel to bow outward, as seen in Figure 20. The strains at the top of the stringer in the proximity of the inner rib, effectively approaching a condition representative of a clamped boundary, are shown in Figure 27 and correspond to location A in Figure 20. A moderate strain level of approximately 0.0040 in./in. is reached in the test at DUL in a linear fashion. The predicted strains are also linear, but the strain values predicted by linear and nonlinear analyses are slightly higher. The difference, at least in part, can be attributed to a simplified stringer rod modeling. Due to the size of the FEM, the pultruded rods were modeled as beam elements coinciding with the top edge of the stringer blade discretized with shell elements. Consequently, the pultruded rod overwrap was not explicitly modeled, while the actual strain gauges on top of the stringer had to be installed on the overwrap rather than on the rod itself.

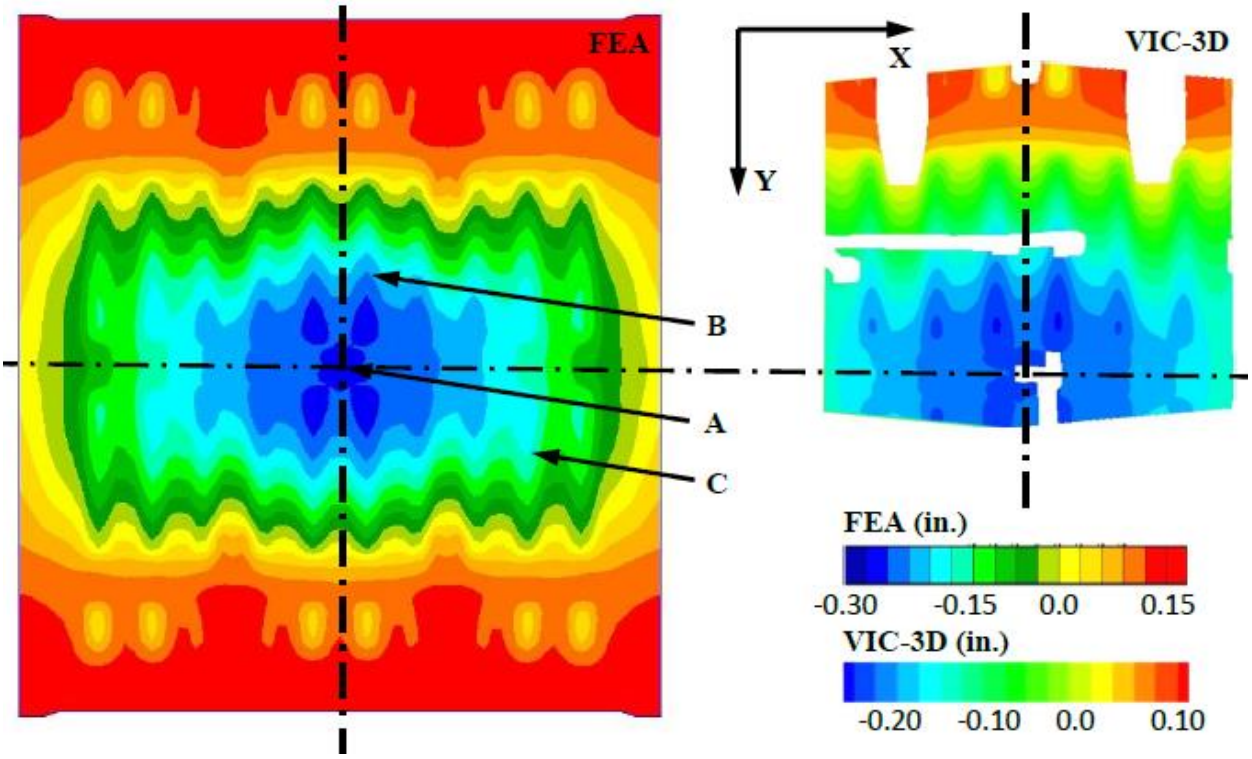

Figure 21. Out-of-plane deformation of the center keel panel under −1-g + 1P DUL.

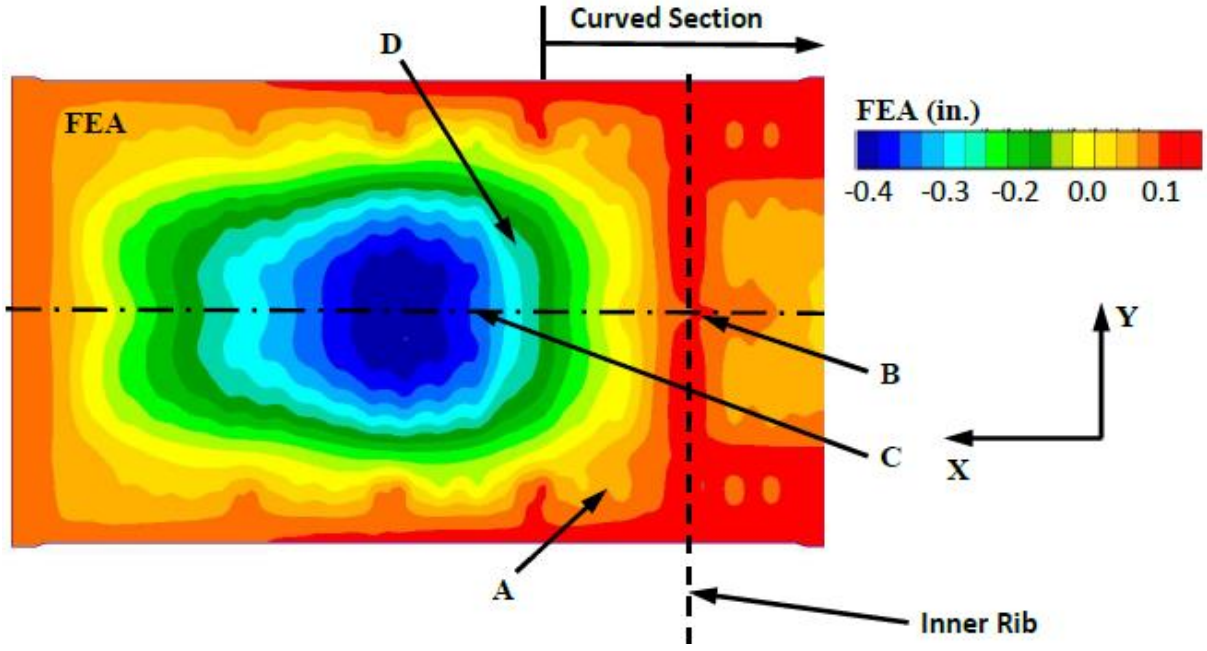

Figure 22. Z-component deformation of the side keel panel under −1-g + 1P DUL.

The strains at the top of the frame and the strains in a vis-à-vis frame location on the skin of the upper bulkhead panel are shown in Figures 28 and 29, respectively, and correspond to locations B and C in Figure 20. At the DUL, the top of the frame strains are approximately 0.0030 in./in. in compression and the skin strains are approximately 0.0020 in./in. in tension. These results are consistent with the pressure-induced outward bending dominating the response at this location, which is a significant distance from both the tensioned crown panel and from the compressed side and center keel panels induced by the −1-g load component. Good agreement between measured and predicted strains is found. The back-to-back upper bulkhead panel skin strains in the adjacent skin bay are shown in Figure 30 and correspond to location D in Figure 20. Low strain levels of approximately 0.0015 in./in. are measured at DUL and show strongly nonlinear characteristics. The measured strains are matched closely by the nonlinear predictions, but the linear analysis results are not accurate. Similar to the discussion of Figure 26, accounting for nonlinear coupling between out-of-plane and in-plane deformations is needed to obtain accurate predictions in the areas dominated by large amplitude pressure-induced bowing. More specifically, accounting for the in-plane stretching needed to achieve large out-of-plane deformation results in the previously discussed hardening type of the displacement response, which in turn suppresses the bending strain component of the response.

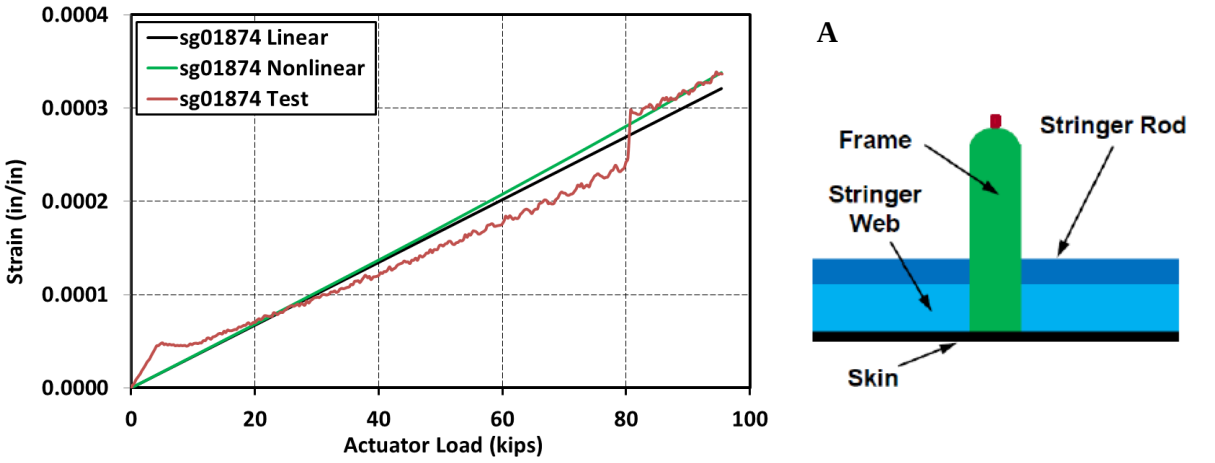

Figure 23. Strains at the top of the crown panel center frame up to −1-g + 1P DUL.

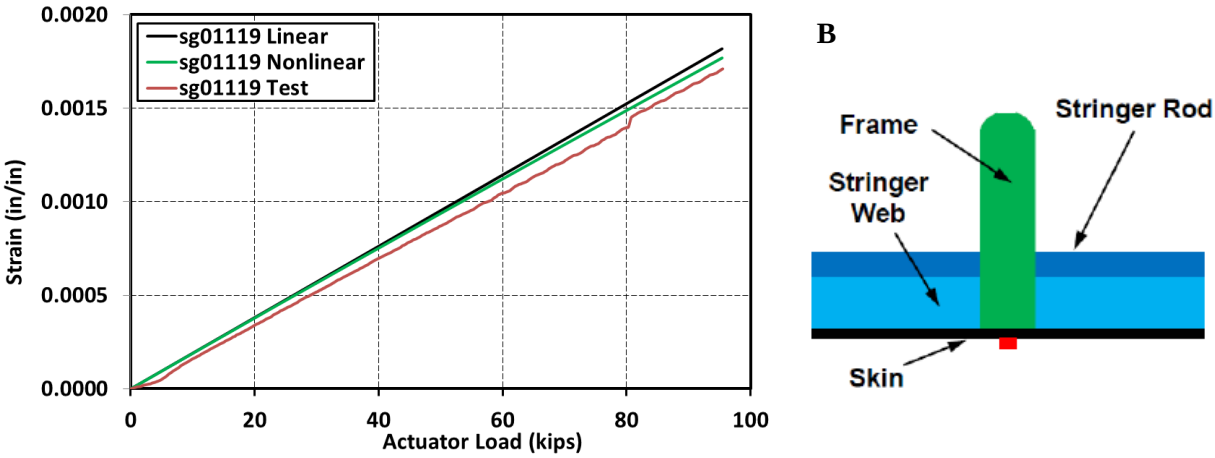

Figure 24. Strains in the skin below the crown panel center frame up to −1-g + 1P DUL.

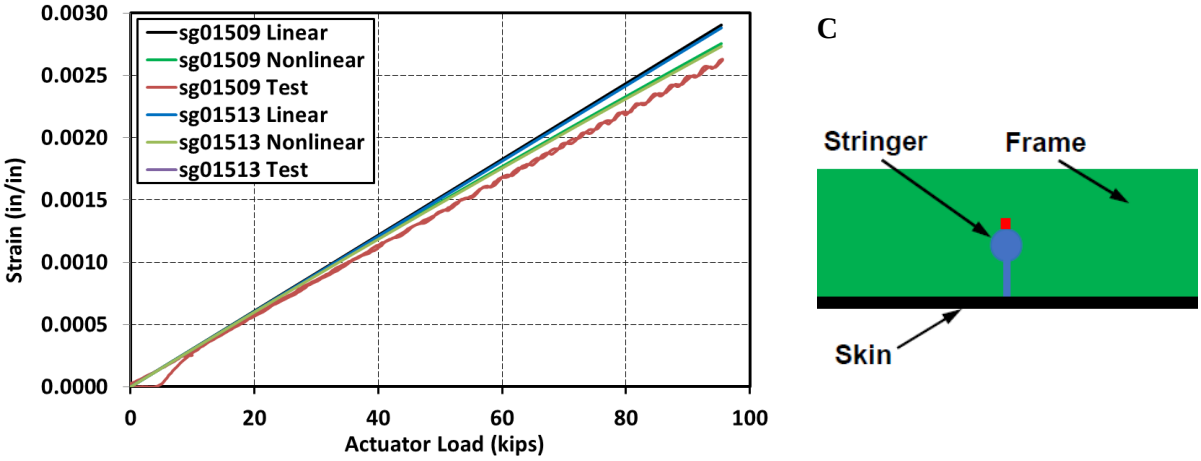

Figure 25. Strains at the top of the crown panel stringer up to −1-g + 1P DUL.

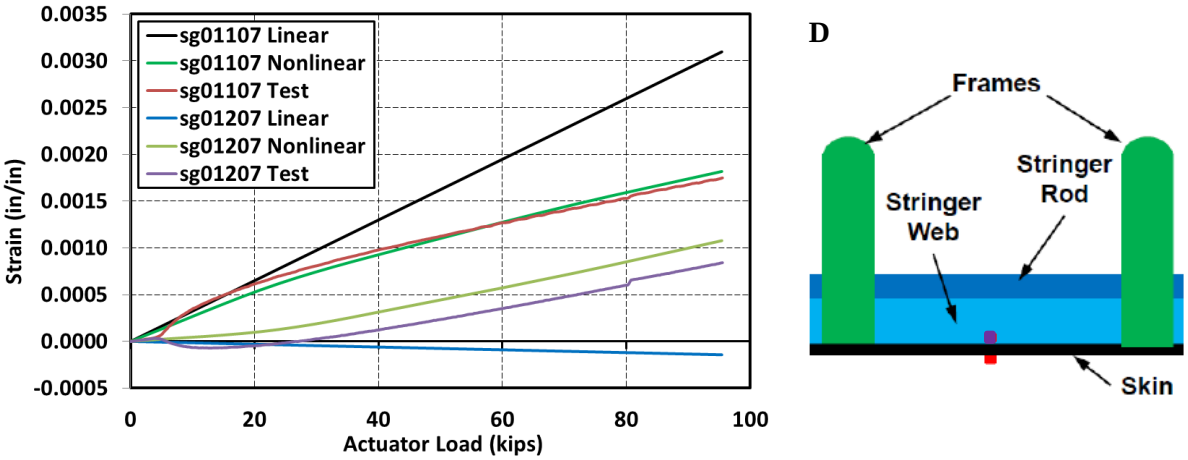

Figure 26. Crown panel back-to-back skin strains up to −1-g + 1P DUL.

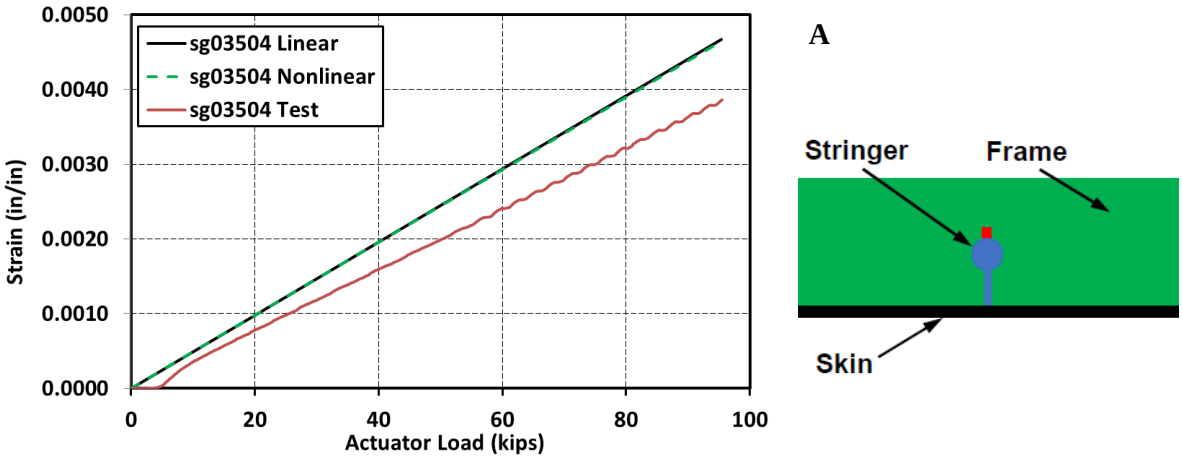

Figure 27. Strains at the top of the aft upper bulkhead panel stringer up to −1-g + 1P DUL.

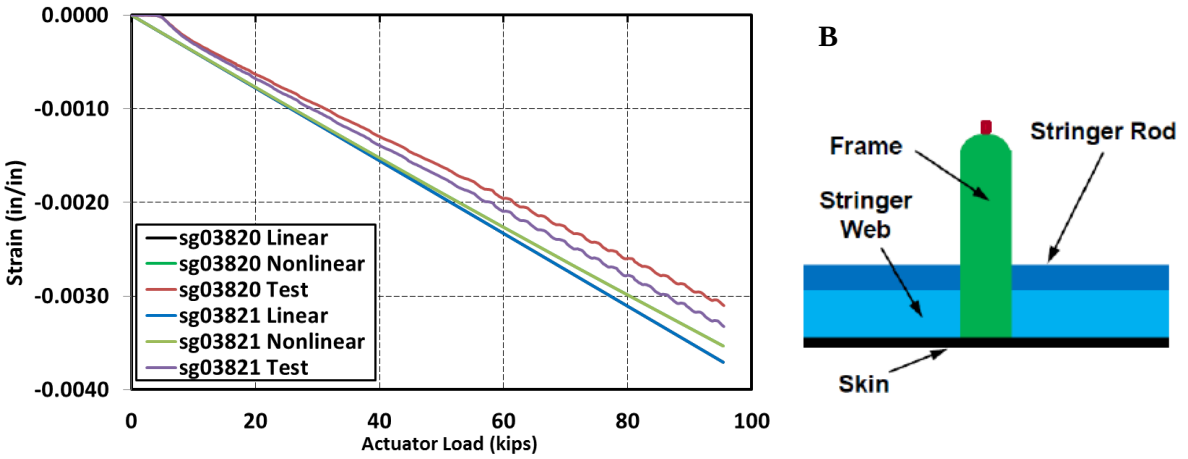

Figure 28. Strains at the top of the aft upper bulkhead panel frame up to −1-g + 1P DUL.

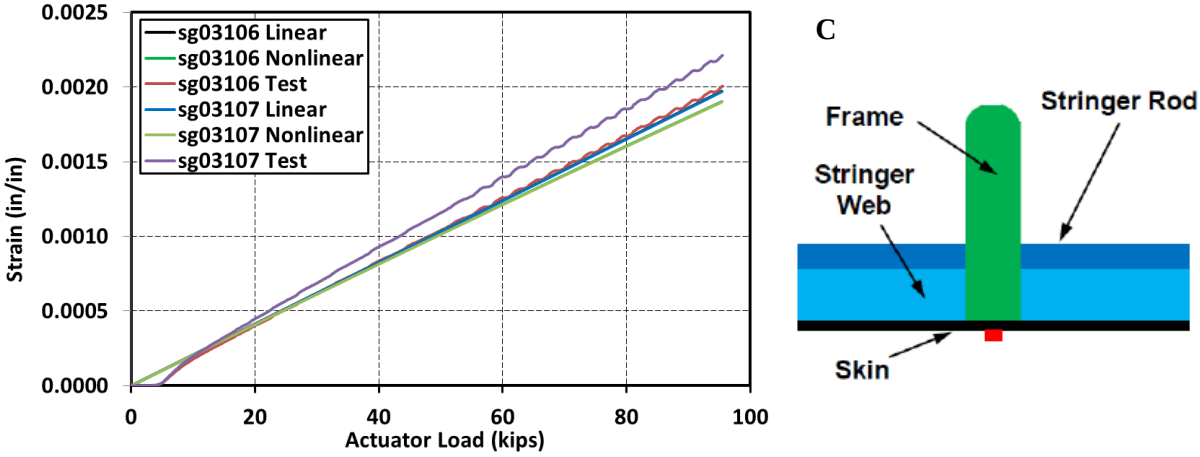

Figure 29. Strains in the skin below the frame of the aft upper bulkhead panel up to −1-g + 1P DUL.

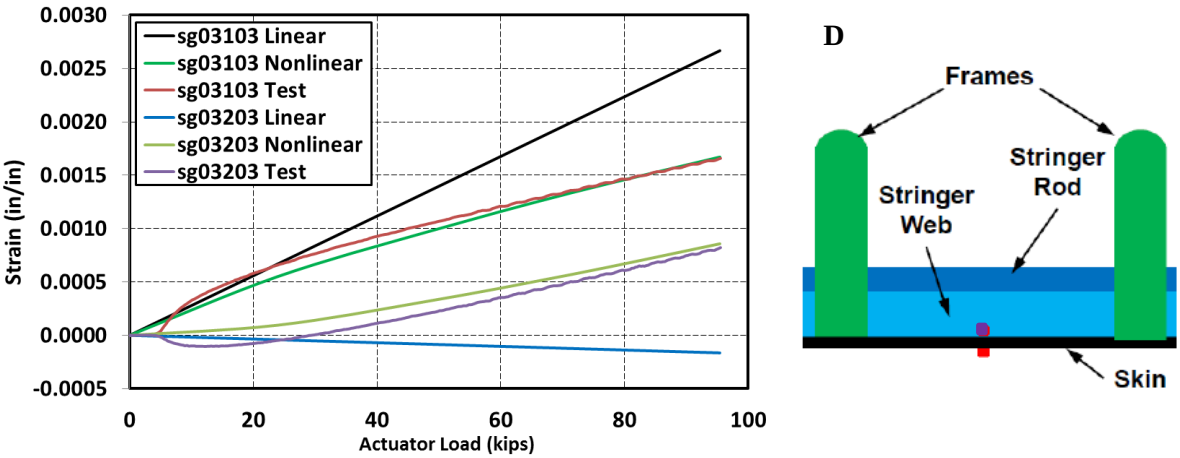

Figure 30. Aft upper bulkhead panel back-to-back skin strains up to −1-g + 1P DUL.

The center keel panel under the −1-g + 1P load undergoes compression due to mechanical loads and bows outwards due to the pressure loads as seen in Figure 21. Strains at the top of the center frame in the center keel panel (location A in Figure 21) are shown in Figure 31 and support the described response characteristic. The outward bending of the center keel panel due to the applied pressure stretches the root of the frame and compresses its top. At the same time, mechanical compression of the panel magnifies the pressure-induced compressive strain. Compressive strain reaching −0.0020 in./in. at DUL is considered low and shows a nearly linear characteristic. While the nearly linear characteristic is accurately captured by the analysis, strain magnitudes are slightly over-predicted.

The center keel panel back-to-back skin strains (locations B and C in Figure 21) are shown in Figure 32. The skin strain levels do not exceed 0.0015 in./in. at DUL and show the previously discussed nonlinear characteristic. Unlike the skin behavior under the −1-g load dominated by the alternating inward and outward buckling, under the −1-g + 1P load, the pressure load component forces all skin bays into the outward deformation.

The side keel response characteristics and the deformation pattern, shown in Figure 22, are generally similar to those of the center keel panel as both panels provide a continuous load path at the lower section of the test article. The strains at the top of the side keel stringer (location A in Figure 22) are shown in Figure 33. These strains, primarily induced by the pressure loads, are of a moderate value (approximately 0.0025 in./in. at DUL), and are reached in a linear fashion. The center frame strains in two different locations are shown in Figure 34. The first location is in the curved section of the frame, closer to the center keel panel (location B in Figure 22). The second location is in the straight section of the frame, farther away from the center keel and the intersection with the inner rib (location C in Figure 22). A large strain gradient in the center frame of the side panel is observed between the two locations. At location C, both mechanical load and pressure load act to compress the top of the frame. At location B, the inner rib reacts the bending moment which results in tensile strains. The transition from tensile to compressive strains is accurately captured by the FEA, however, the predicted values slightly overestimate both measured tensile and compressive strains (0.0039 in./in. and −0.0027 in./in. at DUL, respectively).

The side keel panel back-to-back skin strains (location D in Figure 22) are shown in Figure 35. Similar to other mid-bay skin results presented earlier in this section, a strongly nonlinear response is seen which can be attributed to the in-plane versus bending coupling when pressure loads are inducing large out-of-plane deformations. Overall, low strain levels are predicted and measured at the side keel skin at DUL.

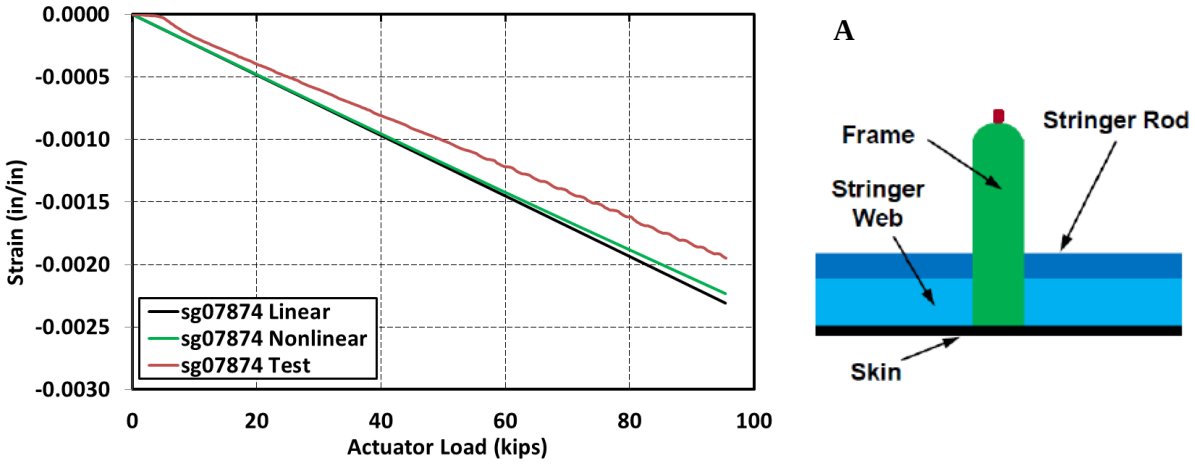

Figure 31. Strains at the top of the center keel panel frame up to −1-g + 1P DUL.

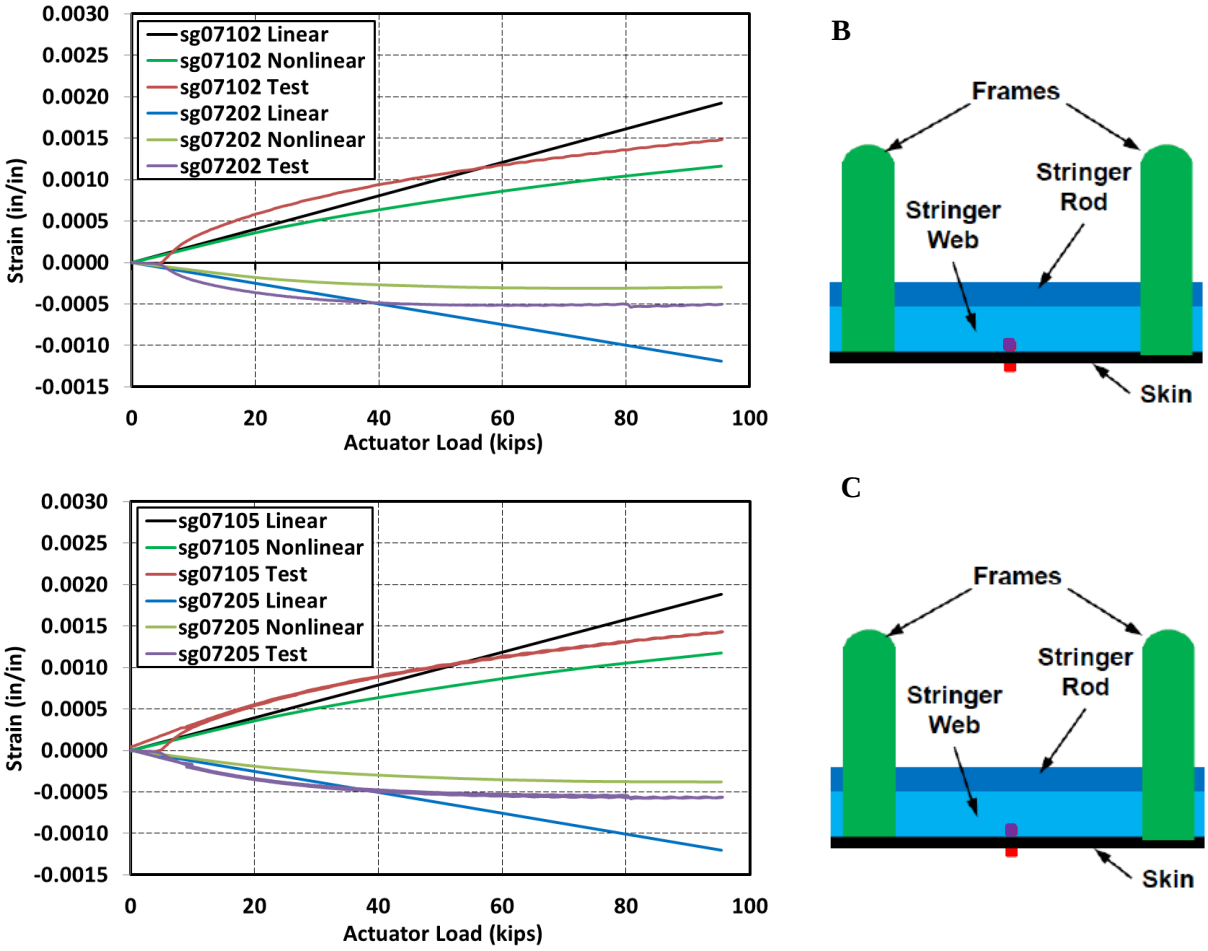

Figure 32. Center keel panel back-to-back skin strains up to −1-g + 1P DUL.

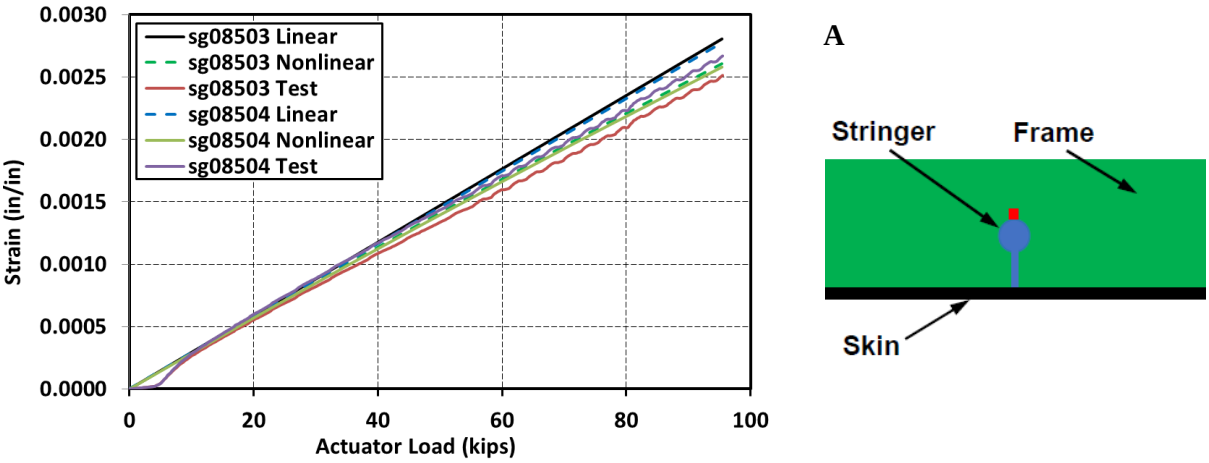

Figure 33. Strains at the top of the side keel panel stringer up to −1-g + 1P DUL.

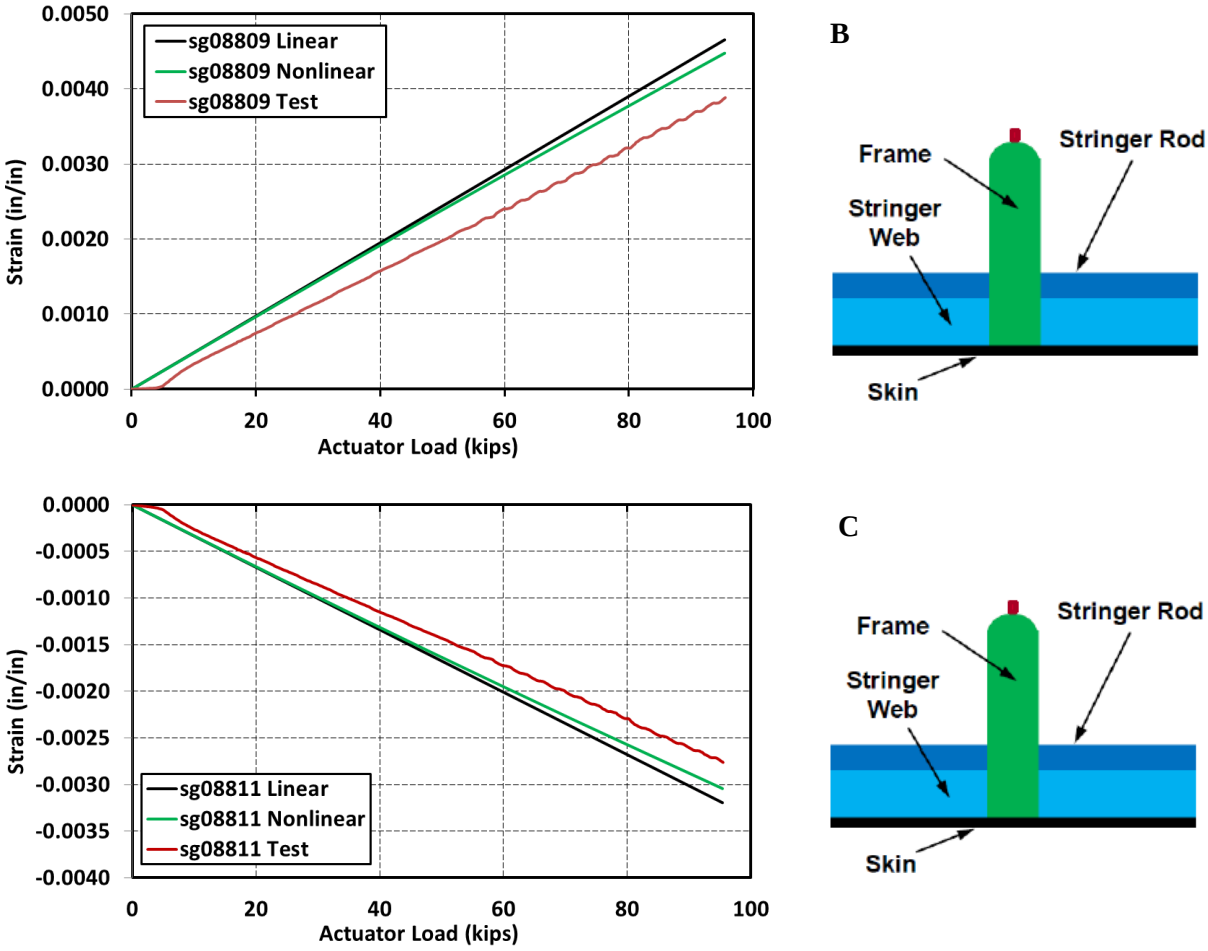

Figure 34. Strains at the top of the side keel panel frame up to −1-g + 1P DUL.

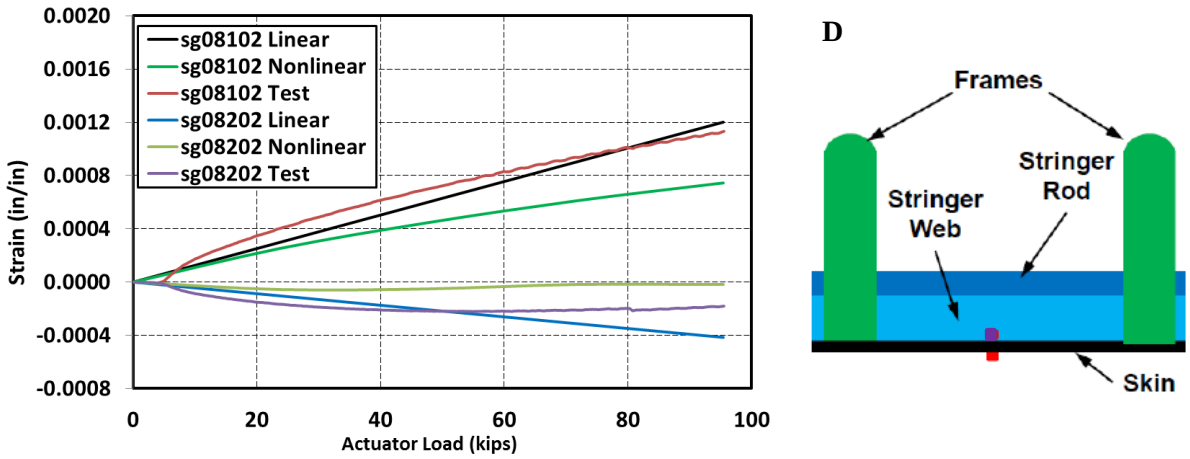

Figure 35. Side keel panel back-to-back skin strains up to −1-g + 1P DUL.

3.1.3. 2P Load

Under the 2P load, the unsupported sections of external panels bowed outward. Out-of-plane deformations of the crown, upper bulkhead, lower bulkhead, center keel, and side keel panels at DUL are shown in Figures 36 through 40, respectively. For the crown, upper aft bulkhead, and center keel panels, FEA results are compared with available VIC-3D measurements, while for the lower bulkhead and side keel panel only the FEA results are shown. All out-of-plane displacement plots under 2P DUL show similar patterns. Namely, they are dominated by global level outward deformations where attachments to the adjacent panels, both external and internal, act as panel edge restraints. In addition, local outward deformations associated with individual skin bays are visible as scalloped color contours, with spacing coinciding with distances between the frames and stringers. Internal metallic struts (not shown) are also a factor affecting deformation shapes and magnitudes of the crown and side keel panels, but due to their secondary role in the response characteristics, their discussion is omitted here for brevity.

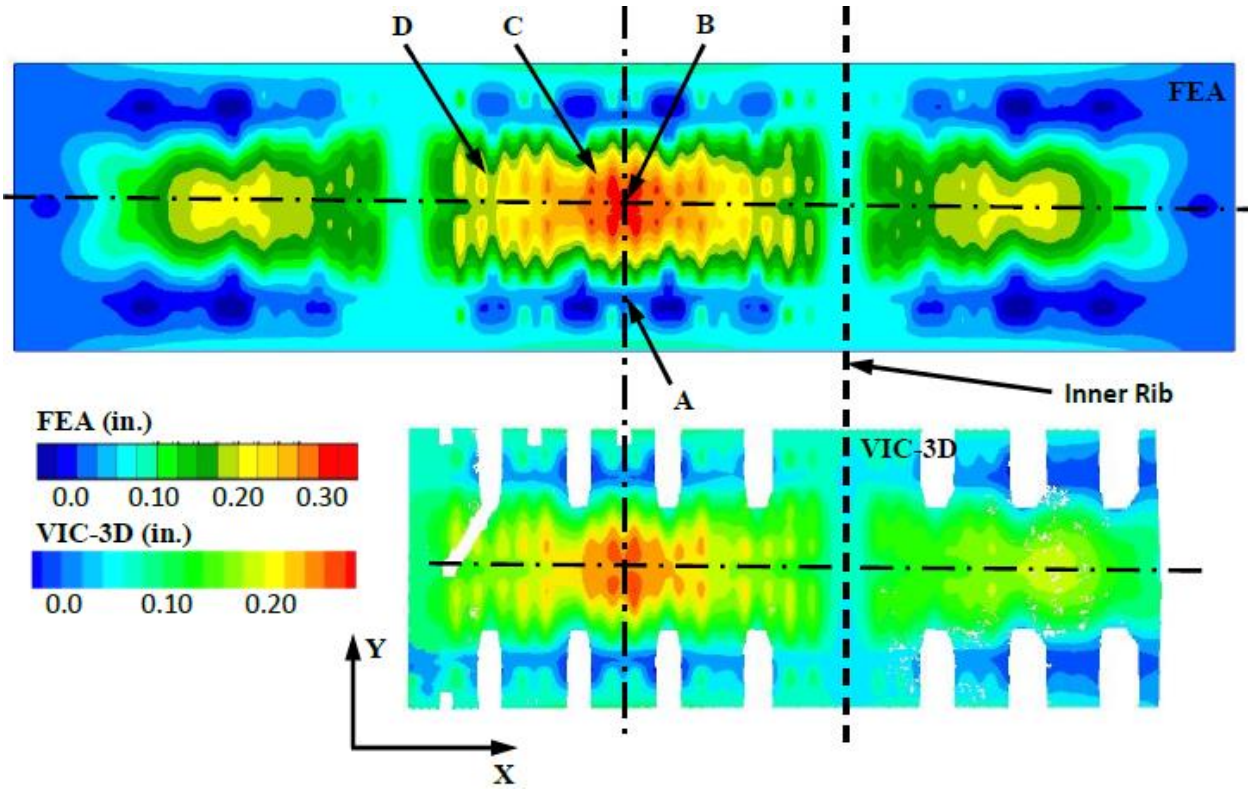

Figure 36. Out-of-plane deformation of the crown panel under 2P DUL.

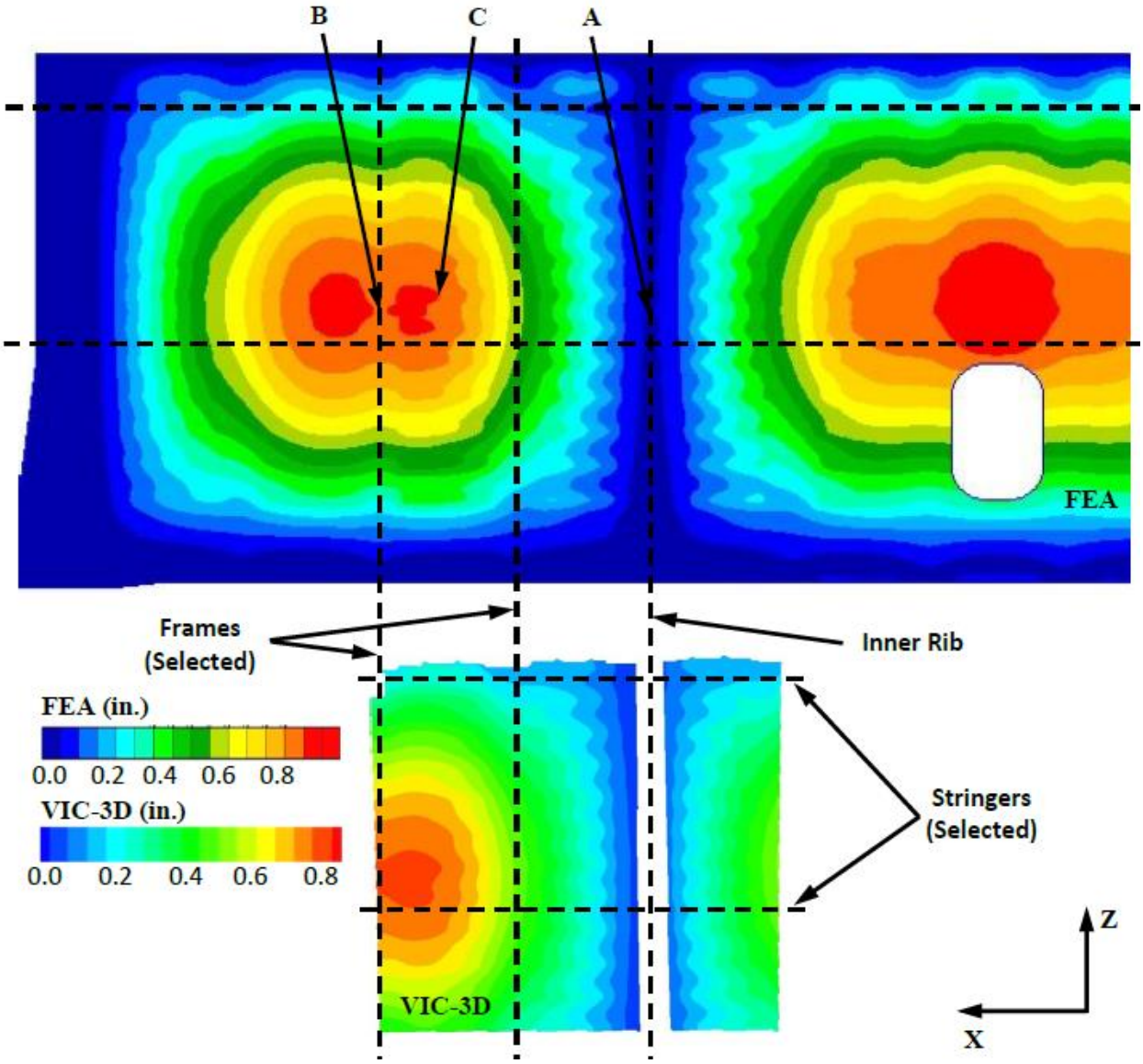

Figure 37. Out-of-plane deformation of the upper bulkhead panel under 2P DUL.

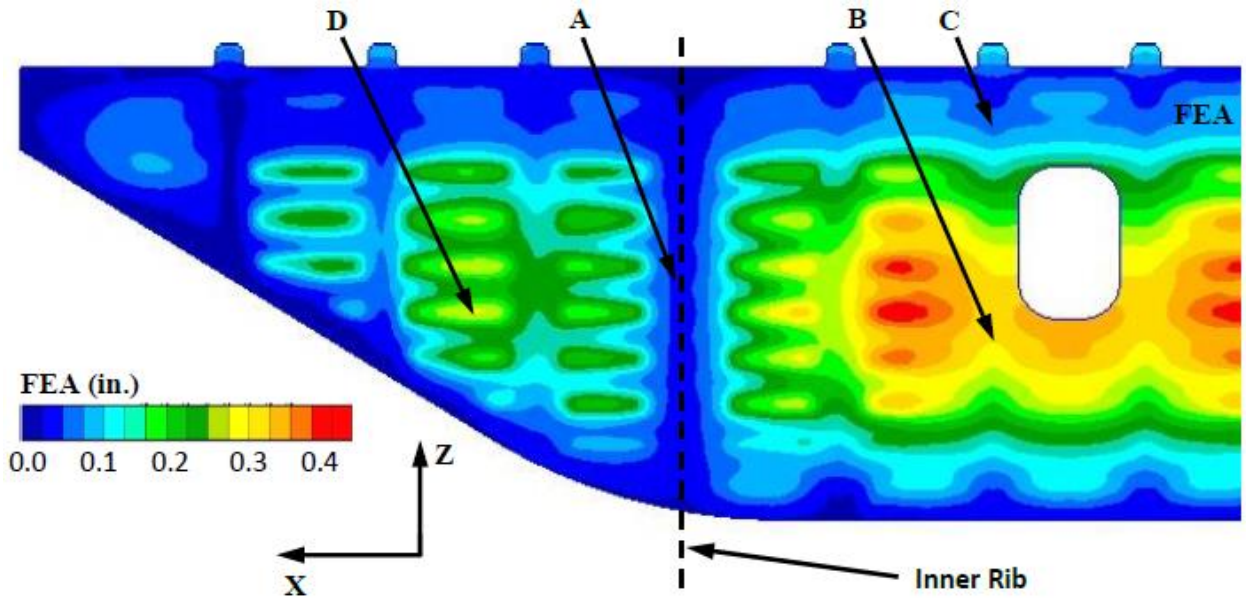

Figure 38. Out-of-plane deformation of the lower bulkhead panel under 2P DUL.

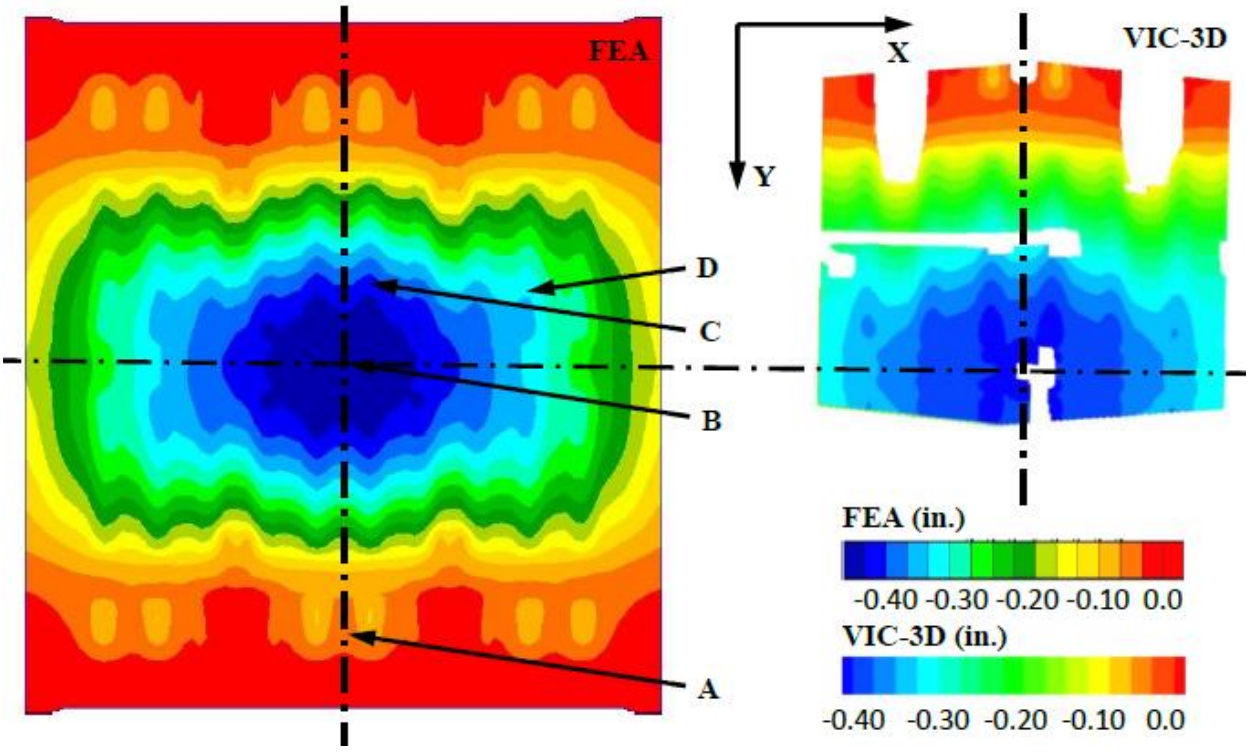

Figure 39. Out-of-plane deformation of the center keel panel under 2P DUL.

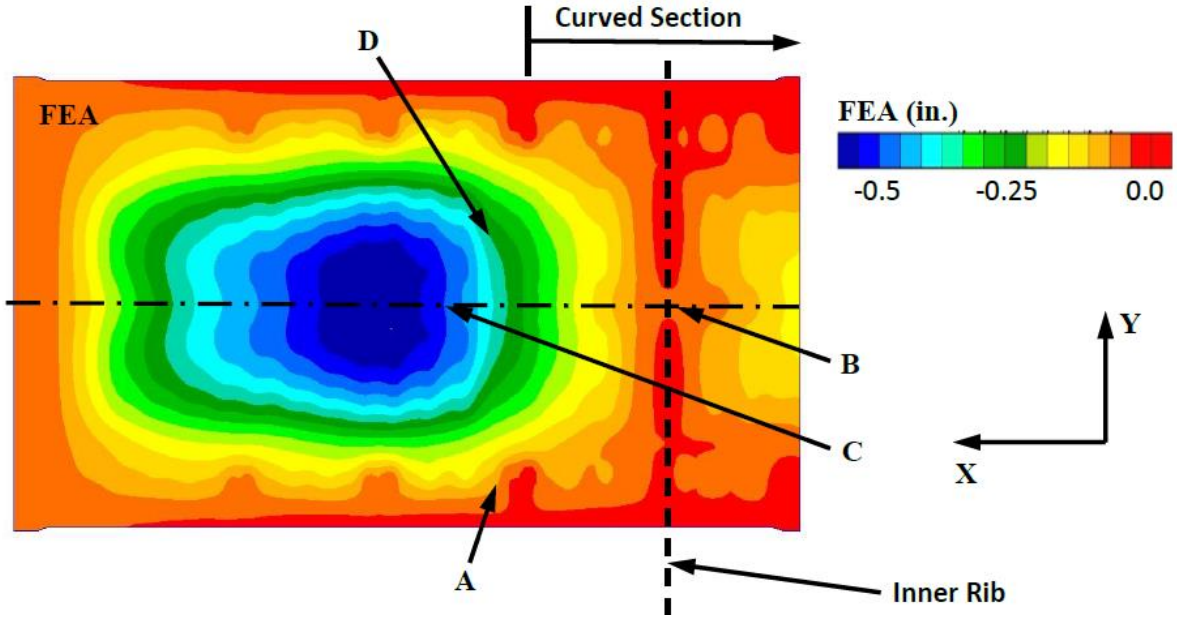

Figure 40. Z-component deformation of the side keel panel under 2P DUL.

The crown panel strains at the top of the mid-span stringer (location A in Figure 36 and the symmetric location with respect to the span-wise axis, not labeled) are shown in Figure 41. Moderate tension strain levels of approximately 0.0035 in./in. are reached at DUL, and only moderately nonlinear behavior is noted. Also, moderately nonlinear behavior is noted at the top of the center frame (location B in Figure 36) shown in Figure 42, where the compressive strain level of approximately 0.0010 in./in. at DUL can be considered low. The crown panel back-to-back skin strain levels at DUL are also low, but display strongly nonlinear characteristics, as shown in Figure 43 for locations C and D in Figure 36. The nonlinear behavior stems from the in-plane panel tensioning that suppresses large out-of-plane deformations when the pressure loads normal to the panel skin surface are applied. Overall, a good comparison between the nonlinear FEA predictions and test measurements is achieved.

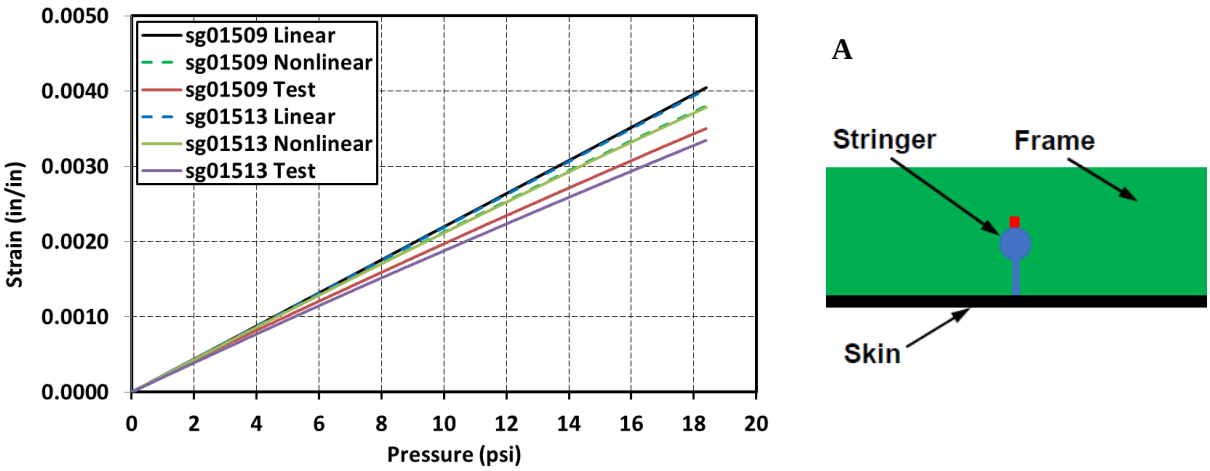

Figure 41. Strains at the top of the crown panel stringer up to 2P DUL.

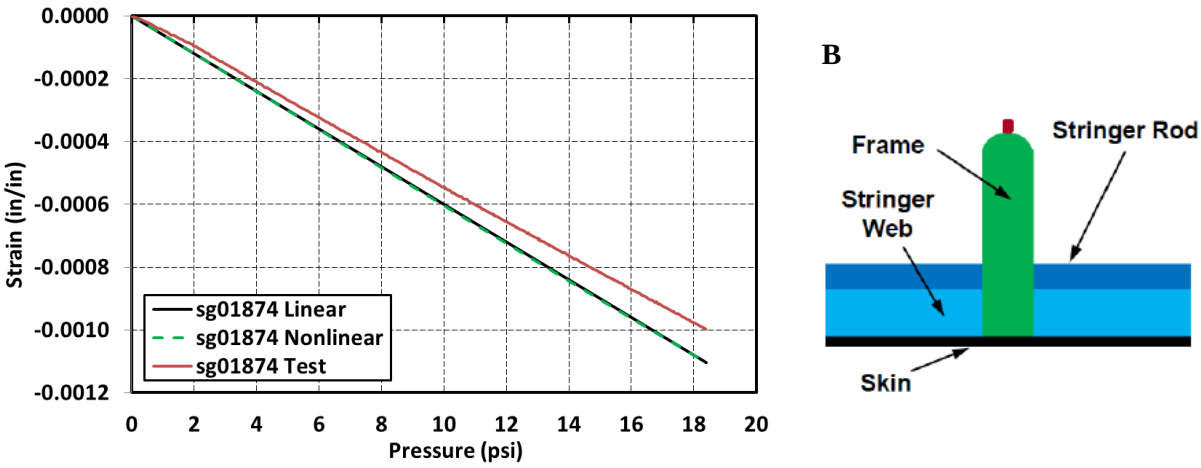

Figure 42. Strains at the top of the crown panel frame up to 2P DUL.

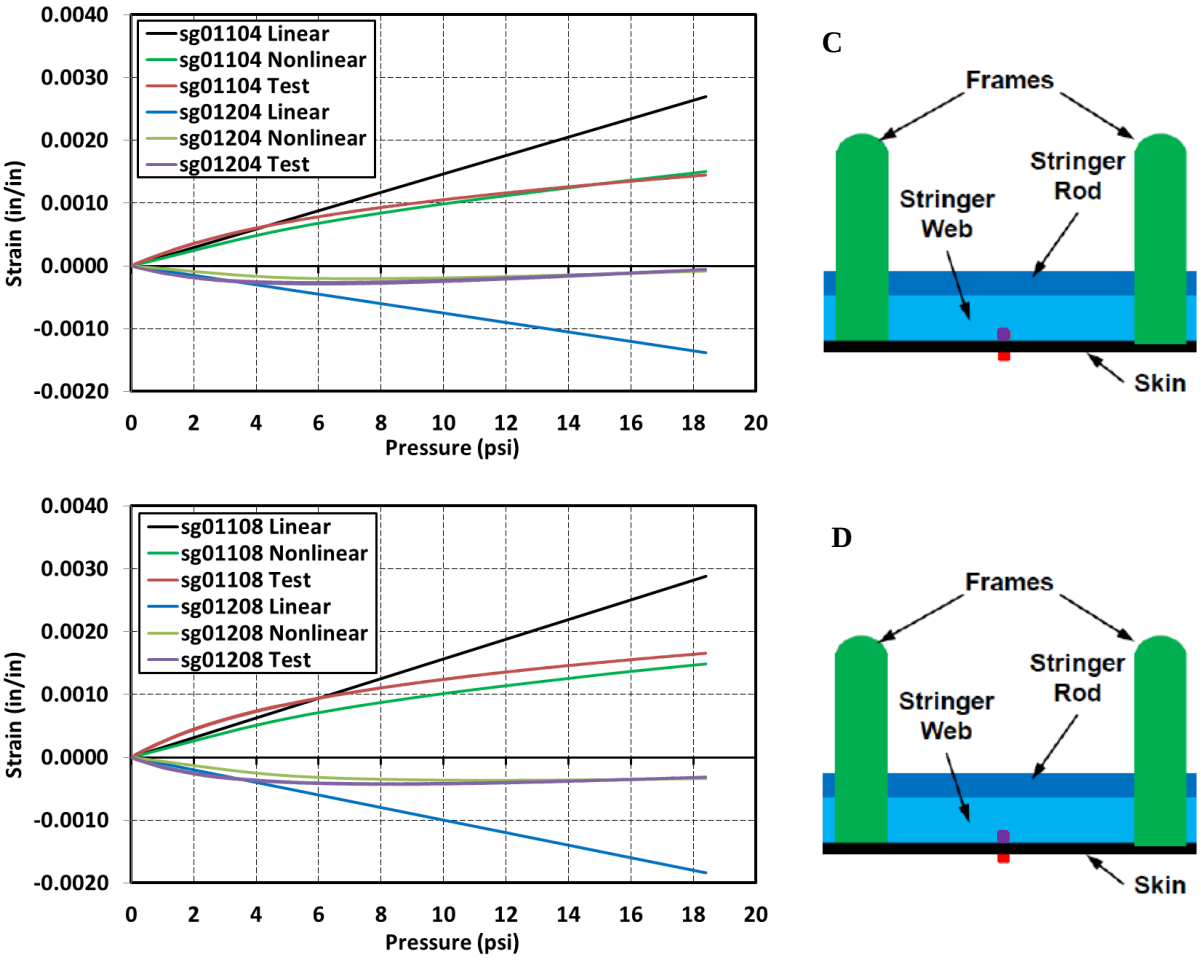

Figure 43. Crown panel back-to-back skin strains up to 2P DUL.

The upper bulkheads are the two panels with the largest unsupported sections within the test article, and thus are highly strained under the pressure loading. Strain results at the top of a stringer (location A in Figure 37) are shown in Figure 44, and at the top of a frame (location B in Figure 37) are shown in Figure 45. In qualitative terms, these outcomes are very similar to those for the stringer top and the frame top of the crown panel, Figures 41 and 42, respectively, and display only slightly nonlinear behavior. In terms of strain magnitudes, however, they are much higher as the stringer top strain reaches 0.0050 in./in. in tension at DUL and the frame top strain exceeds 0.0041 in./in. in compression at DUL. Test results show slightly more nonlinear characteristic when compared to the FEA predictions, and the latter tend to noticeably overestimate both measured tensile and compressive strains.

The upper bulkhead back-to-back skin strains display strongly nonlinear characteristic, as shown in Figure 46. While in qualitative terms, the behavior is also similar to that of the crown panel skin, the strain levels are higher and, on the OML surface, reach approximately 0.0020 in./in. in tension at DUL. Of note is that the crown panel strains at the IML surface under 2P DUL are approximately zero, as the in-plane tensile strains are almost completely compensated by the bending compressive strains, as seen in Figure 43. In the upper bulkhead panel, the relationship between the in-plane and bending strain components on the IML surface is different. In Figure 46, the IML surface responds in tension, but with a smaller magnitude when compared to the OML surface. This difference means that on the IML surface in-plane tensile strains are larger than the bending compressive strains. By averaging the IML and OML strains in Figure 46, the in-plane strain is approximately 0.0015 in./in. in tension at DUL. The difference between 0.0015 in./in. and the OML and IML strains is then on the order of ±0.0005 in./in. Thus, the ratio between the in-plane and the bending strain components is approximately 3.0, which can be regarded as a measure of how strong a role the in-plane versus bending coupling plays under the 2P DUL condition.

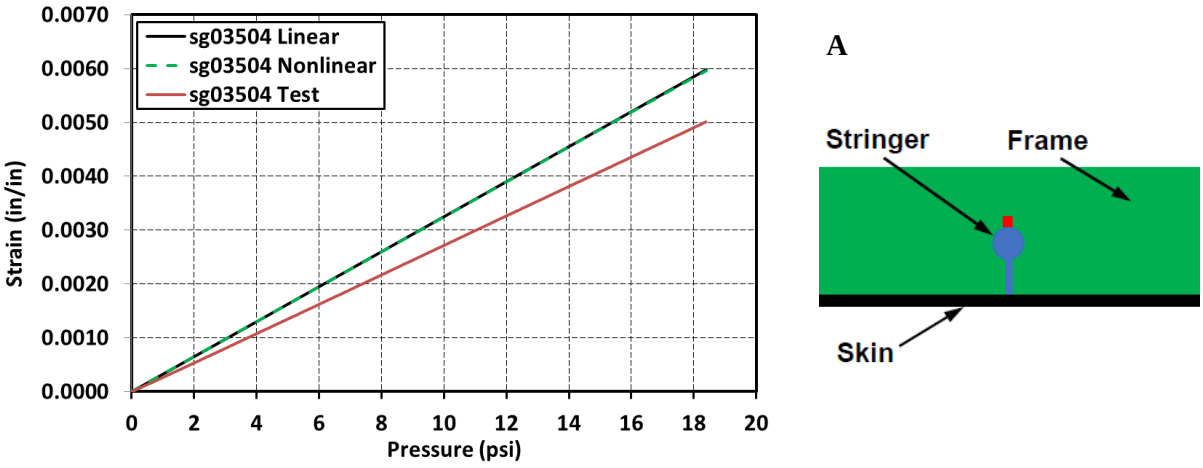

Figure 44. Strains at the top of the upper bulkhead panel stringer up to 2P DUL.

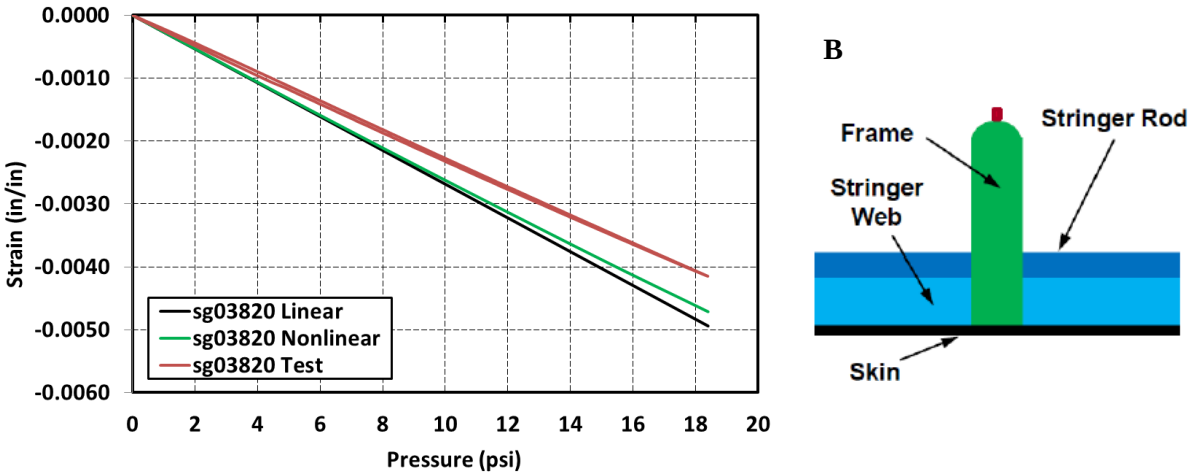

Figure 45. Strains at the top of the upper bulkhead panel frame up to 2P DUL.

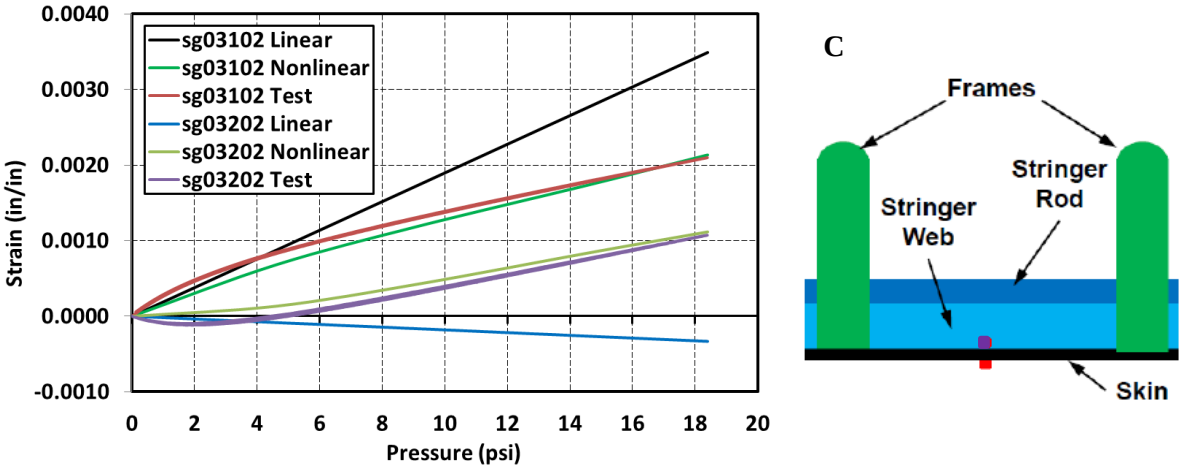

Figure 46. Upper bulkhead panel back-to-back skin strains up to 2P DUL.

The strains at the top of the stringer in the lower bulkhead (location A in Figure 38) are shown in Figure 47. They display a similar characteristic to the upper bulkhead strains at the stringer top shown in Figure 44, but since the unsupported distances in the lower bulkhead panel are smaller than those in the upper bulkhead panel, the strain levels are lower. The strains at the top of the lower bulkhead frames are shown in Figure 48 at locations B and C shown in Figure 38. At location B, i.e., far from the floor and keel panel supports, the frame top undergoes compression while at location C, i.e., close to the attachment to the floor panel, the frame undergoes tension. This observation reinforces the previous statement that the adjacent panels provide supports approximating clamped boundary conditions.

The lower bulkhead panel back-to-back skin strains (location D in Figure 38) are shown in Figure 49. Qualitatively, the skin strain behavior is similar to that of the skin in the upper bulkhead panel, but with a smaller relative contribution of the in-plane strain when compared to the bending strain component. In Figure 49, the averaged OML and IML strain at DUL is approximately 0.0010 in./in., and consequently the bending component is ±0.0010 in./in. Therefore, the ratio between the in-plane and bending strains is approximately 1.0, whereas for the previously discussed upper bulkhead skin section (Figure 46), the same ratio was approximately 3.0.

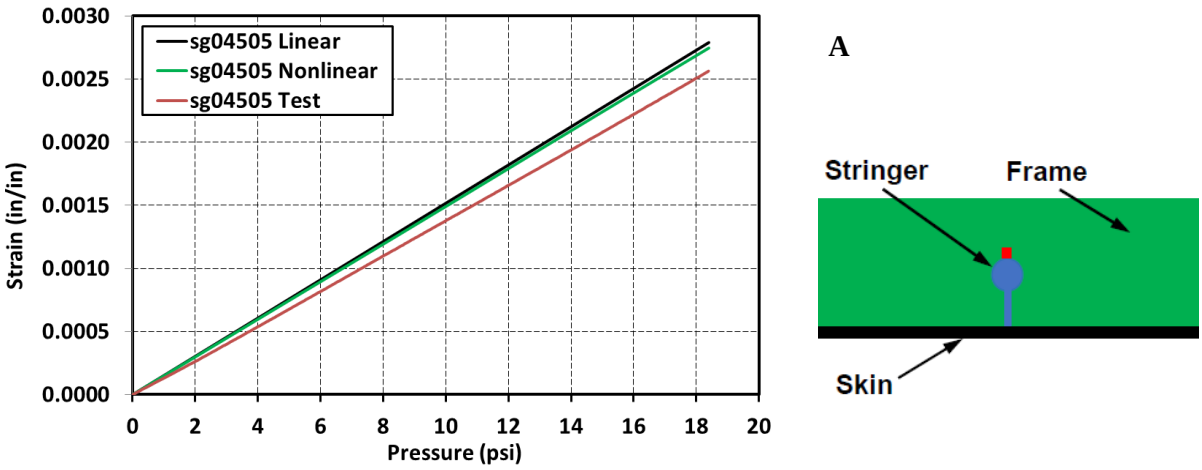

Figure 47. Strains at the top of the lower bulkhead panel stringer up to 2P DUL.

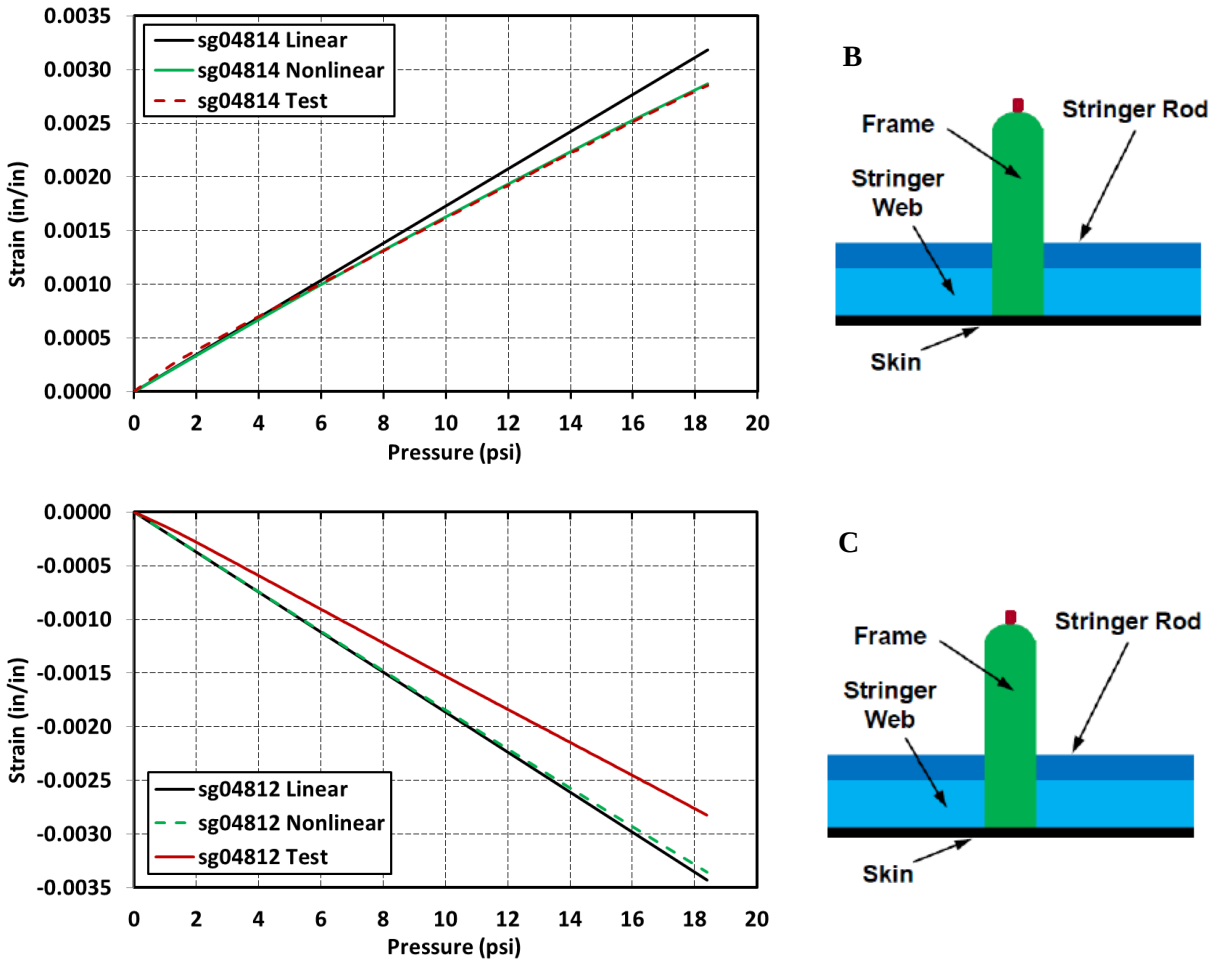

Figure 48. Strains at the top of the lower bulkhead panel frame up to 2P DUL.

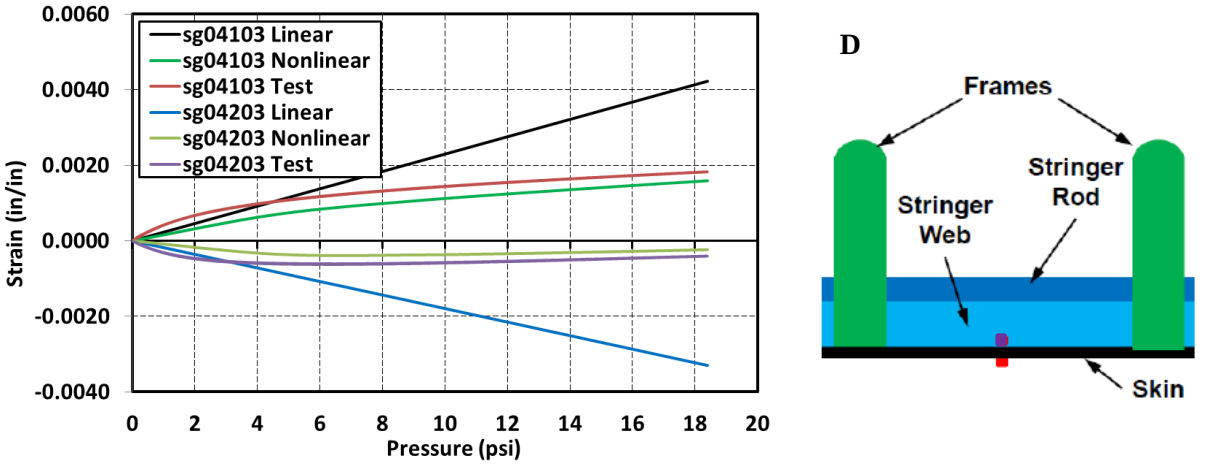

Figure 49. Lower bulkhead panel back-to-back skin strains up to 2P DUL.

The center keel panel strains at the top of a stringer (location A in Figure 39) are shown in Figure 50. They reach a moderate tensile value of 0.0030 in./in. at DUL, and show only slightly nonlinear dependence on the applied load. The same slightly nonlinear behavior is also noted at the top of a frame (location B in Figure 39) where a moderate value of 0.0021 in./in. compressive strain at DUL is achieved, as seen in Figure 51. The center keel panel back-to-back skin strains (locations C and D in Figure 39) are shown in Figure 52, and display levels and characteristics very similar to those of the lower bulkhead panel shown in Figure 49. Mid-bay skin strain behavior does not seem to be significantly influenced by the location of the particular skin bay considered.

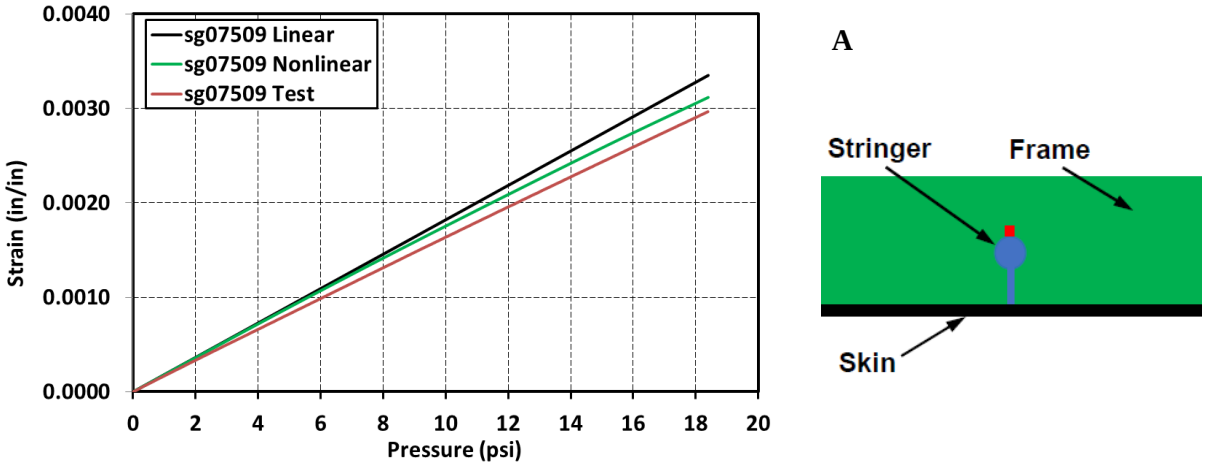

Figure 50. Strains at the top of the center keel panel stringer up to 2P DUL.

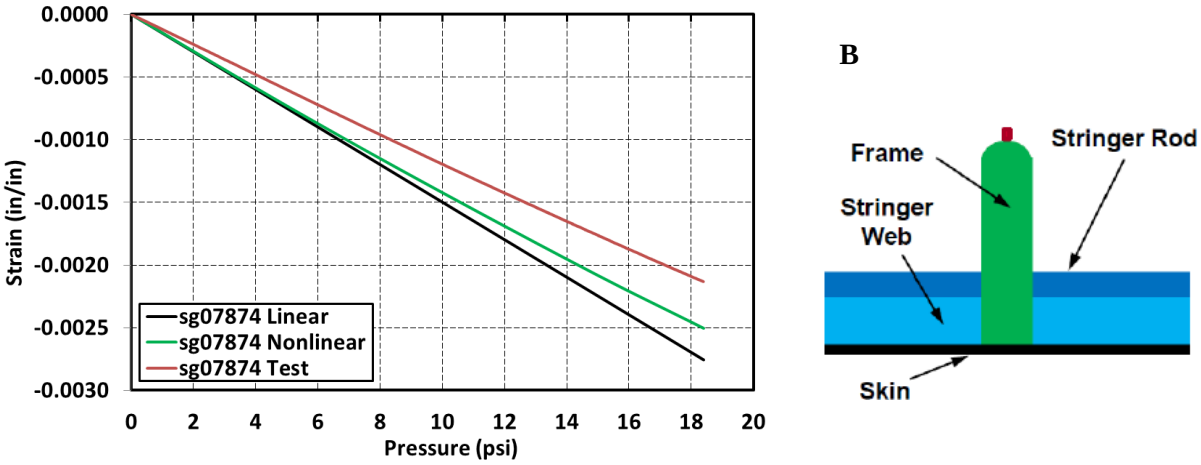

Figure 51. Strains at the top pf the center keel panel frame up to 2P DUL.

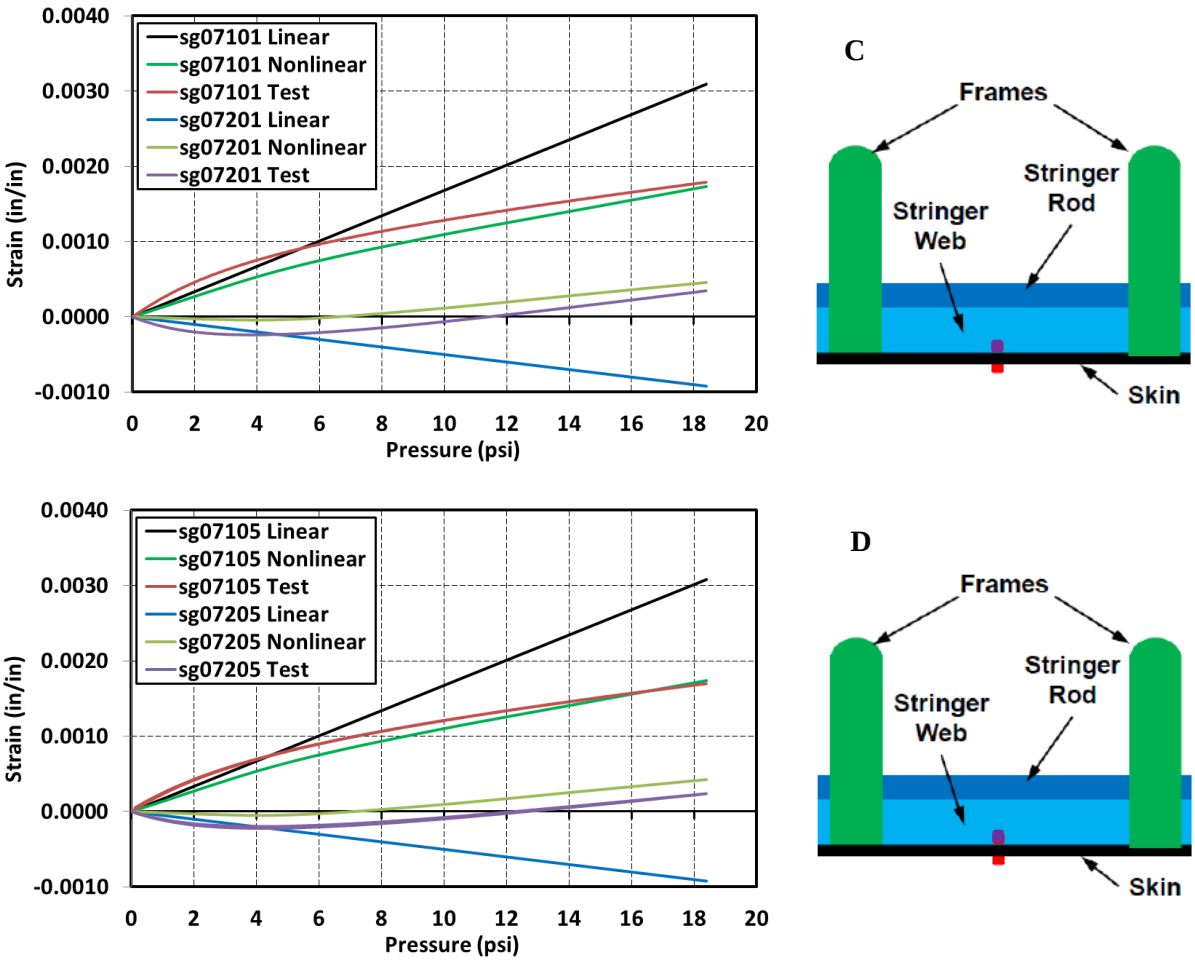

Figure 52. Center keel back-to-back skin strains up to 2P DUL.

Strains at the top of a stringer of the side keel panel are shown in Figure 53; they display a slightly nonlinear behavior and reach a moderate value of 0.0028 in./in. tensile strain under DUL. The center frame strains of the side keel panel are shown in Figure 54 for two different locations. The first location is in the curved section of the frame, closer to the center keel panel and in the proximity of the inner rib (location B in Figure 40). The second location is in the straight section of the frame, farther away from the center keel and the intersection with the inner rib (location C in Figure 40). The two strain plots display only slightly nonlinear behavior up to DUL but a large strain gradient is observed between the two locations. At DUL, the strain gradient between the two locations is approximately −0.0069 in./in., as it changes from approximately 0.0045 in./in. in tension at location B to approximately 0.0024 in./in. in compression at location C. At location C, the pressure load acts to compress the top of the frame. At location B, the inner rib reacts the bending moment tensioning the top of the frame. The transition from tensile to compressive strains is accurately captured by the FEA, however, the predicted values slightly overestimate both measured tensile and compressive strains. Recall, that this response is similar to the one previously shown in Figure 34 and discussed for the side keel panel frame under the −1-g + 1P load in in section 3.1.2.

The side keel panel back-to-back skin strains are shown in Figure 55. A strongly nonlinear behavior discussed before for skin sections of other panels under the 2P load is observed. While the nonlinear characteristic is accurately captured by the analysis, the quantitative comparison for the OML strains is less favorable relative to other panels.

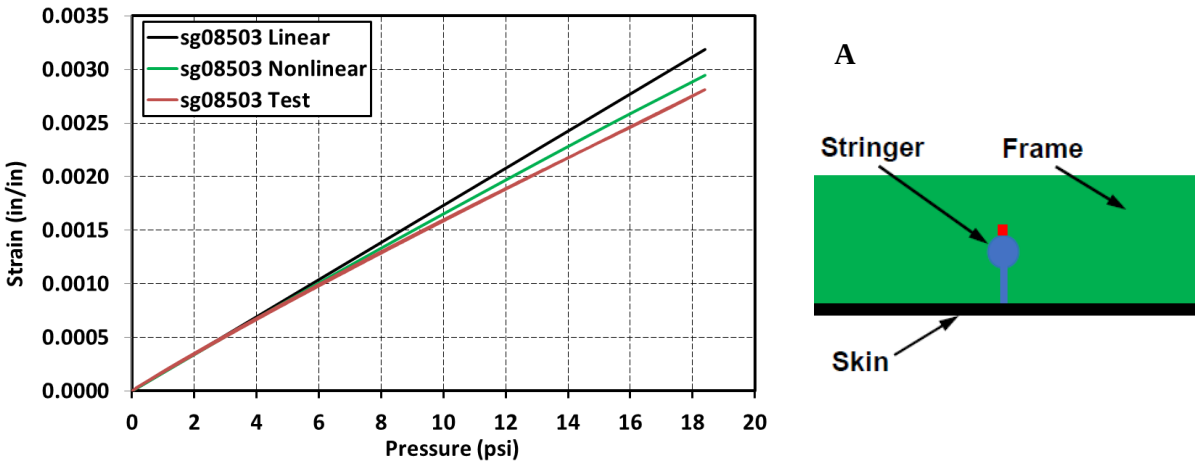

Figure 53. Strains at the top of the side keel panel stringer up to 2P DUL.

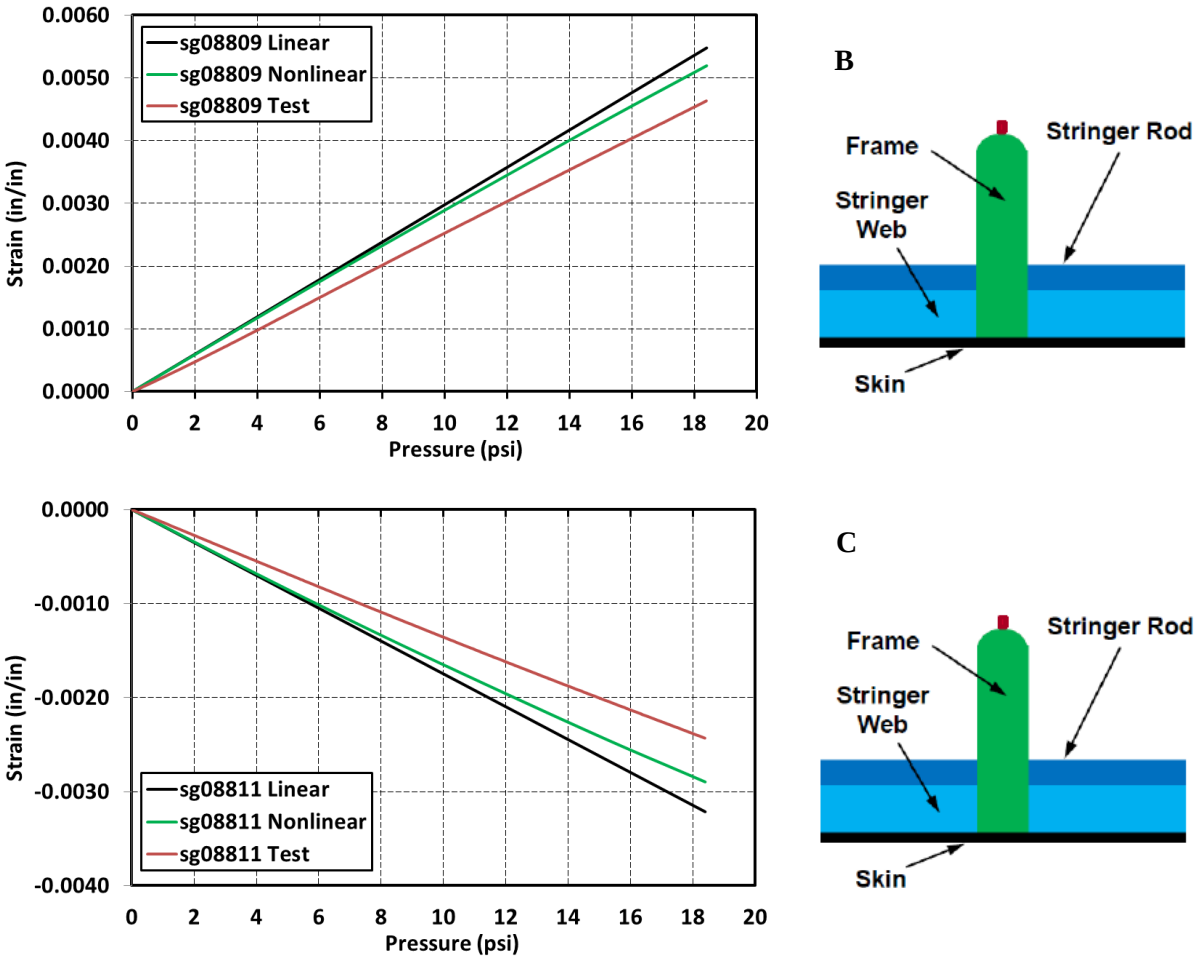

Figure 54. Strains at the top of the side keel panel frame up to 2P DUL.

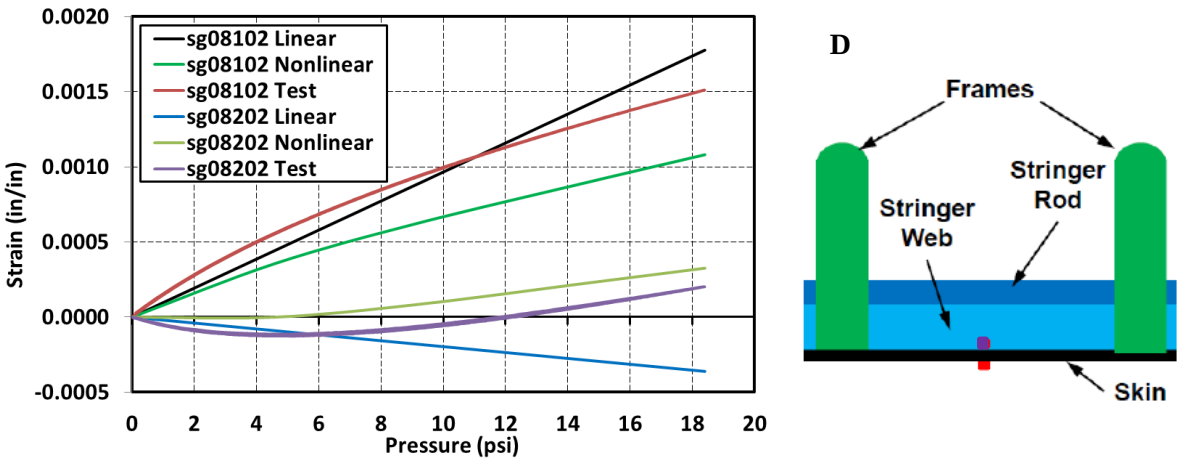

Figure 55. Side keel back-to-back skin strains up to 2P DUL.

As predicted by FEA,[9] the largest strains in the HWB test article metallic fittings occurred under the 2P DUL (this statement does not account for the predictions and measurements obtained for the load introduction fittings that yielded high strains under 165% 2.5-g DLL and 165% 2.5-g + 150% 1P loads, and will be discussed separately in sections 3.1.4 and 3.1.5). The locations of the largest strains measured in the metallic fittings under the 2P DUL are shown in Figure 56. These locations generally correspond to the test article corners, i.e., perpendicular joints between the external panels creating a pressure boundary. Thus, it is intuitive to conclude that the pressure loads acting on the perpendicularly connected panels attempted to widen the right-angle arrangement initially present under the load-free condition. Location A corresponds to external metallic fittings between the crown panel and the upper bulkhead panel (the upper and lower forward bulkhead panels in Figure 56 are removed to obtain a better view of the internal fittings and substructure arrangements). Locations B and C correspond to metallic fittings between the lower bulkhead panels and the side keel panels. The strains in the above-mentioned locations are presented in Figures 57 through 59, respectively. The strain figures include insets presenting more detailed geometry of a particular fitting and the locations of the strain measurements.

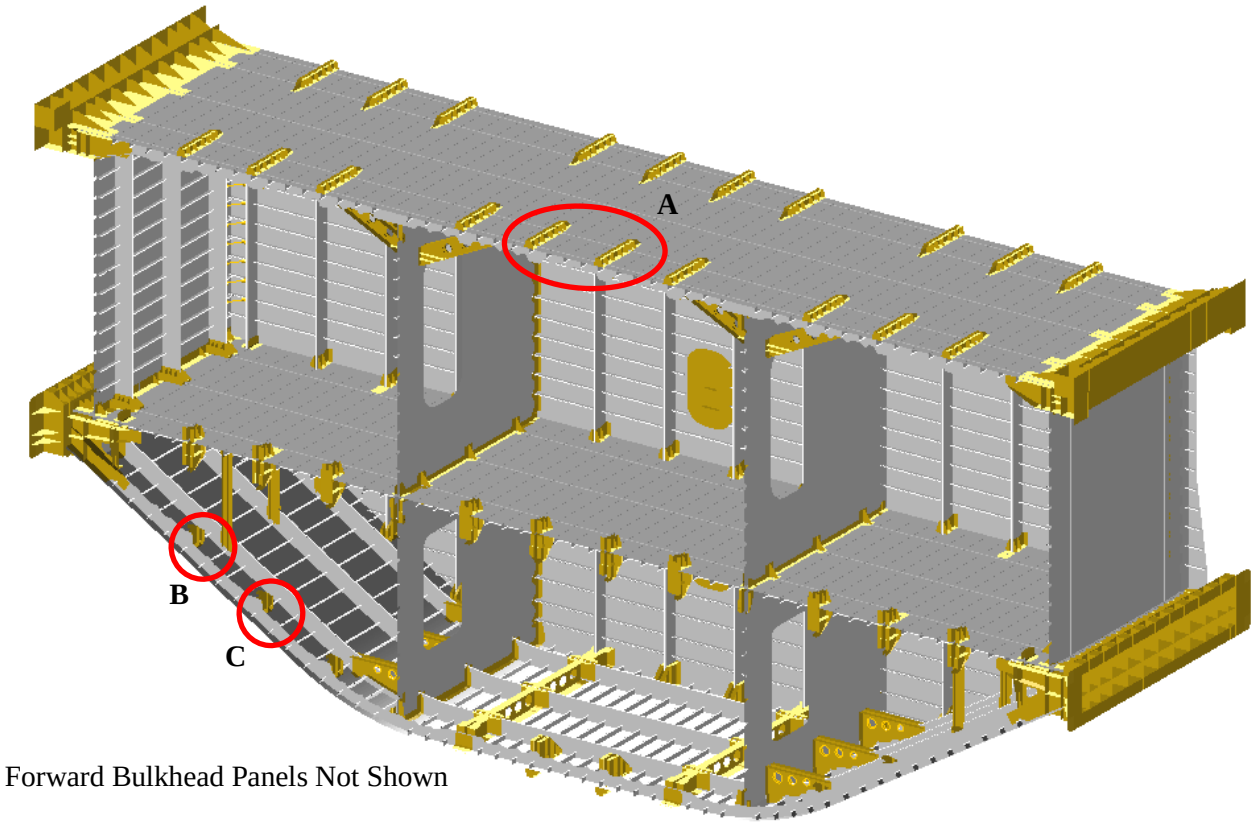

Figure 56. Locations of metallic fittings with measured high strains under 2P DUL.

Results for two identical and span-wise symmetrically placed metallic fittings at location A of Figure 56 are presented in Figure 57. During early stages of the FEA effort,[10] the strain results at location A were not converged due to the coarseness of the mesh and lack of contact interaction between the external metallic fittings and the underlying crown panel. Thus, the modeling of one of the four symmetric locations was revised by locally reducing the element sizes in the adjacent section of the crown panel and by using rigid kinematic constraints to, in a very basic fashion, account for the panel-fitting contact interaction. Such an

approach was dictated by a desire not to significantly increase the computational effort required to solve the problem (which would likely be caused by modeling the full panel-fittings contact interactions and by mesh refinements in all symmetric locations). It was assumed that, due to symmetry of the test article and its loading, one converged location should be representative of other symmetric locations. The simplified modeling of the contact interaction by applying the rigid kinematic constraints between the contact pair was based on the observation that the ability of the top surface of the crown panel to penetrate through the bottom surface of the external metallic fitting would cause a large spike in the local strains, but separation of the above contact pair was largely inconsequential to the convergence of strain results. Thus, Figure 57 includes the results for the unrefined fitting (the three curves corresponding to strain gauge sg16005) and for the refined fitting (the three curves corresponding to strain gauge sg16006). Based on the results presented in Figure 57, the local mesh refinement and addition of the rigid kinematic constraints were sufficient to achieve a good quality of the predictive FEA. After refining one of the four locations and verifying the convergence of the FEM, the results from unrefined locations were disregarded in the post-processing effort and the refined location results were assumed to be representative of all four symmetric locations. While the overall strain level of −0.0035 in./in. at DUL can be regarded as moderately high, such strain levels were limited to the tip of the web of the fitting (i.e., the location of the strain gauge in the inset plot).

Strains at location B, i.e., a web of the internal fitting attaching the lower bulkhead to the side keel panel, are shown in Figure 58 achieving approximately 0.0036 in./in. at DUL. The FEA results matched the test measurements very well without any refinements to the originally developed FEM. This cannot be concluded about the strains in a similar fitting presented in Figure 56 as location C, located just slightly farther away from the load introduction fittings when compared to location B. The measured strains as seen in Figure 59 were approximately five times higher than those predicted by both linear and nonlinear FEA. This location emphasizes the need for further improvements in the modeling practices pertaining to the metallic fittings in perpendicular joints for this type of structure. In other words, modeling of a perpendicular joint under high pressure loads may warrant significant mesh refinement in the vicinity of the joint and accounting for, at least in a simplified fashion, contact interactions between the panel and the fitting. To avoid significant increases in the computational cost needed to solve the problem, a global-local analysis approach might need to be considered.

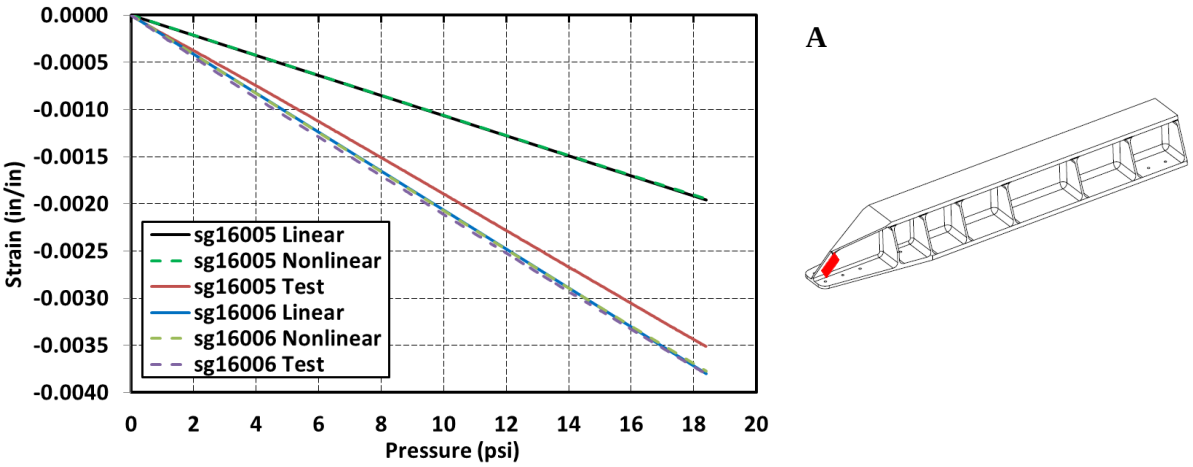

Figure 57. Strains in the metallic fittings connecting crown panel and upper bulkhead up to 2P DUL.

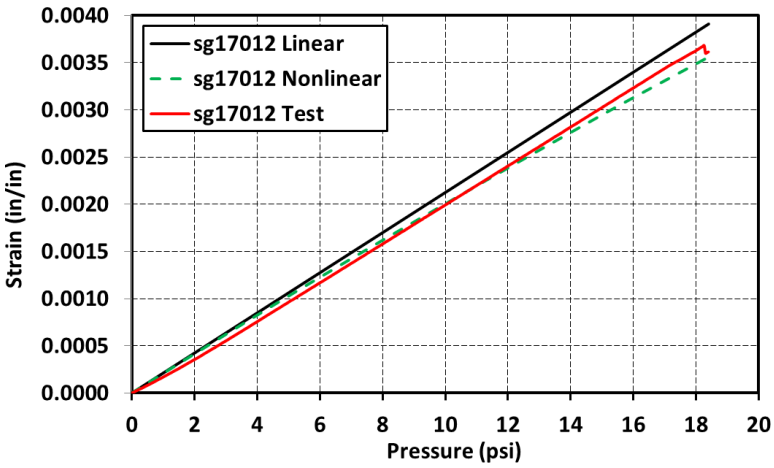

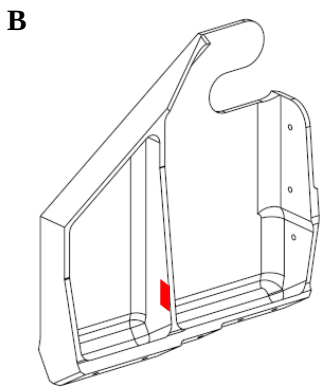

Figure 58. Strains in the web of the metallic fitting connecting side keel panel to lower bulkhead up to 2P DUL.

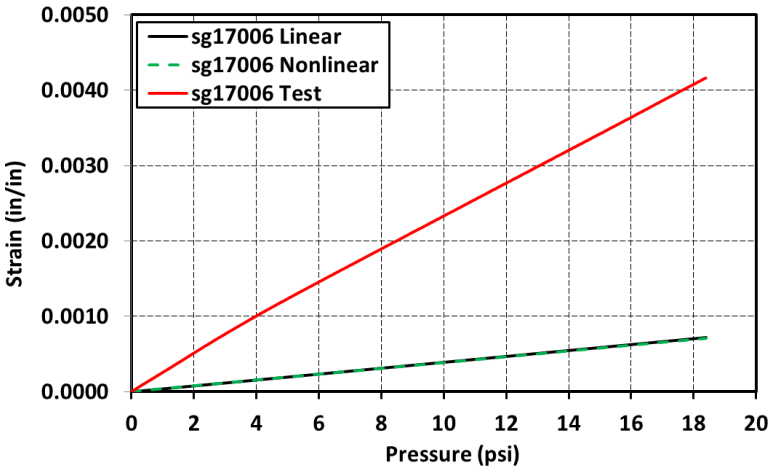

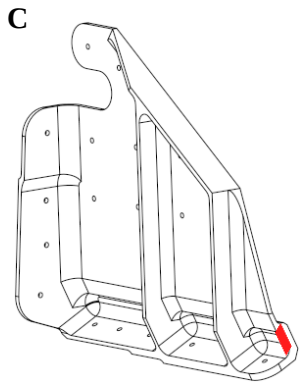

Figure 59. Strains in the flange of the metallic fitting connecting side keel panel to lower bulkhead up to 2P DUL.

3.1.4. 2.5-g Load

Under the 2.5-g load, the top of the test article was compressed and the bottom tensioned by the mechanical loads. The crown panel out-of-plane deformation under 150% DLL (or DUL) is presented in Figure 60 and under 165% DLL (the "beyond DUL" portion of the test described in section 2.1) in Figure 61. While the test to 165% DLL was conducted only once, the 150% DLL (DUL) test was conducted twice, for pristine and BVID conditions. Under the 2.5-g load, both pristine and BVID test out-of-plane deformations are shown in Figure 60 to further highlight certain features associated with testing and nonlinear analysis of structures with periodic construction.

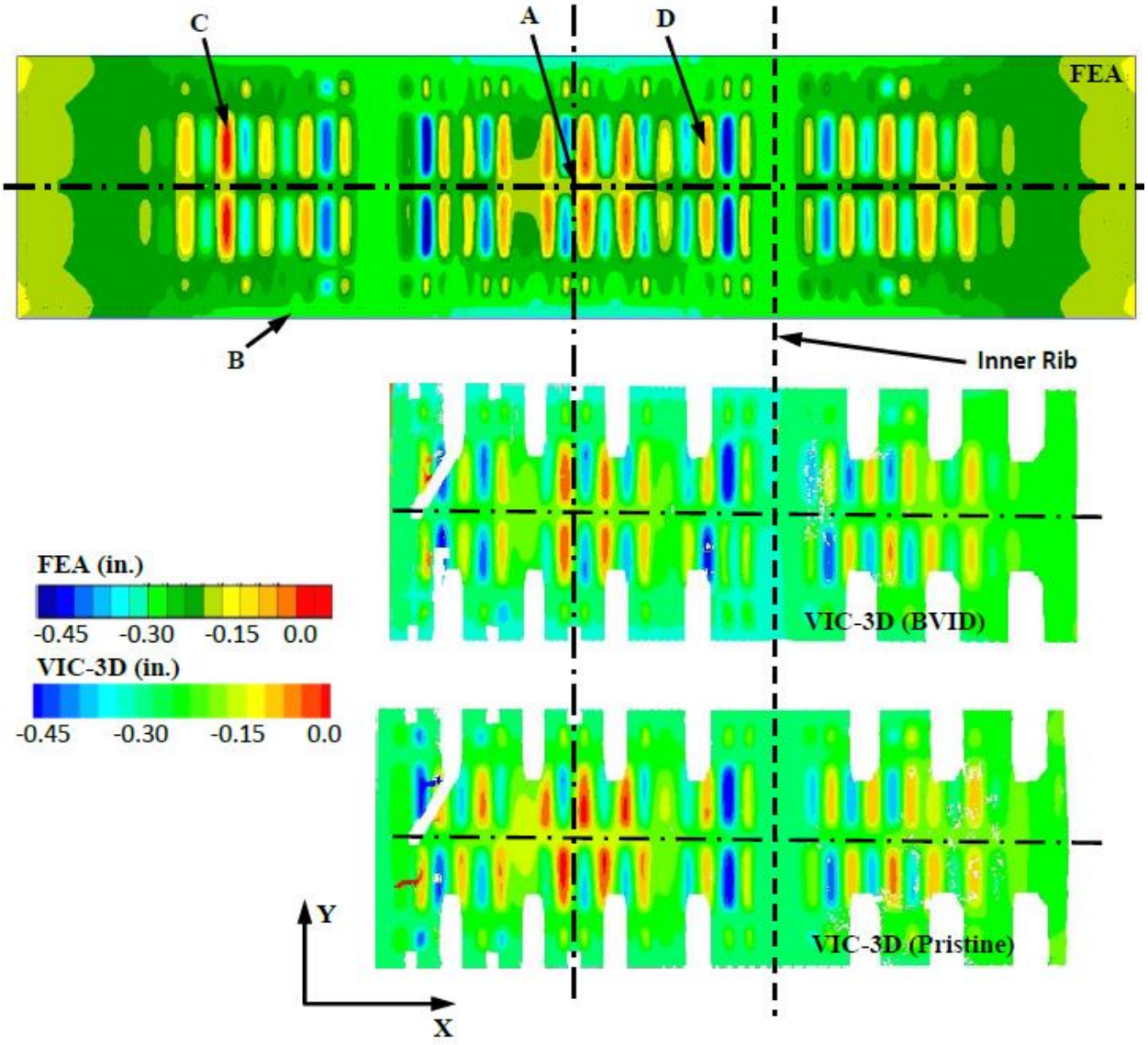

Figure 60. Out-of-plane deformation of the crown panel under 2.5−g DUL.

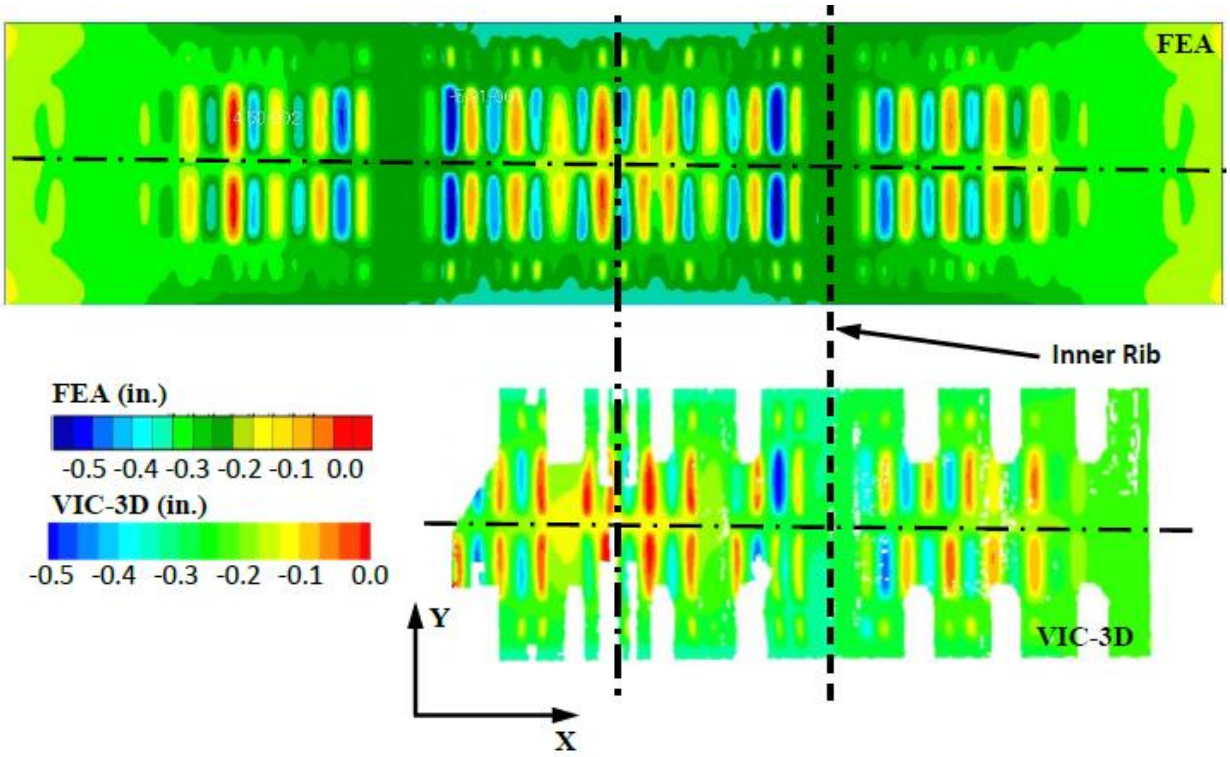

Figure 61. Out-of-plane deformation of the crown panel under 2.5-g 165% DLL.

It is seen in both Figures 60 and 61 that the out-of-plane deformation of the crown panel under the 2.5-g load is dominated by skin buckling extending almost the entire span of the panel. However, each time the test article was loaded to the 150% - 165% DLL range, the final buckling pattern in the crown panel skin sections was different. While it can be argued that the load path leading to the 165% DLL 2.5-g condition (reference Figure 7) was distinct from that of a simple load-unload sequence used to achieve 150% DLL only, even the two measured deformation fields under 150% DLL shown in Figure 60 did not match. Since no appreciable effects of BVID were noted in the far field response, the uniqueness of deformation obtained for structures with periodic features and multiple stable equilibria cannot be guaranteed for each periodic feature. It is likely that a particular buckling pattern obtained in each test was triggered by otherwise globally insignificant factors such as minor manufacturing imperfections, scatter in the applied load path, or minor residual stresses from the previous tests and/or servicing of the test article between the tests.

The lack of the uniqueness of the deformation field was not limited to measurements only. Several nonlinear FEAs executed with slight changes to solver parameters, such as the integration step increment or the magnitude of numerical damping, also resulted in distinct buckling patterns (not shown here for brevity). None of the measured and predicted patterns, however, matched precisely. Nevertheless, the comparison of the measured and predicted displacement results is considered good, as the characteristic buckling behavior was captured, and the minimum and maximum displacement magnitudes also matched well.

The out-of-plane deformation of the upper bulkhead panel is shown for 150% DLL (or DUL) in Figure 62 and for 165% DLL in Figure 63. Both figures demonstrate that the upper bulkhead transfers significant span-wise compressive loads in the top section attached to the crown panel. Similar to the skin sections of the crown panel, these loads manifest themselves in a form of large buckled skin deformations. However, a typical buckling pattern at the top of the upper bulkhead panel is different from that of the crown panel.

The buckled skin sections of the crown panel display one semi-sine-like shape per individual skin bay between the consecutive stringers and frames. In the upper bulkhead panel, most of the skin bays display three to four semi-sine-like shapes that are additionally skewed relative to the frame-stringer orthogonal grid. This type of buckling shape can be explained by the fact that the span-wise edge of each individual skin bay in the bulkhead (24 in. between consecutive frames) is longer than that in the crown panel (6 in. between consecutive stringers). Also, in the upper bulkhead panel the top edge of the each skin bay is compressed more than the bottom edge of the same skin bay. This compressive load variation translates into a shear load component that results in the skewed buckling shapes. Similar to the more regular buckling pattern observed in the crown panel, the skewed buckling shapes are also susceptible to adoption of different stable equilibria, as the out-of-plane deformation patterns in Figures 62 and in 63 differ. Also similar to the crown panel results, the comparison of the measurements and predictions is considered good, as the characteristic behavior and displacement magnitudes match closely.

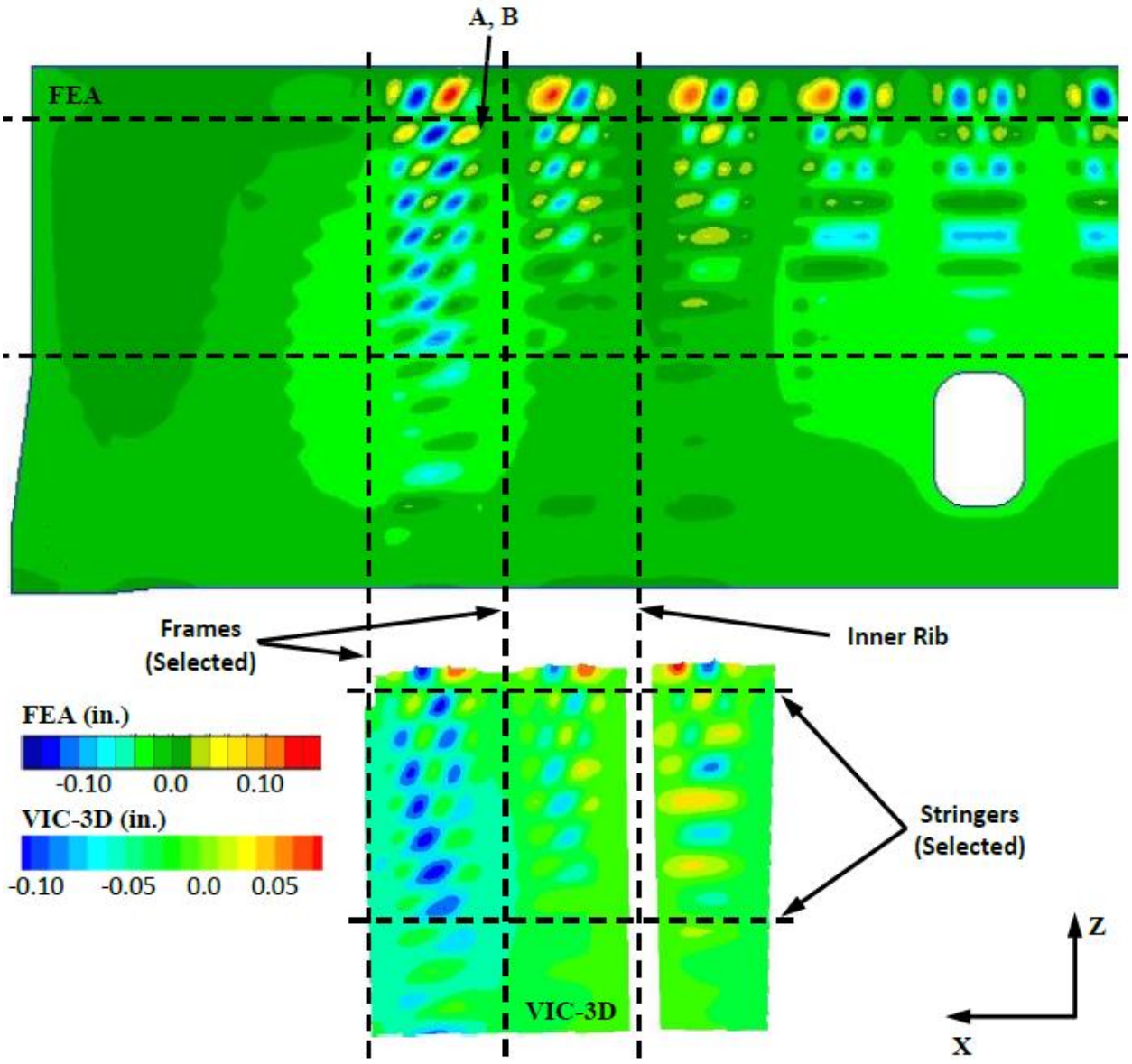

Figure 62. Out-of-plane deformation of the upper aft bulkhead panel under 2.5-g DUL.

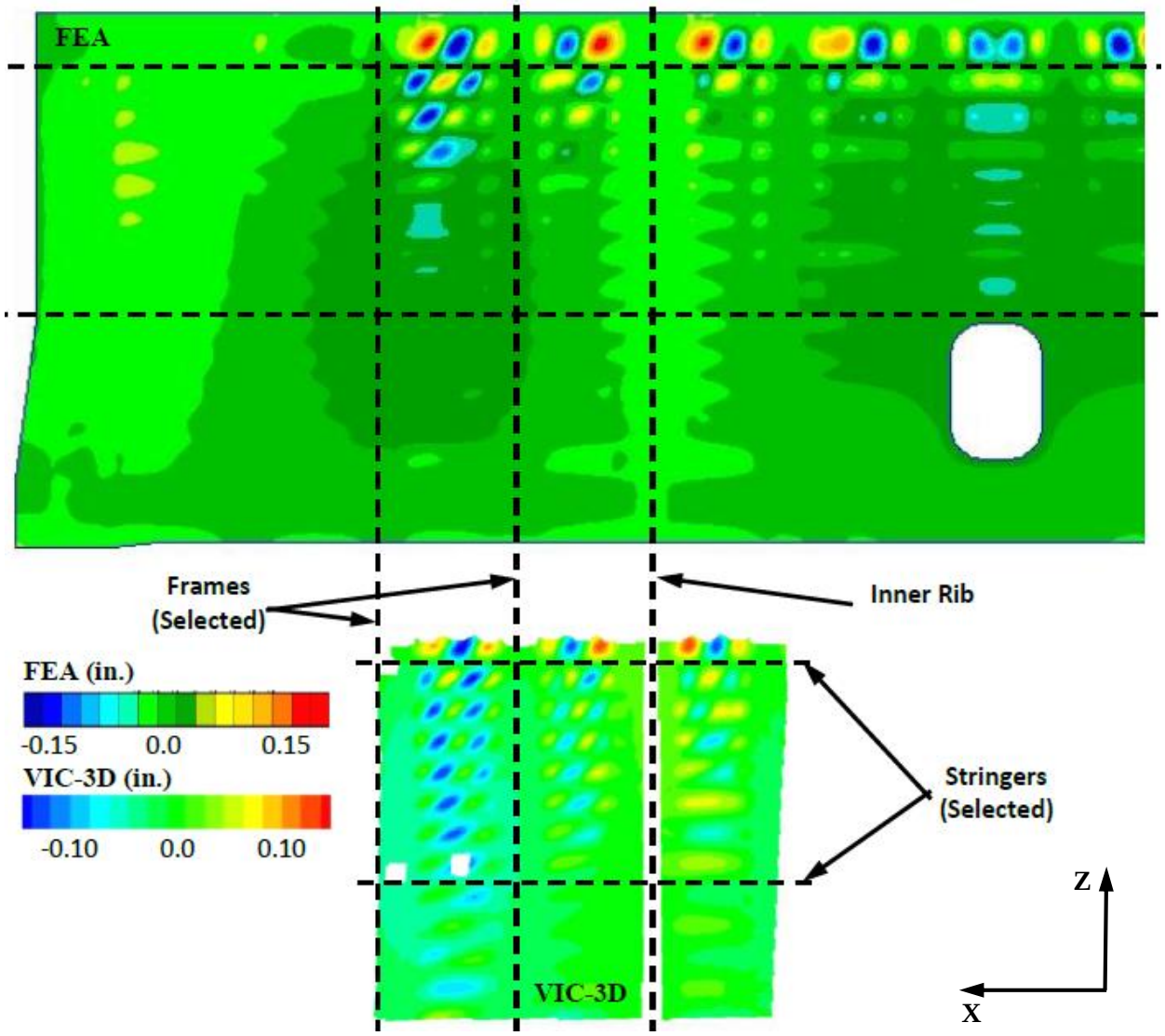

Figure 63. Out-of-plane deformation of the upper aft bulkhead panel under 2.5-g 165% DLL.

The out-of-plane center keel panel deformation under 2.5-g 150% DLL (DUL) is shown in Figure 64 and includes a comparison between test data and FEA results. The agreement between the two displacement fields is good. The Z-component of the side keel deformation obtained from FEA under the same load is shown in Figure 65. Since the center and side keel panels were not considered critical sections of the test article under the 2.5-g loads, results for the 165% DLL are omitted for brevity.

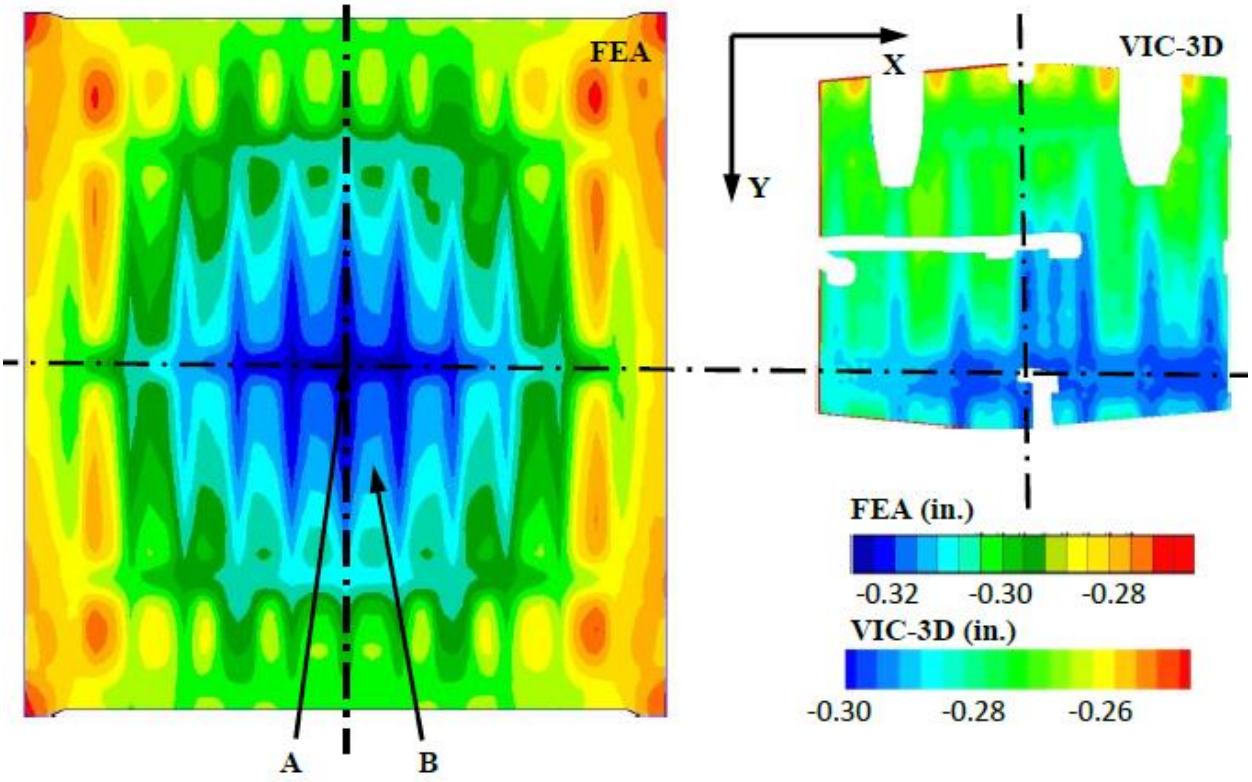

Figure 64. Out-of-plane deformation of the center keel panel under 2.5-g DUL.

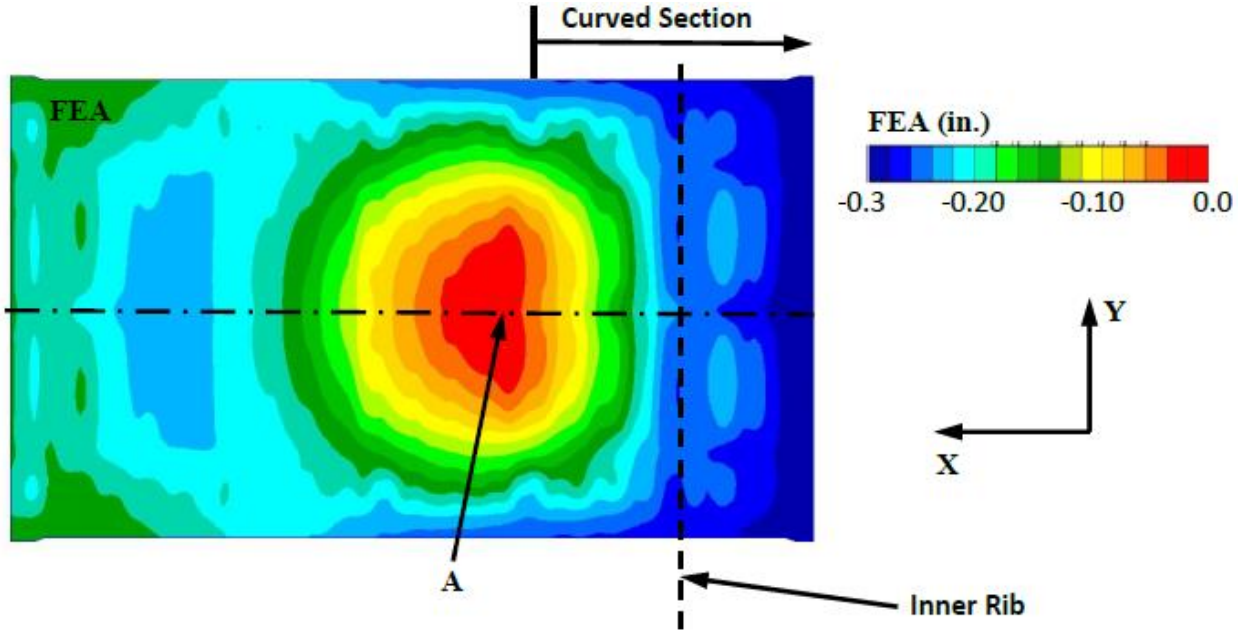

Figure 65. Z-component deformation of the side keel panel under 2.5-g DUL.

The crown panel strains at the top of the center frame are shown in Figure 66. Under the 2.5-g load, the crown panel underwent compression; a slightly nonlinear characteristic of the frame compressive strains is identified. The test strains show slightly stronger nonlinear behavior than the nonlinear FEA prediction and reach approximately −0.0036 in./in. at 150% DLL (or DUL) and −0.0040 in./in. at 165% DLL. A slight discontinuity in the test strain curve seen in Figure 66 around the DUL of 238.5 kips actuator load is due to the fact that the test results for the 2.5-g load are compiled as a sum of the 2.5-g DUL BVID test (up to 238.5 kips) and segment 5 of the "beyond DUL" BVID test presented in Figure 7 (from 238.5 kips to 262.4 kips actuator load). Similar strain discontinuities can also be observed later in this section in other strain plots under the 2.5-g load.

The crown panel T-cap strains are presented in Figure 67. Since the crown panel T-cap runs parallel to the three frames of the crown panel, apart from attaching the crown panel to the upper bulkhead panel, it also carries span-wise loads. The T-cap is a thick laminated structure to enable transfer of the bearing forces originating from the bolts that attach the crown panel to the upper bulkhead panel (bolted joints are not shown in the inset of Figure 67). In that sense, the T-cap construction is different from that of the crown panel frames, as the latter are sandwich construction with a foam core. Consequently, it is not surprising to observe in Figure 67 that the T-cap response characteristic is even closer to the linear characteristic when compared to the frame response.

The crown panel IML-side minimum principal skin strains in the side section of the panel near the aft frame flange (location C in Figure 60) are presented in Figure 68. A strain gauge rosette was used at this location since the nonlinear FEA predicted appreciable shear strain contribution due to the proximity of the stringer-frame intersection and the metallic fittings used to attach the upper bulkhead to the crown panel. The back-to-back strains at the mid-bay in the center section of the panel (location D in Figure 60) are presented in Figure 69. The unidirectional strain gauges were installed there as the span-wise strains were predicted by the FEA to dominate the response in the middle of the skin bays, i.e., away from frames, stringers, and metallic fittings. Both Figures 68 and 69 indicate that the crown panel skin buckling occurred early in the loading sequence. For the center section of the crown panel (location D in Figure 60) where the skin comprises a single stack (0.052 in.), buckling occurred around 30 kips actuator load. For the two stack-thick skin in the side section of the crown panel (location C in Figure 60), the buckling load was higher, at approximately 60 kips actuator load. In Figure 68, the minimum principal strains exhibit what can be called a softening nonlinear response. In other words, once the buckling of the skin occurs around 60 kips, the strain behavior departs from the linear relationship with the applied load, and compressive strains grow much faster than those predicted by the linear analysis. While the linear analysis prediction is approximately −0.0033 in./in. at 165% DLL, the measured strains are close to −0.0063 in./in.: that is, nearly double the linear FEA prediction. The nonlinear analysis accurately captures the buckling load and the post-buckled behavior by closely predicting the strain characteristic and values. A very good comparison between the test and the nonlinear FEA results is also noted in the back-to-back skin strains shown in Figure 69. Since the IML- and OML-measured strains are of similar magnitude but with opposite signs, it can be concluded that the in-plane strain component of the response in the mid-bay skin location is close to zero, with the bending strain component of order of ±0.0032 in./in. strongly dominating the response. This behavior is consistent with a strongly developed post-buckled regime that was shown in Figures 60 and 61 to dominate nearly the entire crown panel surface.

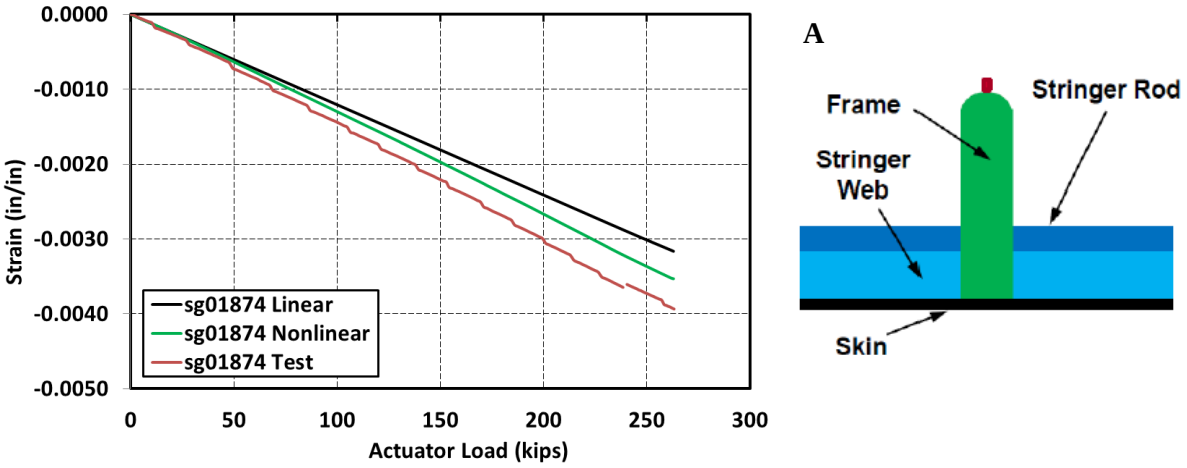

Figure 66. Strains at the top of the crown panel frame up to 2.5-g 165% DLL.

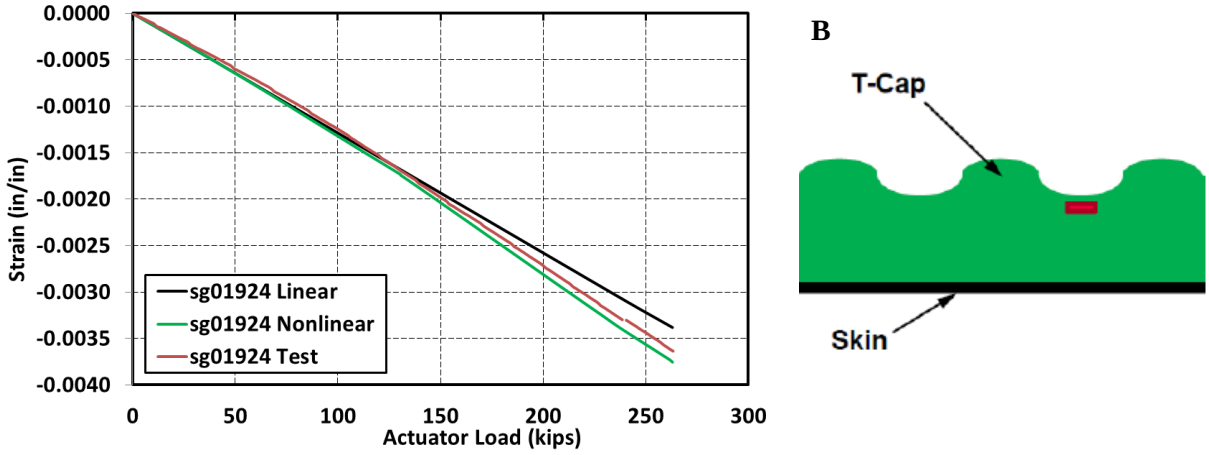

Figure 67. Strains in the crown panel T-cap up to 2.5-g 165% DLL.

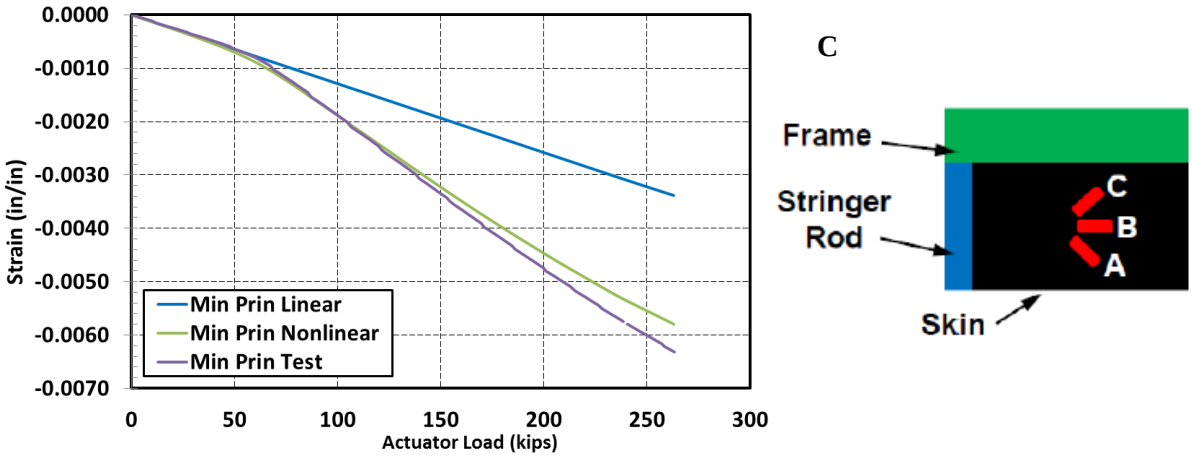

Figure 68. Minimum principal strains in the crown panel skin up to 2.5-g 165% DLL (sg01290A/sg01291B/ sg01292C).

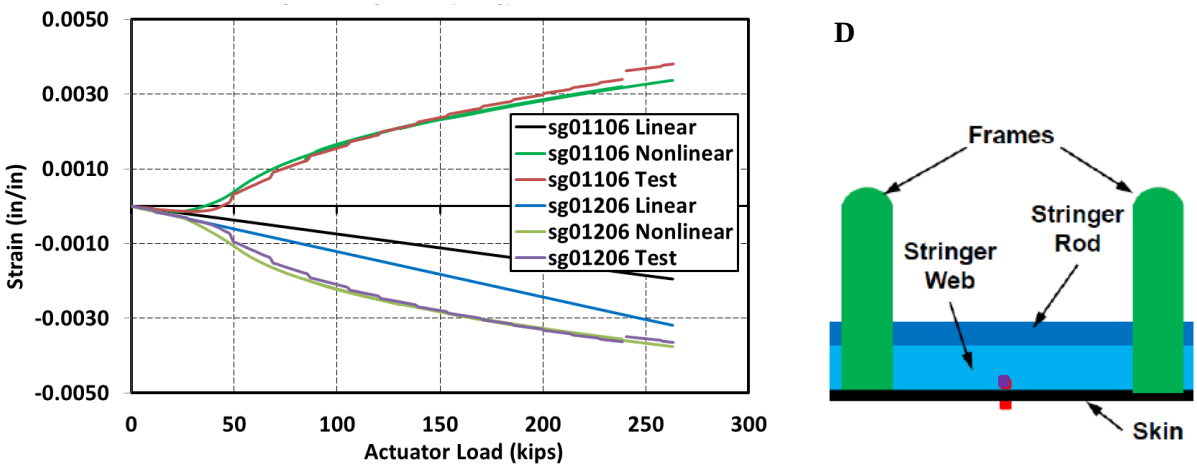

Figure 69. Crown panel back-to-back skin strains up to 2.5-g 165% DLL.

The skin strains in the top section of the upper bulkhead, adjacent to the crown panel undergoing significant compression, also exhibit strongly nonlinear characteristics due to buckling. The principal skin strains on the forward upper bulkhead panel are shown in Figure 70, and on the aft bulkhead panel are shown in Figure 71. The nonlinear behavior can be referred to as softening, since the minimum principal strain dominating the response grows more rapidly above the buckling load than the linear solution. The upper bulkhead skin buckling loads are, however, generally higher than those discussed previously for the crown panel. This result is supported by the fact that the crown panel skin is located at the farthest distance from the neutral bending axis of the entire test article and the top section of the upper bulkhead operates at a distance closer to the afore-mentioned neutral bending axis. As a reminder, the discontinuity of the test strain curves in both upper bulkhead figures is the result of the fact that the presented data are sourced from two distinct tests, as discussed in the beginning of this section.

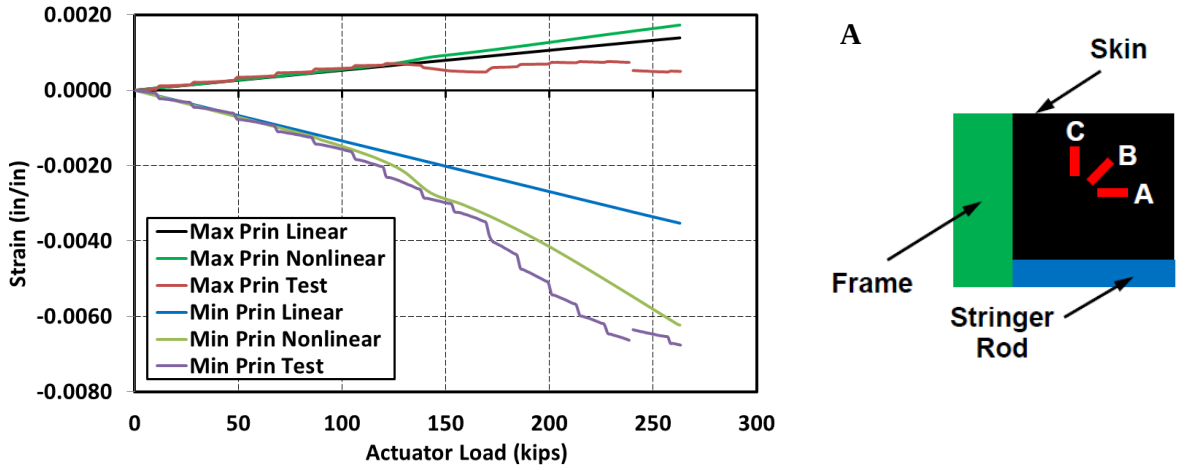

Figure 70. Principal strains in the forward upper bulkhead panel skin up to 2.5-g 165% DLL (sg05117A/ sg05118B/sg05119C).

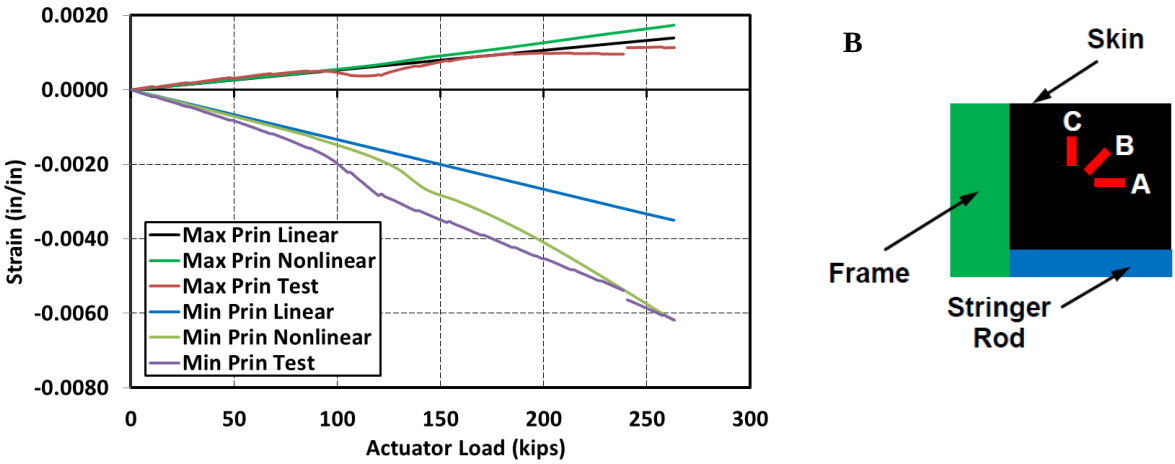

Figure 71. Principal strains in the aft upper bulkhead panel skin up to 2.5-g 165% DLL (sg03111A/ sg03112B/sg03113C).

The center keel strains in the center frame web (location A in Figure 64) are shown in Figure 72. A low level of only 0.0009 in./in. tensile strain is reached at 165% DLL in almost linear fashion. The center keel back-to-back skin strains (location B in Figure 64) are shown in Figure 73 and also achieve only low tensile level of 0.0012 in./in. The response of the tensioned section of the skin in the center keel panel is substantially different from that of the crown panel shown in Figure 69. As seen in Figure 73, the IML and OML strain levels are almost equal, which implies that almost the entire strain is attributable to its in-plane component. Overall, good comparison of the test data and the FEA results is found for the center keel panel.

The side keel strains at the top of the center frame (location A in Figure 65) are shown in Figure 74. Only 0.0038 in./in. tensile strain is reached at 165% DLL in almost linear fashion. Good agreement between test data and FEA results is found.

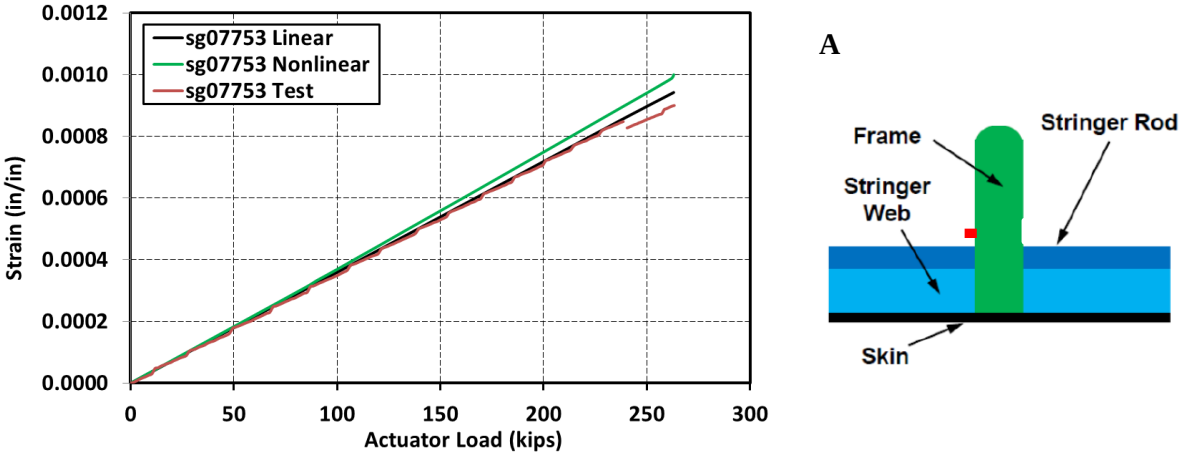

Figure 72. Strains in the web of the center keel panel frame up to 2.5-g 165% DLL.

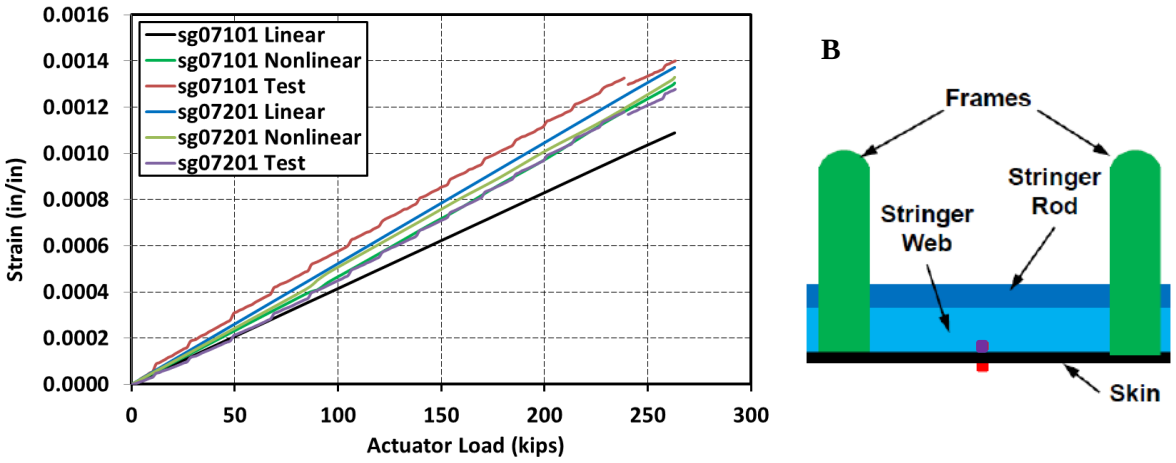

Figure 73. Center keel panel back-to-back skin strains up to 2.5-g 165% DLL.

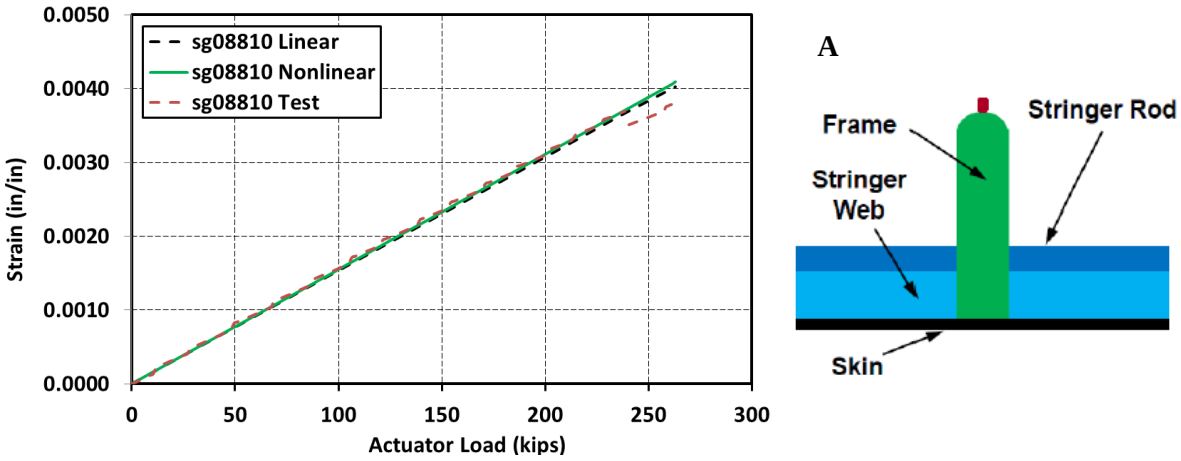

Figure 74. Strains at the top of the side keel panel frame up to 2.5-g 165% DLL.

While the metallic fittings connecting adjacent perpendicular panels, discussed before in section 3.1.3, did not experience high strain levels under the 2.5-g load due the absence of the pressure load component, some other metallic fittings experienced high strain levels. The largest strains in the metallic fittings under the 2.5-g 165% DLL were predicted to occur and identified during tests in the fittings shown in Figure 75 (two out of four symmetric fittings are shown). The fittings shown in Figure 75 transfer loads from the COLTS platens into the bottom section of the test article, as seen in Figure 5. Under the 2.5-g load, these fittings transfer large tension loads, while the fittings near the crown panel transfer large compressive loads. The strains on the bottom web in one of the bottom fittings are shown in Figure 76. As seen in the inset to Figure 76, two strain gauges were installed on the bottom web, one on the outer edge of the fitting web and one next to it, farther away from the web edge. Since the strains in the web were predicted to approach those corresponding to the yielding strain, the second strain gauge away from the web edge was intended to trace the extent of the potential plastic yielding, if such would occur. However, as predicted, the yielding strain was approached, but not exceeded, in the 2.5-g 165% DLL test and both gauges displayed linear behavior indicative of the elastic response regime. The maximum strain on the edge of the fitting web reached approximately 0.0059 in./in., slightly less than the yielding strain of 0.0063 in./in.

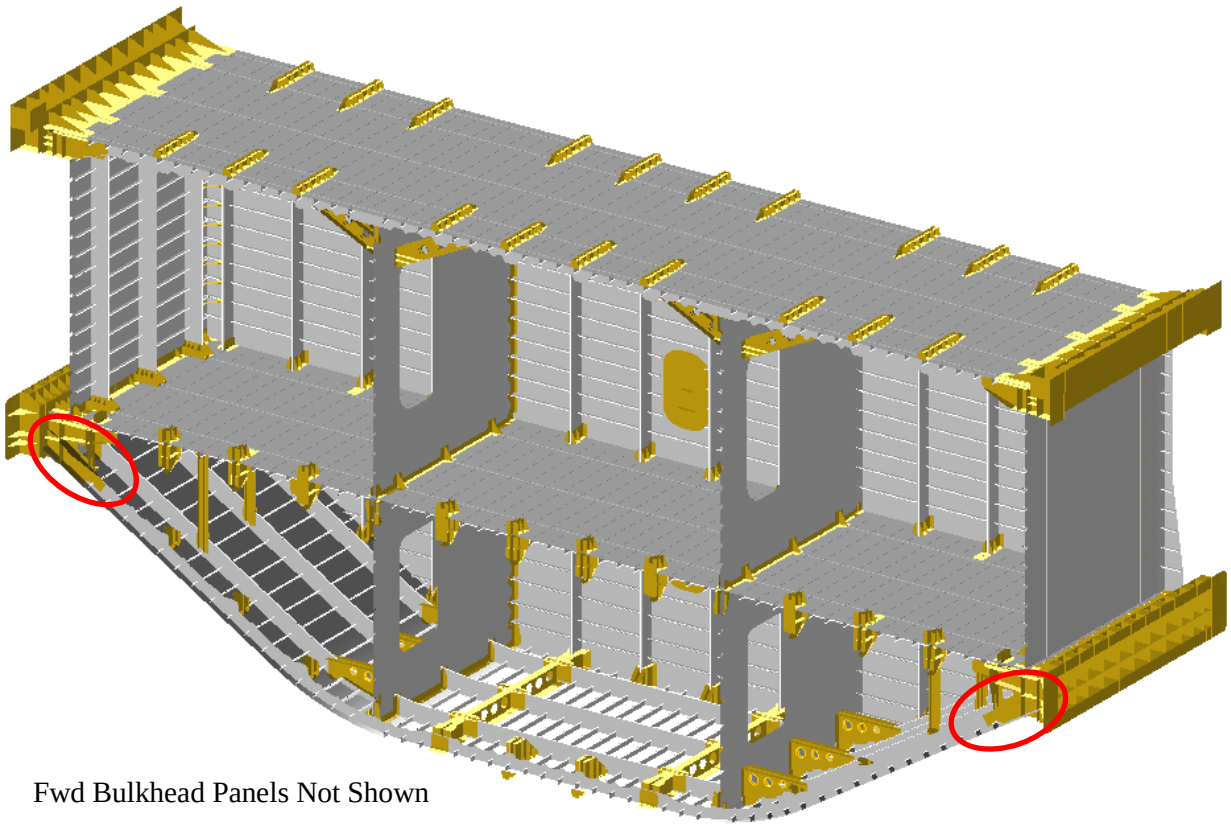

Figure 75. Location of metallic fittings with measured high strains under 2.5-g 165% DLL.

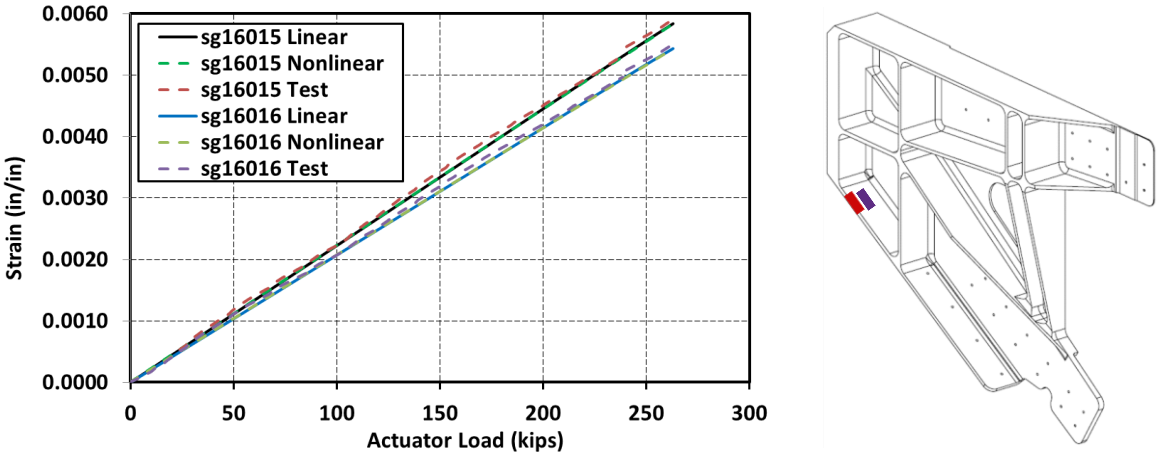

Figure 76. Strains in the metallic fittings connecting the side keel panel to the lower bulkhead up to 2.5-g 165% DLL.

3.1.5. 2.5-g + 1P Load

Under the 2.5-g + 1P load, the top of the test article was compressed and the bottom tensioned by the mechanical loads. The unsupported sections of the external panels bowed outwards due to the internal pressure. The crown panel out-of-plane deformation under 150% DLL (or DUL) is presented in Figure 77 and under 2.5-g 165% DLL + 1P 150% DLL (the "beyond DUL" portion of the test described in section 2.1) in Figure 78. All the skin bays in the center section of the crown panel (except for one covered by an off-center span-wise section of the repair patch shown in Figure 8) are pushed outward by the pressure loading. The outward skin deformation dominates the response even though initially, when the load was being applied to the test article, some of the center section skin bays buckled inward. This behavior took place because only a low level of mechanical loading was needed to buckle individual skin bays, as documented in section 3.1.4. However, as the load application progressed and the pressure load became larger, the normal to the skin-surface pressure forces were able to snap through all the skin bays to the outward position. This was, however, not the case for some of the skin bays in the side sections of the panel, where the skin has a larger thickness. Once such a thicker skin bay buckled due to the mechanical portion of the load, further pressure increase was insufficient to force the inward buckled skin section into the alternate outward equilibrium. While the above-described behavior cannot be conclusively discerned from the individual crown images enclosed in this report, a review of the animation assembled from all the acquired VIC-3D images resulted in the above-described observation. In general, the pressure component of the 2.5-g + 1P load can be regarded as a factor removing some of the uncertainty associated with the out-of-plane displacement results described in section 3.1.4 that documented the 2.5-g only load condition. For example, no distinct deformation patterns between the pristine and the BVID tests were observed. Similarly, numerical simulations conducted with different initial integration steps also yielded identical results. For both load levels shown in Figures 77 and 78, a good qualitative agreement is found between the nonlinear FEA and test measurements.

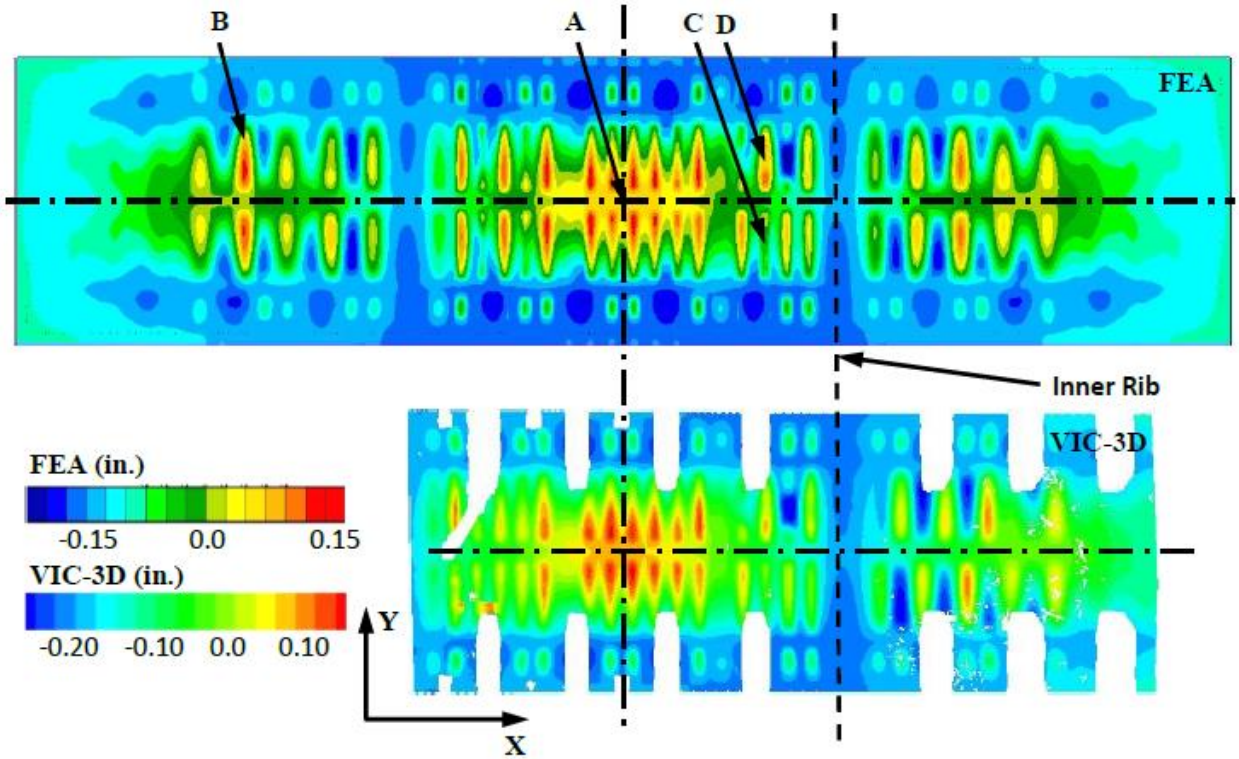

Figure 77. Out-of-plane deformation of the crown panel under 2.5-g + 1P DUL.

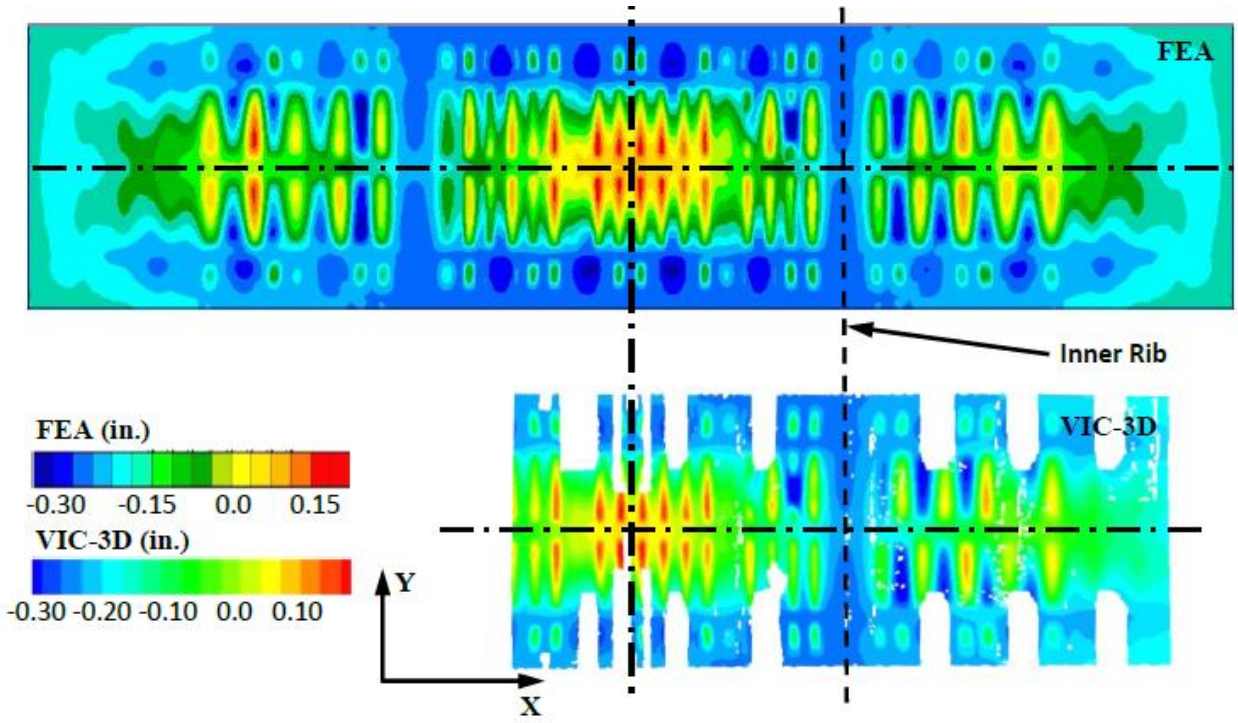

Figure 78. Out-of-plane deformation of the crown panel under 2.5-g 165% DLL + 1P 150% DLL.

The out-of-plane deformation of the upper aft bulkhead panel under 150% DLL (or DUL) is presented in Figure 79 and under the 2.5-g 165% DLL + 1P 150% DLL in Figure 80. In both cases, the distinct outward bowing pattern of the unsupported sections of the upper bulkhead panel can be identified and good qualitative comparison with the nonlinear FEA results is seen. As in the majority of the displacement results presented thus far, the out-of-plane magnitudes predicted by the nonlinear FEAs are slightly larger than the magnitudes measured during the test.

A distinct feature in the results presented at the two loads in Figure 79 and 80 occurs at the top section of the upper bulkhead panel. Recall from Figure 7, that the "beyond DUL" portion of the test required holding of the constant pressure of 1.5P while further increasing the mechanical portion of the load. It is seen while comparing Figures 79 and 80 that the out-of-plane deformation in the unsupported sections of the panels grows only marginally. At the same time, at the very top of the upper bulkhead panel (i.e., above the top-most dashed horizontal line corresponding to the location of the top-most stringer) under the 2.5-g load component increased to 165% DLL, individual skin bays begin to display shapes consistent with the local buckling. These features are best seen in the FEA portion of Figure 80. Only limited sections of the top of the upper bulkhead were acquired using the VIC-3D system due to the interference of the crown panel T-cap (which is not shown in the FEA results presented herein). However, while the test image in Figure 80 is carefully examined, it can be concluded that the same behavior is also distinguishable in the measured data.

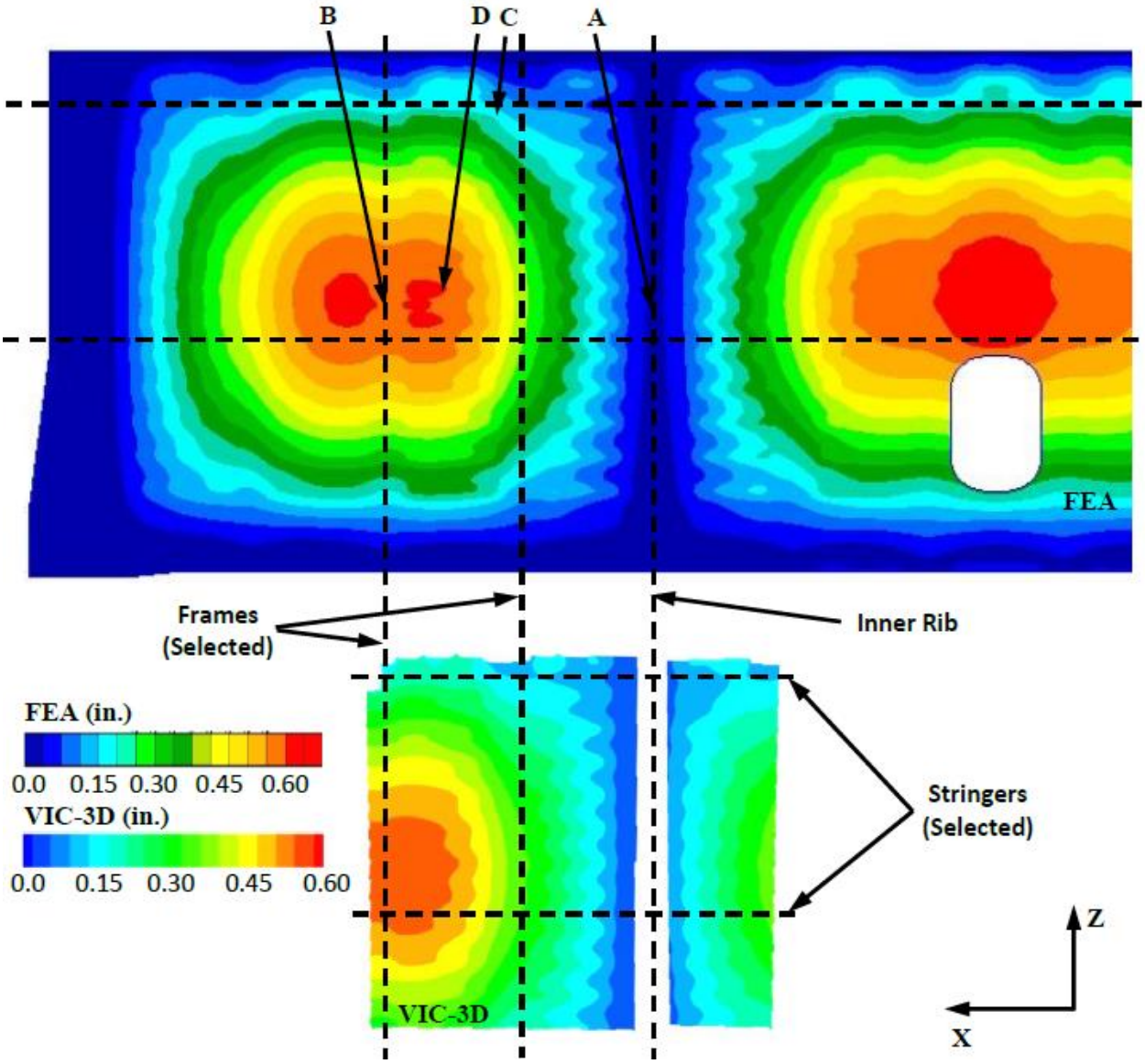

Figure 79. Out-of-plane deformation of the upper bulkhead panel under 2.5-g + 1P DUL.

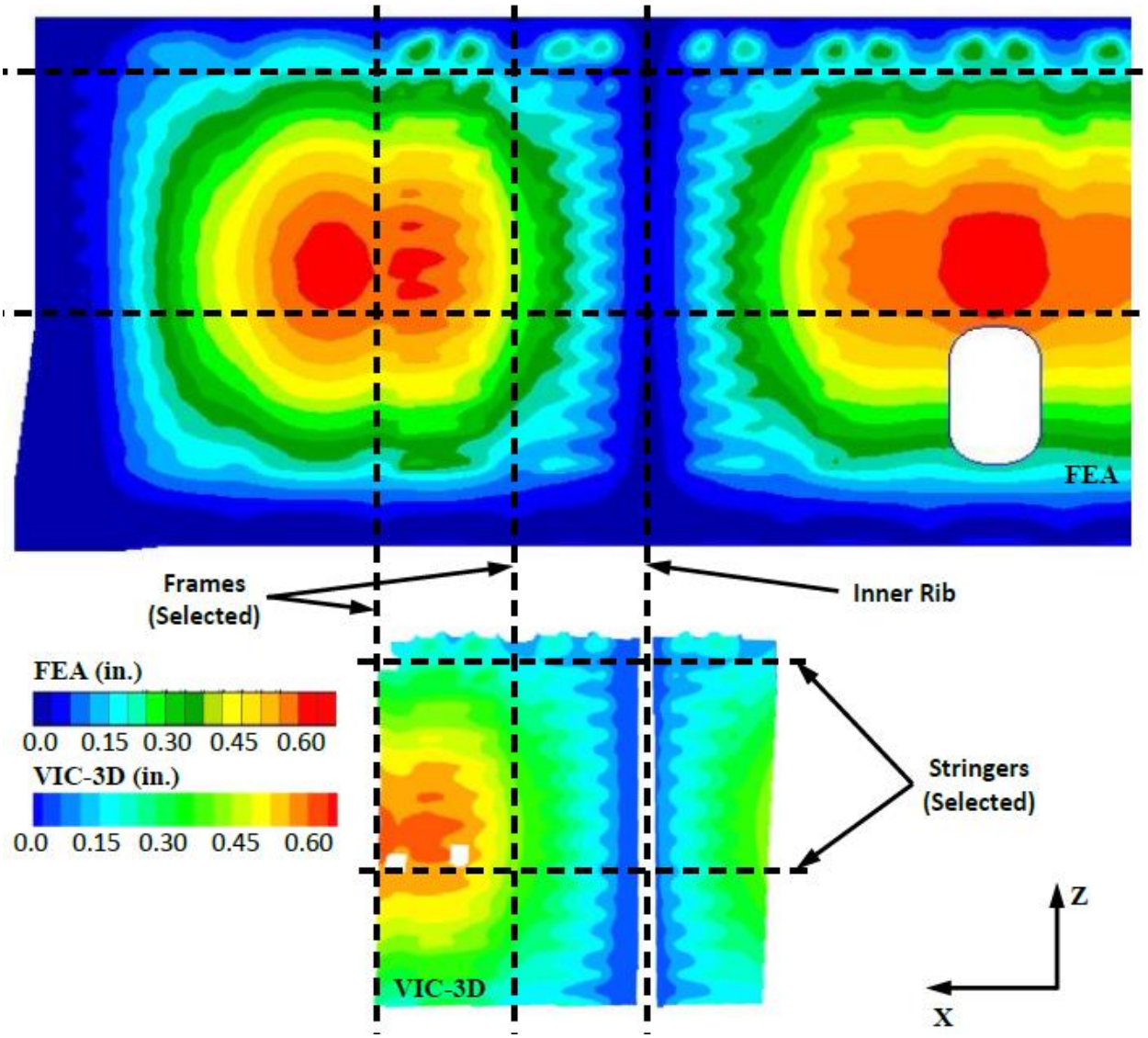

Figure 80. Out-of-plane deformation of the upper bulkhead panel under 2.5-g 165% DLL + 1P 150% DLL.

The out-of-plane center keel deformation under 2.5-g + 1P DUL is shown in Figure 81 and includes a comparison between test data and FEA results. The agreement between the two displacement fields is very good in qualitative terms, and the predicted magnitudes are slightly smaller than those measured in the test. The Z-component of the side keel deformation obtained from FEA under the same load is shown in Figure 82. Since the pressure load component is a strong driver of the out-of-plane deformation in the center and side keel panels, and this component is kept constant relative to the condition shown in Figures 81 and 82, the deformation plots under 2.5-g 165% DLL + 1P 150% DLL are not shown for brevity.

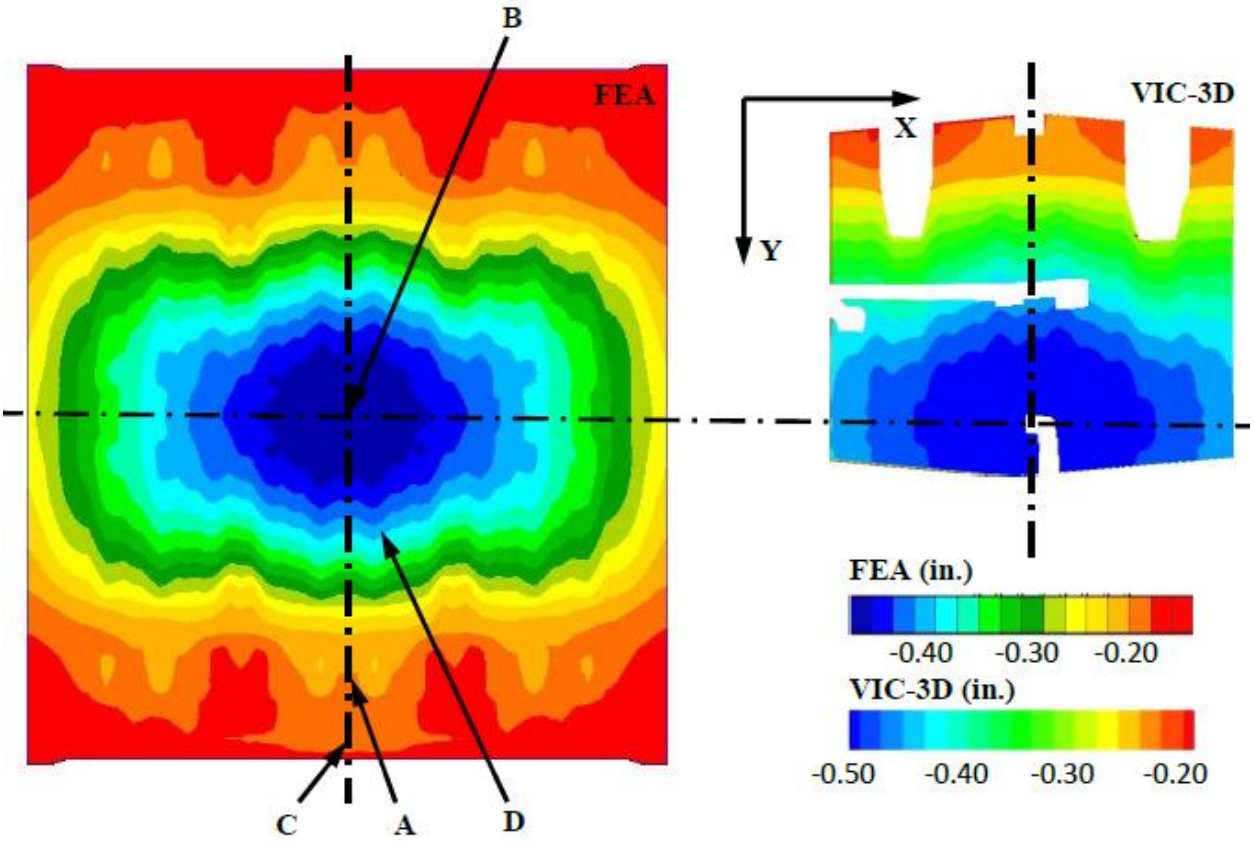

Figure 81. Out-of-plane deformation of the center keel panel under 2.5-g + 1P DUL.

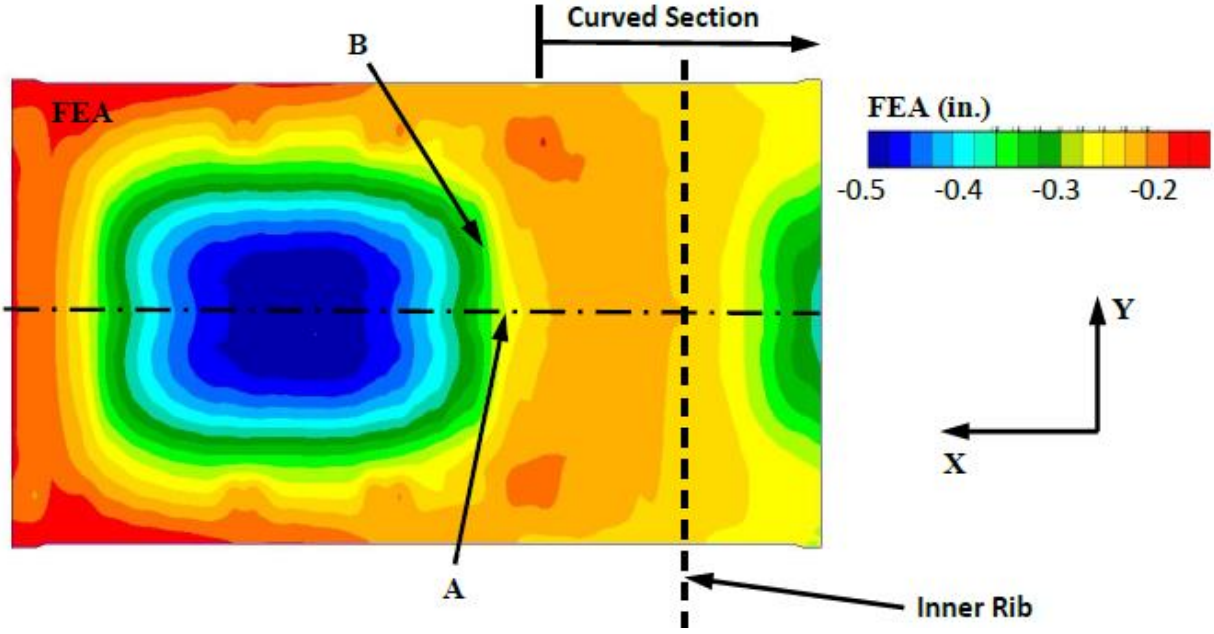

Figure 82. Z-component deformation of the side keel panel under 2.5-g + 1P DUL.

The crown panel strains at the mid-span top of the center frame (location B in Figure 77) are shown in Figure 83. The strain approaches a moderately high compressive value of −0.0045 in./in. at the maximum test load of 2.5-g 165% DLL + 1P 150% DLL (262.4 kips actuator load). The strain displays a nearly linear characteristic over the entire load. Upon closer examination, however, the slope of the strain versus load curve changes slightly at 238.5 kips actuator load, which corresponds to 2.5-g + 1P DUL. Above that load, only the mechanical component of the load is increased further, while the pressure load is kept constant. The behavior observed in Figure 83 is, therefore, indicative of the mechanical load being the primary driver of the frame response in the particular location considered. A very good comparison between the test measurement and the FEA prediction is obtained.

The minimum principal strains in a side section of a skin bay (i.e., close to a frame-stringer intersection) located in a side section of the crown panel (location B in Figure 77) are shown in Figure 84. In the figure, the strain at the maximum test load approaches a very high compressive value of −0.0070 in./in., i.e., approximately 0.0005 in./in. more negative than the same location under the 2.5-g 165% DLL only, shown in Figure 68. The strain departs from the linear characteristic at approximately 75 kips actuator load. A good comparison between the test measurement and the nonlinear FEA prediction is achieved for this post-buckled response.

The back-to-back skin strains at two locations in the center section of the crown panel (locations C and D in Figure 77) are shown in Figure 85. Both tensile strains on the OML skin surface and compressive strains on the IML skin surface reach the absolute value of approximately 0.0040 in./in. and match closely those obtained from the nonlinear FEA. This behavior is indicative of this skin location response being strongly dominated by the bending strain component with almost non-existent in-plane strain participation. This condition is substantially different from the results of the linear FEA. Narrowing down the discussion to location C, the linear prediction of the OML surface strain remains near zero throughout the entire load application, while the IML surface strain reaches the value of −0.0044 in./in. at the maximum test load. The linear FEA results effectively mean that the in-plane strain component at the maximum test load has a value of approximately −0.0022 in./in. (the average of the two OML and IML measurements) and match the absolute value of the bending strain component of ±0.0022 in./in. (the difference between the in-plane strain and the OML/IML values). The linear FEA is therefore producing qualitatively incorrect results because it lacks the ability to accurately account for in-plane versus out-of-plane deformation interactions under large out-of-plane deformations occurring due to skin buckling.

Overall, a very good comparison between test results and nonlinear FEA results is achieved. The earlier than predicted initiation of the nonlinear behavior at location D (red curve in the second plot of Figure 85) can be likely attributed to initial imperfections of the structure not reflected in the nominal FEM, especially since once the nonlinear response becomes fully developed the agreement between the test measurements and the nonlinear FEA results becomes very good.

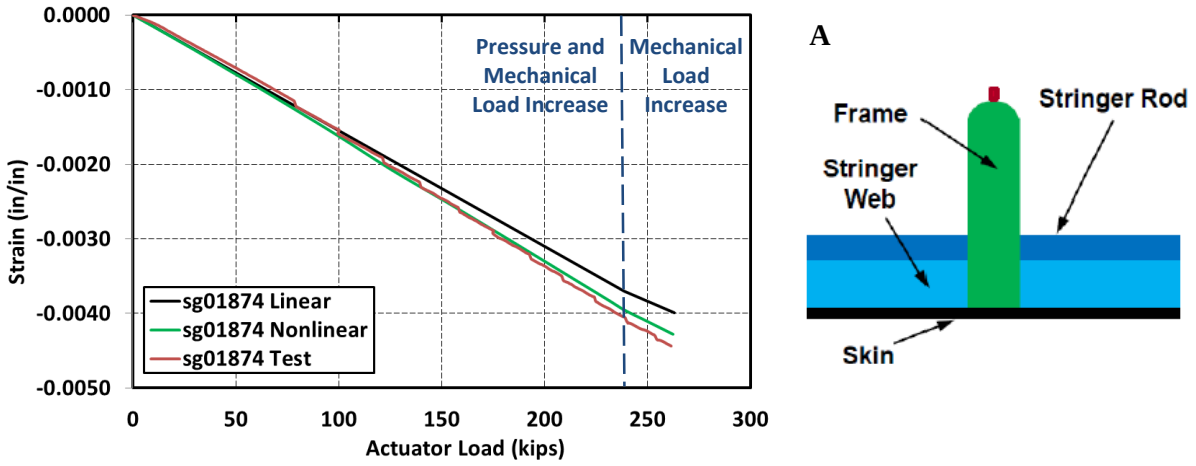

Figure 83. Strains at the top of the crown panel frame up to 2.5-g 165% DLL + 1P 150%.

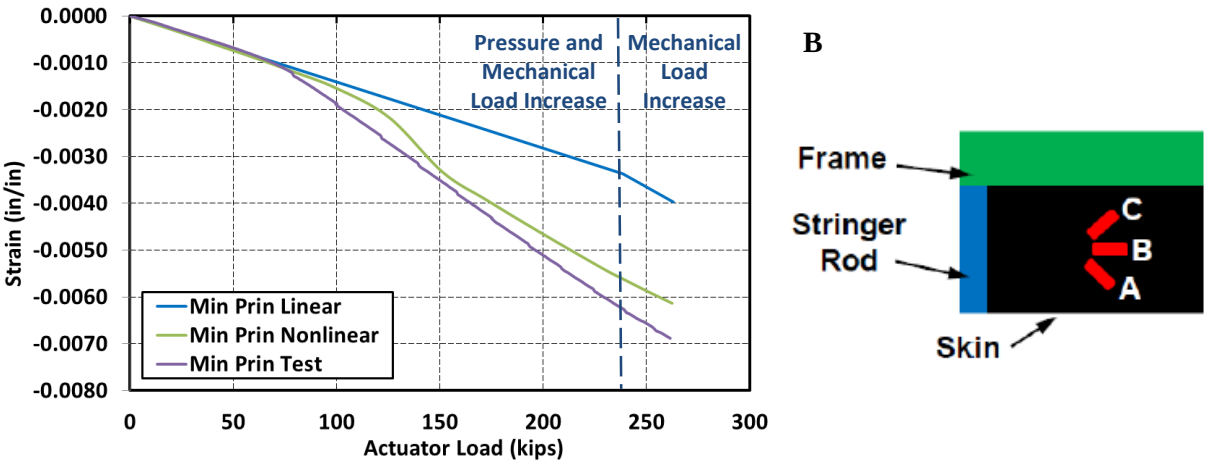

Figure 84. Minimum principal strains at the crown panel skin up to 2.5-g 165% DLL + 1P 150% (sg01290A/ sg01291B/sg01292C).

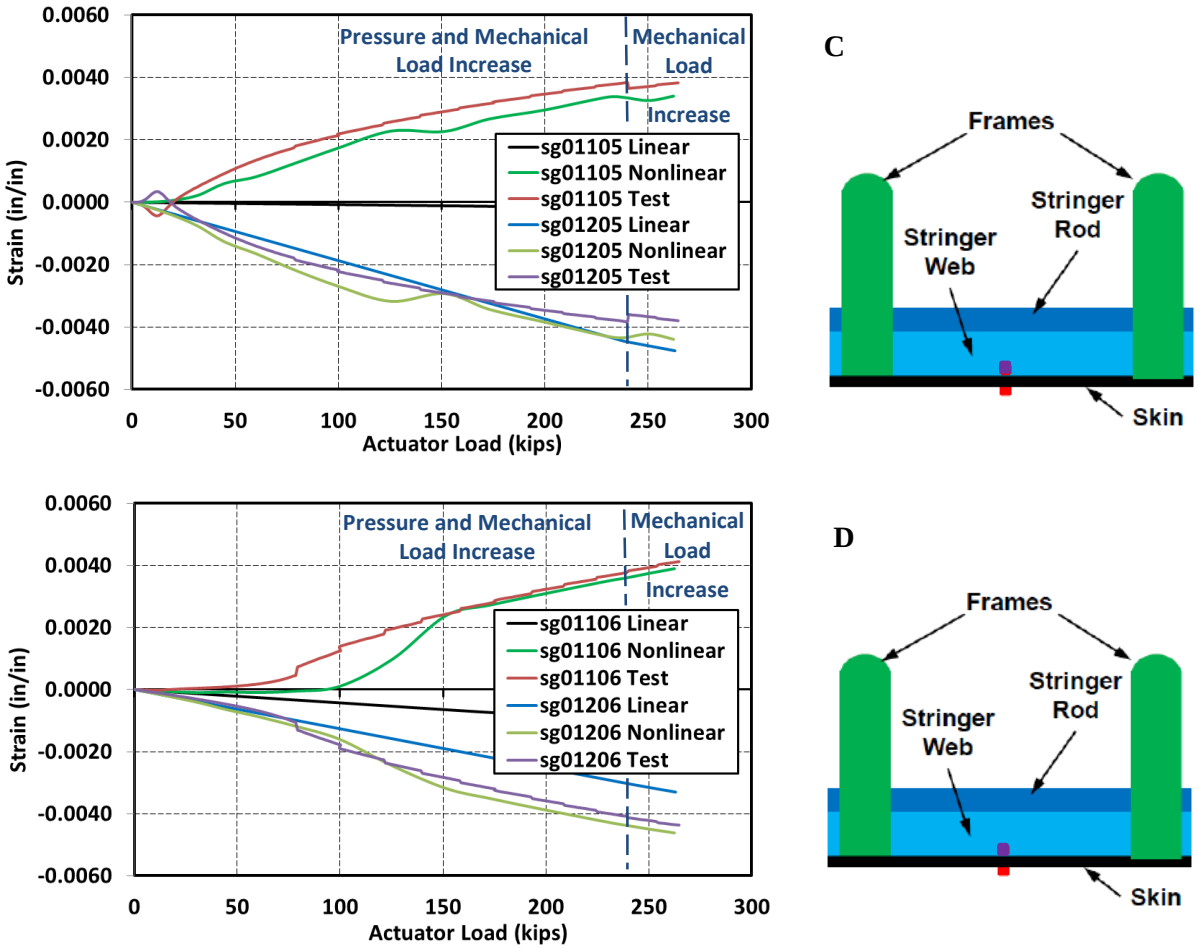

Figure 85. Crown panel back-to-back skin strains up to 2.5-g 165% DLL + 1P 150%.

The upper aft bulkhead strains at the stringer top (location A in Figure 79) are presented in Figure 86. The strains in the stringer are strongly influenced by the pressure loading, and that the mechanical loading component has a negligible effect on the response. This is evidenced by the strain level growing at a steady rate up to the point corresponding to 2.5-g + 1P DUL (238.5 kips actuator load). Above the DUL load, when only the mechanical load component is increased and the pressure is kept constant, the strain response remains almost unchanged. While the FEA analysis accurately captures this behavior, the test data show lower strains compared to those predicted. As indicated before, a simplified pultruded rod modeling, which does not explicitly model the rod overwrap, can be at least partially contributing to the observed difference.

The upper aft bulkhead strains at the frame top (location B in Figure 79) are presented in Figure 87. Similar to the response of the upper bulkhead panel stringer shown in Figure 86, the frame response is also strongly dominated by the pressure load, i.e., compressive strains grow steadily up to the 2.5-g + 1P DUL (238.5 kips actuator load) and remain virtually unchanged above that load when only the mechanical load component is being further increased. The comparison of the strain levels between the test measurements and the FEA results is better than that for the top of the stringer. Initial strain deviation in the proximity of the zero load are, as discussed before, resulting from the pressure control system limitations at the low mechanical load levels.

The upper forward bulkhead principal skin strains (location C in Figure 79) are shown in Figure 88. It is seen that the strain levels achieved in this location under 2.5-g + 1P load are lower than those obtained under the 2.5-g mechanical load only, as presented in Figures 70 and 71. This possibly counterintuitive result at first can be easily explained by examining the out-of-plane deformations for the 2.5-g 150% DLL

and 165% DLL (Figures 62 and 63, respectively) and the corresponding plots for the 2.5-g + 1P DUL and 2.5-g 165% DLL + 1P 150% DLL (Figures 79 and 80, respectively). In the absence of the pressure load, the top section of the upper bulkhead undergoes buckling, and the top skin bays buckling shapes display typically three or four semi-sine-like buckles, which results in large out-of-plane displacements. Addition of the pressure loading pushes the entire skin section outward, thus changing the deformation shape into a single pillowing-out shape, which results in smaller local curvatures, thus lower strains.

The upper aft bulkhead panel back-to-back skin strains measured away from the crown panel (location D in Figure 79) also display a strongly nonlinear characteristic, as shown in Figure 89. The nature of this nonlinear behavior is, however, different than that previously discussed for the crown panel skin, or skin section in the top section of the upper bulkhead panel. Away from the top section of the test article, the compressive mechanical load is not as prevalent as it is in the crown panel and the top section of the upper bulkhead. Therefore, the nonlinear behavior seen in Figure 89 is more aligned with that shown in Figure 46 discussed before for the 2P load in section 3.1.3. In other words, the in-plane stretching rather than compression influences the response and, consequently, the hardening nonlinear response is observed in Figure 89.

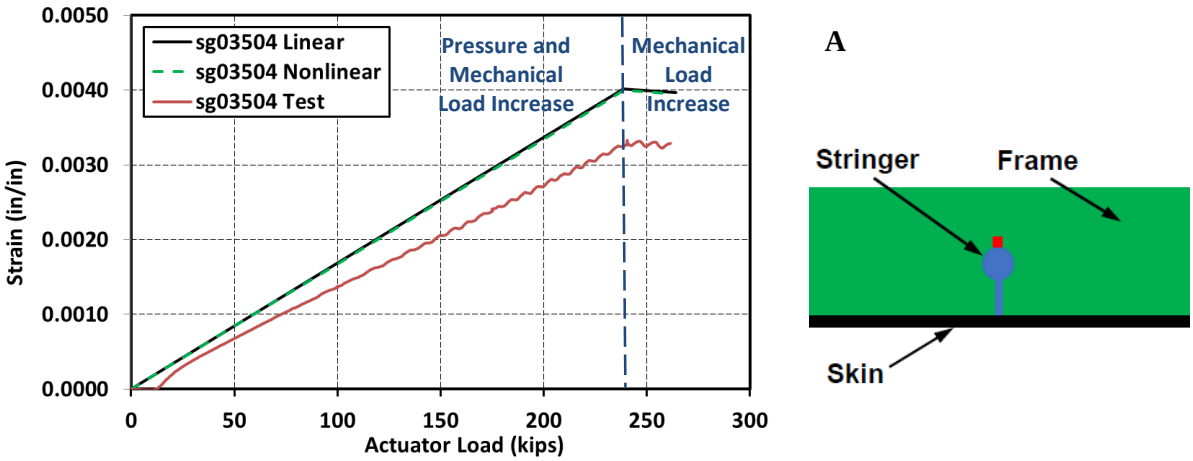

Figure 86. Strains at the top of the upper bulkhead stringer up to 2.5-g 165% DLL + 1P 150%.

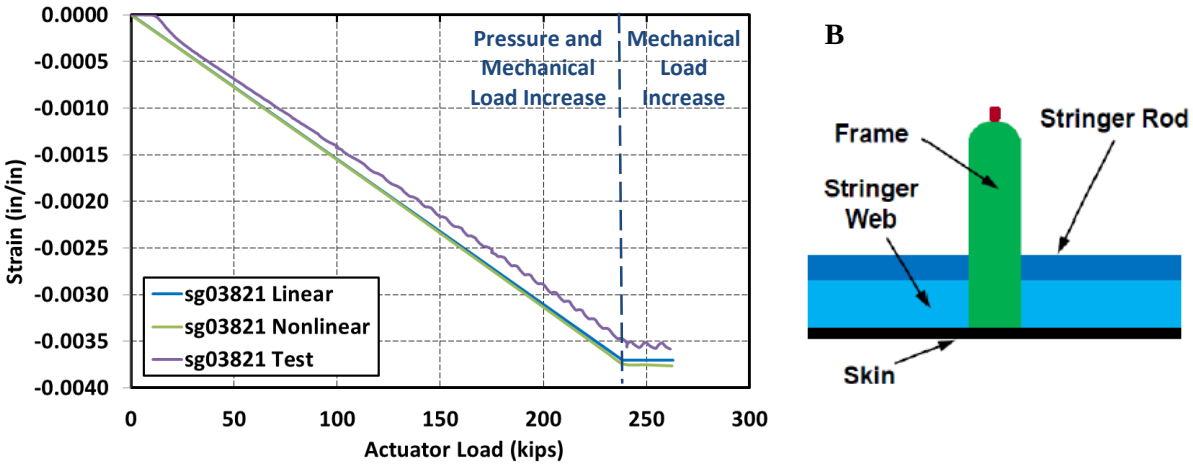

Figure 87. Strains at the top of the upper bulkhead frame up to 2.5-g 165% DLL + 1P 150%.

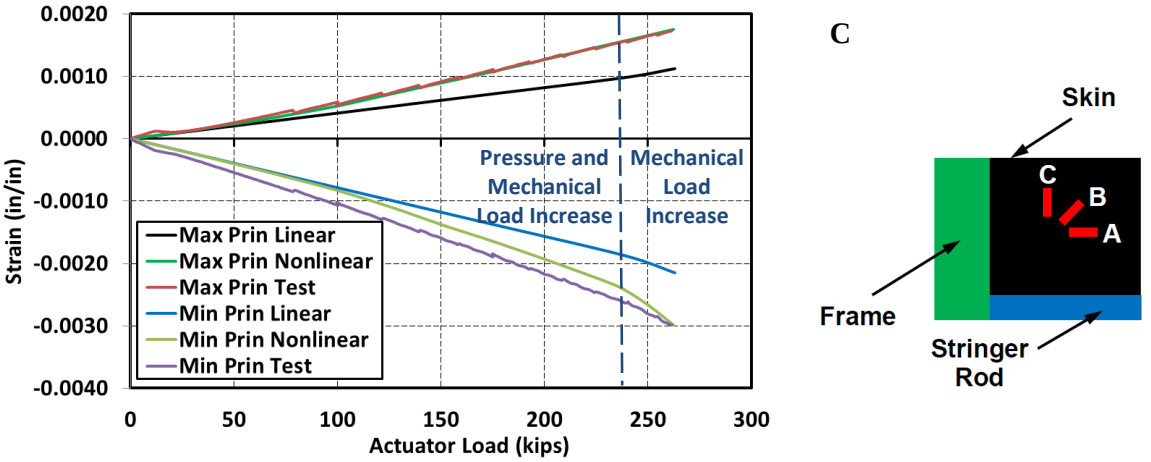

Figure 88. Principal strains in the upper bulkhead panel skin up to 2.5-g 165% DLL + 1P 150% (sg05108A/ sg05109B/sg05110C).

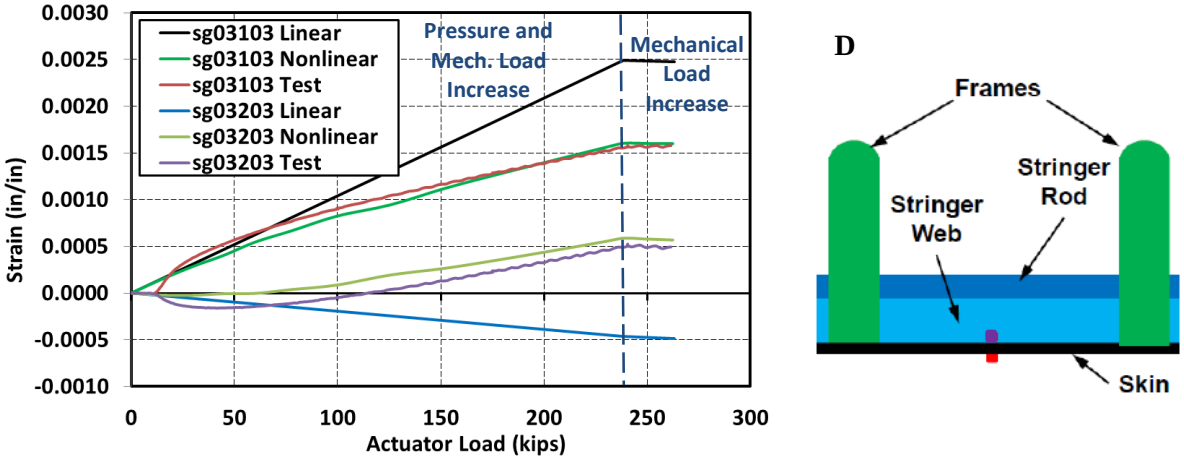

Figure 89. Upper bulkhead panel back-to-back skin strains up to 2.5-g 165% DLL + 1P 150%.

The center keel panel strains at the top of a stringer (location A in Figure 81) are shown in Figure 90. Similar to the behavior of the top of the stringer discussed for the upper bulkhead panel (Figure 86), up to 2.5-g + 1P DUL (238.5 kips actuator load) the response is strongly dominated by the pressure load component. The strains in Figure 90 show no further growth once the pressure load component is kept constant and only the mechanical load is increased further. This behavior is different from that observed in the center keel frame web (location B in Figure 81) shown in Figure 91. The span-wise orientation of the center keel frame makes it the primary load path for the tension loads in the bottom section of the test article, and the influence of the pressure load is minimal. This observation is based on the absence of appreciable strain rate change in the vicinity of the 2.5-g + 1P DUL (238.5 kips actuator load).

The center keel panel T-cap strains (location C in Figure 81) are shown in Figure 92. At first, since the center keel T-caps are aligned with the direction of the center keel frames, the rationale for the strain gauge orientation perpendicular to the span-wise direction may not be intuitive. However, the center keel T-caps not only transfer span-wise loads at the bottom of the test article but are also used to attach lower bulkheads. Lower bulkheads are subject to the pressure load. Consequently, T-cap strains presented in Figure 92 show significant strain values in the direction perpendicular to the span-wise direction, as the T-cap acts as a clamped-like boundary for the lower bulkhead panel. A significantly reduced rate of change in strains

above 2.5-g + 1P DUL (238.5 kips actuator load), i.e., above the load where the pressure load stops increasing, confirms this observation.

The center keel panel back-to-back skin strains (location D in Figure 81) are shown in Figure 93. They show the previously discussed hardening response. Both the OML and IML surface strains are tensile and are not separated by a large margin. This means that the in-plane strain component (the average of the two gauges) is large when compared to the bending strain component. This observation is not surprising, as both mechanical and pressure loads work jointly to stretch the skin of the center keel panel.

Overall, a very good comparison between the measured strains and the nonlinear FEA predictions is achieved for all the locations examined for the center keel panel.

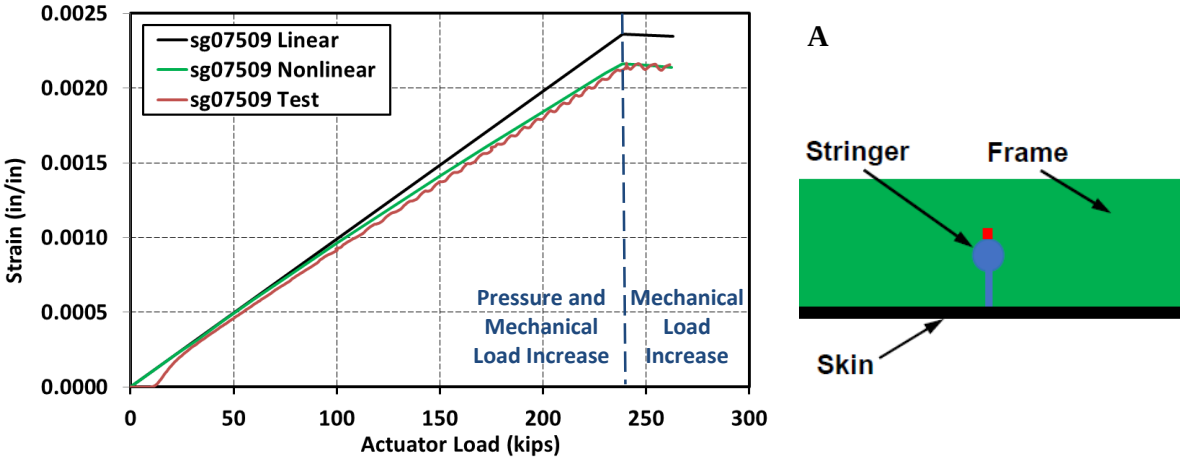

Figure 90. Strains at the top of the center keel panel stringer up to 2.5-g 165% DLL + 1P 150%.

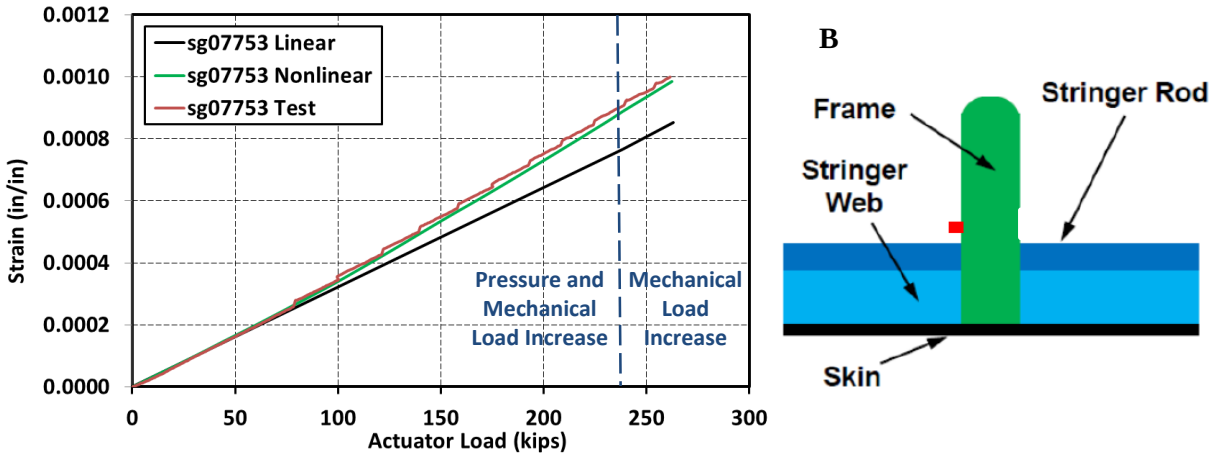

Figure 91. Strains in the web of the center keel panel frame up to 2.5-g 165% DLL + 1P 150%.

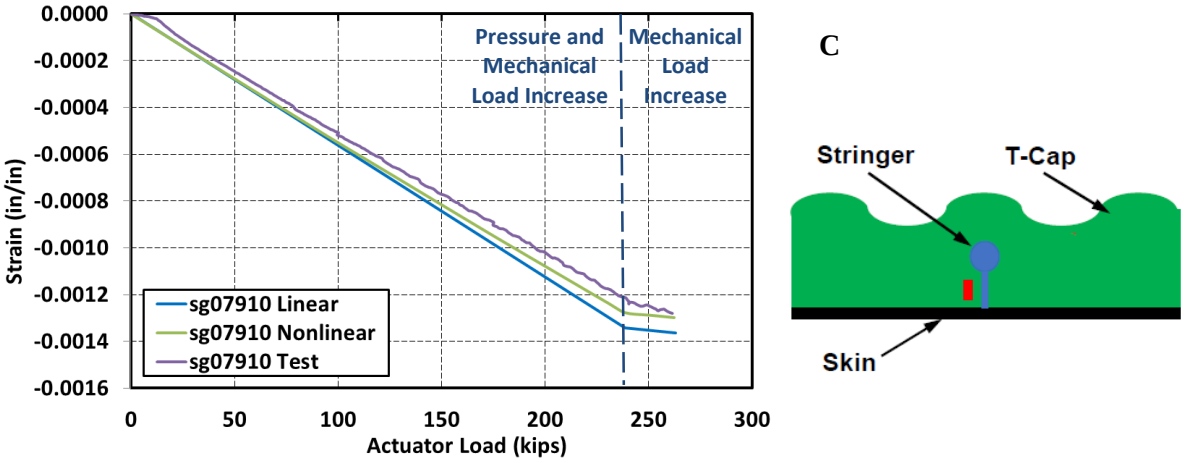

Figure 92. Strains in the center keel panel T-cap up to 2.5-g 165% DLL + 1P 150%.

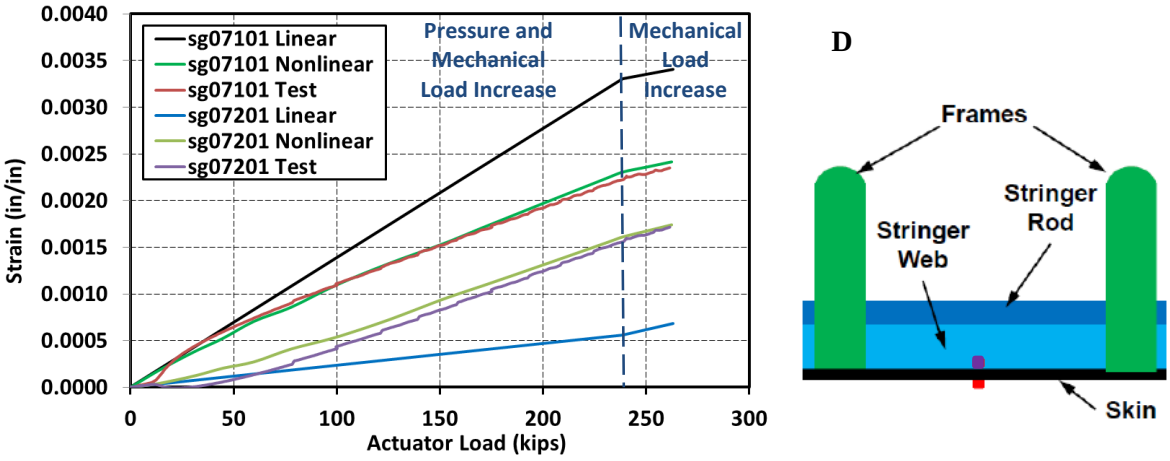

Figure 93. Center keel panel back-to-back skin strains up to 2.5-g 165% DLL + 1P 150%.

The side keel strains at the top of the center frame (location A in Figure 82) are shown in Figure 94 and display almost linear behavior over the entire load application sequence. The fact that the rate of strain change remains unchanged at 2.5-g + 1P DUL (238.5 kips actuator load) means that the mechanical load is the primary strain driver, as it is in the center keel frame, and the pressure load has only minimal effect.

The side keel panel back-to-back strains (location B in Figure 82) are shown in Figure 95. Although their nonlinear characteristic is similar to that of the center keel panel shown in Figure 93, the maximum values on the OML skin surface are smaller, and show less favorable comparison with the nonlinear FEA analysis.

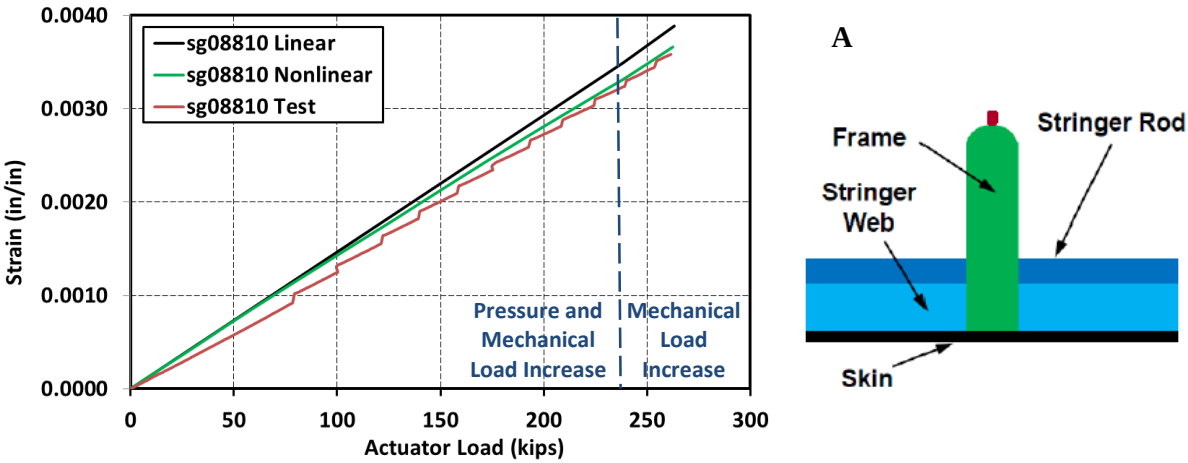

Figure 94. Strains at the top of the side keel panel frame up to 2.5-g 165% DLL + 1P 150%.

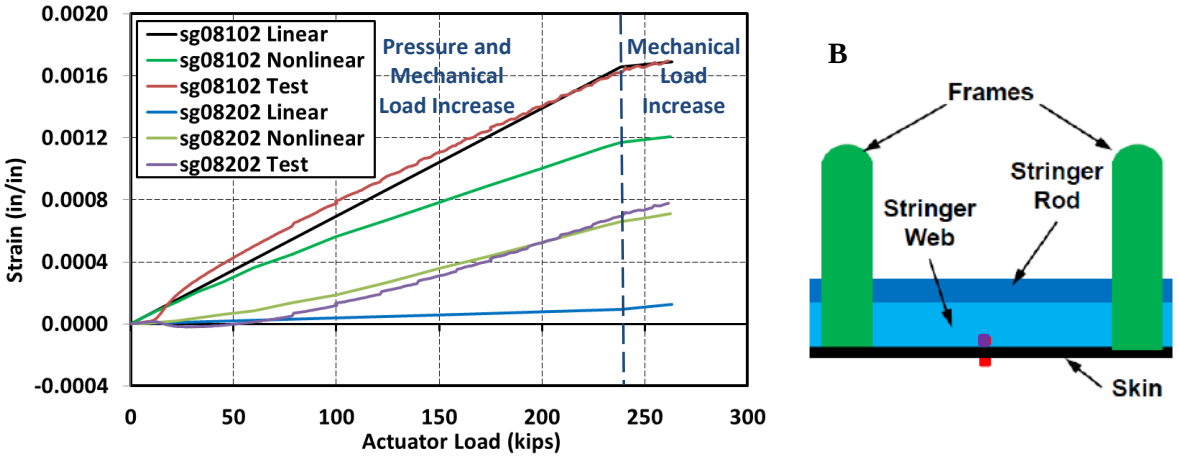

Figure 95. Side keel panel back-to-back skin strains up to 2.5-g 165% DLL + 1P 150%.

Finally, metallic fitting strains are examined for the same critical location introduced in section 3.1.4 for the 2.5-g load. Since this metallic fitting shown in Figure 75 carries the mechanical tension loads from the platens into the bottom section of the test article, then the pressure effect on this fitting was predicted to be minimal. The strain characteristic and values presented in Figure 96 confirm this prediction, as it is seen that strain values almost identical to those shown in Figure 76 for the 2.5-g load are obtained.

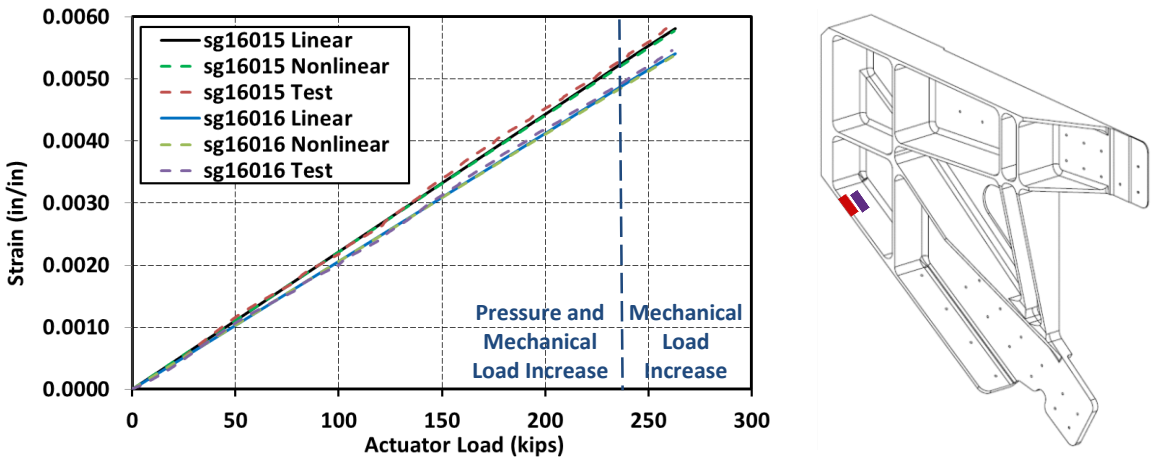

Figure 96. Strains in the metallic fitting connecting side keel panel to lower bulkhead up to 2.5-g 165% DLL + 150% 1P.

3.2. Barely Visible Impact Damage Locations

Three internal and three external impact sites were selected for the HWB center section test article. Both interior and exterior locations were chosen because impact energies assumed in the design process for the exterior and interior of the aircraft structure are different, as are the specific locations most prone to those impacts. For both internal and external impacts, three distinct general locations were chosen, such that all three primary components of PRSEUS panels were impacted. The three general location types were frame, stringer and skin. The exterior impact sites are shown in Figure 97 and the corresponding impact parameters are listed in Table 3. The interior impact sites are shown in Figure 98, and the corresponding impact parameters are listed in Table 4.

As previously indicated, no attempt was made to model actual BVIDs in the FEM. Therefore, the following post-processing paradigm was adopted. Test measurements and FEA results would be compared at the BVID locations under the assumption that the FEA has been, to large extent, validated based on the favorable agreement achieved at the pristine locations. Then, if the agreement between the test measurements and FEA results was verified in a vicinity of a particular BVID site, a conclusion could be reached that the BVID at this location did not result in appreciable detriment to the structure. If the test measurements and the FEA results would differ at a specific impact location, then further investigation would be warranted. This step would be undertaken with the objective of determining if the difference should be attributed to the extent of the damage resulting from BVID, or whether further refinement of the FEM might be warranted in the proximity of subject BVID. As it will become clear in the remainder of this section, in some instances a definite conclusion whether the mismatch between the measurements and predictions is attributable to actual damage, limitations of the FEM, or both and/or other factors, could not be established. Potentially, future FEM sensitivity studies and a detailed review of the non-destructive evaluation results[16] will be able to complement the results presented in this section.

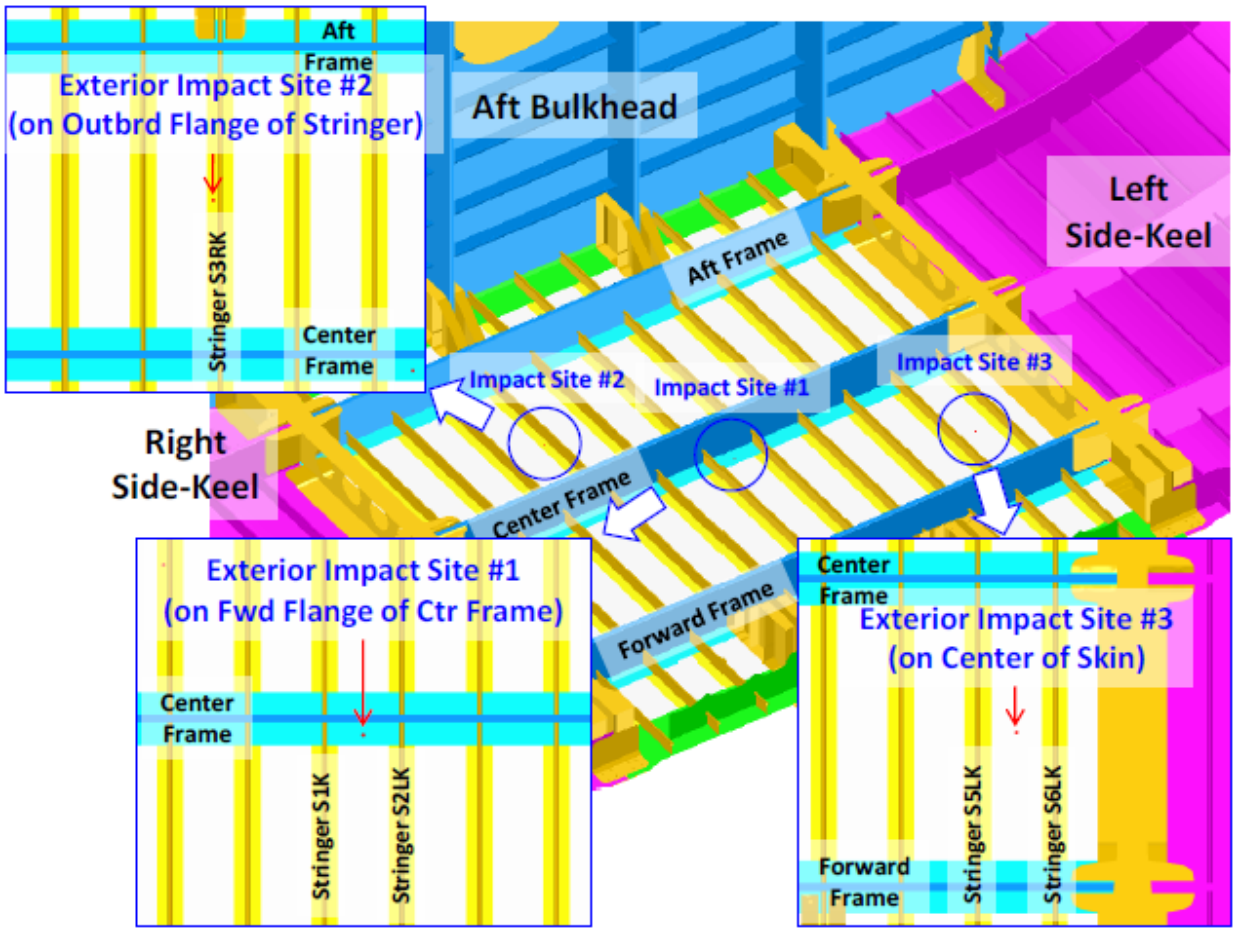

Figure 97. Exterior BVID sites.

Table 3. Exterior impact parameters.

Impact Site	Location	Impactor Mass (lb)	Impact Energy (ft-lb)
#1	Flange of Frame	15	60
#2	Flange of Stringer	15	60
#3	Skin (Mid-bay)	5	15

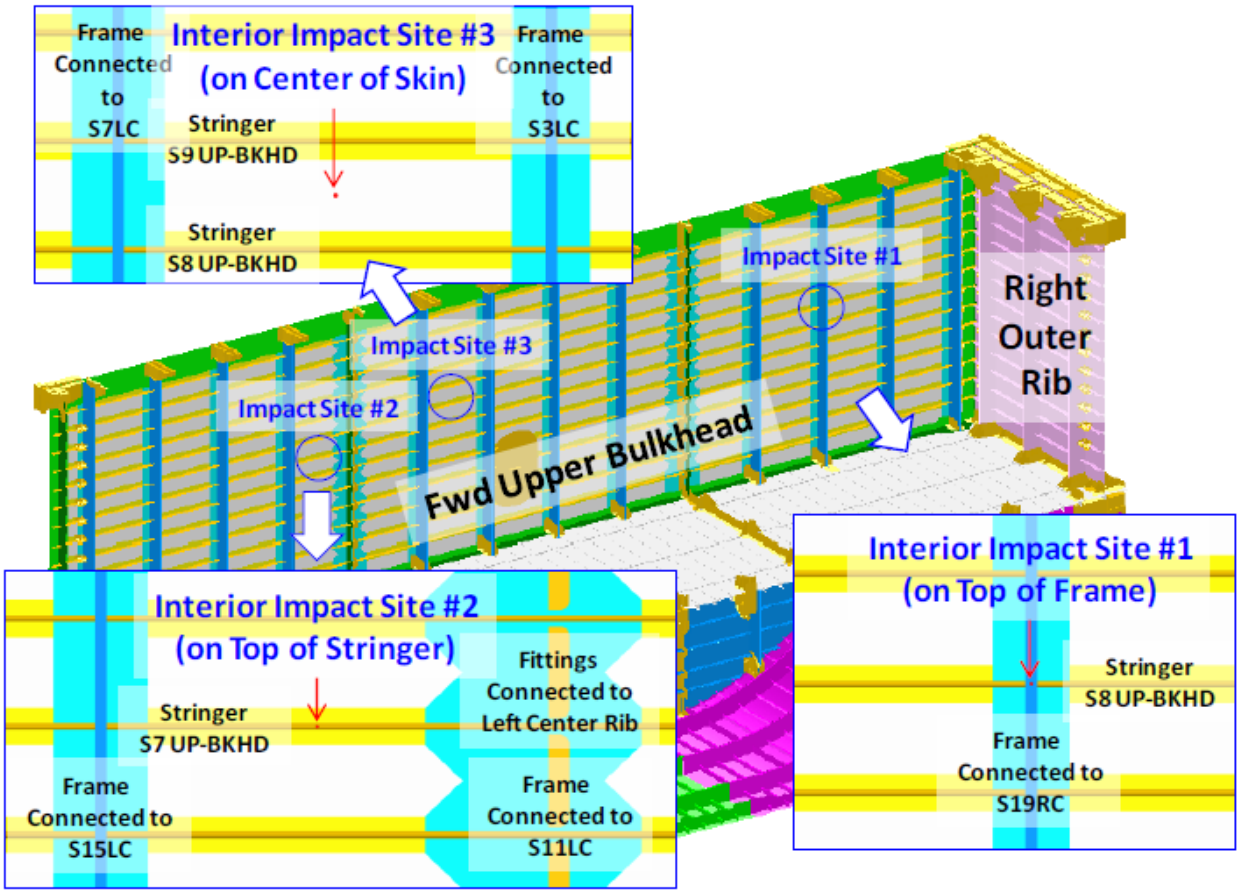

Figure 98. Interior BVID sites.

Table 4. Interior impact parameters.

Impact Site	Location	Impactor Mass (lb)	Impact Energy (ft-lb)
#1	Top of Frame	3.708	20
#2	Top of Stringer Overwrap	3.708	20
#3	Skin (Mid-bay)	3.708	15

In the remainder of this section only selected load cases and impact locations, where either test or analysis would produce meaningful strain levels (i.e., of magnitude exceeding approximately ±0.00075), are presented and discussed. Those cases are listed in Table 5.

Table 5. Selected load cases and impact sites for which BVID effects are discussed.

Impact Site	−1-g	−1-g + 1P	2P	2.5-g	2.5-g + 1P
Interior #1		√	√		√
Interior #2					
Interior #3		√	√		√
Exterior #1			√	√	√
Exterior #2	√	√	√	√	√
Exterior #3	√		√		√

3.2.1. −1-g Load

Strains up to −1-g DUL in the proximity of the external impact site #2, located on the center keel panel stringer flange, are shown in Figure 99. The two plots contain one set of back-to-back strain results each as each red strain gauge in the inset plot represents a back-to-back gauge pair. The overall strain levels at the impact site are very low, not exceeding −0.0012 in./in. at DUL. The agreement between test measurements and FEA results is good for the IML locations (i.e., for the light green nonlinear FEA curves) but much less favorable for the OML locations (i.e., for the dark green nonlinear FEA curves). Specifically, as seen in Figure 99, while the nonlinear behavior on the OML side is captured by the FEA, the predicted strain magnitudes largely overestimate the measured values. The possible reason for this behavior is a coarse discretization of the stringer flange shown in the inset of Figure 99 as the yellow area. One side of the stringer flange (i.e., the width to one side of the stringer web) shown in the inset is discretized only with a single finite element across its width. Further mesh refinement in this area is necessary to verify this hypothesis. No such analysis with a refined stringer flange mesh was conducted in this program.

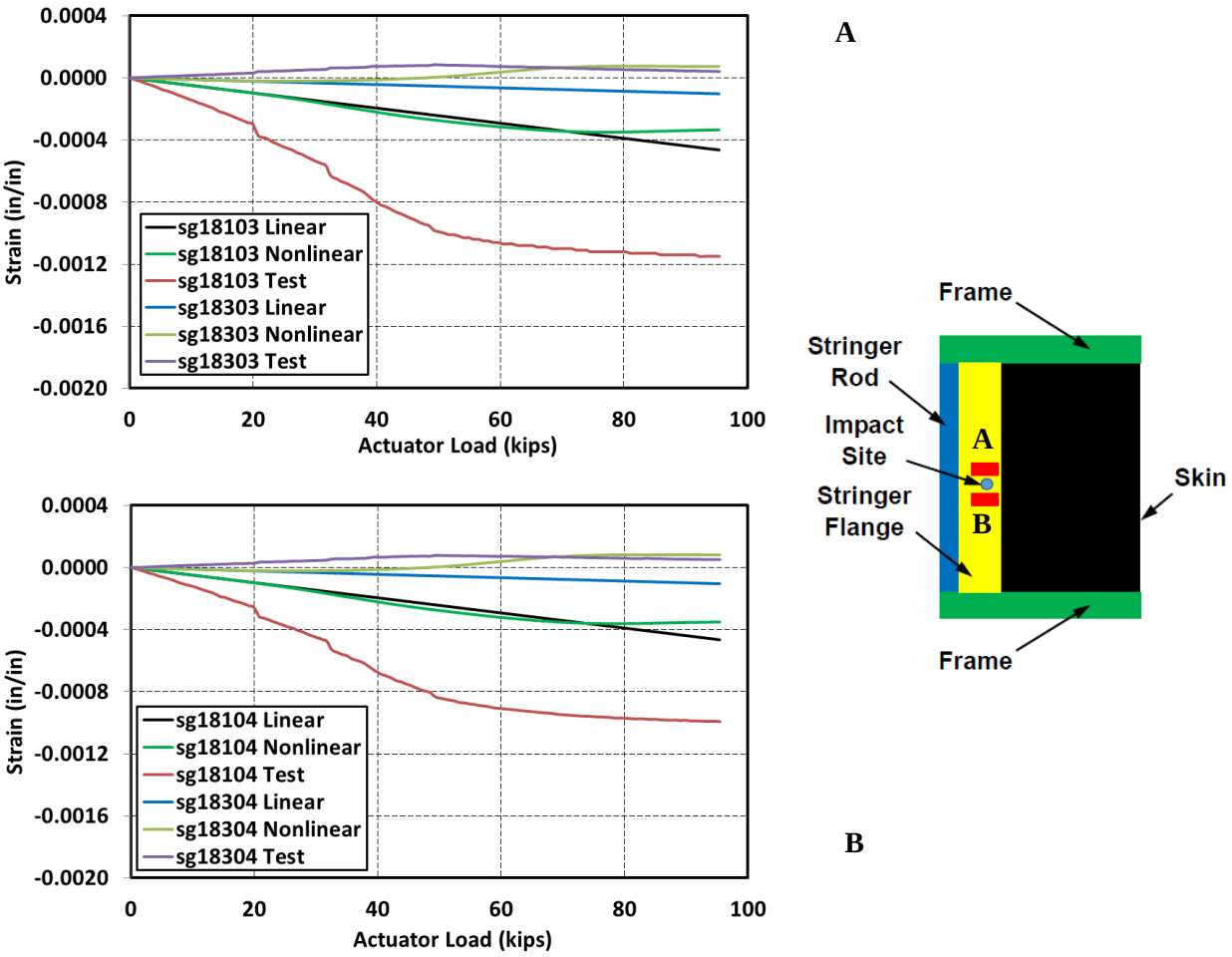

Figure 99. Strains at exterior impact site #2 up to −1-g DUL.

Strains up to −1-g DUL in the proximity of the external impact site #3, located in the middle of the center keel panel skin bay, are shown in Figure 100. The two plots contain one set of back-to-back strain results, as each red strain gauge in the inset represents a back-to-back gauge pair. The strain levels at these locations are very low, barely meeting the −0.00075 in./in. threshold at DUL set for selection of the results being discussed in this section. It is best seen at location B that the skin at the impacted skin bay buckles in the opposite direction relative to that predicted by the nonlinear FEA. This behavior is not unexpected, as discussed previously in section 3.1, and thus the comparison between the test and prediction can be considered acceptable, as the loads corresponding to the onset of nonlinear behavior and overall strain peak magnitudes are generally captured by the nonlinear FEA.

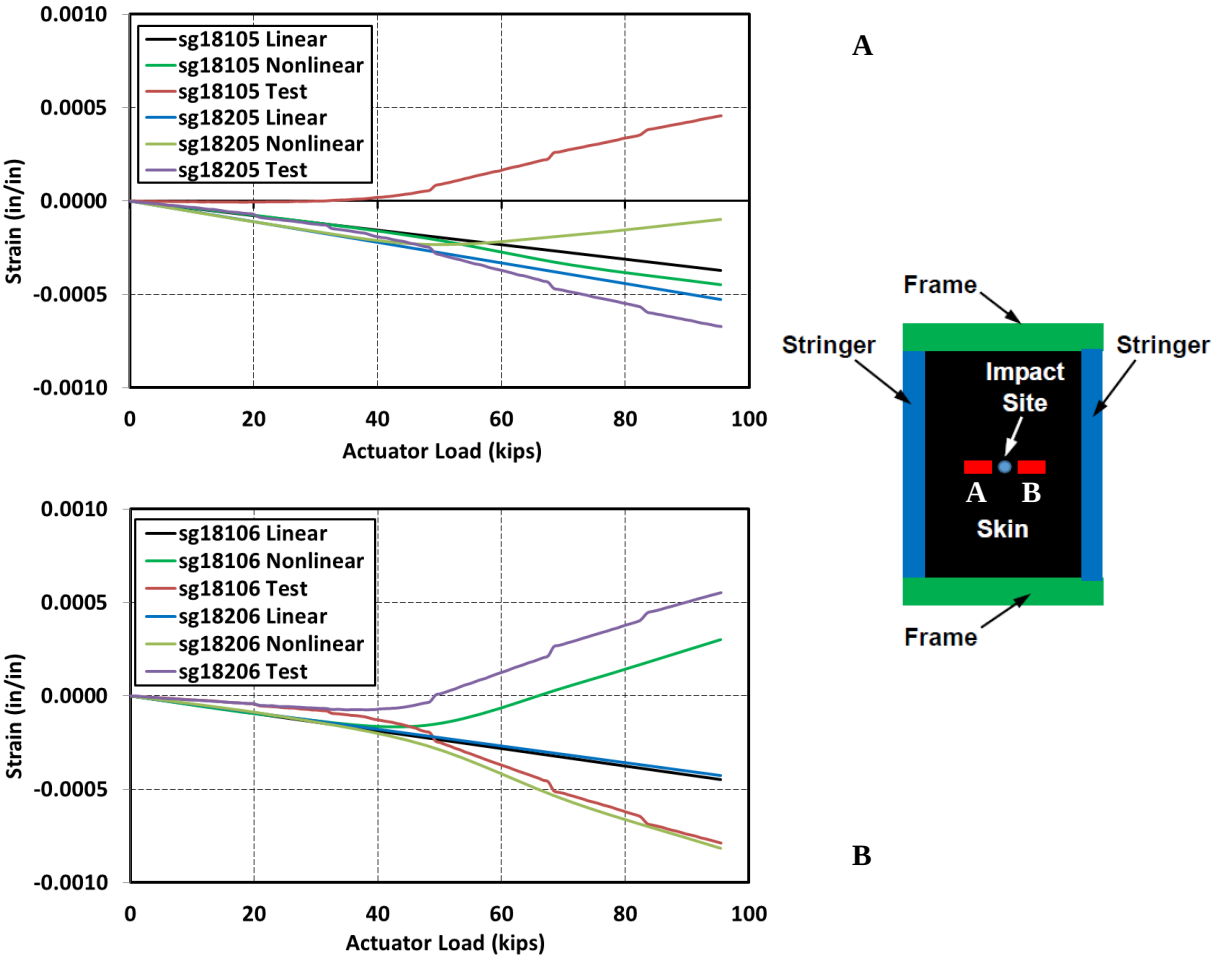

Figure 100. Strains at exterior impact site #3 up to −1-g DUL.

3.2.2. −1g + 1P Load

Strains up to −1-g +1P DUL in the proximity of the external impact site #2, located on the center keel panel stringer flange, are shown in Figure 101. The two plots contain one set of back-to-back strain results, as each red strain gauge in the inset represents a back-to-back pair. It is seen that the overall strain levels at the impact site are low, not exceeding the −0.0012 in./in. to 0.0018 in./in. range at DUL. The agreement between test measurements and FEA results is poor. The possible reason for this behavior is too-coarse discretization of the stringer flange shown via the yellow area in the inset of Figure 100, the same factor previously discussed for this location in section 3.2.1.

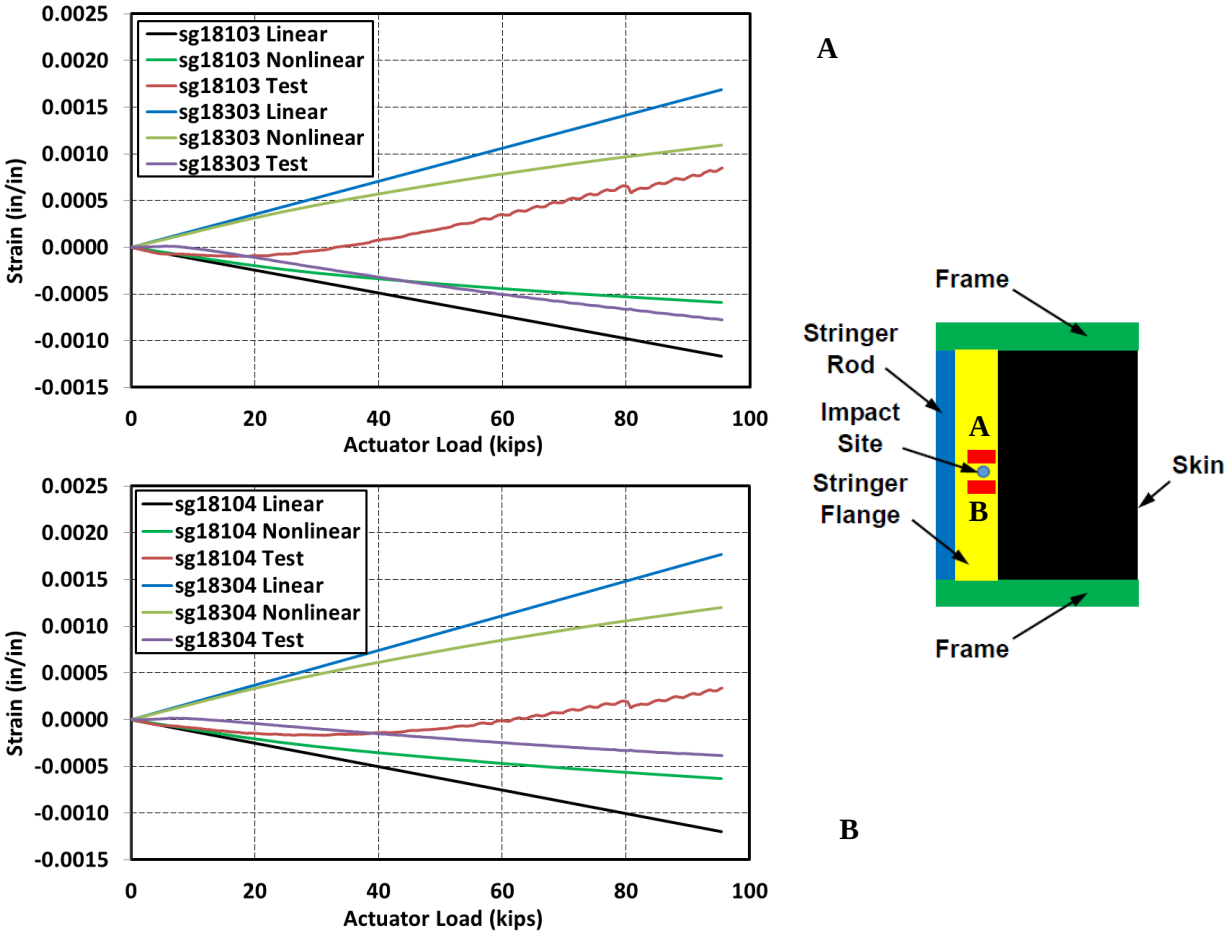

Figure 101. Strains at exterior impact site #2 up to −1-g + 1P DUL.

Strains up to −1-g + 1P DUL in the proximity of the interior impact site #1, located in the upper bulkhead panel on the top of a frame, are shown in Figure 102. The measured strains at this location display nearly linear behavior and achieve a moderate level of −0.0030 in./in. at DUL. The predicted strain characteristic matches the measurement but overestimates the measured values by approximately −0.0005 in./in. at DUL.

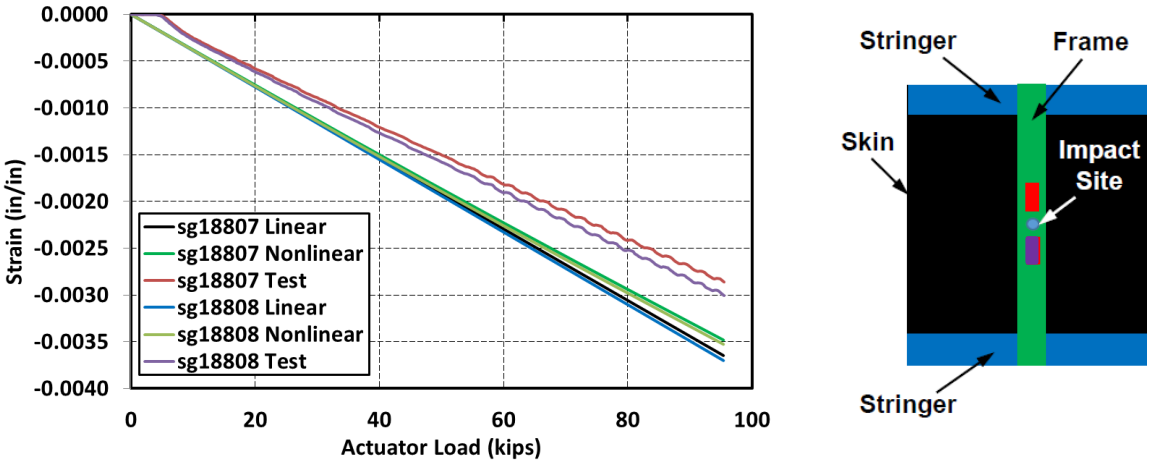

Figure 102. Strains at interior impact site #1 up to −1-g + 1P DUL.

Strains up to −1-g + 1P DUL in the proximity of the interior impact site #3, located in the upper bulkhead panel mid-bay skin, are shown in Figure 103. The two plots contain one set of back-to-back strain results, as each red strain gauge in the inset plot represents a back-to-back gauge pair. The strain levels at these locations are very low, not exceeding 0.0011 in./in. at DUL. The measured values display moderately nonlinear characteristic, and the FEA results show only slightly nonlinear behavior. The FEA over-predicts the measured strain values, and shows very similar strain levels on both OML and IML sides of the skin, which is indicative of the response being strongly dominated by the in-plane strain component. The measured strain values differ by a larger margin between the OML and IML skin surfaces, indicating a larger contribution of the bending strain component than that predicted. Based on the presented results, it cannot be conclusively determined whether the differences between test measurements and FEA predictions originate from actual damage inflicted by BVID or other factors, however, for the majority of the mid-bay skin strain results obtained for pristine upper bulkhead locations, a better comparison was typically found.

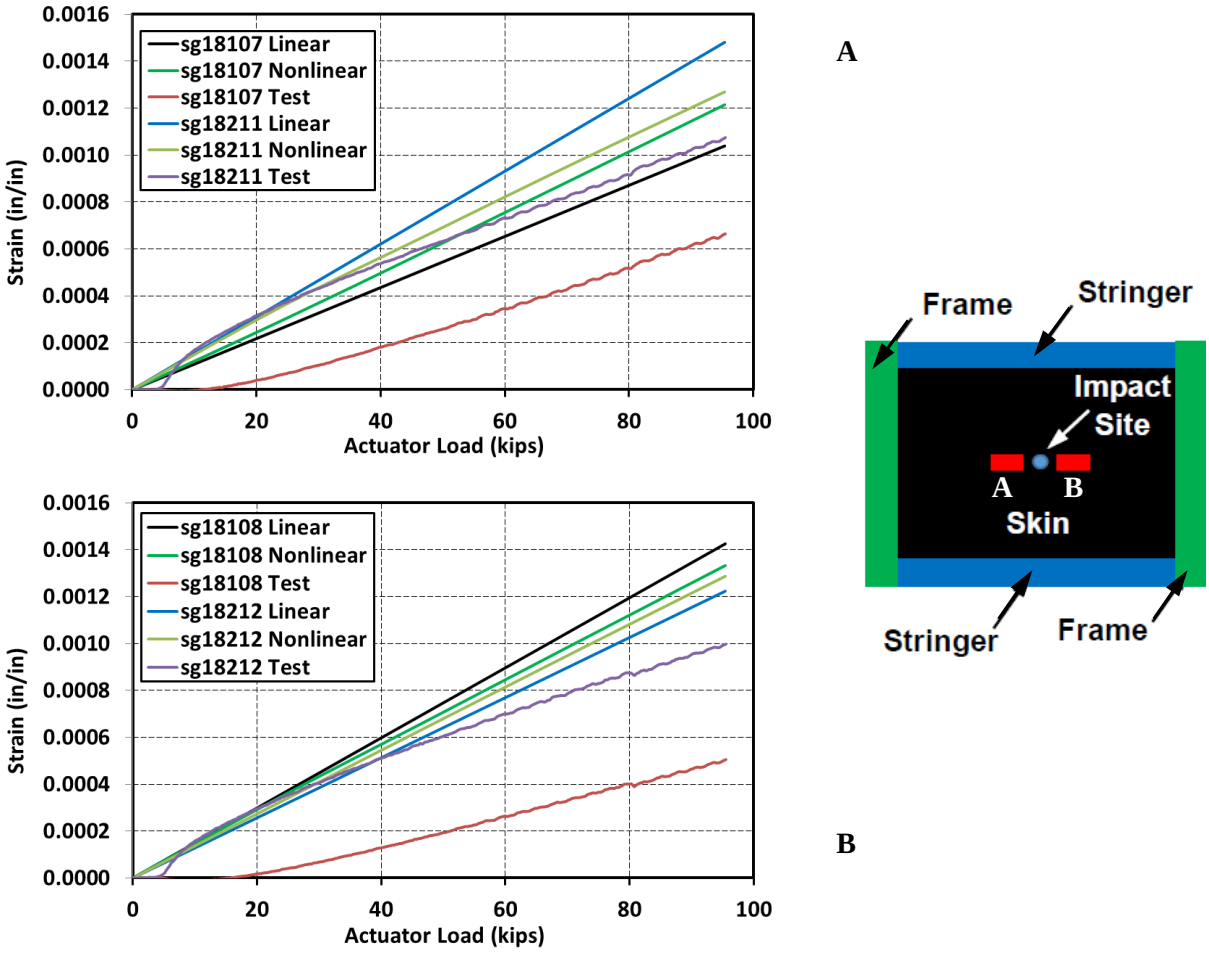

Figure 103. Strains at interior impact site #3 up to −1-g + 1P DUL.

3.2.3. 2P Load

Strains up to 2P DUL in the proximity of the external impact site #1, located near the center frame of the center keel panel, are shown in Figure 104. Very low tensile strain levels at DUL are observed. The two plots contain one set of back-to-back strain results, as each red strain gauge in the inset plot represents a back-to-back gauge pair. The inset plot shows two impact site locations, the intended one and the actual one. Per the test specification, the impact was to be applied on the edge of the center frame flange, i.e., near the right edge of, but still within, the yellow area in the inset plot. However, due to mislabeling of the intended impact location, the actual impact was applied primarily to the adjacent skin, with only approximately ¼ of the impactor tip diameter contacting the flange. As a consequence, the thin skin section was completely penetrated by the impactor tip. The very edge of the center frame flange was also observed to sustain damage exceeding the barely visible status.[13] Because the above-described damages were not reflected in the FEM, it comes as no surprise that the test measurements and FEA results did not match more closely. The measured strains lower than the predicted values are consistent with a portion of the flange loads being diverted to a section of the frame farther away from the damaged location exceeding BVID. Both pairs of the back-to-back strain measurements, however, match the nearly linear characteristic predicted by FEA.

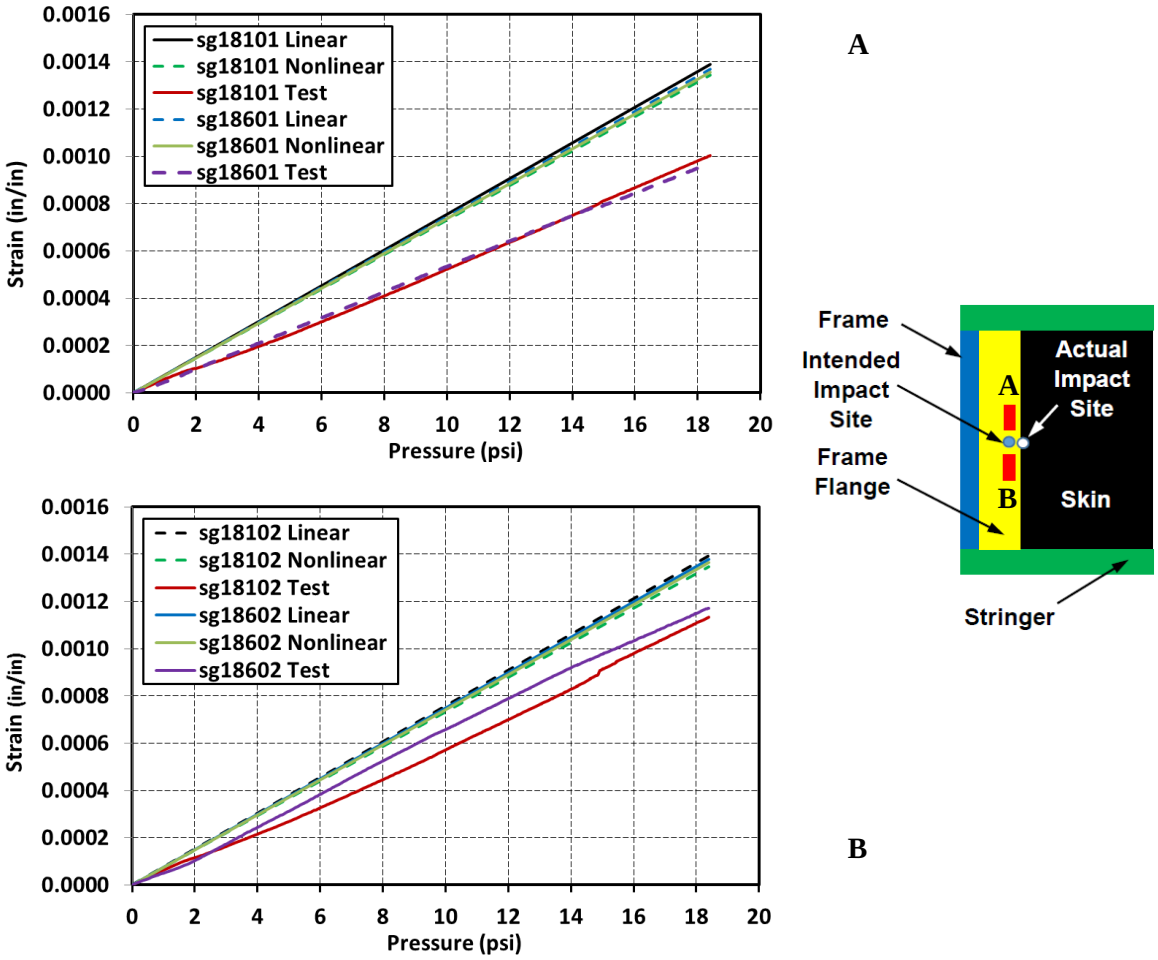

Figure 104. Strains at exterior impact site #1 up to 2P DUL.

Strains up to 2P DUL in the proximity of the external impact site #2 located on the center keel panel stringer flange are shown in Figure 105. The two plots contain one set of back-to-back strain results, as each red strain gauge in the inset plot represents a back-to-back gauge pair. The overall strain levels at the impact site are moderate, slightly exceeding 0.0030 in./in. tensile strain at DUL. The agreement between test measurements and FEA results is poor. A possible reason for this behavior is too-coarse discretization of the stringer flange shown in the inset plot of Figure 105 as the yellow area, the same factor previously discussed for this location in section 3.2.1.

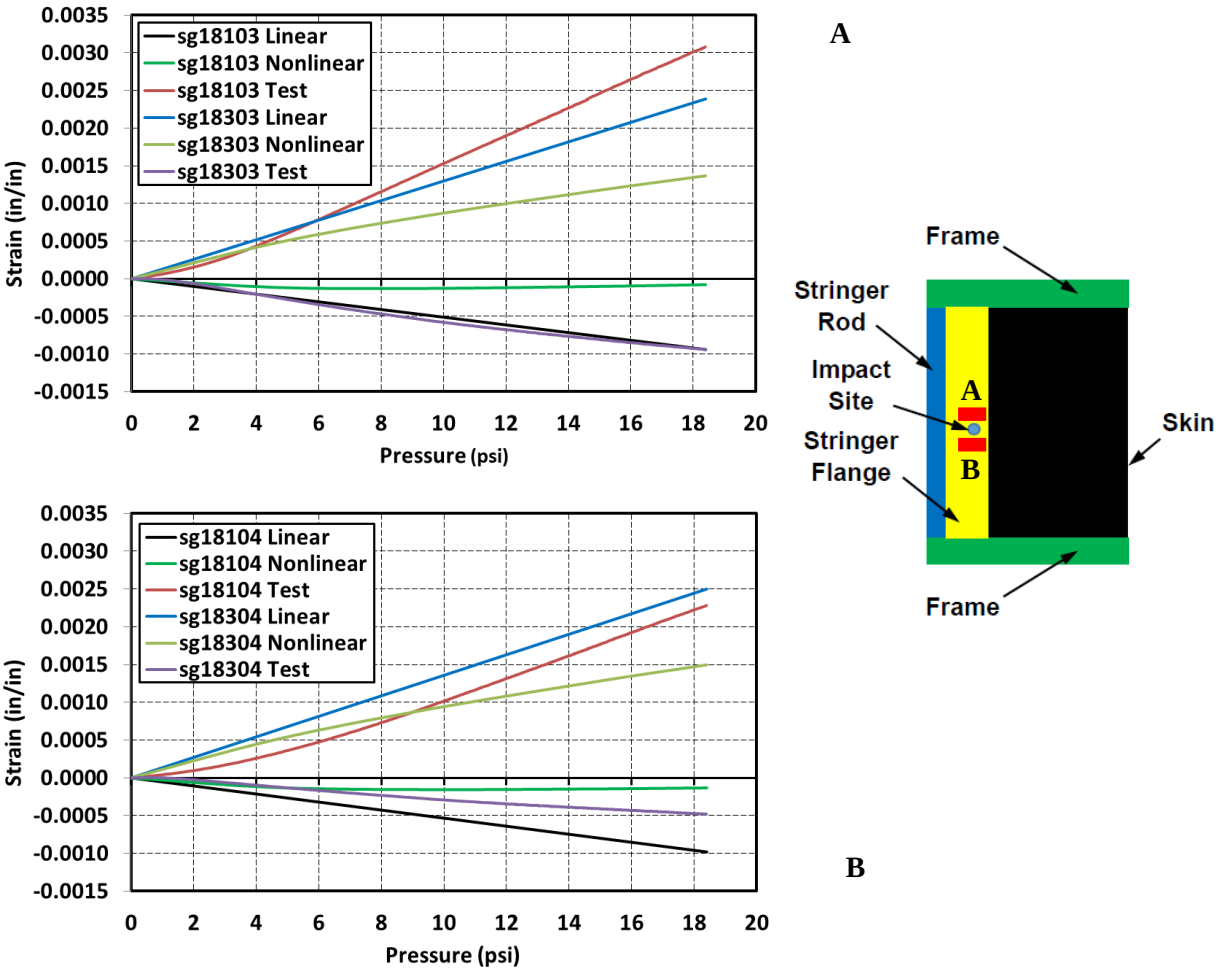

Figure 105. Strains at exterior impact site #2 up to 2P DUL.

Strains up to 2P DUL in the proximity of the external impact site #3, located at the center keel panel mid-bay skin, are shown in Figure 106. The test measurements are generally lower than the FEA results, which may be indicative of the skin loads bypassing the damaged location. Interesting results are obtained when the in-plane strain component (i.e., the average of the OML and IML strains) is considered. In both plots, the in-plane component assumes a similar value of approximately 0.0004 in./in. At location A, however, the bending component is almost absent, while at location B, the bending component is approximately ±0.0003 in./in. Such a significant change in strain characteristic at two proximate and symmetrical locations relative to the impact site may further reinforce the hypothesis of impact damage causing local strain redistribution.

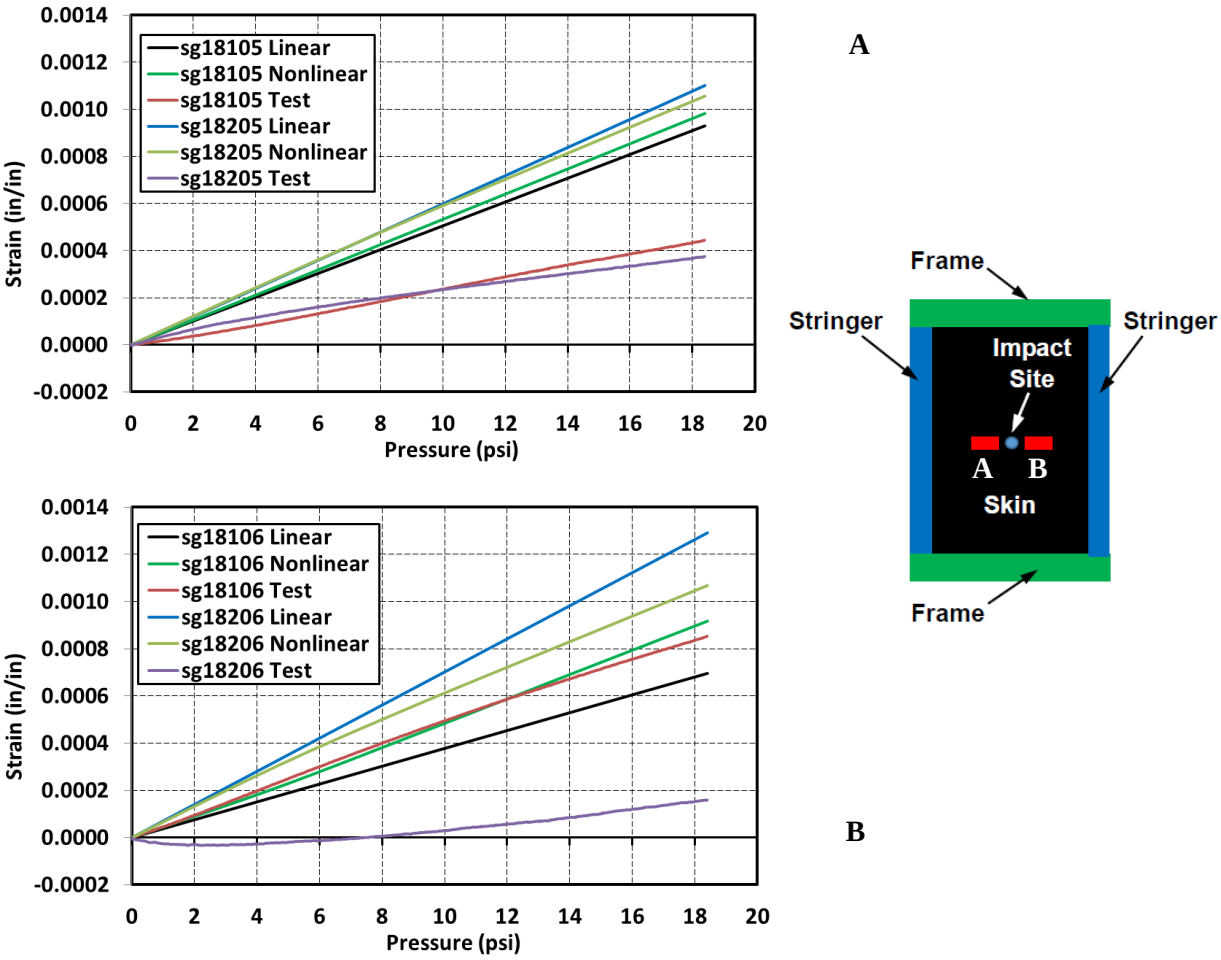

Figure 106. Strains at exterior impact site #3 up to 2P DUL.

Strains up to 2P DUL in the proximity of the internal impact site #1, located in the upper bulkhead panel on the top of a frame, are shown in Figure 107. The measured strains at this location display nearly linear behavior and achieve a moderate level of −0.0040 in./in. at DUL. The predicted strain characteristic is similar to the measurement, but overestimates the measured values by approximately −0.0010 in./in. The strain behavior at this location is consistent with the previously introduced results obtained under −1-g + 1P DUL (Figure 102). Specifically, the nearly linear characteristic is maintained but due to higher pressure load, strains have larger negative values.

Strains up to 2P DUL in the proximity of the interior impact site #3 located in the upper bulkhead panel mid-bay skin are shown in Figure 108. The two plots contain one set of back-to-back strain results, as each red strain gauge in the inset plot represents a back-to-back gauge pair. The strain levels at these locations are low, not exceeding 0.0014 in./in. at DUL. The measured values display moderately nonlinear characteristic, and the FEA results show only slightly nonlinear behavior. The FEA over-predicts the measured strain values and shows very similar strain levels on both OML and IML sides of the skin, which is indicative of the response being strongly dominated by the in-plane strain component. The measured strain values differ by a larger margin between the OML and IML skin surfaces indicating a larger contribution of the bending strain component than that predicted. Based on the presented results, it cannot be conclusively determined whether the differences between test measurements and FEA predictions originate from actual damage inflicted by BVID or other factors, however for the majority of the mid-bay skin strain results obtained for pristine upper bulkhead locations, a better comparison was typically found.

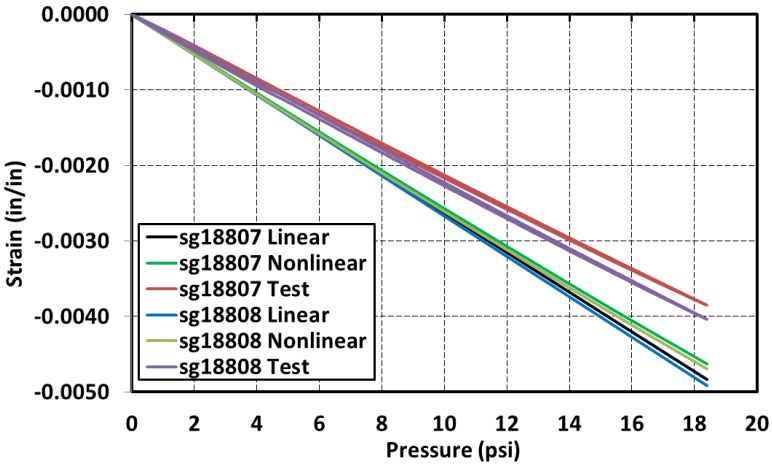

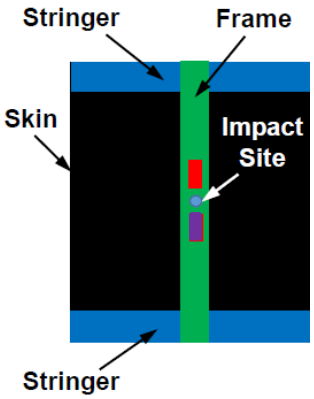

Figure 107. Strains at interior impact site #1 up to 2P DUL.

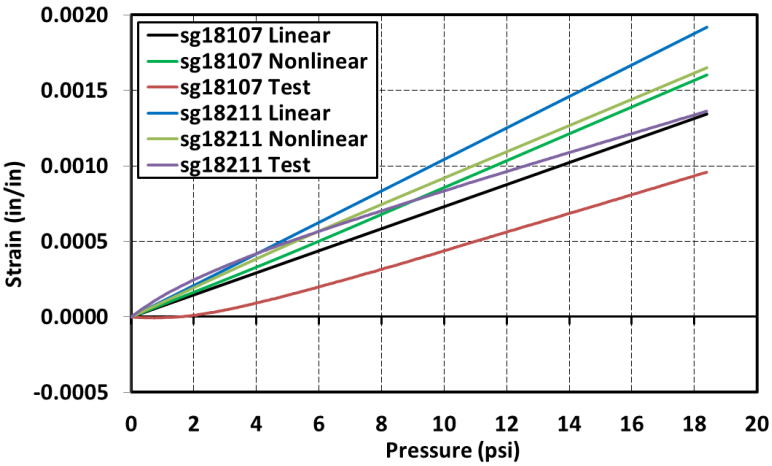

A

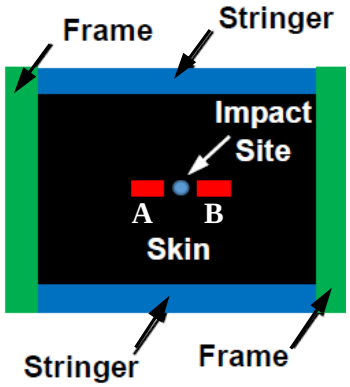

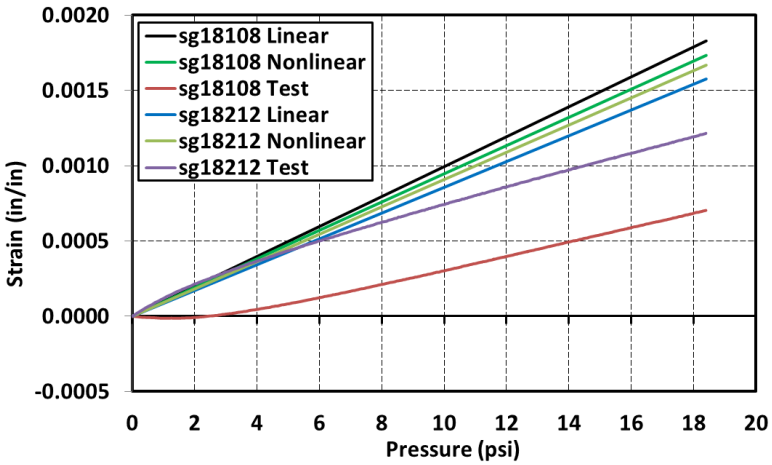

B

Figure 108. Strains at interior impact site #3 up to 2P DUL.

3.2.4. 2.5-g Load

Strains up to 2.5-g 165% DLL in the proximity of the external impact site #1, located near the center frame of the center keel panel, are shown in Figure 109. As discussed at the beginning of section 3.2.3, the intended impact site was missed, and the impact was applied primarily to the adjacent and much thinner skin structure resulting in more extensive damage than BVID. Since under the 2.5-g load, the extensively damaged keel panel skin does not carry large loads, this damage seems to be inconsequential to the strain measurements taken on the frame flange. The predicted and measured strains are nearly linear and do not exceed 0.0015 in./in. Overall, good agreement between test measurements and FEA predictions is found.

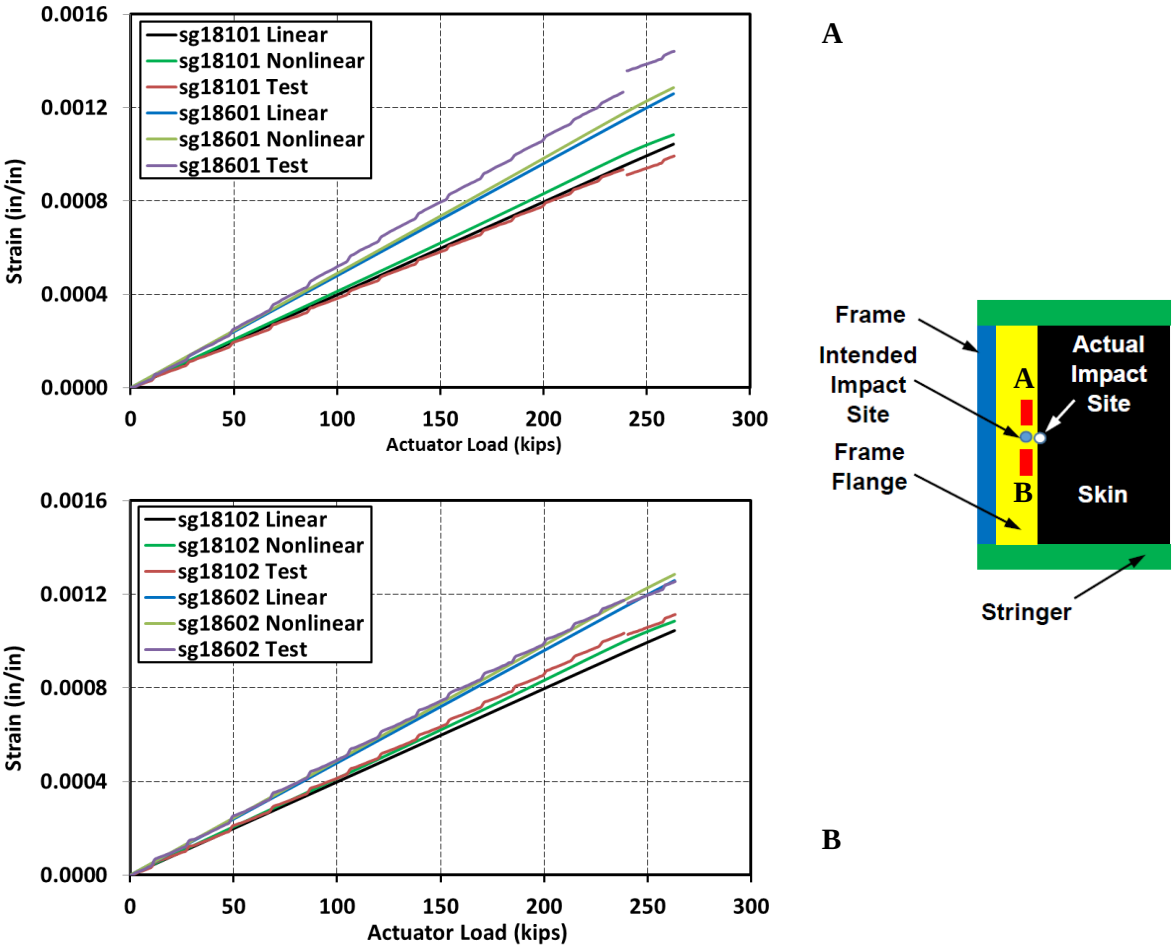

Figure 109. Strains at exterior impact site #1 up to 2.5-g 165% DLL.

Strains up to 2.5-g 165% DLL in the proximity of the external impact site #2, located on the center keel panel stringer flange, are shown in Figure 110. The two plots contain one set of back-to-back strain results, as each red strain gauge in the inset plot represents a back-to-back gauge pair. The overall strain levels at the impact site are moderately high, approaching 0.0045 in./in. tensile strain on the more critical side of the impact (location A). The agreement between test measurements and FEA results is poor. A possible reason for this behavior is too-coarse discretization of the stringer flange shown in the inset plot of Figure 110 as the yellow area, the same factor previously discussed for this location in section 3.2.1.

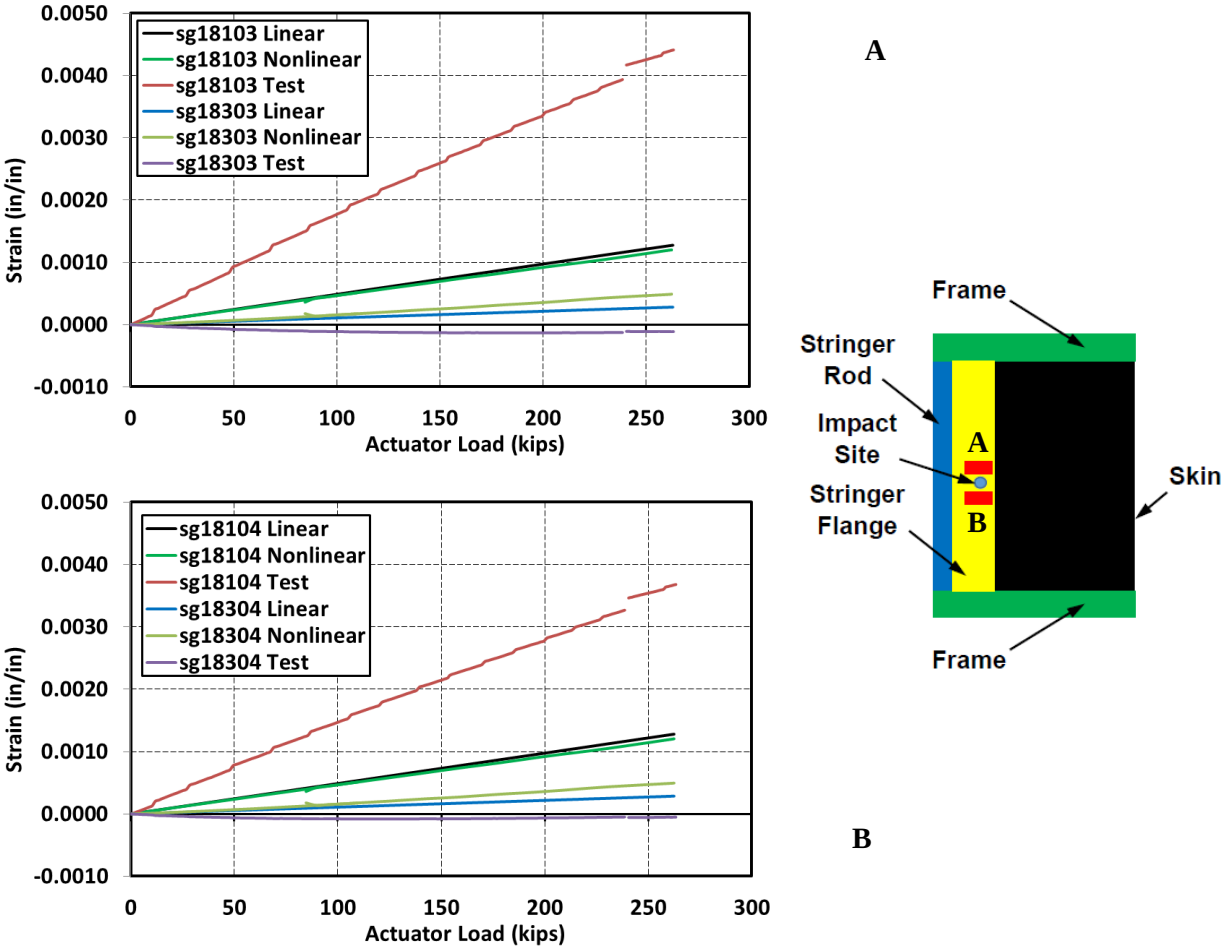

Figure 110. Strains at exterior impact site #2 up to 2.5-g 165% DLL.

3.2.5. 2.5-g + 1P Load

Strains up to 2.5-g 165% DLL + 1P 150% DLL in the proximity of the external impact site #1, located near the center frame of the center keel panel, are shown in Figure 111. As discussed at the beginning of section 3.2.3, the intended impact site was missed, and the impact was applied primarily to the adjacent much thinner skin structure resulting in a more extensive damage than BVID. Generally, the FEA accurately captures a nearly linear response characteristic, but at the same time, overestimates the measured strain values.

Strains up to 2.5-g 165% DLL + 1P 150% DLL in the proximity of the external impact site #2 located on the center keel panel stringer flange are shown in Figure 112. The two plots contain one set of back-to-back strain results, as each red strain gauge in the inset plot represents a back-to-back gauge pair. The overall strain levels at the impact site are high, approaching 0.0058 in./in. tensile strain on the more critical side of the impact (location A). The agreement between test measurements and FEA results is poor. A possible reason for this behavior is too-coarse discretization of the stringer flange shown in the inset plot of Figure 112 as the yellow area, yet again the same factor previously discussed for this location in section 3.2.1.

Strains up to 2.5-g 165% DLL + 1P 150% DLL in the proximity of the interior impact site #3, located in the upper forward bulkhead panel mid-bay skin, are shown in Figure 113. The two plots contain one set of back-to-back strain results, as each red strain gauge in the inset plot represents a back-to-back gauge pair. The strain levels at these locations are very low, not exceeding 0.0012 in./in. The measured and predicted strains display almost linear behavior, but the FEA largely over-predicts the measured values.

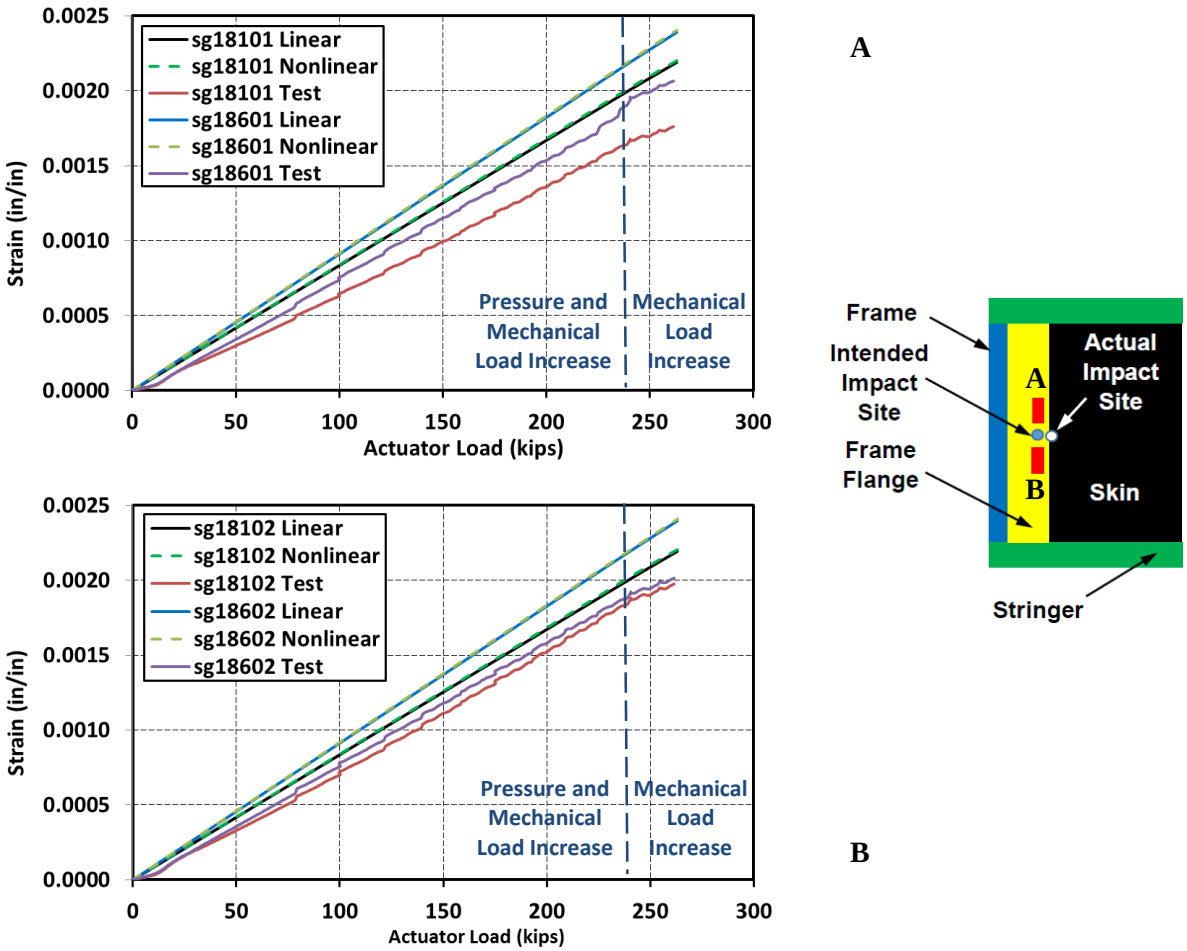

Figure 111. Strains at exterior impact site #1 up to 2.5-g 165% DLL + 1P 150% DLL.

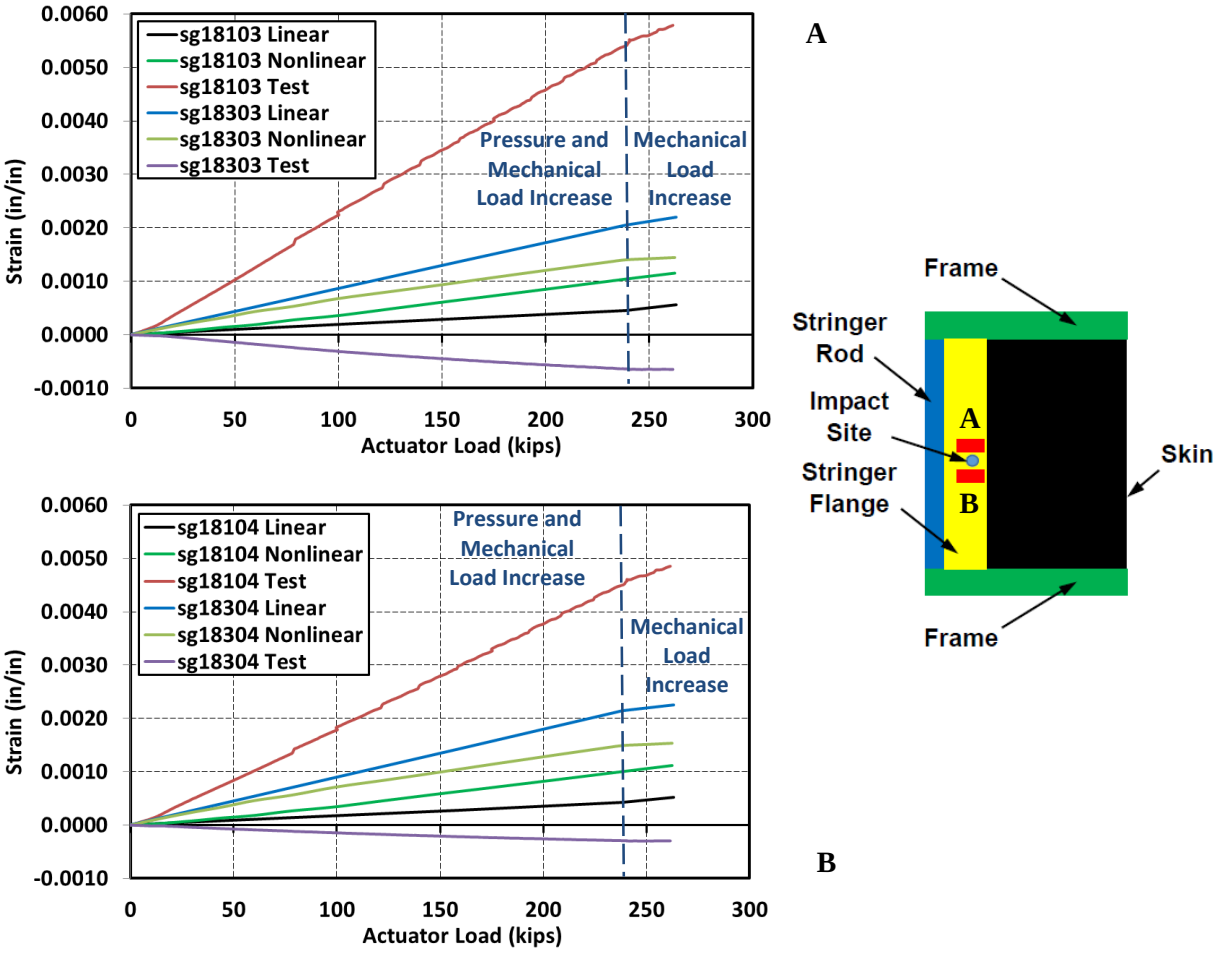

Figure 112. Strains at exterior impact site #2 up to 2.5-g 165% DLL + 1P 150% DLL.

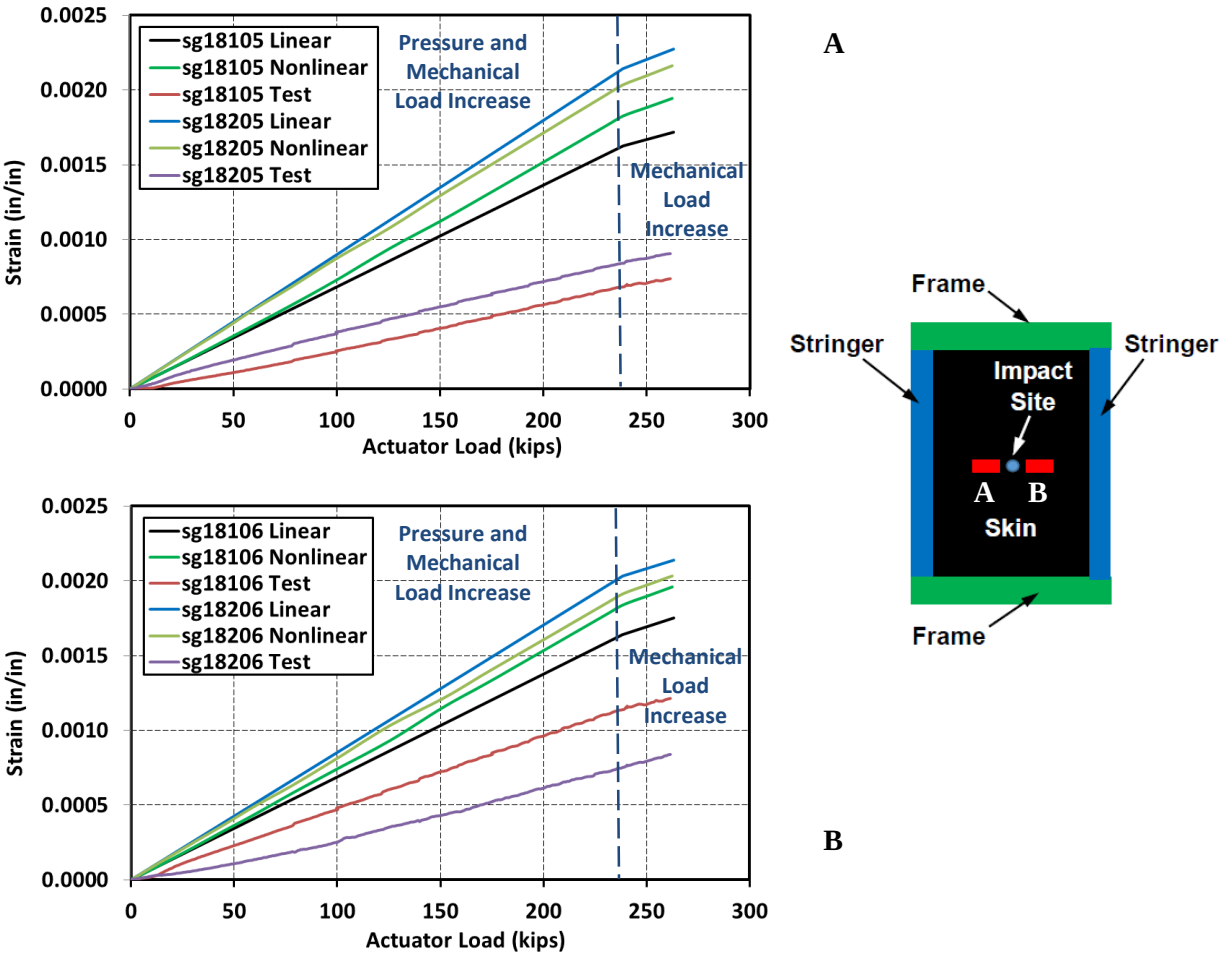

Figure 113. Strains at exterior impact site #3 up to 2.5-g 165% DLL + 1P 150% DLL.

Strains up to 2.5-g 165% DLL + 1P 150% DLL in the proximity of the internal impact site #1, located in the upper bulkhead panel on the top of a frame, are shown in Figure 114. The measured and predicted strains at this location agree well in qualitative terms. They both display nearly linear behavior when the pressure component of the load is increased, and asymptote when pressure is held constant and only the mechanical component of the load is further increased beyond the DUL. At the maximum test load, measured strains achieve a moderate level of −0.0032 in./in., and the predictions overestimates this value by approximately −0.0005 in./in.

Strains up to 2.5-g 165% DLL + 1P 150% DLL in the proximity of the interior impact site #2 located in the upper bulkhead panel on the top of a stringer are shown in Figure 115. The two plots contain one set of back-to-back strain results, as each red strain gauge in the inset plot represents a back-to-back gauge pair. The measured strain levels at these locations are very low, not exceeding 0.0010 in./in. at DUL. Up to the point when the pressure load component is being increased, the measured values display moderately nonlinear characteristic, and the FEA results show nearly linear behavior. Above that level, i.e., when only the mechanical component of the load is being further increased, both measured and predicted strain values remain almost unchanged. This observation confirms that strains at the location are strongly driven by the pressure load. Overall, the FEA over-predicts the measured strain values. In qualitative terms, it captures the asymptotic behavior beyond the 238.5 kips actuator load, but fails to capture the degree of nonlinearity below that load.

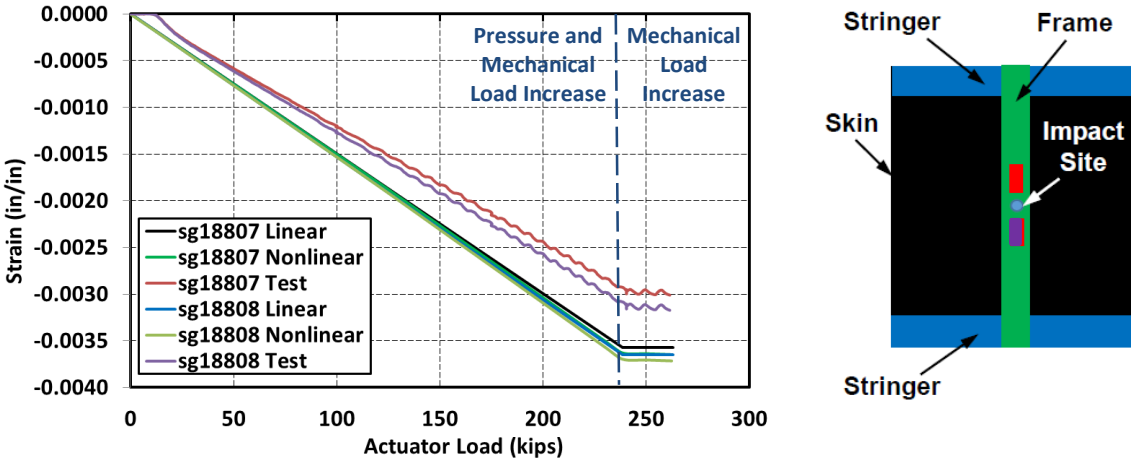

Figure 114. Strains at interior impact site #1 up to 2.5-g 165% DLL + 1P 150% DLL.

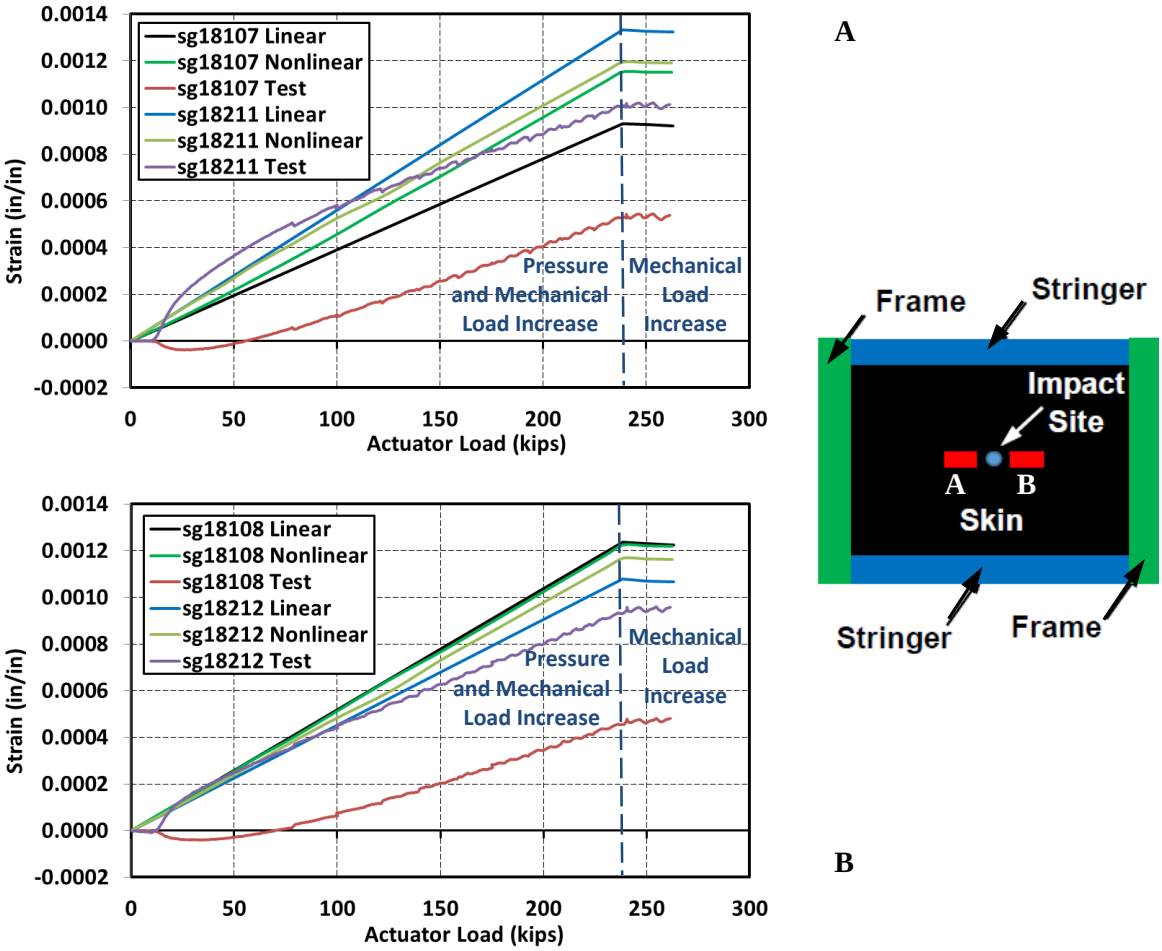

Figure 115. Strains at interior impact site #3 up to 2.5-g 165% DLL + 1P 150% DLL.

3.3. Severe Damage Condition

The DSD location was chosen in the center section of the crown panel of the test article and is shown in Figure 116. Because the crown panel undergoes strong compression under the 2.5-g load, severing the center frame and the surrounding area effectively eliminated a critical load path in the panel. The span of the damage in the Y-direction was chosen to be 24 in., i.e., skin mid-bay to mid-bay. A preferred DSD location along the X-axis would be exactly at the mid-span of the panel, although a stringer present at this location motivated moving the center of DSD 3 in. from the centerline, as shown in Figure 116. The 3 in. shift from the midspan placed the DSD half-way between two consecutive crown panel stringers spaced at 6 in. The bottom view of the crown panel skin cut and the side view of the crown panel center frame cut are shown in Figure 117. The DSD was applied to the crown panel without removing the test article from the COLTS apparatus. A photograph of the DSD taken from the inside of the test article is shown in Figure 118.

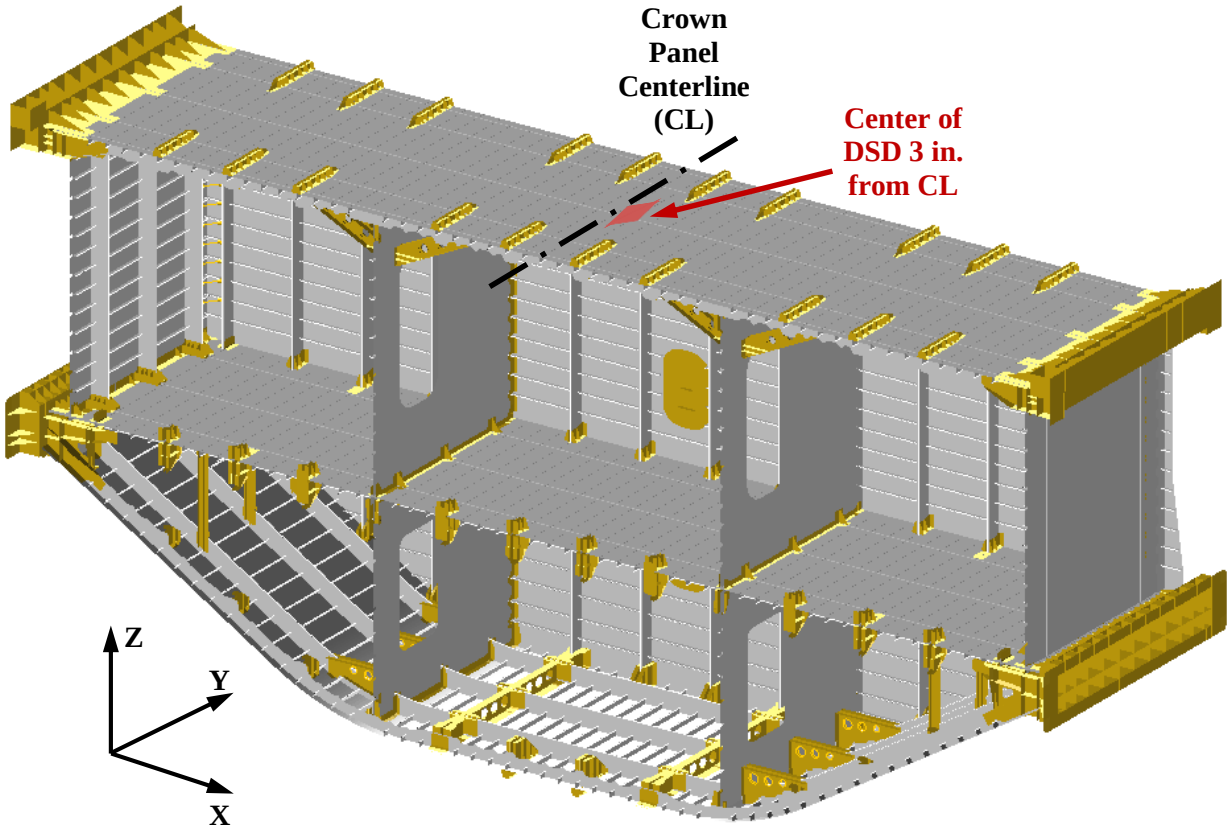

Figure 116. Location of the DSD.

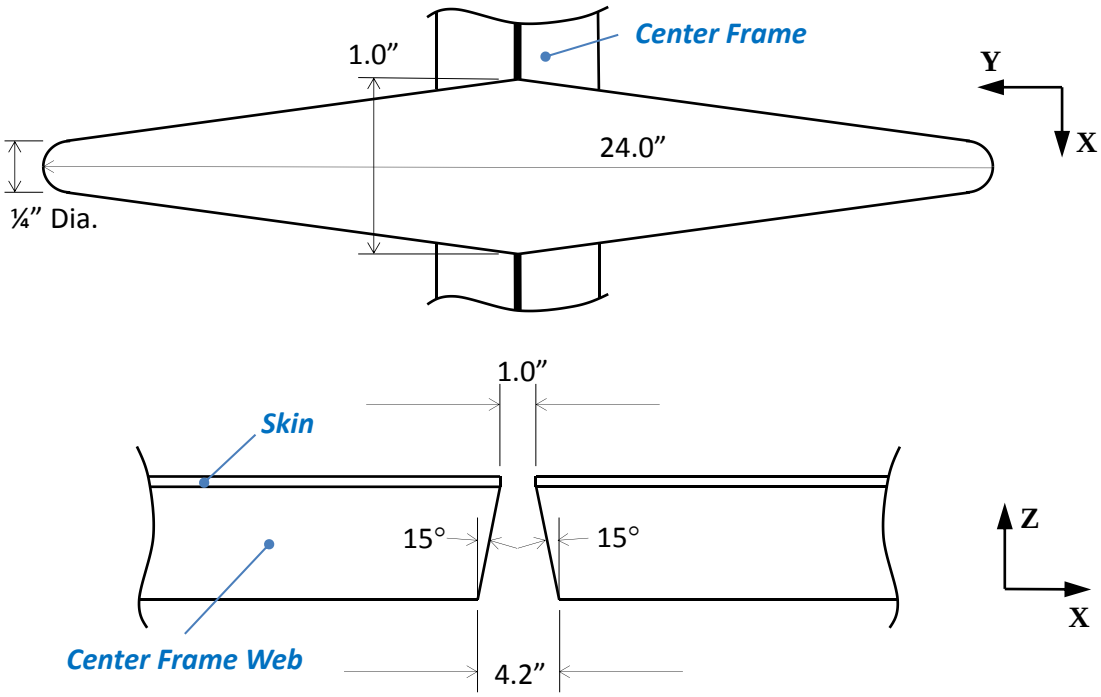

Figure 117. Geometry of the diamond shape crown panel cut out: view of the skin from the inside and side view of frame taper (not to scale).

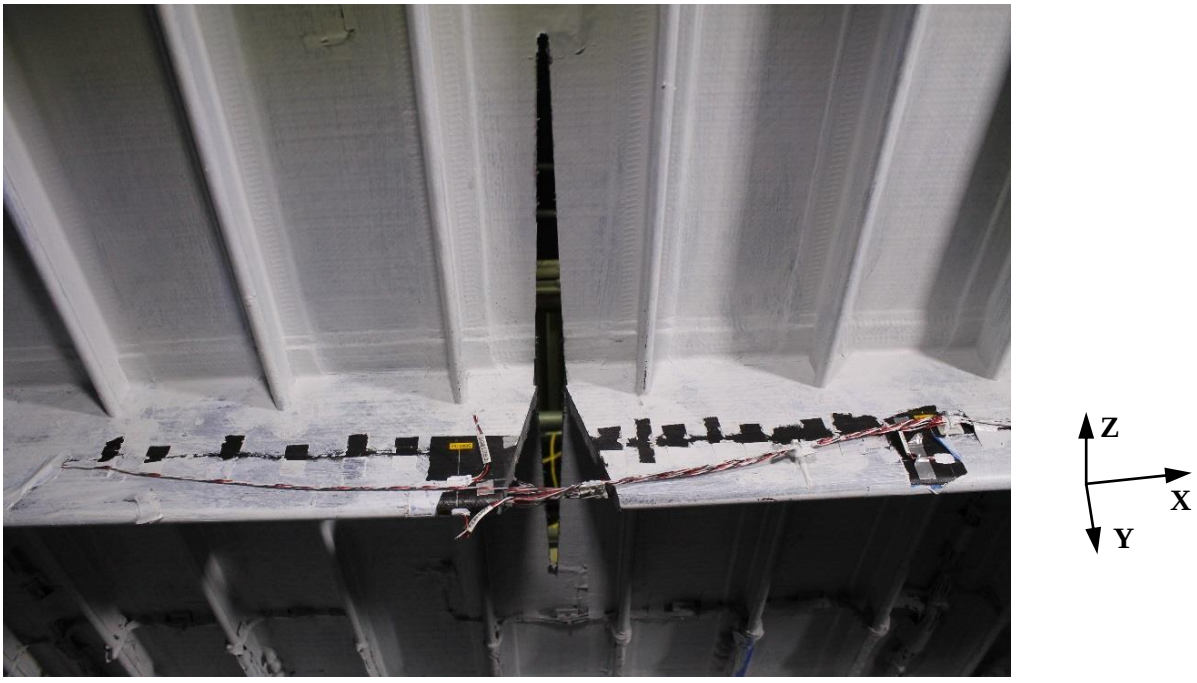

Figure 118. Crown panel cut out as seen from the inside of the test article.

The DSD test was added to the test plan late during the project, leaving only limited time available to develop a corresponding FEM and conduct the predictive analysis. The FEM of the pristine test article was used as the basis of the DSD model. The modifications of the pristine model in the span-wise direction were confined to the area between the two consecutive stringers in between which the DSD was located. In the direction along the stringers, the FEM modifications were confined between the forward and aft frames. After modeling the geometry of the DSD itself, the proximity of the DSD was meshed using significantly smaller shell elements when compared to the rest of the FEM. The smallest shell elements at the tip of the saw-cut were approximately 0.025 in. along the circumference of the tip by 0.05 in. across. The element edge size would gradually increase away from the saw-cut tip up to 0.25 in., i.e., approximately ¼ of the typical element size used in the pristine FEM. The refined area was joined with the coarser mesh away from the DSD using Nastran RSPLINE functionality[19] that uses spline curves to interpolate displacements between mesh regions with dissimilar node grids.

The DSD test was intended to be carried out until a catastrophic damage of the test article occurred. While the airframe certification standards for a transport category airframe[17] require structure with DSD to support 70% of DLL, some airframe manufacturers apply a more conservative value of 100% DLL. Thus, the FEA with DSD was initially executed up to the 2.5-g DLL (it was assumed that the fuselage structure with DSD does not retain ability to maintain pressure, thus the pressure component was not considered). Since the 2.5-g DLL analysis indicated that the allowable strain values were not exceeded and, thus, catastrophic damage should not occur up to this load, an additional analysis was conducted up to 2.5-g DUL. While the DUL analysis also did not predict a catastrophic failure, the crown panel substructure results approached their allowable values. Consequently, no analysis beyond DUL was conducted, as the value of such an analysis was deemed limited. Specifically, the FEA strains at the saw-cut tips were large enough to conclude that some local skin damage in the vicinity of the DSD will develop even below the DLL. Consequently, the localized load redistribution not being accounted for in the global fidelity FEA would likely take place. As these incremental damages would continue to develop and grow, the confidence in the analysis results not accounting for the aforementioned load redistributions would be diminished.

The pre-test decision not to carry out the FEA beyond 2.5-g DUL was substantiated by the final test results. While the initial localized damages at the tips of the skin saw-cut were noted at 130.3 kips actuator load (2.05-g or 81.9% DLL), the final failure did not occur until 241.8 kips actuator load (3.80-g or 152.1% DLL), i.e., just 1.4% above the DUL. Additional damages, as evidenced by strain gauge and VIC-3D measurements, occurred in between the first traceable damage initiation at 2.05-g and the final failure of 3.80-g, but were confined to the section of the panel within the direct proximity of the DSD. In the remainder of this section, the full field VIC-3D out-of-plane displacement results will be discussed first at both DLL and DUL levels. Similar to the previous results sections, the strain gauge results as a function of the actuator load will be shown next for the selected locations. The predictive FEA results are shown up to DUL of 238.5 kips actuator load, while the test results are shown up to the final failure of 241.8 kips actuator load.

While the VIC-3D acquisition system on the upper bulkhead panel remained unchanged relative to the previous testing (pristine and BVID), the crown panel measurements were conducted differently. Since the final damage was predicted to occur in the direct vicinity of the DSD, the global VIC-3D crown system was refocused on this smaller section of the panel, permitting higher-resolution measurements. Additionally, two local VIC-3D systems, set up with even higher resolution, were focused on small areas at both saw-cut tips. Finally, no VIC-3D data were acquired for the center keel panel. Consequently, the remainder of this section focuses heavily on the discussion of the crown panel results where, apart from the VIC-3D systems modifications, additional strain gauges were added around the DSD. The upper bulkhead VIC-3D results are also discussed. The behavior of other panels was inconsequential to the final outcome of the test and, therefore, is omitted for brevity.

The out-of-plane deformation of the crown panel with DSD under 2.5-g DLL is shown in Figure 119, and under 2.5-g DUL in Figure 120. The out-of-plane deformations of the aft upper bulkhead panel for the same two loads are shown in Figures 121 and 122, respectively. In Figures 119 and 120 the overall out-of-plane displacement characteristic of the crown panel is not significantly changed when compared to the

results obtained without the DSD. The deformation pattern is still dominated by the buckling of individual skin bays, including those with the saw-cuts. With the exception of the skin bays affected by the saw-cut, the overall displacement magnitudes are also similar (reference Figure 60 for the pristine 2.5-g DUL results). The FEA results differ from those measured during the test primarily due to differences in which skin bays buckled inward and which buckled outward. Specifically, it is seen that during the test, the saw-cut skin bay located above the span-wise centerline in Figures 119 and 120 buckled outward and this measurement is matched by the FEA results. The saw-cut skin bay located below the span-wise centerline in the same two figures, however, buckled inward and this result is not matched by the FEA analysis. As discussed before in sections 3 and 4, individual skin bays under compression have a potential to adopt one of two stable equilibria. Which one of the two is actually realized depends on several imperfections of the structure that are not accounted for in the FEA that is based on the nominal dimensions, and on the assumption that the structure is completely stress free when the external load is not applied. Thus, the saw-cut bay results are not unique when compared with the previously discussed results without the DSD. Furthermore, for the specific skin bay in question, the technicians who worked on imparting the DSD reported that once the saw-cut was made, they observed a slight tendency of this particular skin bay to display an inward displacement bias in a load-free condition. This observation further confirms the validity of geometry imperfection and/or residual stress being responsible for the differences observed between the test and FEA results in the skin bay areas.

It is seen in Figures 121 and 122 that the overall out-of-plane displacement characteristic of the upper bulkhead panel is also not significantly changed when compared to the results obtained without the DSD (Figure 62). The deformation pattern is still dominated by the buckling of individual skin bays, with the same characteristic pattern of multiple skewed semi-sine-like shapes within individual skin bays. The range of displacement magnitudes for the pristine and DSD crown panel conditions is also comparable.

Overall, a good comparison between the FEA and the measured results is obtained, with the FEA results showing slightly smaller displacement magnitudes for the upper bulkhead panel, especially under the 2.5-g DUL.

The strain results in the forward frame flange, i.e., in the vicinity where the final failure likely originated, are shown in Figure 123. The largest recorded strain in the crown panel substructure just before the final failure of −0.0079 in./in. is seen being reached in this plot. The two strain gauges shown in Figure 123 are located on the side of the DSD where the skin buckled in the direction opposite to that predicted, see location A in Figure 119. Thus, the nearby forward frame flange was also affected by this behavior and, consequently, the FEA and test results correspond to two distinct buckled equilibria. This conclusion is supported by the strain results shown in Figure 124, i.e., on the side of the DSD where the predicted and test results both showed outward buckling. While the agreement between the predicted and test results shown in Figure 124 is not very favorable, it is noticeably better than that of Figure 123. The discrepancy between the prediction and test seen in Figure 124 can be, at least in part, attributed to the presence of several panel thickness discontinuities in the vicinity of the two gauges, introduced by intersections of the frame and stringer flanges. This effect is likely combined with insufficient mesh resolution to accurately capture the local effects associated with thickness changes originating from stack overlaps and terminations. Also, since the initial local damages at the saw-cut tips were noted at 130.3 kips (2.05-g or 81.9% DLL) on the forward frame side and at 131.8 kips (2.07-g or 82.9% DLL) on the aft frame side, their progressing presence could have also contributed to the degraded comparison at the higher loads (the test results evidencing local damages are presented later in this section).

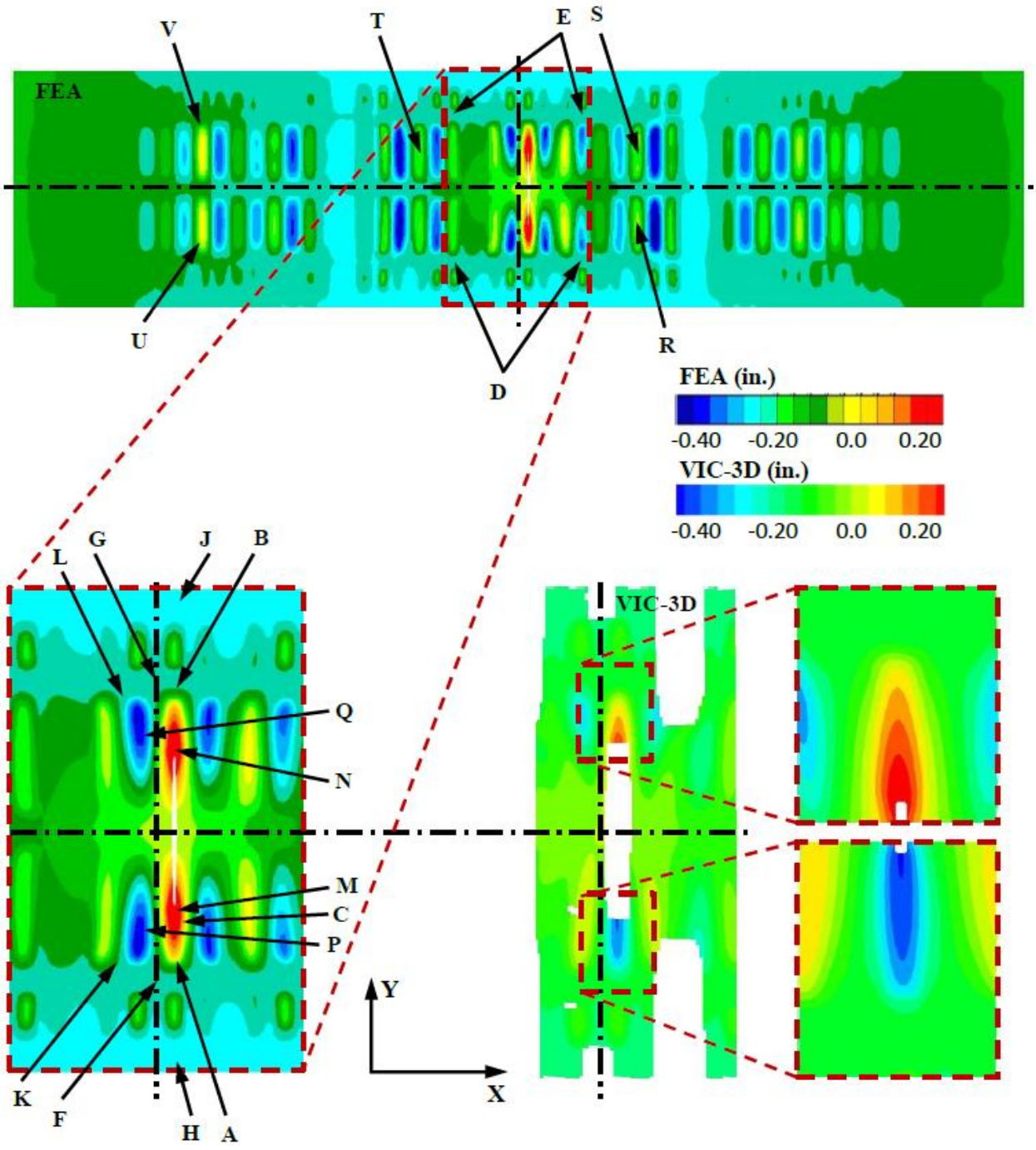

Figure 119. Out-of-plane deformation of the crown panel with DSD under 2.5-g DLL.

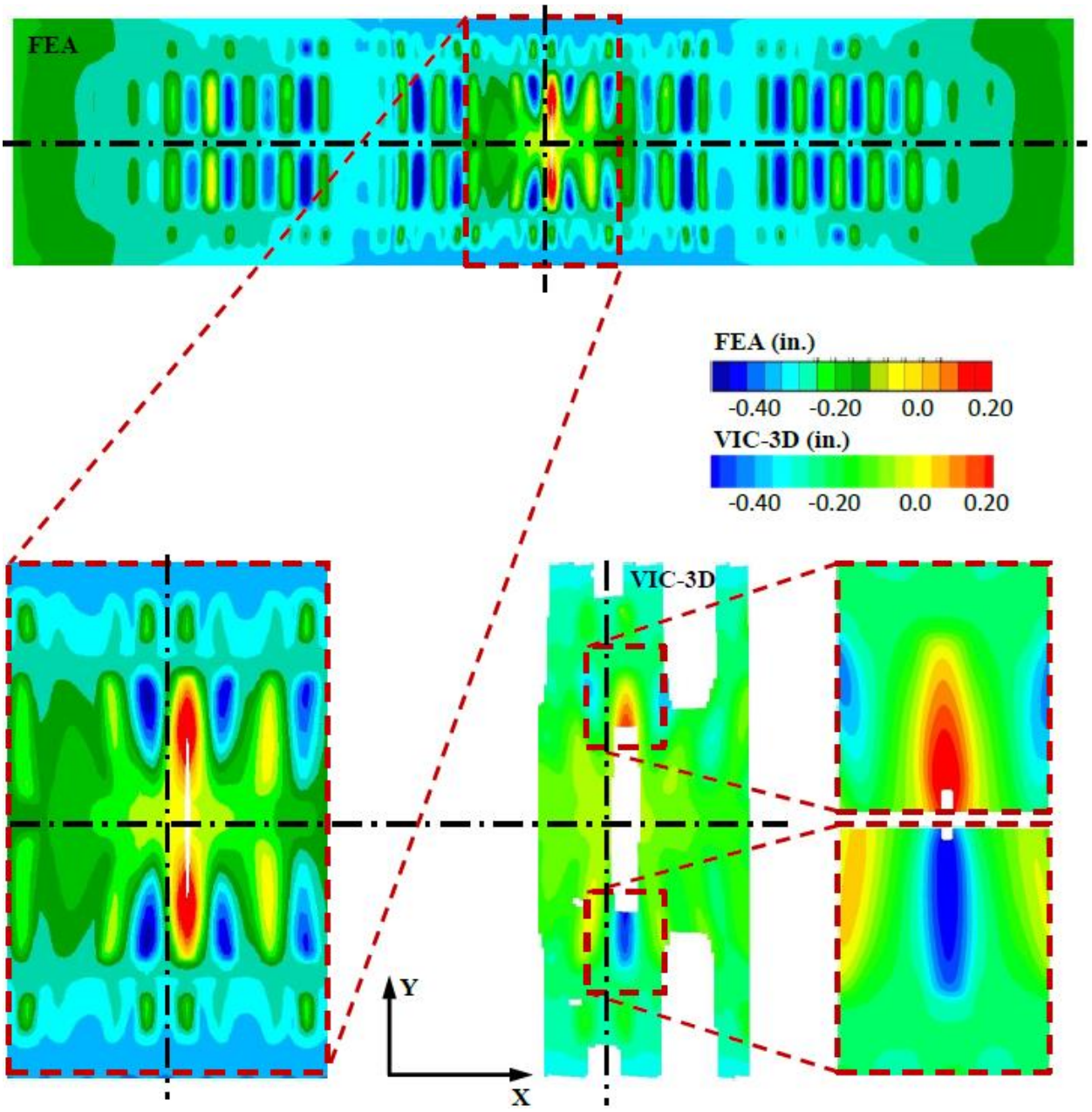

Figure 120. Out-of-plane deformation of the crown panel with DSD under 2.5-g DUL.

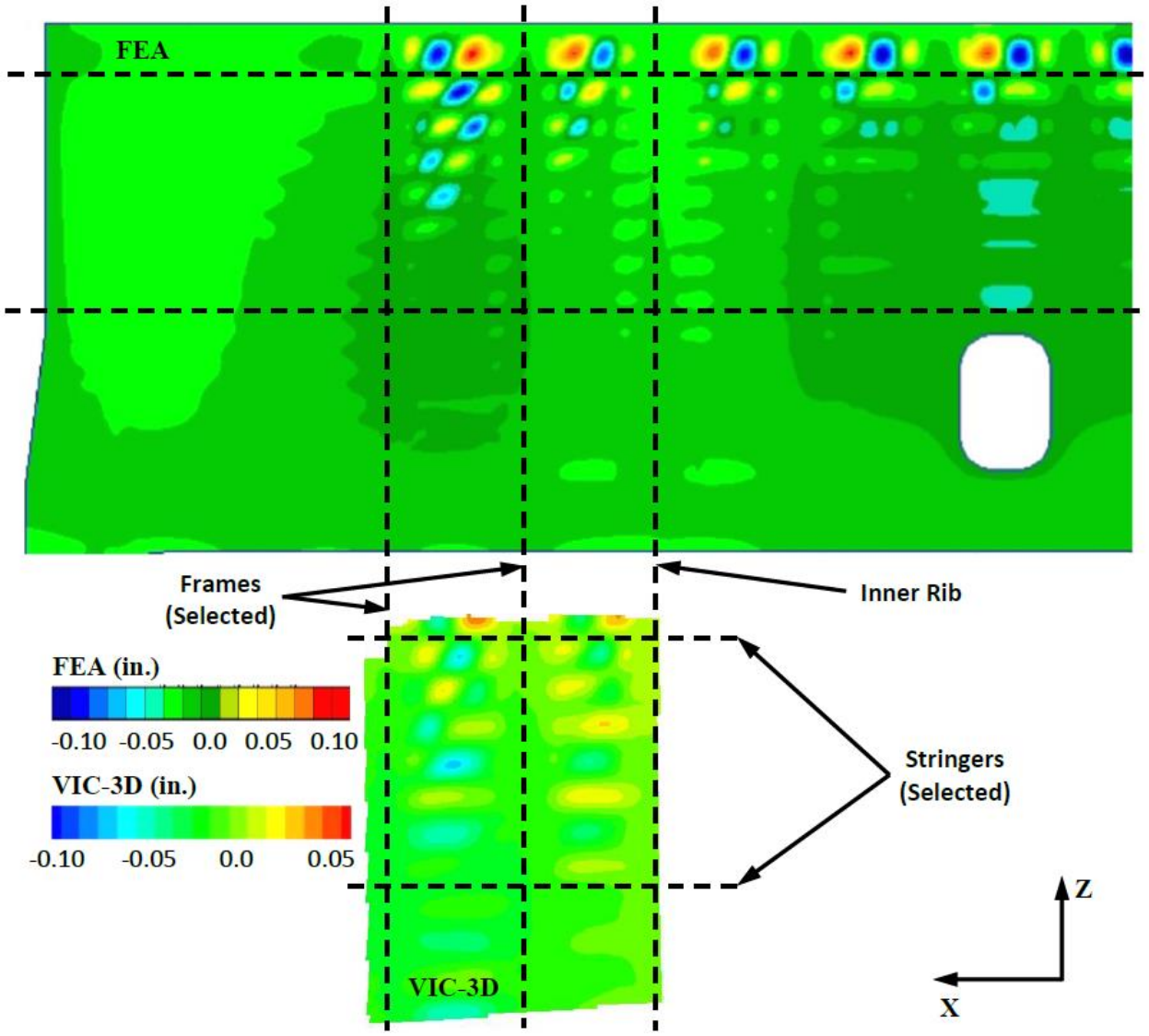

Figure 121. Out-of-plane deformation of the upper bulkhead panel with the crown panel DSD under 2.5-g DLL.

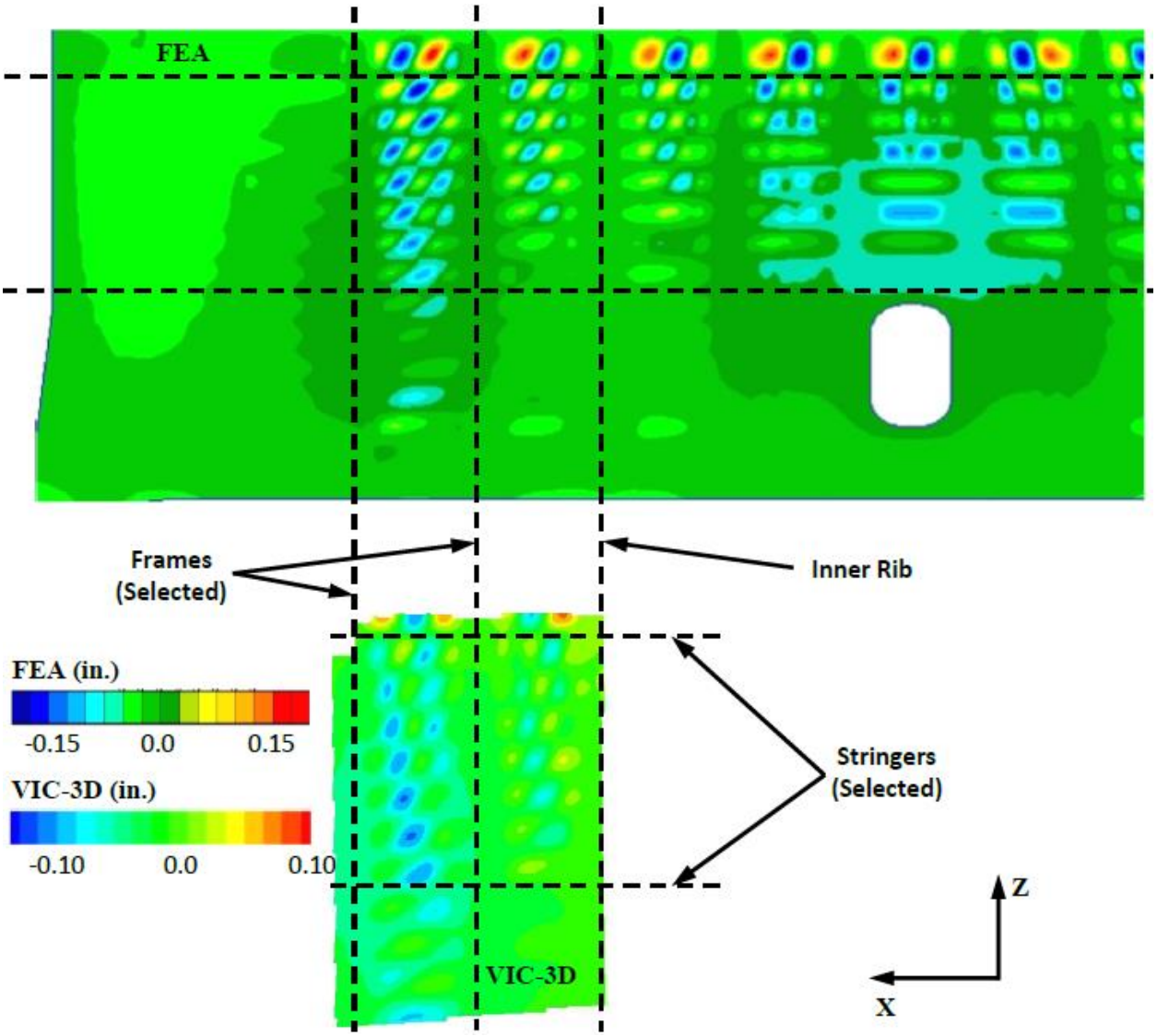

Figure 122. Out-of-plane deformation of the upper bulkhead panel with the crown panel DSD under 2.5-g DUL.

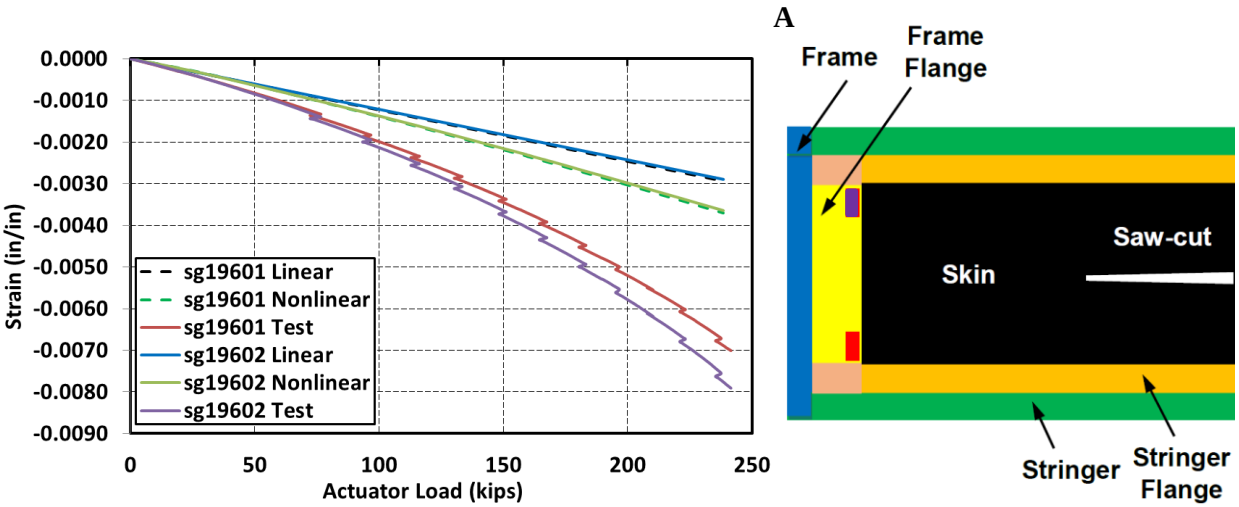

Figure 123. Forward frame flange strains in the vicinity of the DSD up to 2.5-g DUL.

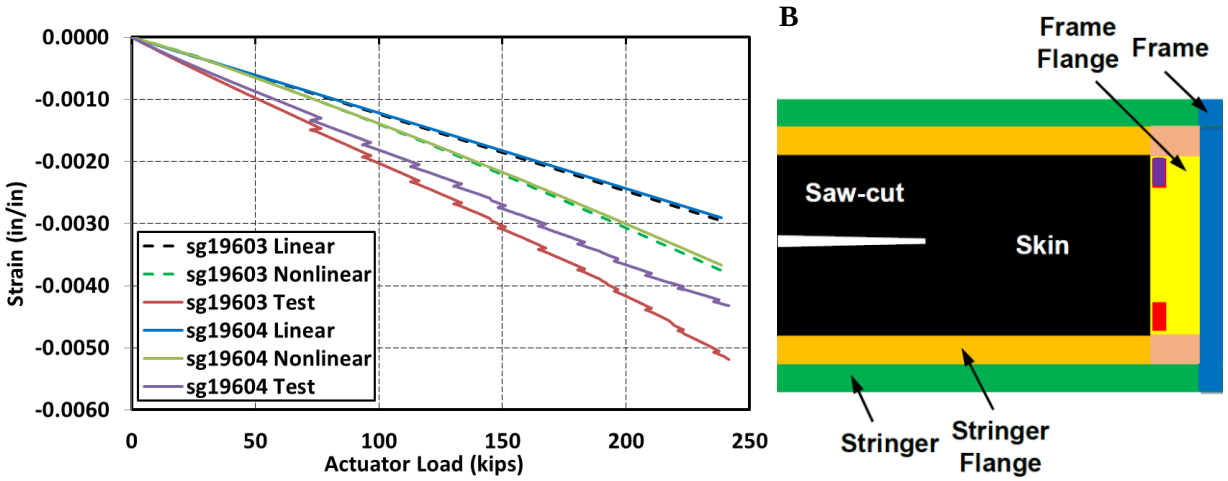

Figure 124. Aft frame flange strains in the vicinity of the DSD up to 2.5-g DUL.

Strain results in the flanges of the two stringers in the vicinity of the DSD are shown in Figure 125. Since the two gauges are affixed in the direction perpendicular to the span-wise direction in which the main loads are carried under the 2.5-g condition, very low strain levels not exceeding 0.00075 in./in. are obtained. The comparison of small values from the FEA prediction and test measurements is not very good, however the main purpose of installing the gauges is achieved. Namely, the two stringer flange gauges were intended to track potential damage progression originating from the saw-cut tips (they are installed on a 45-degree direction extending from the saw-cut tips, which in other PRSEUS tests was found to be a common damage propagation path). In Figure 125, gauge sg19302 corresponding to location C in Figure 119 is showing an event consistent with a localized damage progression at 207.7 kips (or 3.27-g). Since the gauge continues to provide strain measurements above this load, it is concluded that the damage must have occurred in the direct vicinity of the gauge but not directly at the gauge location. This observation is consistent, e.g., with a local skin damage propagation being arrested at the stitch line of the stringer flange in the vicinity of the gauge.

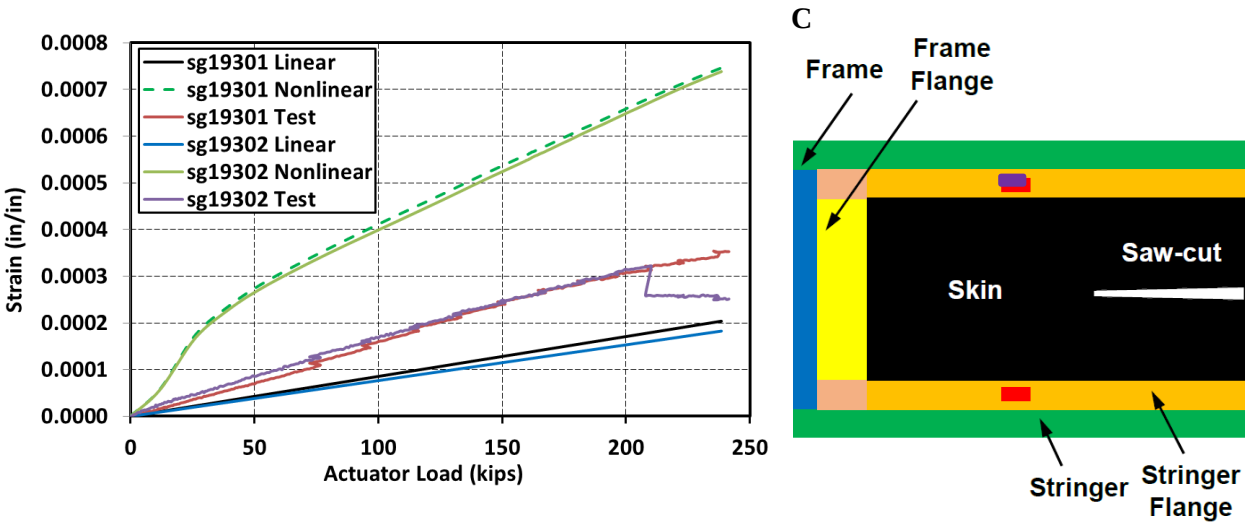

Figure 125. Stringer flange strains in the vicinity of the DSD up to 2.5-g DUL.

The strain results at the tops of the forward and aft frames in the proximity of the DSD are shown in Figures 126 and 127, respectively, and correspond to locations D and E in Figure 119. The strains display moderately nonlinear characteristics reaching approximately −0.0040 in./in. at DUL and, generally, the comparison between the FEA and test results is good. The only gauge among the four symmetrical gauges in Figures 126 and 127 which compares more poorly with increased load is the left gauge at location D in Figure 119, i.e., sg19802. This location corresponds to the quadrant of the panel where the side frame flange gauge, sg19602, produced the largest substructure compressive strain, as presented in Figure 123. This further substantiates the observation that the lower left quadrant of the panel, relative to the DSD as seen in Figures 119 and 120, was the one that experienced the highest strains and where the final failure originated.

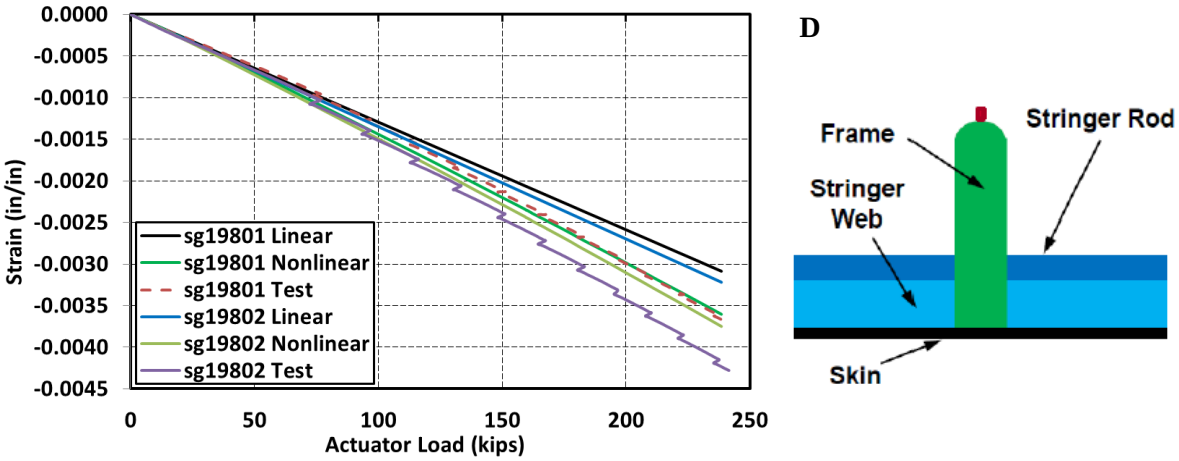

Figure 126. Strains at the top of the forward frame in the vicinity of the DSD up to 2.5-g DUL.

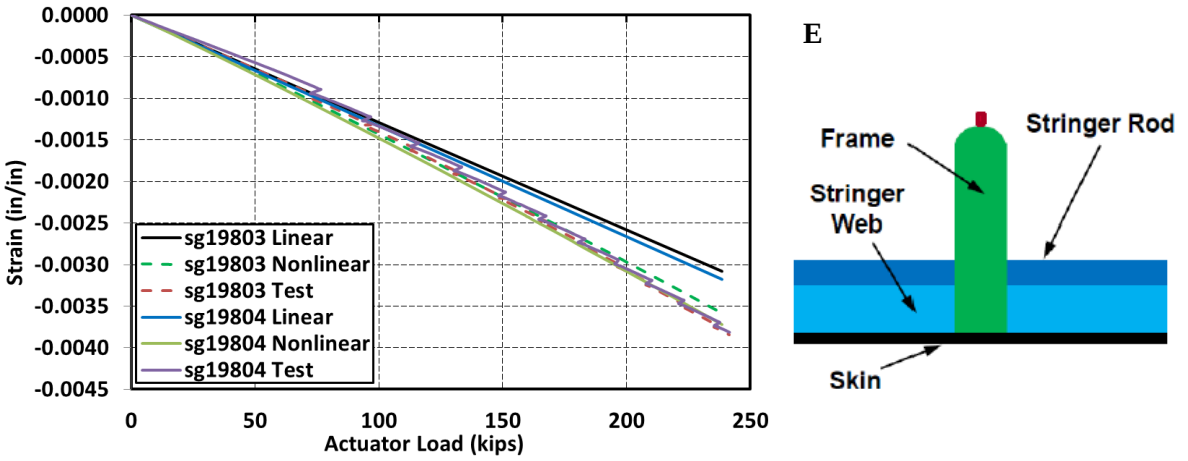

Figure 127. Strains at the top of the aft frame in the vicinity of the DSD up to 2.5-g DUL.

The strain results at the webs of the forward and aft frames in the proximity of the DSD are shown in Figures 128 and 129, respectively, and correspond to locations F and G in Figure 119. The strains display moderately nonlinear characteristics reaching approximately −0.0035 in./in. at DUL and, generally, the comparison between the FEA and test results is very good. More importantly, the strain levels on both sides of the two frame webs are similar: proof that the frames are uniformly compressed across their thicknesses, and no meaningful sideways bending of the frames exist until the failure load is reached. This observation means that buckling of the side frames was not a factor, and that they ultimately failed in strength rather than due to buckling, which is the preferred failure mode, resulting in a higher load carrying capability.

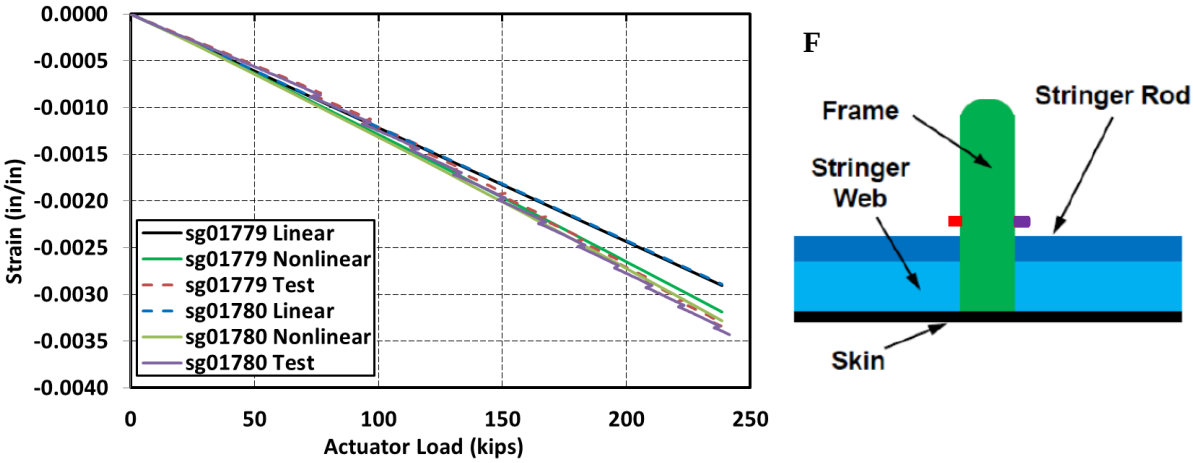

Figure 128. Side-to-side strains in the forward frame web in the vicinity of the DSD up to 2.5-g DUL.

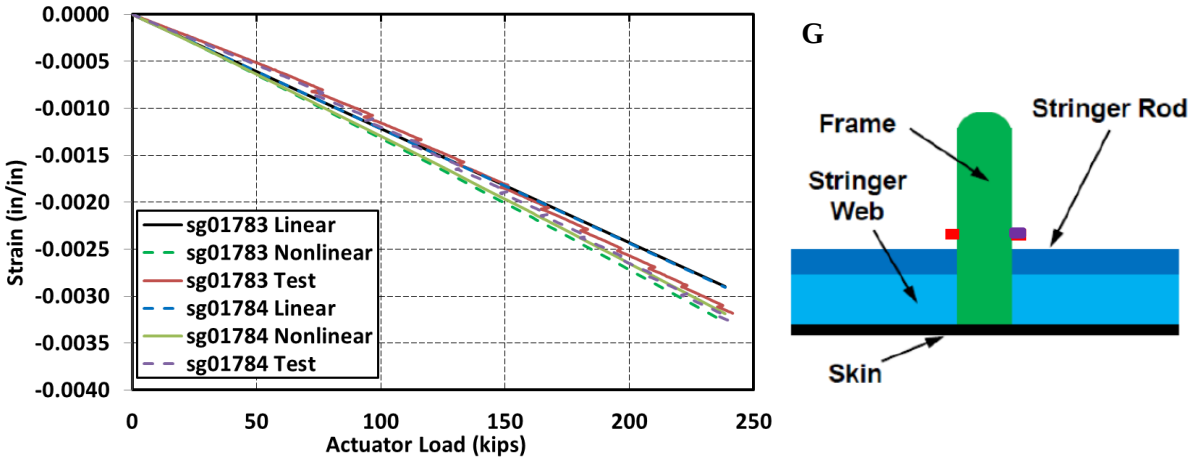

Figure 129. Side-to-side strains in the aft frame web in the vicinity of the DSD up to 2.5-g DUL.

The strain results at the forward and aft T-caps in the proximity of the DSD are shown in Figures 130 and 131, respectively, and correspond to locations H and J in Figure 119. Both predicted and measured strains depart from linear behavior at very similar loads, but the type of the nonlinear behavior differs. The measured strains reach the −0.0034 in./in. to −0.0039 in./in. range at DUL, higher than those predicted. While the predicted strains in the forward and aft T-caps are different, the actual test measurements differ by an even larger margin. Furthermore, in the results discussed thus far, the forward frame flanges (Figure 123), tops (Figure 126), and webs (Figure 128) were typically carrying slightly larger loads than those on the aft side (Figures 124, 127, and 129, respectively). This trend is reversed in the case of the T-caps, where the aft T-cap at failure shows a larger compressive strain than the forward T-cap. The reason for this behavior was not conclusively established.

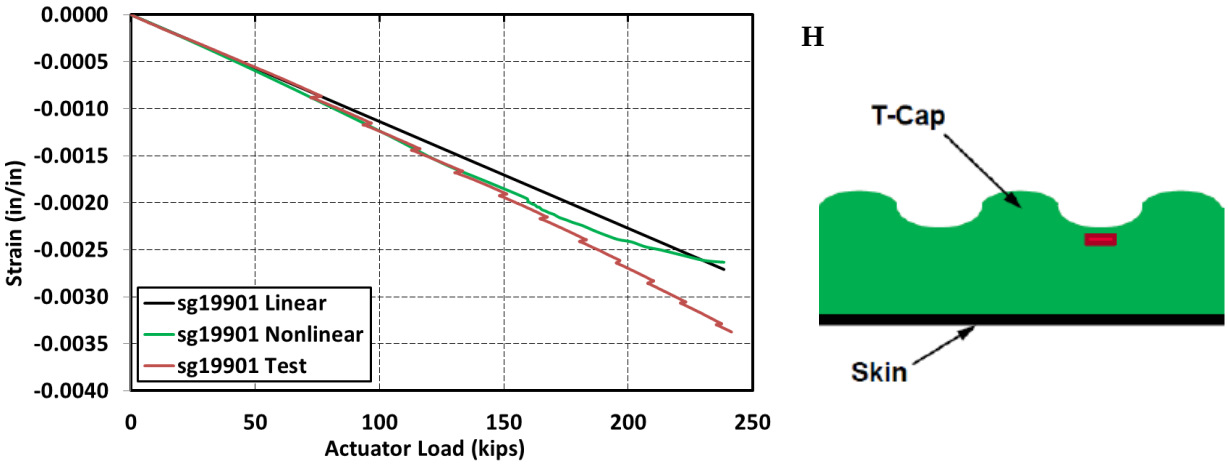

Figure 130. Strains in the forward T-cap in the vicinity of the DSD up to 2.5-g DUL.

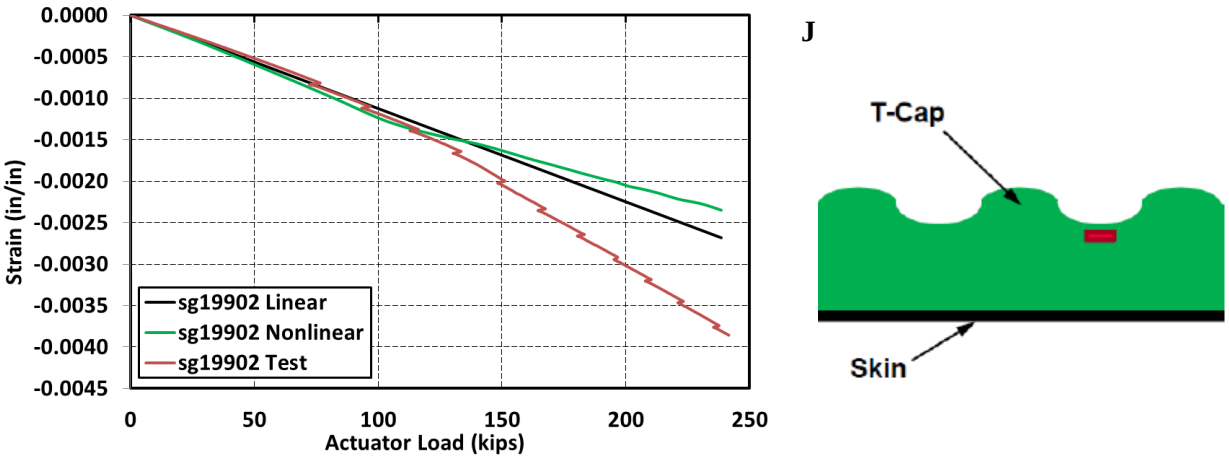

Figure 131. Strains in the aft T-cap in the vicinity of the DSD up to 2.5-g DUL.

The principal strain results at the webs of the stringer in the proximity of the DSD are shown in Figures 132 and 133 and correspond to locations K and L in Figure 119, respectively. The two locations are in the vicinity of the stringer intersection with the forward and aft frames. The strains display slightly nonlinear characteristics, and do not exceed 0.0010 in./in. before final failure, which is a relatively low principal strain level. The nonlinear analysis compares better with the test results than the linear solution, but the agreement is only satisfactory. Since the strain gauges in Figures 132 and 133 are placed very close to the frame-stringer intersections, a factor that might have influenced the comparison was the approach taken to model these intersections. During the development of the FEM it was decided that the bonds between the frames and the stringers are a byproduct of the manufacturing process rather than a by-design bonded joint. Consequently, in the FEM, the frame-stringer intersections were modeled as completely independent surfaces that do not share nodes or are otherwise connected. This modeling assumption warrants further investigation.

Upon closer examination, in both Figures 132 and 133, minimum and maximum strains show discontinuities. For the location near the forward frame intersection, those discontinuities are seen at 189.8 kips actuator load (or 2.98-g) and for the location near the aft frame intersection, at 218.3 kips actuator load (or 3.43-g). The strain discontinuities are indicative of the damage developing in the proximity of the DSD, but not in the subject stringer, as evidenced by the otherwise smooth and continuous strain response after the strain jumps are encountered.

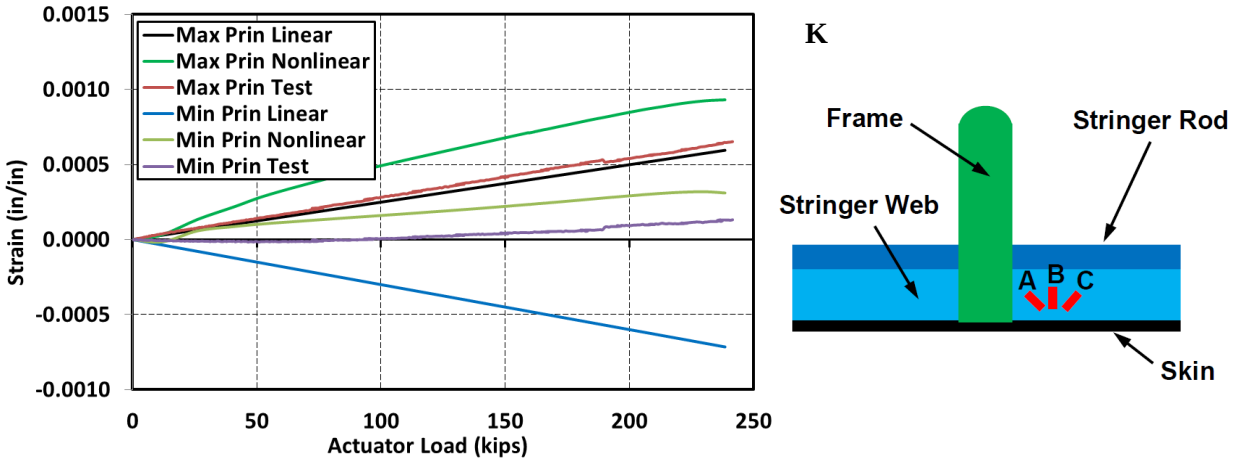

Figure 132. Principal strains in the stringer web near the forward section of the DSD up to 2.5-g DUL (sg01426A/sg01427B/sg01428C).

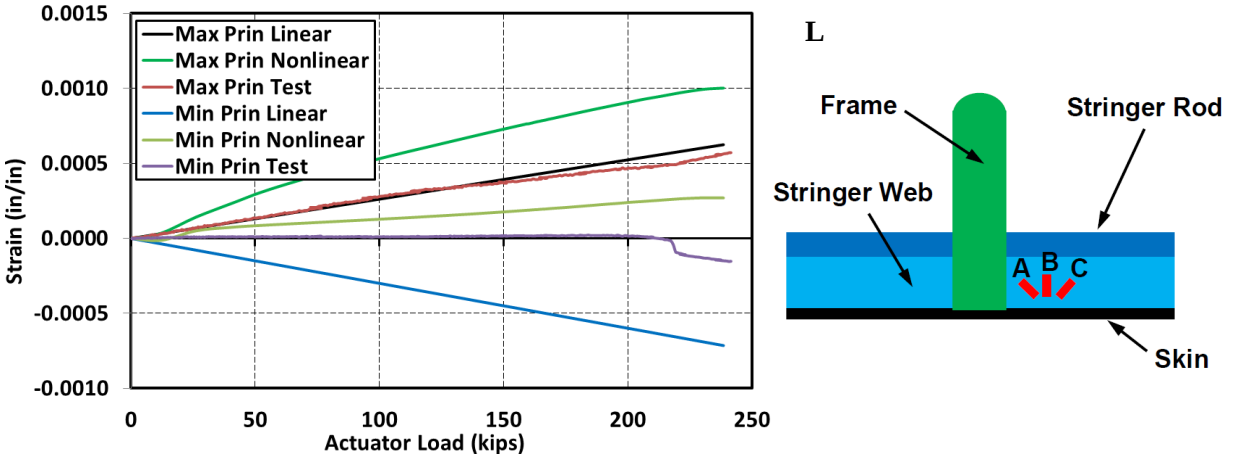

Figure 133. Principal strains in the stringer web near the aft section of the DSD up to 2.5-g DUL (sg01430A/sg01431B/sg01432C).

As briefly mentioned at the beginning of this section, the first evidence of damage occuring in the vicinity of the DSD was noted at 130.3 kips actuator load (or 2.05-g). The two strain gauge measurements taken at the tip of the forward side of the saw-cut are shown in Figure 134. The strain gauge located closer to the saw-cut tip stops producing meaningful readings at the afore-mentioned load. The second gauge, further away from the saw-cut tip, stops recordng meaningful data soon thereafter at 154.0 kips (2.42-g). Such a behavior is indicative of the damage directly affecting the site where the strain gauges are installed.

The FEA results and test measurements shown in Figure 134 do not agree well. This is due to the fact that, per discussion of the out-of-plane displacement results in Figures 119 and 120, the skin bay on the forward side of the DSD buckled in the inward direction, i.e., opposite to the outward direction predicted by the FEA.

A similar damage development sequence to the one described on the forward DSD side was also observed on the aft side of the DSD, as shown in Figure 135. The strain gauge closer to the saw-cut tip stops producing meaningful readings at 131.8 kips actuator load (or 2.07-g), i.e., just 1.5 kips above the symmetric gauge on the forward DSD side. The damage to the area where the second gauge is installed slightly further away from the saw-cut tip can be noted at 173.1 kips actuator load (or 2.72-g).

All four strain values associated with the saw-cut tip damage intiation and progression shown in Figures 134 and 135 are below those discussed for the stringer web strain gauge discontinuities shown in Figures 132 and 133. Thus, it can be concluded that the stringer web strain discontinuities are associated with further damage progression than that at the saw-cut tips.

Finally, in Figure 135, for the aft side saw-cut skin bay that buckled in the outward direction matching the FEA prediction, the agreement between the predicted and measured strains is much more favorable when compared to that of Figure 134.

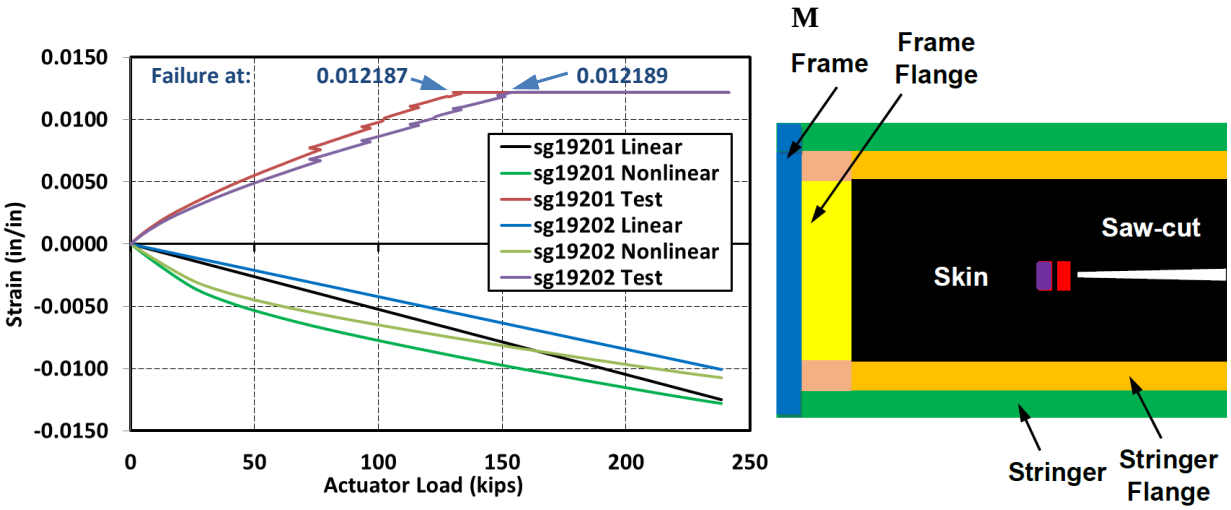

Figure 134. Strains in the forward section of the crown panel skin near the tip of the DSD up to 2.5-g DUL.

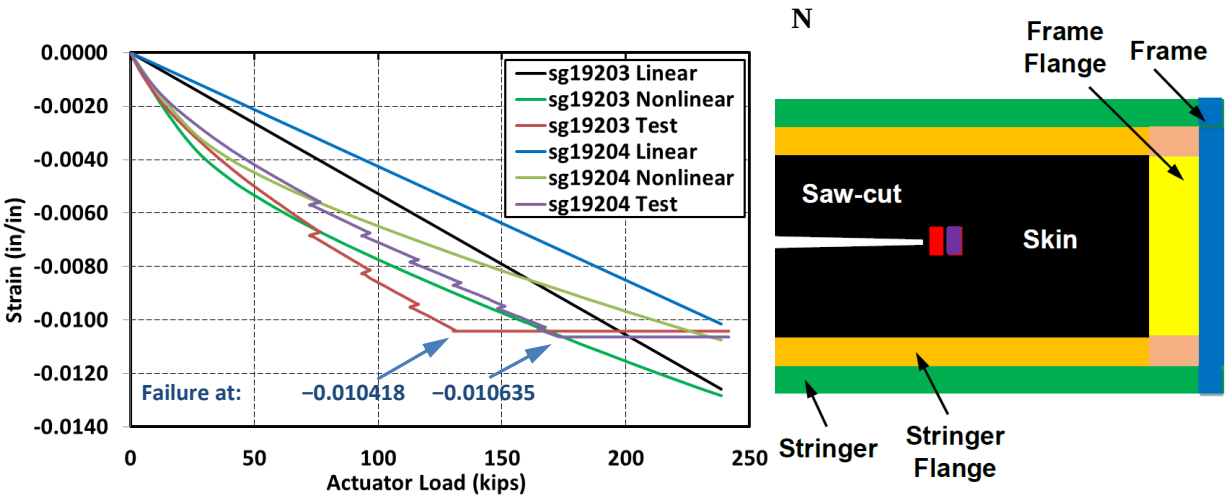

Figure 135. Strains in the aft section of the crown panel skin near the tip of the DSD up to 2.5-g DUL.

The back-to-back strains in the skin bays next to the skin bays with the DSD are shown in Figure 136, and correspond to locations P and Q in Figure 119. In location M, the strain agreement is good except for the fact that the IML test strains compare well with the OML strain predictions, and vice versa. This behavior is consistent with the out-of-plane test displacements shown in Figures 119 and 120. Since the skin bay with the DSD on the forward frame side shows the displacement opposite to that predicted, the next skin bay over also adopts the opposite displacement. Thus, the strain sign reversals between the IML and OML surfaces.

Results at location Q of Figure 119 are shown in Figure 136. A good agreement exists between the FEA results and test measurements at the lower load levels. As the load increases, the comparison deteriorates. This deterioration is likely a result of the damage progressing outwards from the DSD vicinity. While the entire skin bay does not snap through to the opposite equilibrium, the damages developing near the DSD are likely causing the buckled skin shape to become distorted and, consequently, for the strain comparison to deteriorate.

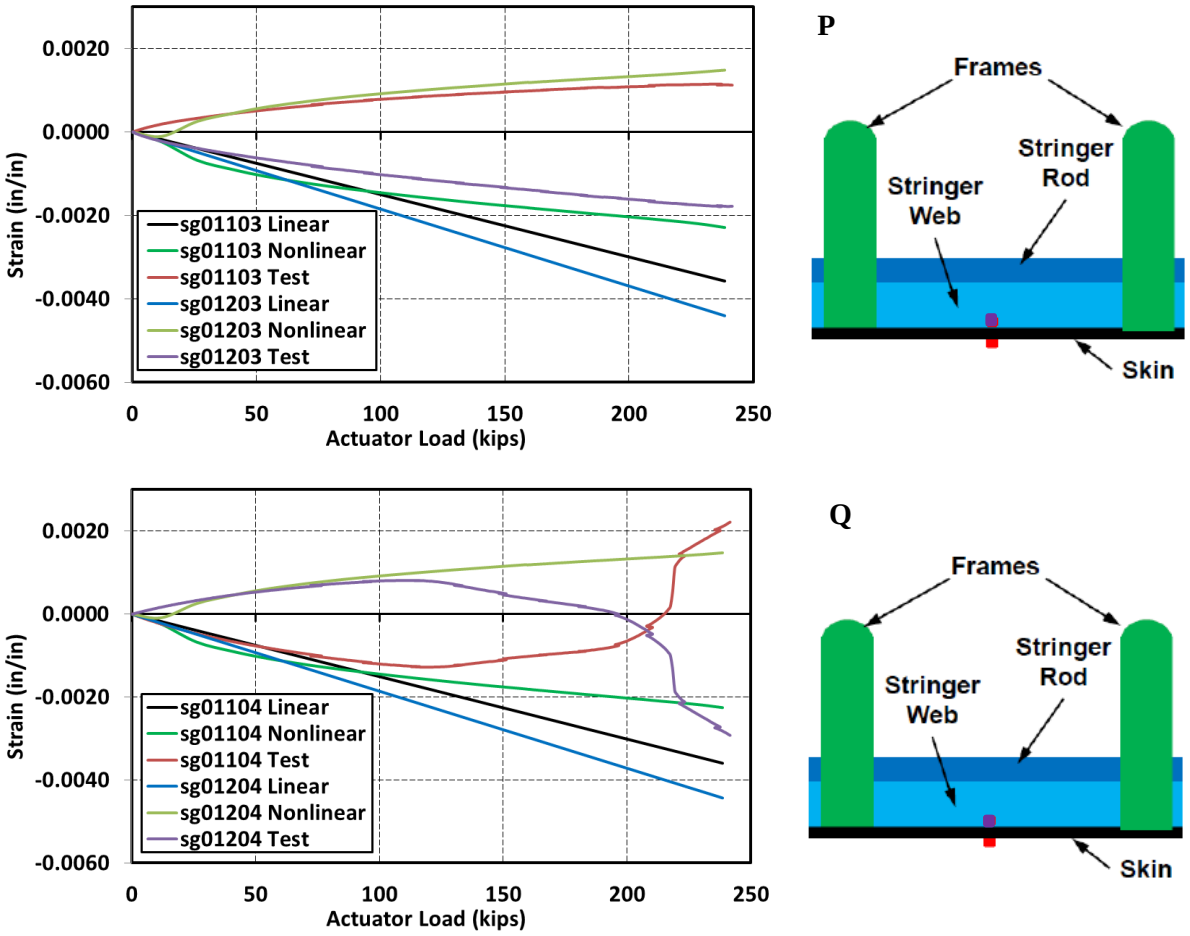

Figure 136. Crown panel back-to-back skin strains in the vicinity of the DSD up to 2.5-g DUL.

The back-to-back skin strains in the skin bays farther away from the DSD, relative to those of Figure 136, are shown in Figure 137 and correspond to locations R, S and T in Figure 119. Overall, a favorable comparison between the FEA results and test measurements is found for locations S and T. These are the two locations on the aft side of the crown panel, the side where the buckling pattern agreed between the prediction and the test. Results at location R shown in Figure 137 display test strains with the opposite sign relative to those predicted, i.e., the IML predictions fall close to the OML test results and vice versa. This behavior is due to the test buckling pattern being the opposite relative to the one predicted.

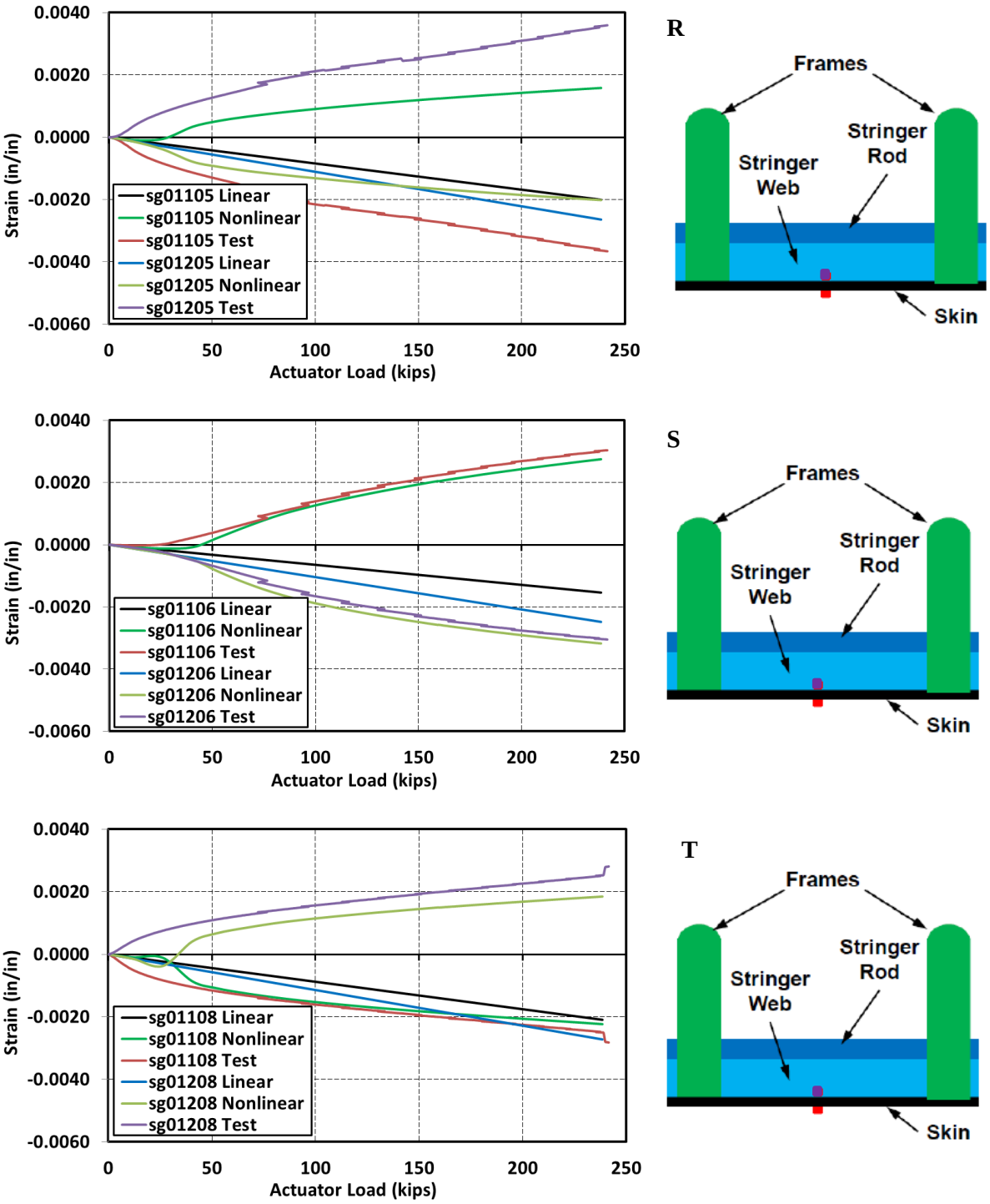

Figure 137. Crown panel back-to-back skin strains away from the DSD up to 2.5-g DUL.

The principal skin strains in the skin bays in the side section of the crown panel are shown in Figure 138 and Figure 139, and correspond to locations U and V in Figure 119, respectively. Favorable agreement between the FEA and test results is found at both locations (at DUL, the difference between the predicted and measured minimum principal strain is 17% at location U and 8.8% at location V). At both locations,

that are distant from the DSD, the strain characteristics are very similar to those obtained for the pristine crown panel condition (see Figure 68 for the pristine strain results at location V).

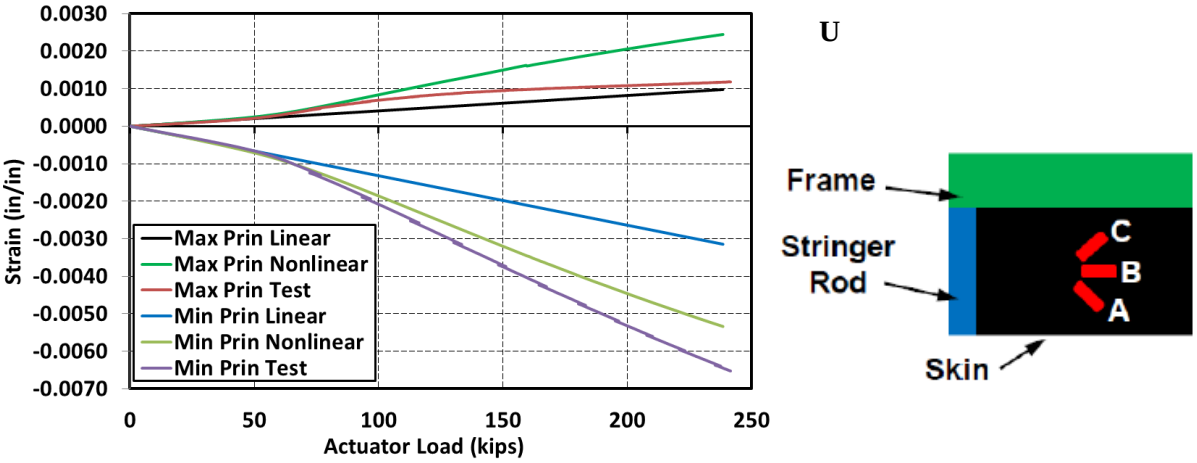

Figure 138. Principal strains in the crown panel skin up to 2.5-g DUL (sg01287A/sg01288B/sg01289C).

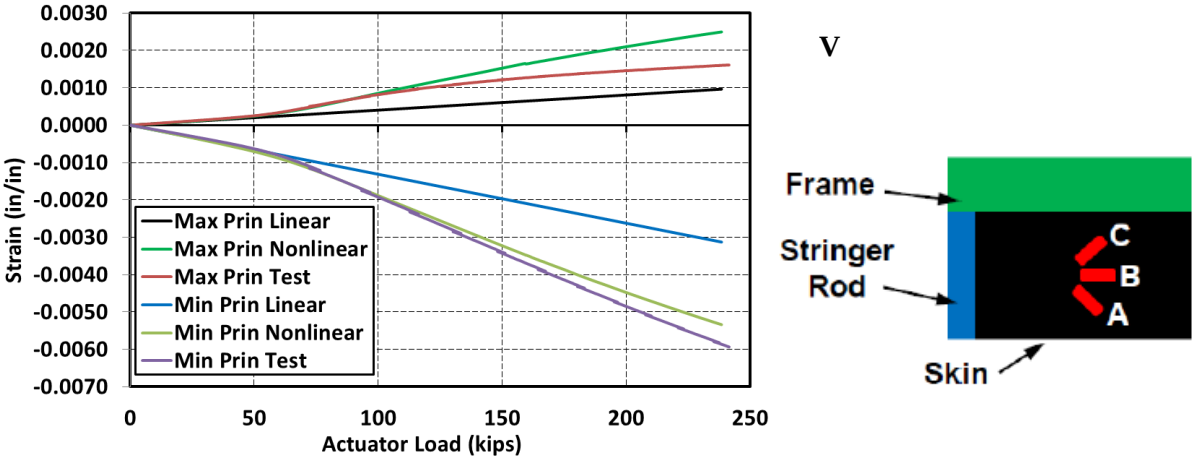

Figure 139. Principal strains in the crown panel skin up to 2.5-g DUL (sg01292C/sg01291B/sg01290A).

To summarize the strain predictions for the crown panel with the DSD, the overall level of agreement was comparable to the pristine 2.5-g case in the low range of the applied load, i.e., below the level where damages originating from the DSD began to develop. Several instances of strain jumps stemming from the damage development and progression were noted at the following actuator load levels: 130.3 kips (shown in Figure 134), 131.8 kips (Figure 135), 154.0 kips (Figure 134), 173.1 (Figure 135), 189.8 kips (Figure 132), and 207.7 kips (Figure 125) and 218.3 (Figure 133). While the list of the actuator load levels where the events occurred is complete, the list of figures that can be used to identify them is selective. With that many incremental damages occurring over nearly half of the entire load range, certain discrepancies between the analysis that does not support progressive damage and the test results can be expected. Thus, given the limited time to prepare and execute the analysis with DSD, as well as the size and computational complexity of the strongly nonlinear analysis with several sections undergoing buckling, the overall outcome of the analysis is considered favorable. The analysis was able to guide a selection of additional strain gauges and other instrumentation, such that a meaningful test data set was acquired.

4. Concluding Remarks

The FEA was used as the primary tool in designing the HWB test article and in guiding its test sequence and instrumentation. Due to computational expediency, a linear FEA was conducted first and provided fairly accurate predictions for sizing of the test article substructure. A nonlinear analysis was conducted next and required significantly longer time to complete. The nonlinear analysis provided higher-fidelity insight into the mechanics of the HWB structure and filled significant analysis gaps remaining due to inherent limitations of the linear analysis. Especially, understanding of the behavior associated with local buckling permitted by the PRSEUS design philosophy was greatly enhanced by the nonlinear analysis. This analysis permitted a design of test instrumentation that produced a more complete data set since the critical locations on the test article were precisely identified and appropriately instrumented.

Conclusions pertaining to the nonlinear FEA as applied to a non-conventional airframe structure constructed using the PRSEUS concept are discussed next in the context of: (1) the global analysis approach, (2) its value as applied to the BVID locations, and (3) the ability to predict failure in the presence of a DSD.

4.1. Global Analysis

The nonlinear FEA provided a reliable analysis tool for a non-conventional HWB configuration constructed using the PRSEUS concept. The analysis was able to accurately predict the significant response characteristics of the structure under several different load conditions of interest. This included precise identification of responses associated with extensive local buckling. The above was achieved using mostly straightforward and intuitive modeling practices, used routinely in aerospace structural analysis. The strain levels in the substructure components, such as frames, stringers, and T-caps were generally predicted with a very good level of accuracy. The skin sections of several panels of the HWB center section test article presented a greater challenge, but the overall mechanics and stability were also effectively captured by the nonlinear analysis.

Only a few locations in the HWB test article FEM necessitated an iterative modeling approach to produce reliable results. PRSEUS analysis efforts prior to the HWB center section analysis involved significantly smaller structures, and a typical element size of 0.25-0.50 in. was used in FEMs to produce converged solutions. The large dimensions of the present test article motivated the use of larger elements to keep the computational effort required to solve the problem within manageable bounds. Thus, an element size of approximately 1 in. was chosen. With such an approach, it came as no surprise that some sections of the original 1-in. grid had to be refined, once the preliminary analysis results became available. Such locations included stringer webs near perpendicular panel joints in proximity of the metallic fittings. These areas were typically characterized by significant changes in the panel thicknesses and the presence of discrete bolt attachments associated with the metallic fittings used to assemble the structure. Local mesh refinements reducing an element size to approximately 0.27 in. were typically sufficient to achieve a converged solution. In most instances, the symmetry of the structure and loads was taken advantage of when refining the mesh. Namely, only one of the four symmetric locations would be refined to minimize the model size increase, and the results from the converged location would be assumed in the remaining three locations that were not re-meshed.

Another modeling challenge stemming from the presence of the metallic fittings was associated with contact modeling. Initially, only bolted joints between composite panels and metallic fittings were modeled using connector elements. This approach effectively permitted penetration of fitting surfaces and composite panel surfaces away from the locations of the bolts. The above behavior in some locations resulted in a large overestimation of strains in the sections of composite panels located adjacent to metallic fittings. To address this issue, but again not to increase the computational size of the problem in a substantial manner, a simplified modeling approach was adopted. Namely, rigid kinematic constraints between the two contact surfaces were used in lieu of modeling the full contact problem. Such an approach accurately accounted

for the contact between the two surfaces, when such existed, but did not permit the two surfaces to become separated. The use of the simplified approach was based on the observation that the local strain results become unrealistically high when a metallic fitting surface was permitted to penetrate the underlying section of the composite panel. At the same time, lack of ability of the metallic fitting to separate from the surface of the underlying panel was significantly less consequential for the strain results. Finally, mesh refinement in only one out of four symmetrical locations is not the only alternative when increasing the overall size of the FEM is of primary concern. Conducting a global-local analysis is another viable option.

The FEM used in the effort reflected the nominal condition of the structure. Namely, any imperfections of geometry of the PRSEUS panels stemming from the thermal warping in the manufacturing process or any residual stresses introduced during the assembly process were not reflected in the FEM. The structure comprised several skin bays that underwent buckling under certain loading conditions. For these skin sections, typically multiple stable buckled equilibria existed. Which buckled equilibrium was actually adopted during the test was often dependent on small structural imperfections not accounted for in the FEM. Thus, several buckled skin bays displayed displacements opposite to those predicted. In many instances, this behavior in the crown panel demonstrated itself in the OML strain gauge reading matching the IML FEA prediction and vice versa, which generally should not be considered detrimental to the quality of the solution. However, switching of more complicated buckling shapes can result in appreciable strain prediction errors. This type of situation was more often experienced in the upper section of the upper bulkhead panel, where individual skin bays would often show three or four skewed semi-sine-like buckled shapes rather than just one simple semi-sine-like shape, very typical for the crown panel. Addressing this problem by reflecting all structural imperfections in the model can be very tedious and requires input data that very often are not available to an analyst. However, few alternatives exist. Perturbing the model in a random fashion to generate a statistical and/or worst case solution would require multiple nonlinear solutions, thus it is also not an appealing alternative.

4.2. BVID Locations

No attempt was made to reflect BVIDs in the FEM. Thus, the comparison of the FEA results with test measurements from the dedicated set of strain gauges installed in proximity of the impact sites in several instances turned out to be inconclusive. To preclude damaging strain gauges dedicated to the BVID sites, these gauges were not installed on the test article until the impacts were imparted, i.e., after the pristine condition testing was concluded. Thus, there existed no pristine condition measurements in the vicinity of the BVID sites. Given the absence of the pristine reference state, one of two possible conclusions was reached when the FEA results and BVID test data were compared at a given impact location. When the comparison was good, there existed a high probability that the effect of BVID on the surrounding structure was minimal. However, when the FEA results did not agree with the test measurements, determining whether actual damage, limitations of FEA, or both factors were responsible for such a state of affairs was more complex. In retrospect, acquiring strain gauge measurements in the vicinities of the intended impact sites ahead of imparting BVIDs seems advantageous, even though some of the gauges might have been damaged in the process of imparting BVID and would need to be replaced. In part (i.e., at the OML impact locations), the decision not to affix impact strain gauges before the impacts was dictated by a desire to maximize the area of the VIC-3D system acquisition. Nevertheless, having strain gauge measurements before and after imparting BVID would create a more direct and straightforward opportunity for comparison.

Further ambiguity stemmed from the fact that some of the external impact sites were located near the edges of substructure flanges, i.e., close to the stack terminations resulting in thickness changes of the panel. Such a selection was motivated by a desire to assess effectiveness of through-the-thickness stitching reinforcement in preventing potential damage propagation. In that sense, the location of the impact strain gauges was unique when compared to those used in the initial pristine testing. Thus, even though a good confidence in the FEA results was developed for the substructure results based on the pristine condition testing, the measurements taken in the pristine condition were not targeting some types of locations that

became of interest in the BVID testing. In other words, the FEA validation based on the pristine condition test results was not inclusive of some of the FEM features potentially important to the BVID effort. For example, a good comparison of stringer or frame results under dominant axial or bending loads acting along the length of the stiffener does not guarantee that strains in the direction perpendicular to the length of the stiffener are accurate at its flange edge.

4.3. Final Test to Failure

As noted previously, because the final test to failure was added to the test plan late in the test planning stage, the extent and scope of the supporting analysis was limited by the schedule. After the DSD was added to the FEM with a refined mesh in its proximity, the same type of nonlinear analysis was executed as previously executed for the pristine test article. No attempt was made to include a progressive failure analysis in the effort. Consequently, the analysis was anticipated to produce accurate results until the damages begin to develop and propagate. After that point, the analysis quality was expected to gradually diminish.

Despite the above limitations, the DSD nonlinear FEA performed before the test was very useful in defining the geometry of the DSD and developing a modified instrumentation plan for the DSD test. First, the analysis provided a guidance as for how wide the DSD saw-cut was needed near the center frame of the panel, so that the edges of the DSD do not come in contact before the final failure occurs. The analysis correctly identified the locations of the first damage origination at the tips of the saw-cut and also the critical final failure locations at the flanges of the side frames (rather than at the frame tops) in the vicinity of the DSD. The analysis also correctly predicted that the side frames and the T-caps of the crown panel would fail in the strength rather than the stability mode (side frame and T-cap crushing rather than buckling). The above information was used to make informed choices with regard to locations of additional strain gauges near the DSD, and also with regard to the extent of the crown panel area for which the full field VIC-3D measurements would be acquired.

The DSD analysis was also prone to predicting buckling shapes opposite to those realized in the test. Since the skin bays with the saw-cut tips also buckled before the onset of initial damage, one of the saw-cut skin bays buckled in the direction opposite to that predicted. While the reason and the potential mitigation measures for this behavior are not different than the ones discussed before for the pristine analysis, it has to be stressed that predicting the correct buckled equilibrium near the DSD is likely more consequential for the DSD analysis than it is for the pristine condition analysis. As stated above, while quantifying and modeling initial geometry imperfections for the entire large FEM does not seem practical nor necessary, such an extra modeling fidelity may be practical and warranted in the most direct proximity of the DSD.

Acknowledgements

The authors express their gratitude to Hsi-Yung (Tom) Wu of Boeing Research and Technology, Huntington Beach, Calif., for his priceless contribution to the development of the FEM and lending his in-depth FEA expertise throughout the analysis task. The authors also acknowledge the entire team at The Boeing Company: Alex Velicki, Kim Linton, Krishna Hoffman, Jaime Baraja, and Peter Shaw. Frank Leone of the NASA Langley Research Center, Hampton, Va., is also gratefully acknowledged for his thorough review of this document.

References

1. Collier, F., Russell, T., Burley, C. L., Nickol, C., Lee, C.-M., and M. T., "Environmentally Responsible Aviation - Real Solution for Environmental Challanges Facing Aviation," *Proceedings of the 27th International Congress of the Aeronautical Sciences*, 2010, Nice, France.
2. Jegley, D. C., Przekop, A., Rouse, M., Lovejoy, A. E., Velicki, A., Linton, K., Wu, H.-Y. T., Baraja, J., Thrash, P., and Hoffman, K., "Development of Stitched Composite Structure for Advanced Aircraft," *Proceedings of the American Socitey for Composites 30th Technical Conference*, Paper 1840, 2015, East Lansing, Mich.
3. Jegley, D. C., and Velicki, A. "Development of the PRSEUS Multi-bay Pressure Box for a Hybrid Wing Body Vehicle," *Proceedings of the 56th AIAA/ASME/ASCE/AHS/ASC Structures, Structural Dynamics, and Materials Conference*, AIAA-2015-1871, 2015, Kissimmee, Fla.
4. Thrash, P., "Manufacturing of a Stitched Resin Infused Fuselage Test Article," *The Composites and Advanced Materials Expo*, 2015, Orlando, Fla.
5. Velicki, A., "Damage Arresting Composites for Shaped Vehicles - Phase I Final Report," NASA/CR-2009-215932, NASA Langley Research Center, 2009, Hampton, Va.
6. Velicki, A., and Jegley, D. C., "PRSEUS Structural Concept Development," *Proceedings of the 55th AIAA Structures, Structural Dynamics, and Materials Conference*, AIAA-2014-0259, 2014, National Harbor, Md.
7. Velicki, A., Yovanov, N., Baraja, J., Linton, K., Li, V., Hawley, A., Thrash, P., DeCoux, S., and Pickell, R., "Damage Arresting Composites for Shaped Vehicles - Phase II Final Report," NASA/CR-2011-216880, NASA Langley Research Center, 2011, Hampton, Va.
8. Przekop, A., Jegley, D. C., Rouse, M., Lovejoy, A. E., and Wu, H.-Y. T., "Nonlinear Analysis and Preliminary Testing Results of a Hybrid Wing Body Center Section Test Article," *Proceedings of the American Socitey for Composites 30th Technical Conference*, Paper 1838, 2015, East Lansing, Mich.
9. Przekop, A., Wu, H.-Y. T., and Shaw, P., "Nonlinear Finite Element Analysis of a Composite Non-cylindrical Pressurized Aircraft Fuselage Structure," *Proceedings of 55th AIAA/ASME/ASCE/ AHS/ASC Structures, Structural Dynamics, and Materials Conference*, AIAA-2014-1064, 2014, National Harbor, Md.
10. Wu, H.-Y. T., Shaw, P., and Przekop, A., "Analysis of a Hybrid Wing Body Center Section Test Article," *Proceedings of 54th AIAA/ASME/ASCE/AHS/ASC Structures, Structural Dynamics, and Materials Conference*, AIAA-2013-1734, 2013, Boston, Mass.
11. Ambur, D. A., Rouse, M., Starnes, J. H., and Stuart, M. J., "Facilities for Combined Loads Testing of Aircraft Structures to Satisfy Structural Technology Development Requirements," *Proceedings of the 5th Annual Advanced Composite Technology Conference*, 1994, Seattle, Wash.
12. Jegley, D. C., Rouse, M., Przekop, A., and Lovejoy, A., "The Behavior of a Stitched Composite Large-Scale Multi-Bay Pressure Box," NASA/TM-2015-218972, 2015, NASA Langley Research Center, Hampton, Va.

13. Lovejoy, A. E., and Przekop, A., "Imparting Barely Visible Impact Damage to a Stitched Composite Large-Scale Pressure Box," *Proceedings of 57th AIAA/ASME/ASCE/AHS/ASC Structures, Structural Dynamics, and Materials Conference*, 2016, San Diego, Calif.
14. Horne, M. R., and Madaras, E., "Acoustic Emission SHM of PRSEUS Multi-Bay Box Tests," NASA/CR-2015-218976, 2015, NASA Langley Research Center, Hampton, Va.
15. Moore, J. P., Przekop, A., Juarez, P. D., and Roth, M. C., "Fiber Optic Rosette Strain Gauge Development and Application on a Large-Scale Composite Structure," NASA/TM-2015-218970, 2015, NASA Langley Research Center, Hampton, Va.
16. Johnston, P. H., and Juarez, P. D., "Ultrasonic Nondestructive Evaluation of PRSEUS During Large-Scale Load Testing and Rod Push-Out Testing," NASA/TM-2015-000000, 2015, NASA Langley Research Center, Hampton, Va.
17. Title 14 Code of Federal Regulation, Part 25 "Airworthiness Standards: Transport Category Airplanes," Subpart C "Structure," Electronic Code of Federal Regulations, http://www.ecfr.gov/cgi-bin/text-idx?c=ecfr&tpl=/ecfrbrowse/Title14/14cfr25_main_02.tpl."
18. "Composite Aircraft Structure, Advisory Circular AC No. 20-107B, U.S. Department of Transportation, Federal Aviation Administration," August 2010.
19. "MSC Nastran 2012.2 quick reference guide,." MSC Software Corporation, 2012, Santa Ana, Calif.
20. McGowan, D. M., Ambur, D. R., and McNeil, S. R., "Full-field Structural Response of Composite Structures: Analysis and Experiment," *Proceedings of the 44th AIAA/ASME/ASCE/AHS/ASC Structures, Structural Dynamics and Materials Conference*, AIAA-2003-1623, 2003, Norfolk, Va.

Appendix A. Strain Gauge Numbering Scheme

The strain gauge numbering scheme used during the HWB center section testing is shown below.

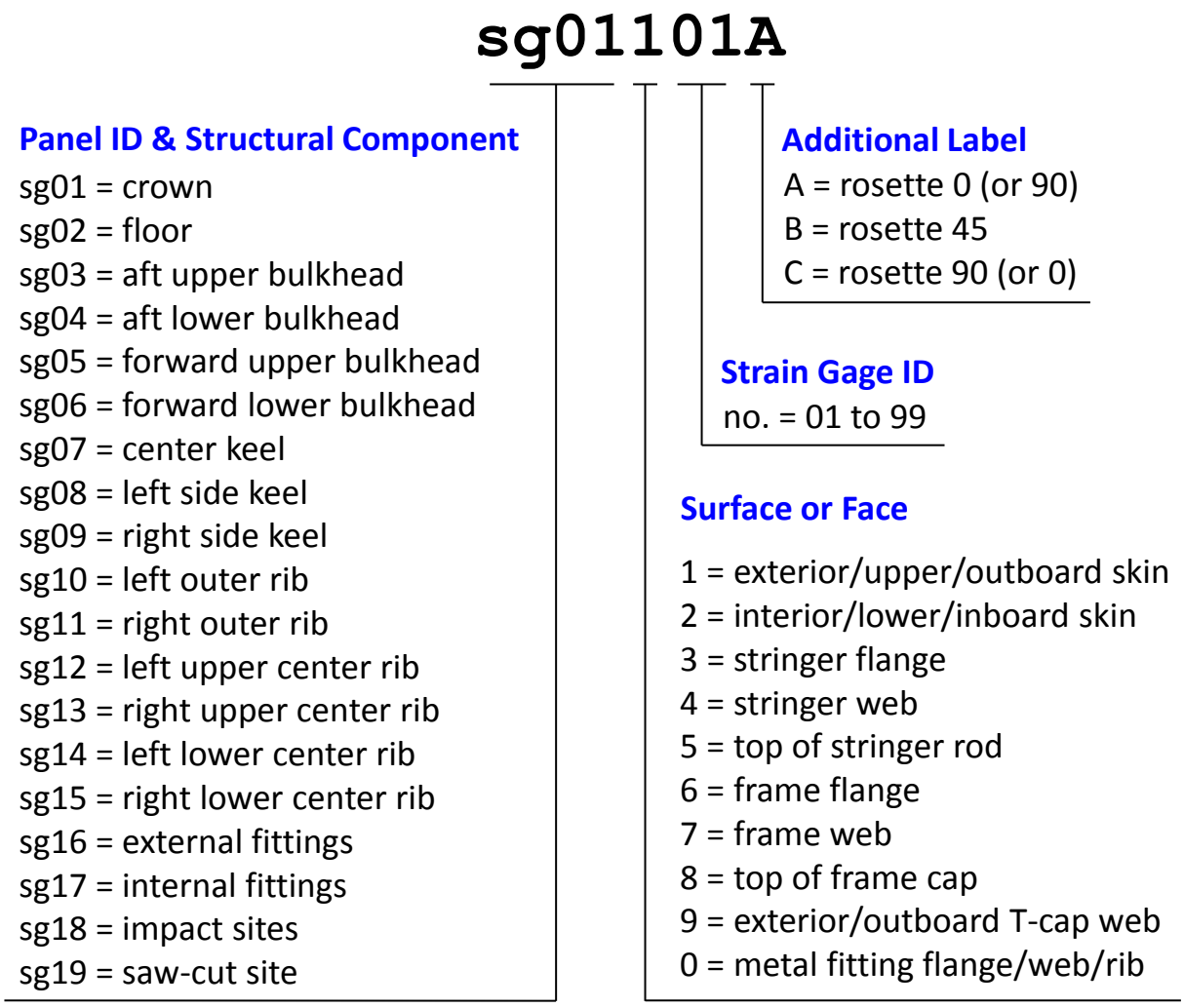

REPORT DOCUMENTATION PAGE

Form Approved
OMB No. 0704-0188

1. REPORT DATE *(DD-MM-YYYY)*	2. REPORT TYPE	3. DATES COVERED *(From - To)*
01-04-2016	Technical Memorandum	

4. TITLE AND SUBTITLE

Finite Element Analysis and Test Results Comparison for the Hybrid Wing Body Center Section Test Article

5a. CONTRACT NUMBER

5b. GRANT NUMBER

5c. PROGRAM ELEMENT NUMBER

6. AUTHOR(S)

Przekop, Adam; Jegley, Dawn C.; Rouse, Marshall; Lovejoy, Andrew E.

5d. PROJECT NUMBER

5e. TASK NUMBER

5f. WORK UNIT NUMBER

338881.02.22.07.01.01

7. PERFORMING ORGANIZATION NAME(S) AND ADDRESS(ES)

NASA Langley Research Center
Hampton, VA 23681-2199

8. PERFORMING ORGANIZATION REPORT NUMBER

L-20629

9. SPONSORING/MONITORING AGENCY NAME(S) AND ADDRESS(ES)

National Aeronautics and Space Administration
Washington, DC 20546-0001

10. SPONSOR/MONITOR'S ACRONYM(S)

NASA

11. SPONSOR/MONITOR'S REPORT NUMBER(S)

NASA-TM-2016-218973

12. DISTRIBUTION/AVAILABILITY STATEMENT

Unclassified - Unlimited
Subject Category 39
Availability: NASA STI Program (757) 864-9658

13. SUPPLEMENTARY NOTES

14. ABSTRACT

This report documents the comparison of test measurements and predictive finite element analysis results for a hybrid wing body center section test article. The testing and analysis efforts were part of the Airframe Technology subproject within the NASA Environmentally Responsible Aviation project. Test results include full field displacement measurements obtained from the video image correlation in three dimensions systems and discrete strain measurements obtained using both unidirectional and rosette resistive gauges. Most significant results are presented for the critical five load cases exercised during the test. Final test to failure after inflicting severe damage to the test article is also documented. Overall, good comparison between predicted and actual behavior of the test article is found.

15. SUBJECT TERMS

Blended wing body; Composite; Graphite-epoxy; Hybrid wing body; PRSEUS; Stitching

16. SECURITY CLASSIFICATION OF:			17. LIMITATION OF ABSTRACT	18. NUMBER OF PAGES	19a. NAME OF RESPONSIBLE PERSON
a. REPORT	b. ABSTRACT	c. THIS PAGE			STI Help Desk (email: help@sti.nasa.gov)
					19b. TELEPHONE NUMBER *(Include area code)*
U	U	U	UU	119	(757) 864-9658